Brooijmans, G. et al. (2019) Les Houches 2019 Physics at TeV Colliders: New Physics Working Group Report. In: 11th Les Houches Workshop on Physics at TeV Colliders : PhysTeV Les Houches (PhysTeV 2019), Les Houches, France, 10-28 Jun 2019.

There may be differences between this version and the published version. You are advised to consult the publisher's version if you wish to cite from it.

http://eprints.gla.ac.uk/212402/

Deposited on: 18 March 2020

LES HOUCHES 2019: PHYSICS AT TEV COLLIDERS
NEW PHYSICS WORKING GROUP REPORT

G. Brooijmans[1], **A. Buckley**[2], **S. Caron**[3,4], **A. Falkowski**[5],
B. Fuks[6,7], **A. Gilbert**[8], **W. J. Murray**[9,10], **M. Nardecchia**[11],
J. M. No[12], **R. Torre**[13,14], **T. You**[14,15], **G. Zevi Della Porta**[16], **(convenors)**
G. Alguero[17], J. Y. Araz[18], S. Banerjee[19], G. Bélanger[20], T. Berger-Hryn'ova[21],
J. Bernigaud[22,23], A. Bharucha[24], D. Buttazzo[25], J. M. Butterworth[26], G. Cacciapaglia[27],
A. Coccaro[13], L. Corpe[26], N. Desai[28], A. De Simone[29,30], J. Dutta[31,32], A. Farbin[33], S. Fichet[34],
T. Flacke[35], S. Ganguly[36], S. Gascon-Shotkin[27], T. Gonzalo[37], A. Goudelis[38], P. Gras[39],
R. S. Gupta[19], M. Habedank[40], J. Heisig[41], L. Hendriks[3], S. Jain[42], A. Jueid[43], D. Kar[44],
S. Kraml[17], A. Kvellestad[45,46], K. D. Lane[47], J. Langford[45], A. Leinweber[48], A. Lesauvage[27],
A. Lessa[49], J. Mamuzic[50], D. Marzocca[30], E. Merényi[51], A. Mjallal[20], K. A. Mohan[52],
A. Morandini[29,30], G. Moreau[5], S. Mutzel[24], C. Nellist[3,4], S. Otten[3,53], P. Pani[54], L. Panizzi[55],
M. Pierini[56], G. Polesello[57], W. Porod[58], H. B. Prosper[59], A. Pukhov[60], J. Quevillon[17],
A. Raklev[46], H. Reyes-González[17], R. Ruiz[41], R. Ruiz de Austri[50], J. Schouwenberg[3,4],
S. Sekmen[61], D. Sengupta[62], C. Smith[17], M. Son[63], D. Sperka[47], B. Stienen[3,4], K. Tobioka[59],
M. van Beekveld[3,4], E. Venturini[64], N. Vignaroli[25,65], R. Vilalta[66], W. Waltenberger[67],
N. Wardle[45], G. Watt[19], M. White[48], S. L. Williamson[7,68], D. Yallup[26], J. Zurita[22,23]

[1] Physics Department, Columbia University, New York, NY 10027, USA

[2] School of Physics and Astronomy, University of Glasgow, Glasgow, UK

[3] IMAPP, Radboud University, Nijmegen, the Netherlands

[4] Nikhef, Amsterdam, the Netherlands

[5] Laboratoire de Physique des 2 Infinis Irène Joliot-Curie d'Orsay (IJCLab), Bât. 100, CNRS / PARIS-SACLAY, F-91898 ORSAY Cedex, France

[6] Institut Universitaire de France, 103 Boulevard Saint-Michel, 75005 Paris, France

[7] Laboratoire de Physique Théorique et Hautes Energies (LPTHE), UMR 7589, Sorbonne Université et CNRS, 4 place Jussieu, 75252 Paris Cedex 05, France

[8] Northwestern University, Evanston, USA

[9] Department of Physics, University of Warwick, Coventry, United Kingdom

[10] Particle Physics Department, Rutherford Appleton Laboratory, Didcot, United Kingdom

[11] Sapienza - Universita di Roma, Piazzale Aldo Moro 2, 00185, Roma, Italy

[12] Departamento de Fisica Teorica and Instituto de Fisica Teorica, IFT-UAM/CSIC, Cantoblanco, 28049, Madrid, Spain,

[13] INFN, Sezione di Genova, Via Dodecaneso 33, I-16146 Genova, Italy

[14] CERN, Theoretical Physics Department, Geneva, Switzerland

[15] DAMTP, University of Cambridge, Wilberforce Road, Cambridge, CB3 0WA, UK; Cavendish Laboratory, University of Cambridge, J.J. Thomson Avenue, Cambridge, CB3 0HE, UK

[16] CERN, Beams Department, Geneva, Switzerland

[17] Laboratoire de Physique Subatomique et de Cosmologie, Université Grenoble-Alpes, CNRS/IN2P3, 53 Avenue des Martyrs, F-38026 Grenoble, France

[18] Concordia University, 7141 Sherbrooke St. West, Montréal, QC, Canada H4B 1R6

[19] Institute for Particle Physics Phenomenology, Department of Physics, Durham University, Durham DH1 3LE, United Kingdom

[20] LAPTh, Univ. Grenoble Alpes, USMB, CNRS, 9 Chemin de Bellevue, F-74940 Annecy, France

[21] Univ. Grenoble Alpes, Univ. Savoie Mont Blanc, CNRS, IN2P3-LAPP, Annecy, France

[22] Institute for Nuclear Physics (IKP), KIT Karlsruhe Institute of Technology, Hermann-von-Helmholtz-Platz 1, D-76344 Eggenstein-Leopoldshafen, Germany

[23] Institute for Theoretical Particle Physics (TTP), Karlsruhe Institute of Technology, Engesserstraße 7, D-76128 Karlsruhe, Germany

[24] Aix Marseille Univ, Université de Toulon, CNRS, CPT, Marseille, France

[25] INFN Sezione di Pisa, Largo Bruno Pontecorvo 3, 56127 Pisa, Italy

[26] Department of Physics & Astronomy, University College London, Gower St., London, WC1E 6BT, UK

[27] Univ. Lyon, Université Claude Bernard Lyon 1, CNRS/IN2P3, UMR5822 IPNL F-69622 Villeurbanne, France

[28] Department of Theoretical Physics, Tata Institute of Fundamental Research, Mumbai 400005, India

[29] SISSA, Trieste, Italy

[30] INFN Sezione di Trieste, SISSA, Via Bonomea 265, 34136, Trieste, Italy

[31] Regional Centre for Accelerator-based Particle Physics, Harish-Chandra Research Institute, HBNI, Chhatnag Road, Jhunsi, Allahabad-211019, India

[32] II. Institut für Theoretische Physik, Universität Hamburg, Luruper Chaussee 149, 22761 Hamburg, Germany,

[33] University of Texas Arlington, USA

[34] International Institute of Physics, UFRN, Av. Odilon Gomes de Lima 1722 - Capim Macio - 59078-400 - Natal-RN, Brazil

[35] Center for Theoretical Physics of the Universe, Institute for Basic Science (IBS), Daejeon, 34126, Korea

[36] Weizmann Institute of Science, Israel

[37] School of Physics and Astronomy, Monash University, Melbourne, VIC 3800, Australia

[38] Laboratoire de Physique de Clermont (UMR 6533), CNRS/IN2P3, Univ. Clermont Auvergne, 4 Av. Blaise Pascal, F-63178 Aubière Cedex, France

[39] CEA Institut de Recherche sur les lois Fondamentales de l'Univers, Université Paris-Saclay, Gif-sur-Yvette, France

[40] Department of Physics, HU Berlin, Germany

[41] Centre for Cosmology, Particle Physics and Phenomenology (CP3), Université catholique de Louvain, Chemin du Cyclotron 2, B-1348 Louvain-la-Neuve, Belgium

[42] School of Physics & Astronomy, University of Minnesota, Minneapolis MN 55455, United States of America

[43] Department of Physics, Konkuk University, Seoul 05029, Republic of Korea

[44] School of Physics, University of Witwatersrand, Johannesburg, South Africa

[45] Department of Physics, Imperial College London, UK

[46] Department of Physics, University of Oslo, Norway

[47] Department of Physics, Boston University, Boston, MA 02215, USA

[48] University of Adelaide, Adelaide, Australia

[49] Centro de Ciências Naturais e Humanas, Universidade Federal do ABC, Santo André, 09210-580 SP, Brazil

[50] Instituto de Física Corpuscular, CSIC-Universitat de València, Spain

[51] Rice University, Houston, Texas, USA

[52] Department of Physics and Astronomy, Michigan State University, East Lansing, Michigan-48824, USA

[53] GRAPPA, University of Amsterdam, the Netherlands

[54] Deutsches Elektronen Synchrotron, DESY, 15738 Zeuthen, Germany

[55] Department of Physics and Astronomy, Uppsala University, Box 516, SE-751 20 Uppsala, Sweden

[56] CERN, Experimental Physics Department, Geneva, Switzerland

[57] INFN, Sezione di Pavia, Via Bassi 6, 27100 Pavia, Italy

[58] Uni. Würzburg, Campus Hubland Nord, D-97074 Würzburg, Germany

[59] Department of Physics, Florida State University, Tallahassee, Florida 32306, USA

[60] Skobeltsyn Institute of Nuclear Physics, Moscow State University, Moscow 119992, Russia

[61] Department of Physics, Kyungpook National University, Daegu, South Korea

[62] Department of Physics and Astronomy, 9500 Gilman Drive, University of California, San Diego, USA

[63] Department of Physics, Korea Advanced Institute of Science and Technology, 291 Daehak-ro, Yuseong-gu, Daejeon 34141, Republic of Korea

[64] Physik-Department, Technische Universität München, 85748 Garching, Germany

[65] Dipartimento di Fisica "E. Fermi", Università di Pisa, Largo Bruno Pontecorvo 3, 56127 Pisa, Italy

[66] University of Houston, Houston, Texas, USA

[67] Institut für Hochenergiephysik, Österreichische Akademie der Wissenschaften, Nikolsdorfer Gasse 18, 1050 Wien, Austria

[68] Institute for Theoretical Physics (ITP), Karlsruhe Institute of Technology, 76128 Karlsruhe, Germany

Abstract

This report presents the activities of the 'New Physics' working group for the 'Physics at TeV Colliders' workshop (Les Houches, France, 10–28 June, 2019). These activities include studies of direct searches for new physics, approaches to exploit published data to constrain new physics, as well as the development of tools to further facilitate these investigations. Benefits of machine learning for both the search for new physics and the interpretation of these searches are also presented.

Acknowledgements

Contents

Tools and Methods   122

Machine Learning   178

Introduction

G. Brooijmans, A. Buckley, S. Caron, A. Falkowski, B. Fuks, A. Gilbert, W. J. Murray, M. Nardecchia, J. M. No, R. Torre, T. You, G. Zevi Della Porta

This document is the report of the New Physics session of the 2019 Les Houches Workshop 'Physics at TeV Colliders'. The workshop brought together theorists and experimenters who discussed a significant number of novel ideas related to beyond the Standard Model and Higgs physics. New computational methods and techniques, including machine learning, were considered, with the aim of improving the technology available for theoretical, phenomenological and experimental new physics studies.

A first set of contributions uses the precise measurements of high mass Drell-Yan e^+e^- and $\mu^+\mu^-$ production to constrain new physics, either using their ratio to investigate signals related to the hints for lepton flavor universality violation observed by LHCb, or using a SMEFT analysis to put model-independent constraints on all the dimension-six effective operators which can interfere with the Standard Model contribution. A second set of contributions examines leptoquarks and vector-like quarks: one evaluates whether a leptoquark solution to the $R_{D^{(*)}}$ deviations can be tested at the LHC through final states including the hadronic decay of a τ lepton, a heavy quark (b or t) and missing transverse momentum. Another uses CONTUR to study bounds on cascade decays of leptoquarks and vector-like quarks from existing searches. A last contribution in this area tests if in a simplified model a vanilla leptoquark solution to the $R_{D^{(*)}}$ deviations can meet relic abundance constraints if the leptoquark is the mediator to a dark sector. Two other contributions are oriented towards dark sectors: there is a study of freeze-in scenarios where the mediator to the dark sector is a heavy vector-like fermion with a mass that is higher than the reheating temperature, making prompt LHC dark matter searches become relevant again, unlike in conventional scenarios of freeze-in. This is followed by a study of long-lived particle signatures of freeze-out at the LHC, identifying blind spots in the current analyses and making suggestions for improvement.

The next series of contributions are directed at the Higgs boson. Two of these use CONTUR to study in one case bounds on Gildener-Weinberg models of electroweak symmetry breaking and in a second the sensitivity of ATLAS, CMS and LHCb measurements to a Dark Matter model involving two Higgs doublets and an additional pseudoscalar mediator. The Higgs Yukawa couplings for charm and top are studied in the context of off-shell Higgs measurements, with sensitivity projections for the HL-LHC in these processes. There is an estimate of the LHC sensitivity to exotic Higgs decays to Za, with $a \to \gamma\gamma, \mu\mu, \tau\tau$ and its interpretation when a is an axion-like particle, as well as one that examines the potential for discovery and measurement of CP properties for a light scalar decaying to a pair of photons produced through vector boson fusion. A final Higgs-focused contribution considers probing the $Zt_R\bar{t}_R$ and $hZt_R\bar{t}_R$ interactions using $pp \to t\bar{t}hZ$ and $pp \to t\bar{t}hj$ processes at future hadron colliders.

This is followed by reports on development of a variety of tools: EFT2OBS is a tool to map an effective field theory parametrization to experimental constraints, demonstrated using the Higgs Effective Lagrangian. With ATLAS and CMS having made progress towards publishing more details of their results, the usage of simplified or full likelihood information in two public re-interpretation tools, MADANALYSIS 5 and SMODELS is tested. A complementary set of contributions evaluate on the one hand a probabilistic approach to identify pairs of

analyses that can safely be considered uncorrelated in global BSM reinterpretation fits, and on the other hand the potential of analysis description languages to assist, and even automate, the comparison of multiple analyses. There is an overview of functional and technical updates to CONTUR, and a description and comparison of public tools that can utilise experimental information to reproduce and recast the LHC results with acceptable accuracy. Two final topics in this section examine whether it is possible to preserve searches in the same way as measurements are preserved, and thus automate the re-interpretation process for searches to be as fast and efficient as it is for measurements, and for a given measurement expected to be performed at the LHC, what precision needs to be achieved in order to exclude a certain region of parameter space of a specific new physics model.

Finally, in a section on machine learning, a first report evaluates whether Machine Learning (ML) can be used to examine models of new physics in their full dimensionality, and a second studies model-independent signal detection algorithms, with a particular focus on approaches that are based on unsupervised machine learning. This last contribution also provides a benchmark LHC dataset, for example for the comparison of signal detection algorithms.

The meeting in Les Houches has fostered a large number of discussions between theorists and experimenters. On the timescale required for these proceedings, only a fraction of the ideas could be examined in depth. Even those that could not converge to a written contribution have paid off through the breadth of searches conducted by experimenters and the understanding of the challenges placed on an experiment by the ever-changing theoretical landscape. We expect that many more future results will benefit from the discussions held at the workshop.

New physics

Contribution 1

Lepton flavor universality ratio in high-mass dilepton production at LHC

T. Berger-Hryn'ova, D. Buttazzo, J. Dutta, D. Marzocca, M. Son

While the Standard Model has proven tremendously successful, much experimental evidence points to it not being a complete description of our universe. The searches for new phenomena are therefore an important component of the LHC experimental program, where a number of analyses are looking for signs of new heavy particles decaying to different final states. Although up to date there is no direct evidence for BSM phenomena at the LHC, there are several 2–3σ hints of deviations of from the SM predictions in decays of B mesons, in $b \to sll$ and $b \to c\tau\nu_\tau$ transitions [1–4].

If these and other deviations of a similar kind are confirmed, they signal a potential departure from lepton flavour universality (LFU). LFU follows directly from the assumption that the SM gauge group, SU(3)×SU(2)×U(1), is one and the same for all three generations of fermions. This implies that all leptons couple universally to the gauge bosons, and that the only difference in their interactions is caused by the difference in mass, e.g. in their interactions with the Higgs field. Thus any departure from LFU is a sign of the existence new phenomena at the next energy scale, similar to nuclear beta decay and other weak transitions pointing to the existence of electroweak W and Z bosons.

The $b \to sll$ and $b \to c\tau\nu_\tau$ transitions are connected to $b\bar{s} \to \ell\ell$ and $b\bar{c} \to \ell\nu$ scattering processes by crossing symmetry [5]. Thus any new phenomena which affect these B meson decays should lead to a deviation from the SM prediction in the dilepton mass spectra, in a LFU-violating manner.

The most precise differential high-mass Drell-Yan (HMDY) cross-section measurement to date is based on the 20.3 fb^{-1} of proton–proton (pp) collision data at centre-of-mass energy of 8 TeV collected by the ATLAS experiment in 2012 [6]. It covers dielectron and dimuon final states in mass range between 116 and 1500 GeV and electron and muon pseudo-rapidities ($|\eta|$) up to 2.5. A total experimental precision of better than 2 (11)% in each channel below 200 (1000) GeV. Dominant systematic uncertainties are due to $t\bar{t}$ and multijet backgrounds. Above approximately 250 GeV statistical uncertainties become dominant in each of the channels.

Inspired by the LFU tests done in B-physics at low energy, We propose to study the differential LFU ratio

$$R_{\mu\mu/ee}(m_{\ell\ell}) \equiv \left(d\sigma(pp \to \mu^+\mu^-)/dm_{\ell\ell}\right)\left(d\sigma(pp \to e^+e^-)/dm_{\ell\ell}\right)^{-1} ,$$

as a both theoretically and experimentally cleaner observable, although in the current implementation of the analysis only the luminosity and pdf uncertainties are expected to cancel in the ratio. It is important for future measurements to reduce uncertainties on this ratio as much as possible to investigate any potential discrepancy with respect to the SM expectation of one. The measured $R_{\mu\mu/ee}(m_{ll})$ from the ATLAS 8 TeV analysis, with the 1σ band, is shown in Fig. 1 (left). All uncertainties in each channel have been summed in quadrature. Fig. 1 (right)
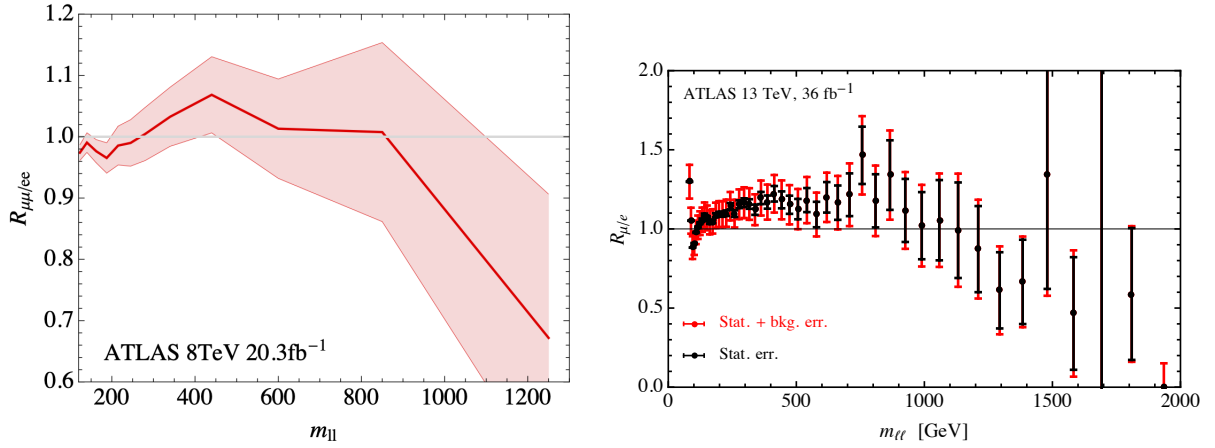
Figure 1: Ratio of dimuon to dielectron high-mass Drell-Yan cross-sections as a function of dilepton mass. Input data from (right) Ref. [6] and (left) Ref. [7].

shows that a similar precision is reached in narrow resonance search with $36\,fb^{-1}$ of pp collision data at centre-of-mass energy of 13 TeV collected by the ATLAS experiment in 2015–2016 [7]. Potential impact on this ratio from various BSM scenarios is discussed in Ref. [8].

The experimental results in the dielectron and dimuon channels will be improved by addition of the full Run 2 data set which has about 14–21 times higher statistics (depending on dilepton mass) and should decrease the available statistical uncertainties approximately by a factor of 4 (per experiment), making the measurement statistically limited only above 500 GeV assuming the current binning. For the ATLAS measurement in the dielectron final state, there is also possibility to double the studied pseudo-rapidity range up to 4.9 (for one of the two electrons), which would provide better sensitivity to BSM due to additional coverage in the angular distributions of the final states.

Contribution 2

Global SMEFT analysis of LHC dilepton tails

J. Bernigaud, A. Bharucha, D. Buttazzo, J. Dutta, D. Marzocca, P. Pani, G. Polesello, M. Son, E. Venturini, N. Vignaroli

Abstract

The high-energy tail of the Drell-Yan production of two leptons at the LHC is a powerful probe of new physics. In this proceedings the AT-LAS 8 TeV data is used to put model-independent constraints on all the dimension-six effective operators which can interfere with the Standard Model contribution, without assumptions on the flavor structure. The ATLAS analysis provides fiducial measurements of differential cross sections in invariant mass and in the two-dimensional plane of invariant mass and dilepton rapidity. Likelihoods are derived for both, as well as using only the linear or also the quadratic dependence of the cross section on the effective field theory coefficients. Code containing these likelihoods is provided,[1] allowing for a straightforward derivation of the limits in any specific model.

1 Introduction

It is well known that the high-energy tail of the dilepton invariant mass distribution in $pp \rightarrow \ell^+\ell^-$ at a hadron collider is potentially sensitive to very high New Physics (NP) scales, possibly even above the on-shell production threshold. In this case the effect of heavy NP can be parametrised in a model-independent way using an effective field theory (EFT) approach, adding to the Standard Model (SM) a set of higher-dimension effective operators, the leading contribution to this process being generated by those of dimension six. Specifically, semi-leptonic four-fermion effective operators contribute to the Drell-Yan process with a leading contribution growing, with respect to the SM one, as $\delta\mathcal{A}/\mathcal{A}_{\rm SM} \sim s/(g_{\rm SM}^2\Lambda^2)$, where s is the invariant mass of the dilepton system, $g_{\rm SM}$ is a typical SM electroweak coupling, and $1/\Lambda^2$ is the coefficient of the effective operators. It is then clear that the high-energy tail of the dilepton invariant mass distribution has an enhanced sensitivity to the effect of these operators. The constraints derived from this process have been shown to be competitive with some limits from flavour physics [9, 10] and electroweak precision measurements at LEP, even though the LHC precision is worse than that of LEP [11,12]. Ref. [8] used the limits from this process to put constraints on some specific flavor structures in relation to possible solutions of the experimental anomalies in B-physics.

While several new physics models can potentially be constrained by this process, a general, model-independent, and easily applicable set of constraints is still not available. In Ref. [8] a fit in the Gaussian approximation was performed including all semi-leptonic dimension-six operators with an energy-growing interference with the SM, however the analysis used a 13 TeV

---

[1]The likelihoods can be downloaded at this address: `people.sissa.it/~dmarzocc/dileptonATLAS8TeVchiSQ.zip`.

ATLAS analysis [7] (now updated in [13]) which was more focussed on resonance searches than precision SM measurements, therefore treating the uncertainties less carefully, and didn't provide the general global likelihood from the fit.

In this work we use the ATLAS 8 TeV analysis of $pp \to \ell^+\ell^-$ (with $\ell = e, \mu$) with 20.3 fb^{-1} of luminosity [6], which provides both the unfolded differential cross section in invariant mass $\frac{d\sigma}{dm_{\ell\ell}}$, as well as the double-differential cross section in invariant mass and (pseudo-)rapdity $\frac{d^2\sigma}{dm_{\ell\ell}d|y_{\ell\ell}|}$ (or $\frac{d^2\sigma}{dm_{\ell\ell}d|\Delta\eta_{\ell\ell}|}$) at the Born-level in QED, separately for the electron and muon channels, in bins of invariant mass from 116 to 1500 GeV. Our goal is to provide general constraints on EFT coefficients from LHC dilepton tails, studying also the effect of adding information on the rapidity distribution to the fit.

Much stronger constraining power is expected from 13 TeV data, which however is still not analysed at the same level of sophistication as the 8 TeV data, see however [14] for an early study by CMS and [13, 15] for NP resonance searches in dilepton tails by CMS and ATLAS.

2 EFT dependence

The SM effective field theory (SMEFT) is constructed by adding to the SM a set of gauge-invariant higher-dimension operators, suppressed by powers of the cutoff scale Λ, corresponding to the mass scale of the new physics states. Such an effective theory can be used to study in a model-independent way new physics effects in processes with a typical energy $E \ll \Lambda$. Assuming baryon and lepton number conservation, the leading effects are described by dimension-six operators

$$\mathcal{L}_{\text{EFT}} = \sum_j \frac{c_j}{\Lambda^2} \mathcal{O}_j + O(\Lambda^{-4}). \tag{1}$$

In the Warsaw basis [16], those which contribute at the tree-level to the high-energy tails of $pp \to \ell^+\ell^-(+j)$, with $\ell = e, \mu$, and interfere with the Standard Model Drell-Yan contribution growing like E^2/Λ^2, are the following semileptonic four-fermion operators: [2]

$$\begin{array}{|ll|l|}
\hline
(\mathcal{O}_{lq}^{(1)})_{\alpha i} = (\bar{l}_\alpha \gamma_\mu l_\alpha)(\bar{q}_i \gamma^\mu q_i) & (\mathcal{O}_{lq}^{(3)})_{\alpha i} = (\bar{l}_\alpha \gamma_\mu \sigma^a l_\alpha)(\bar{q}_i \gamma^\mu \sigma^a q_i) \\
(\mathcal{O}_{qe})_{i\alpha} = (\bar{q}_i \gamma^\mu q_i)(\bar{e}_\alpha \gamma^\mu e_\alpha) & \\
(\mathcal{O}_{lu})_{\alpha i} = (\bar{l}_\alpha \gamma_\mu l_\alpha)(\bar{u}_i \gamma^\mu u_i) & (\mathcal{O}_{ld})_{\alpha i} = (\bar{l}_\alpha \gamma_\mu l_\alpha)(\bar{d}_i \gamma^\mu d_i) \\
(\mathcal{O}_{eu})_{\alpha i} = (\bar{e}_\alpha \gamma_\mu e_\alpha)(\bar{u}_i \gamma^\mu u_i) & (\mathcal{O}_{ed})_{\alpha i} = (\bar{e}_\alpha \gamma_\mu e_\alpha)(\bar{d}_i \gamma^\mu d_i) \\
\hline
\end{array}, \tag{2}$$

where l and q are the $SU(2)_L$ left-handed doublets, e, u and d are the right-handed singlets, and α (i) is a lepton (quark) flavor index. In order to work with dimensionless parameters, we can reabsorb the EFT scale Λ redefining the coefficients as:

$$C_i \equiv c_i \frac{v^2}{\Lambda^2} = \frac{c_i}{\sqrt{2}G_f \Lambda^2}, \tag{3}$$

with $v = 246$ GeV. Excluding operators with t_R or t_L (which cannot be probed in $pp \to \ell\ell$), there are 36 independent flavor-diagonal operators (18 for muons and 18 for electrons) [8]. The complete list of coefficients is given in Tab. 1.

---

[2] Another set of operators contributing to the $pp \to \ell^+\ell^-$ process are those which affect the Z couplings to leptons and quarks. These, however, are already well constrained by LEP data [17], and their effect does not increase with the energy but scales as v^2/Λ^2, therefore it remains always too small to have a sizable impact in the high-energy tails.

$(C^{(1)}_{lq})_{\alpha 1}$	$(C^{(1)}_{lq})_{\alpha 2}$	$(C^{(+)}_{lq})_{\alpha 3}$
$(C^{(3)}_{lq})_{\alpha 1}$	$(C^{(3)}_{lq})_{\alpha 2}$	
$(C_{qe})_{1\alpha}$	$(C_{qe})_{2\alpha}$	$(C_{qe})_{3\alpha}$
$(C_{lu})_{\alpha 1}$	$(C_{lu})_{\alpha 2}$	
$(C_{ld})_{\alpha 1}$	$(C_{ld})_{\alpha 2}$	$(C_{ld})_{\alpha 3}$
$(C_{eu})_{\alpha 1}$	$(C_{eu})_{\alpha 2}$	
$(C_{ed})_{\alpha 1}$	$(C_{ed})_{\alpha 2}$	$(C_{ed})_{\alpha 3}$

Table 1: List of the EFT coefficients included in our analysis, the index $\alpha = 1, 2$ describes lepton flavor. We defined $(C^{(+)}_{lq})_{\alpha 3} \equiv (C^{(1)}_{lq})_{\alpha 3} + (C^{(3)}_{lq})_{\alpha 3}$ since the dilepton process is not sensitive to the top quark component.

$m_{\ell\ell}$ [GeV]	[300-380]	[380-500]	[500-700]	[700-1000]	[1000-1500]
$\frac{1}{\Delta m_{\ell\ell}}\sigma^{\text{SM NNLO}}_{\text{bin}}$ [fb/GeV]	2.00	0.651	0.161	2.9×10^{-2}	3.64×10^{-3}
δ^{th} [%]	3.7	4.6	5.7	7.6	11.6
$\frac{1}{\Delta m_{\ell\ell}}\sigma^{ee,\text{exp}}_{\text{bin}}$ [fb/GeV]	1.84	0.599	0.152	2.64×10^{-2}	3.23×10^{-3}
δ^{stat} [%]	2.6	3.6	5.3	10.2	22.5
δ^{syst} [%]	2.5	2.7	2.6	3.3	5.8
$\frac{1}{\Delta m_{\ell\ell}}\sigma^{\mu\mu,\text{exp}}_{\text{bin}}$ [fb/GeV]	1.90	0.640	0.154	2.66×10^{-2}	2.17×10^{-3}
δ^{stat} [%]	2.3	3.2	5.0	9.6	26
δ^{syst} [%]	1.9	1.8	2.0	2.1	2.7

Table 2: Invariant mass bins with the associated predicted and measured cross section and uncertainties (theoretical, statistical, and total systematic) from the ATLAS 8 TeV analysis [6] .

The EFT coefficients C_i enter linearly in the scattering amplitude of this process, therefore the cross section in any given bin is necessarily given by a quadratic function of the EFT coefficients:

$$\sigma_{\text{bin}}(\vec{C}) = \sigma_{\text{SM,bin}} + 2\Re[C_i \, \sigma^i_{\text{SM}-\text{EFT,bin}}] + C_i C^*_j \, \sigma^{ij}_{\text{EFT}^2,\text{bin}} \, . \tag{4}$$

Since operators with different flavor content (different quarks or leptons) or different chirality do not interfere with each other (in the limit of massless fermions), the matrix $\sigma^{ij}_{\text{EFT}^2}$ is diagonal.[3] The formula above thus reduces to:

$$\sigma_{\text{bin}}(\vec{C}) = \sigma_{\text{SM,bin}} + 2C_i \, \sigma^i_{\text{SM}-\text{EFT,bin}} + (C_i)^2 \, \sigma^i_{\text{EFT}^2,\text{bin}} \, . \tag{5}$$

In order to obtain this dependence we implemented the operators in Eq. (2) in FEYNRULES [18] and used the exported UFO model files to generate SM and new physics events in MG5_AMC [19]. Using the MG5_AMC ability to generate events using only the linear or quadratic terms, (NP^2==1 or NP^2==2, respectively) it is straightforward to obtain the complete EFT dependence.

The results in the ATLAS 8 TeV analysis [6] are unfolded in the fiducial region

$$(p^\ell_T)_{\text{leading}} > 40 \, \text{GeV}, \quad (p^\ell_T)_{\text{sub}-\text{leading}} > 30 \, \text{GeV}, \quad |\eta^\ell| < 2.5, \quad m_{\ell\ell} < 1500 \, \text{GeV} \, . \tag{6}$$

---

[3]A non-vanishing interference is present between singlet and triplet operators $\mathcal{O}^{(1)}_{lq}$ and $\mathcal{O}^{(3)}_{lq}$ since they share the same field content (both have $\bar{d}^i_L \gamma_\mu d^i_L$ and $\bar{u}^i_L \gamma_\mu u^i_L$ terms). However also in this case there are only two ways in which the coefficients enter the quadratic terms: $(C^{(1)}_{lq} \pm C^{(3)}_{lq})^2$.
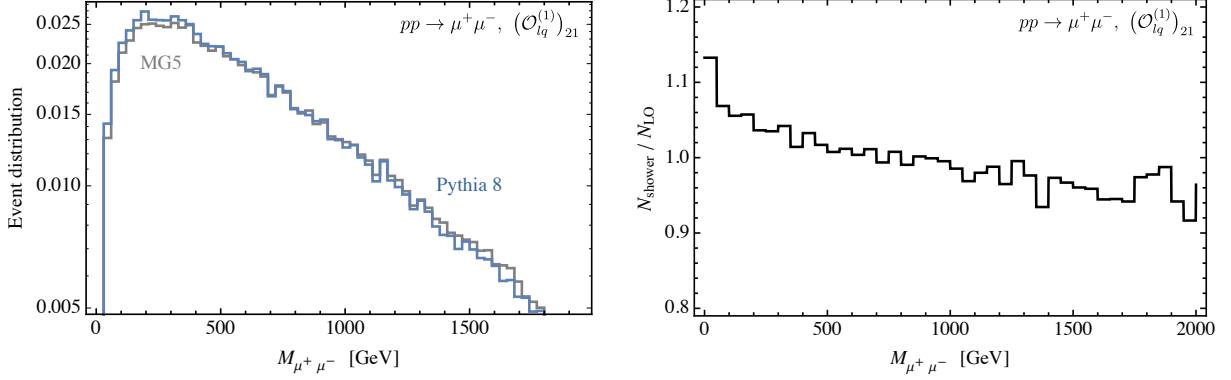
Figure 1: Left: Invariant mass distribution of dimuon signal events; the gray line is generated with MG5_AMC, the blue line includes PYTHIA8 parton showering. Right: relative correction due to parton showering as function of dimuon invariant mass.

Final state QED radiation effects are also unfolded, and the Born-level cross section in each fiducial bin is presented. We generate all events at the leading order (LO) with the same cuts the same fiducial region. Since we are interested in the high-energy tail, we also require $m_{\ell\ell} > 300\,\text{GeV}$. The five bins of invariant mass distribution we consider are: $[300 - 380 - 500 - 700 - 1000 - 1500]$ GeV, see Table 2 for the values of the predicted and measured cross sections and uncertainties. For the two-dimensional distribution we choose $d^2\sigma/(dm_{\ell\ell}d|y_{\ell\ell}|)$, since the dilepton rapidity shows a stronger sensitivity to the different EFT operators when compared to the distribution in $|\Delta\eta_{\ell\ell}|$, as is discussed in Sec. 2.1. In this case the invariant mass bins are merged into two large bins $[300 - 500 - 1500]$ GeV for each $|y_{\ell\ell}|$ bin in $[0 - 0.4 - 0.8 - 1.2 - 1.6 - 2.0 - 2.4]$. Unfortunately, the additional information gained from the rapidity comes with a reduced sensitivity from the invariant mass, since the potential new physics effects, largest in the highest invariant mass bin, are partially washed out by the merging with the lower invariant mass bins, which have a larger absolute cross section but smaller sensitivity to the EFT coefficients. This aspect is analysed quantitatively in Sec. 4

The events for each run are analysed in MADANALYSIS 5 [20] to obtain the cross section in each bin. The MADANALYSIS 5 analysis has been cross-checked with a custom ROOT analysis code. We generated 2M events for each new physics run, and 5M events for the SM one, reducing the statistical uncertainty in the determination of the coefficients in the EFT dependence in each bin to be $\lesssim 1\%$. These LO cross sections are then rescaled by the ratio of the SM cross section computed at NNLO QCD and NLO EW, taken directly from [6], over the LO SM one:

$$\sigma_{\text{bin}}^{\text{NNLO}}(\vec{C}) \approx \frac{\sigma_{\text{SM,bin}}^{\text{NNLO}}}{\sigma_{\text{SM,bin}}^{\text{LO}}}\,\sigma_{\text{bin}}(\vec{C})\,. \tag{7}$$

In this way the very precise SM prediction for the cross section is reproduced in the limit of zero new physics, and only possible small differences in how QCD corrections apply to new physics vs. the SM are neglected. We checked explicitly that the effects on QCD showering amounts to at most a (few)% correction on the new physics effect. This can be seen in the right panel of Fig. 1, which shows the ratio of the invariant mass distributions of signal events before and after PYTHIA8 showering.

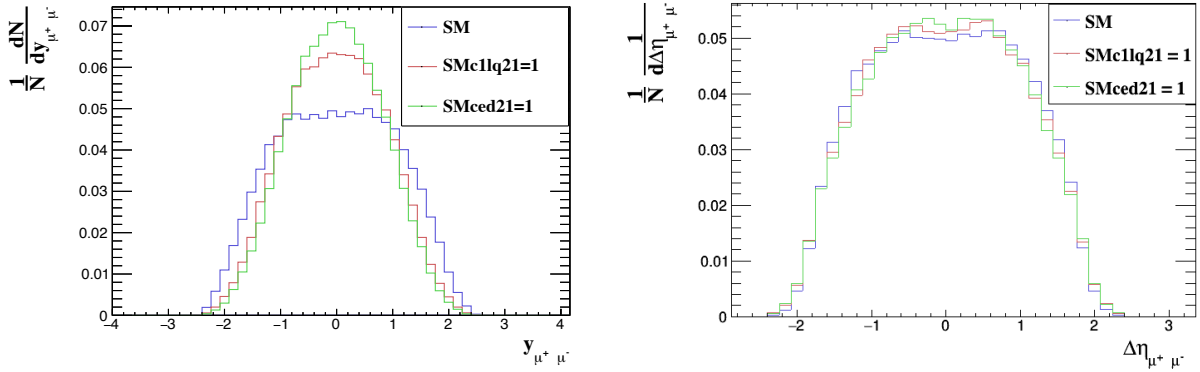**Figure 2:** Distributions for the dimuon rapidity $y_{\mu\mu}$ and differences of the pseudo-rapidity $\Delta\eta_{\mu\mu}$ for some benchmark points: SM (blue), $(C_{lq}^{(1)})_{21} = 1$ (red), and $(C_{ed})_{21} = 1$ (green).

2.1 New physics in the rapidity and pseudo-rapidity distributions

Fig. 2 shows the distribution in the rapidity of the dimuon pair (left plot) and in the difference of pseudo-rapidity between the two muons (right plot) for SM and for some NP benchmarks, after using the kinematic cuts outlined in Sec 2. One observes some differences in the rapidity $y_{\ell\ell}$ and pseudorapidity $\Delta\eta_{\ell\ell}$ for the effective operators as compared to the SM, with the former being more sensitive to the presence of the effective operators.

3 Building the likelihood

From the full EFT dependence in Eq. (7) and the fiducial measurement in each bin we build the likelihood $\mathcal{L}$ in the Gaussian approximation:

$$\chi^2(\{C\}) = -2\log\mathcal{L}(\{C\}) = \sum_{\alpha,\beta\in\text{bins}} (X_\alpha(\vec{C}) - X_\alpha^{\text{exp}})(\Sigma^{-1})_{\alpha\beta}(X_\beta(\vec{C}) - X_\beta^{\text{exp}}) , \quad (8)$$

where α, β are indices which run over all bins (either the 1D invariant mass distribution or the 2D one), $X_\alpha(\vec{C}) \equiv \sigma_{\text{bin}_\alpha}^{\text{NNLO}}(\vec{C})$ is the EFT dependence for that bin as computed in Eq. (7), X_α^{exp} the fiducial measurement, and Σ the full variance matrix. In the case of uncorrelated uncertainties $\Sigma_{\alpha\beta} = \delta_{\alpha\beta}\sigma_\alpha^2$, and σ_α^2 contains the sum in quadrature of all uncertainties (theory, statistical, and systematic) in that bin. As can be seen in Tab. 2 the dominant uncertainties are statistical, thus correlations between the small systematic uncertainties can be neglected in first approximation. We are further obliged to neglect these correlations due to the fact that the correlations between systematic uncertainties (or, alternatively, the response functions in each bin) are not provided by the experiment.[4] Substituting in Eq. (8) X_α^{exp} with the SM prediction $X_\alpha^{\text{SM}} = X_\alpha(\vec{0})$, we obtain the expected likelihoods.

---

[4]The only systematic uncertainty for which we do know the response function is due to the luminosity, and amounts to 1.9%. This can be treated as a nuisance parameter δ_{lumi} with a response function corresponding to a simple overall rescaling of all bins, $X_\alpha^{\text{exp}} \to X_\alpha^{\text{exp}}(1 + \delta_{\text{lumi}})$, and a given uncertainty $\sigma_\delta = 1.9\%$. We thus add to the χ^2 in Eq. (8) the term $\delta_{\text{lumi}}^2/\sigma_\delta^2$. Thanks to the simplicity of the response function for this uncertainty we can profile over δ_{lumi} analytically, obtaining a modified expression for $\Sigma_{\alpha\beta}^{-1}$ which takes the form

$$(\Sigma^{-1})_{\alpha\beta} = \delta_{\alpha\beta}\frac{1}{\sigma_\alpha^2} - \frac{X_\alpha^{\text{exp}} X_\beta^{\text{exp}}}{\sigma_\alpha\sigma_\beta}\bar{\sigma}^2 , \qquad \text{where} \qquad \frac{1}{\bar{\sigma}^2} = \frac{1}{\sigma_\delta^2} + \left(\frac{X_\alpha^{\text{exp}}}{\sigma_\alpha}\right)^2 . \quad (9)$$

Note that in this case, in the uncorrelated uncertainty of each bin, σ_α, the luminosity uncertainty is not included.

$\chi^2_{m_{\ell\ell},\text{lin}}$	`Chi2MllLin.txt`
$\chi^2_{m_{\ell\ell},\text{quad}}$	`Chi2MllQuadr.txt`
$\chi^2_{m_{\ell\ell}|y_{\ell\ell}|,\text{lin}}$	`Chi2MYllLin.txt`
$\chi^2_{m_{\ell\ell}|y_{\ell\ell}|,\text{quad}}$	`Chi2MYllQuadr.txt`

Table 3: χ^2 functions obtained with our analysis, and the corresponding ancillary file name.

We obtain the χ^2 function for the datasets corresponding to the differential cross section measurement in the dilepton invariant mass $\frac{d\sigma}{dm_{\ell\ell}}$ or in the dilepton invariant mass and rapidity $\frac{d^2\sigma}{dm_{\ell\ell}d|y_{\ell\ell}|}$, for both electrons and muons. We combine the measurements for electrons and muons but keep the separate dependence on the EFT coefficients for the two lepton flavors, so that lepton flavour universality tests can be performed. Furthermore, one can choose to limit the dependence on the EFT coefficients in Eq. (5) to the linear terms, or to include also the quadratic terms. We thus have four χ^2 functions, which we make available alongside this work in the ancillary files listed in Tab. 3 (downloadable here). These are functions of the coefficients in Tab. 1. The notation used in the ancillary files is: $(C^{(1)}_{lq})_{21} \equiv$ `C1lq[2, 1]`, $(C^{(+)}_{lq})_{13} \equiv$ `Cplq[1, 3]`, $(C^{(3)}_{lq})_{22} \equiv$ `C3lq[2, 2]`, $(C_{qe})_{32} \equiv$ `Cqe[3, 2]`, and so on.

4 Some example fits and discussion

In this Section we show some examples of how the four likelihoods we obtain from dilepton data can be used to constrain the SMEFT coefficients. We start by considering each of the coefficients in Tab. 1 one at a time and derive the 95% CL[5] constraint for that coefficient with each likelihood. The expected limits are collected in Tab. 4 while the observed ones are in Tab. 5.

When reading these results one should keep in mind the definition of the C_i coefficients in Eq. (3), $C_i \equiv c_i \frac{v^2}{\Lambda^2}$, therefore requiring a NP scale much above the EW scale implies $C_i \ll 1$. Furthermore, since the dilepton invariant mass goes up to 1.5 TeV, the EFT expansion is valid if $\Lambda \gg 1.5$ TeV. For reference, fixing $c_i = 1$ values of $C_i = \{10^{-1}, 10^{-2}, 10^{-3}\}$ correspond to $\Lambda = \{0.78, 2.5, 7.8\}$ TeV, respectively. Larger values of c_i, i.e. a strongly coupled UV completion, imply also higher values of the NP scale for a given C_i, thus improving the EFT expansion validity.

Quadratic terms in the EFT dependence of the cross section, proportional to $(c_i^{(6)})^2/\Lambda^4$, are formally of the same order in Λ as the interference of dimension-eight operators with the SM, which would be proportional to $c_i^{(8)}/\Lambda^2$. For weakly coupled UV completions, $c_i \lesssim 1$, it is thus inconsistent to include the former without the latter. Expecting the leading contribution to come from the linear dimension-6 terms, quadratic terms should not be included. This is the approach of the linear fits. On the other hand, for strongly-coupled UV completions, $1 \ll c_i \lesssim 4\pi$, quadratic dimension-6 terms are enhanced compared to linear dimension-8 ones and it is thus possible to include them in the fit in a consistent way. Unless some degeneracy is present in the fit, one would expect that if the EFT expansion is valid, linear and quadratic fits should give approximately the same results.

Comparing the expected (Tab. 4) and observed limits (Tab. 5) we observe that the latter are often quite asymmetric, especially for the linear fits. This is due to the deviations between the

---

[5]In practice we impose $\chi^2 - \chi^2_{\text{min}} = 3.84$ or 5.99 for 1D and 2D distributions, respectively.

95%CL int.	$\chi^2_{m_{\ell\ell},\text{quad}}$		$\chi^2_{m_{\ell\ell},\text{lin}}$		$\chi^2_{m_{\ell\ell}|y_{\ell\ell}|,\text{quad}}$		$\chi^2_{m_{\ell\ell}|y_{\ell\ell}|,\text{lin}}$	
	min	max	min	max	min	max	min	max
$(C^{(1)}_{lq})_{11}$	-0.0019	0.0035	-0.0037	0.0037	-0.0024	0.0055	-0.0040	0.0040
$(C^{(1)}_{lq})_{12}$	-0.016	0.015	-0.22	0.22	-0.020	0.018	-0.20	0.20
$(C^{(+)}_{lq})_{13}$	-0.066	0.051	-0.17	0.17	-0.083	0.056	-0.15	0.15
$(C^{(3)}_{lq})_{11}$	-0.0034	0.0020	-0.0043	0.0043	-0.0053	0.0026	-0.0047	0.0047
$(C^{(3)}_{lq})_{12}$	-0.017	0.015	-0.11	0.11	-0.021	0.018	-0.097	0.097
$(C_{ed})_{11}$	-0.0085	0.0043	-0.0072	0.0072	-0.014	0.0052	-0.0077	0.0077
$(C_{ed})_{12}$	-0.032	0.026	-0.11	0.11	-0.041	0.030	-0.097	0.097
$(C_{ed})_{13}$	-0.062	0.055	-0.38	0.38	-0.075	0.063	-0.33	0.33
$(C_{ld})_{11}$	-0.0076	0.0052	-0.015	0.015	-0.011	0.0068	-0.016	0.016
$(C_{ld})_{12}$	-0.030	0.027	-0.22	0.22	-0.038	0.033	-0.20	0.20
$(C_{ld})_{13}$	-0.061	0.057	-0.78	0.78	-0.072	0.066	-0.69	0.69
$(C_{lu})_{11}$	-0.0030	0.0069	-0.0045	0.0045	-0.0037	0.012	-0.0050	0.0050
$(C_{lu})_{12}$	-0.035	0.041	-0.17	0.17	-0.040	0.051	-0.16	0.16
$(C_{eu})_{11}$	-0.0019	0.0028	-0.0022	0.0022	-0.0022	0.0028	-0.0024	0.0024
$(C_{eu})_{12}$	-0.032	0.044	-0.085	0.085	-0.035	0.057	-0.076	0.076
$(C_{qe})_{11}$	-0.0028	0.0050	-0.0055	0.0055	-0.0036	0.0080	-0.0060	0.0060
$(C_{qe})_{21}$	-0.021	0.024	-0.13	0.13	-0.025	0.031	-0.12	0.12
$(C_{qe})_{31}$	-0.057	0.061	-0.66	0.66	-0.064	0.071	-0.57	0.57
$(C^{(1)}_{lq})_{21}$	-0.0017	0.0031	-0.0032	0.0032	-0.0023	0.0054	-0.0037	0.0037
$(C^{(1)}_{lq})_{22}$	-0.014	0.014	-0.20	0.20	-0.019	0.018	-0.19	0.19
$(C^{(+)}_{lq})_{23}$	-0.059	0.046	-0.16	0.16	-0.081	0.054	-0.14	0.14
$(C^{(3)}_{lq})_{21}$	-0.0030	0.0018	-0.0037	0.0037	-0.0051	0.0025	-0.0044	0.0044
$(C^{(3)}_{lq})_{22}$	-0.015	0.013	-0.098	0.098	-0.020	0.017	-0.092	0.092
$(C_{ed})_{21}$	-0.0077	0.0037	-0.0062	0.0062	-0.013	0.0049	-0.0072	0.0072
$(C_{ed})_{22}$	-0.028	0.023	-0.096	0.096	-0.040	0.029	-0.091	0.091
$(C_{ed})_{23}$	-0.056	0.050	-0.35	0.35	-0.073	0.061	-0.32	0.32
$(C_{ld})_{21}$	-0.0067	0.0046	-0.013	0.013	-0.011	0.0065	-0.015	0.015
$(C_{ld})_{22}$	-0.027	0.024	-0.20	0.20	-0.037	0.032	-0.19	0.19
$(C_{ld})_{23}$	-0.055	0.052	-0.72	0.72	-0.070	0.064	-0.65	0.65
$(C_{lu})_{21}$	-0.0026	0.0062	-0.0039	0.0039	-0.0035	0.011	-0.0046	0.0046
$(C_{lu})_{22}$	-0.031	0.037	-0.16	0.16	-0.039	0.050	-0.15	0.15
$(C_{eu})_{21}$	-0.0017	0.0024	-0.0019	0.0019	-0.0021	0.0025	-0.0022	0.0022
$(C_{eu})_{22}$	-0.028	0.039	-0.078	0.078	-0.033	0.056	-0.072	0.072
$(C_{qe})_{12}$	-0.0025	0.0045	-0.0048	0.0048	-0.0034	0.0078	-0.0056	0.0056
$(C_{qe})_{22}$	-0.019	0.022	-0.12	0.12	-0.024	0.030	-0.11	0.11
$(C_{qe})_{32}$	-0.052	0.055	-0.62	0.62	-0.062	0.069	-0.54	0.54

Table 4: Expected 95%CL intervals for all the EFT coefficients when taken one at a time, for the four different χ^2 functions. We recall that $(C^{(+)}_{lq})_{\alpha 3} \equiv (C^{(1)}_{lq})_{\alpha 3} + (C^{(3)}_{lq})_{\alpha 3}$.

15

95%CL int.	$\chi^2_{m_{\ell\ell},\text{quad}}$		$\chi^2_{m_{\ell\ell},\text{lin}}$		$\chi^2_{m_{\ell\ell}|y_{\ell\ell},\text{quad}}$		$\chi^2_{m_{\ell\ell}|y_{\ell\ell}|,\text{lin}}$	
	min	max	min	max	min	max	min	max
$(C_{lq}^{(1)})_{11}$	-0.00083	0.0033	-0.00027	0.0071	-0.00060	0.0048	0.00039	0.0084
$(C_{lq}^{(1)})_{12}$	-0.012	0.011	-0.47	-0.029	-0.014	0.011	-0.47	-0.070
$(C_{lq}^{(+)})_{13}$	-0.055	0.029	-0.36	-0.027	-0.064	0.025	-0.35	-0.057
$(C_{lq}^{(3)})_{11}$	-0.0031	0.0010	-0.0084	0.00033	-0.0045	0.00088	-0.0099	-0.00044
$(C_{lq}^{(3)})_{12}$	-0.013	0.010	-0.23	-0.014	-0.015	0.010	-0.23	-0.034
$(C_{ed})_{11}$	-0.0083	0.0013	-0.014	0.00042	-0.012	0.00025	-0.017	-0.0012
$(C_{ed})_{12}$	-0.026	0.016	-0.22	-0.012	-0.031	0.015	-0.23	-0.033
$(C_{ed})_{13}$	-0.048	0.037	-0.81	-0.058	-0.053	0.036	-0.79	-0.13
$(C_{ld})_{11}$	-0.0067	0.0031	-0.028	0.0010	-0.0092	0.0031	-0.034	-0.0023
$(C_{ld})_{12}$	-0.024	0.019	-0.45	-0.023	-0.027	0.019	-0.47	-0.066
$(C_{ld})_{13}$	-0.045	0.040	-1.7	-0.11	-0.049	0.040	-1.6	-0.25
$(C_{lu})_{11}$	-0.00060	0.0069	-0.00046	0.0086	0.00010	0.011	0.00016	0.010
$(C_{lu})_{12}$	-0.022	0.033	0.023	0.37	-0.021	0.038	0.055	0.37
$(C_{eu})_{11}$	1.7×10^{-6}	0.0087	-0.00020	0.0043	0.00020	0.0087	0.00011	0.0050
$(C_{eu})_{12}$	-0.016	0.038	0.012	0.18	-0.013	0.046	0.027	0.18
$(C_{qe})_{11}$	-0.0013	0.0047	-0.00040	0.011	-0.00092	0.0069	0.00063	0.013
$(C_{qe})_{21}$	-0.014	0.020	0.017	0.27	-0.014	0.023	0.041	0.27
$(C_{qe})_{31}$	-0.039	0.046	0.12	1.4	-0.038	0.048	0.23	1.4
$(C_{lq}^{(1)})_{21}$	-0.00057	0.0022	0.00094	0.0073	-0.0010	0.0046	-0.00077	0.0067
$(C_{lq}^{(1)})_{22}$	-0.0086	0.0077	-0.43	-0.032	-0.014	0.012	-0.37	0.0029
$(C_{lq}^{(+)})_{23}$	-0.038	0.023	-0.33	-0.016	-0.061	0.028	-0.28	-0.0012
$(C_{lq}^{(3)})_{21}$	-0.0021	0.00068	-0.0086	-0.0011	-0.0043	0.0012	-0.0079	0.00092
$(C_{lq}^{(3)})_{22}$	-0.0090	0.0073	-0.21	-0.015	-0.015	0.011	-0.18	0.0015
$(C_{ed})_{21}$	-0.0056	0.0010	-0.014	-0.0018	-0.012	0.0015	-0.014	0.00086
$(C_{ed})_{22}$	-0.018	0.012	-0.21	-0.016	-0.030	0.017	-0.18	0.0020
$(C_{ed})_{23}$	-0.034	0.027	-0.74	-0.037	-0.052	0.037	-0.64	-0.0027
$(C_{ld})_{21}$	-0.0045	0.0021	-0.029	-0.0036	-0.0087	0.0035	-0.028	0.0018
$(C_{ld})_{22}$	-0.016	0.013	-0.43	-0.034	-0.027	0.020	-0.37	0.0047
$(C_{ld})_{23}$	-0.032	0.029	-1.5	-0.079	-0.048	0.041	-1.3	-0.0063
$(C_{lu})_{21}$	-0.00044	0.0048	0.0012	0.0089	-0.0012	0.010	-0.0012	0.0080
$(C_{lu})_{22}$	-0.017	0.023	0.022	0.34	-0.023	0.036	-0.0012	0.30
$(C_{eu})_{21}$	0.00040	0.0057	0.00057	0.0044	-0.00057	0.0050	-0.00059	0.0039
$(C_{eu})_{22}$	-0.014	0.026	0.011	0.17	-0.016	0.043	-0.00057	0.14
$(C_{qe})_{12}$	-0.00087	0.0032	0.0014	0.011	-0.0015	0.0066	-0.0011	0.010
$(C_{qe})_{22}$	-0.010	0.013	0.019	0.25	-0.015	0.022	-0.0016	0.22
$(C_{qe})_{32}$	-0.029	0.033	0.042	1.3	-0.039	0.048	0.0054	1.1

Table 5: 95%CL intervals for all the EFT coefficients when taken one at a time, for the four different χ^2 functions built with the published 8TeV dilepton data. We recall that $(C_{lq}^{(+)})_{\alpha 3} \equiv (C_{lq}^{(1)})_{\alpha 3} + (C_{lq}^{(3)})_{\alpha 3}$.

SM prediction and the data (see Tab. 2), which can push the coefficients in a specific direction depending on the sign of the interference term, while the quadratic terms are always necessarily positive. In case of operators with first-generation quarks, the linear and quadratic fits differ only by some $\mathcal{O}(1)$ factor and the limits are at the per-mille level on the C_i's, implying NP scales above few TeV, well above the partonic collision energy. In the case of operators with heavier quarks, instead, the difference between linear and quadratic fits becomes very large, with the limits from the linear fits becoming very weak, hinting a possible breakdown of the EFT validity. Some of these limits could possibly still be applied in strongly coupled UV completions, however a more detailed analysis would require a direct comparison with some explicit UV models, which is beyond the scope of this work.

We also observe that the constraints from the 2D distribution are of the same order (or somewhat weaker) than those obtained using only the invariant mass distribution. As already mentioned in Sec. 2, this is due to the merging of the high-invariant mass bins with lower invariant masses, which dilutes the sensitivity on the EFT coefficients of the bins for which it is would be the strongest. In this case, the gain from the extra information on the rapidity distribution is not enough to offset this effect. On the other hand, we expect that the main benefit of the rapidity distribution is in disentangling the contributions from operators with different chiral structures.

In order to show this, and to show the presence of large degeneracies in the linear likelihoods, we perform a few fits keeping two EFT coefficients at the same time. The observed 95% CL limits in the plane of the two coefficients are shown in Figs. 3,4.

The top-left plot in Fig. 3 shows a test of lepton-flavor-universality assuming flavor-independent coefficients in the quark sector. The two combinations of coefficients we test are $(C_{lq}^{(1)})_{1i}$ vs. $(C_{lq}^{(1)})_{2i}$. In this case we see that the linear and quadratic fits differ only by a $\mathcal{O}(1)$ factor (constraints from the linear fit being the weakest). The deviation from the SM in the linear fits is due to the deficit in the measured cross section in both channels compared to the SM prediction seen in Tab. 2. Since the quadratic contributions are strictly positive and are observed to dominate the quadratic fit, in this case the observed deviation cannot be completely saturated and thus the resulting fits are more compatible with the SM.

In all the other plots we see that the quadratic fits provide quite strong constraints and that those from the 2D distribution offer weaker limits, due to the wash-out effect discussed above. The linear fits, on the other hand, show very shallow flat directions, along which the constraining power is mostly lost. These flat directions can be understood by looking at the linear EFT dependence of the highest invariant mass bin, of $m_{\ell\ell} \in [1000 - 1500]$ GeV, which is proportional to (normalised to the SM contribution):

$$
\begin{aligned}
K_{\text{flat dir}} = &-73.0(C_{lq}^{(1)})_{\alpha 1} + 0.765(C_{lq}^{(1)})_{\alpha 2} + 62.1(C_{lq}^{(3)})_{\alpha 1} + 1.55(C_{lq}^{(3)})_{\alpha 2} + 0.830(C_{lq}^{(+)})_{\alpha 3} \\
&+ 36.6(C_{ed})_{\alpha 1} + 1.66(C_{ed})_{\alpha 2} + 0.380(C_{ed})_{\alpha 3} - 124(C_{eu})_{\alpha 1} - 1.85(C_{eu})_{\alpha 2} \\
&+ 18.1(C_{ld})_{\alpha 1} + 0.822(C_{ld})_{\alpha 2} + 0.188(C_{ld})_{\alpha 3} - 61.5(C_{lu})_{\alpha 1} - 0.922(C_{lu})_{\alpha 2} \\
&- 48.0(C_{qe})_{1\alpha} - 1.31(C_{qe})_{2\alpha} - 0.189(C_{qe})_{3\alpha} \, .
\end{aligned}
\tag{10}
$$

The $K_{\text{flat dir}} = 0$ direction is shown in the plots as dashed gray line and we see that it describes very well the flat direction of the fits done in the linear approximation, also when including the rapidity distribution information. This reflects the expectation that most of the sensitivity on the EFT operators comes from the highest invariant mass bin. Comparing the dashed blue (linear

17

Figure 3: 95%CL contours in some 2D spaces of EFT coefficients with quadratic (solid) or linear (dashed) EFT dependence using only the dilepton invariant mass distribution (blue) or also the information on the absolute rapidity of the dilepton system (red). The thin dashed black line corresponds to the direction in EFT space which leaves the linear dependence of the highest invariant mass bin unchanged, Eq. (10). Right plots are zoomed-out version of the left ones.
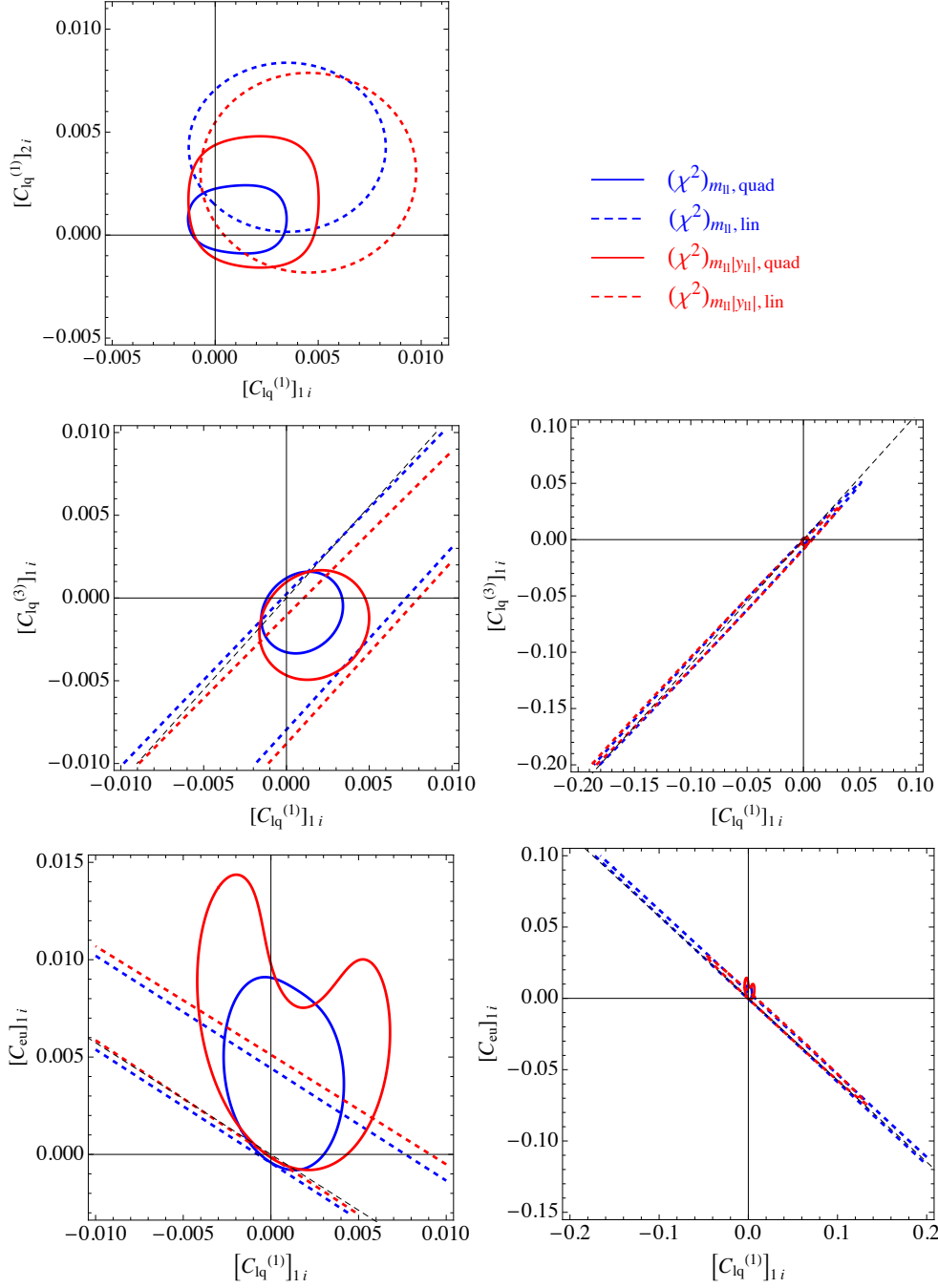
Figure 4: 95%CL contours in some 2D spaces of EFT coefficients with quadratic (solid) or linear (dashed) EFT dependence using only the dilepton invariant mass distribution (blue) or also the information on the absolute rapidity of the dilepton system (red). The thin dashed black line corresponds to the direction in EFT space which leaves the linear dependence of the highest invariant mass bin unchanged, Eq. (10). Right plots are zoomed-out version of the left ones.
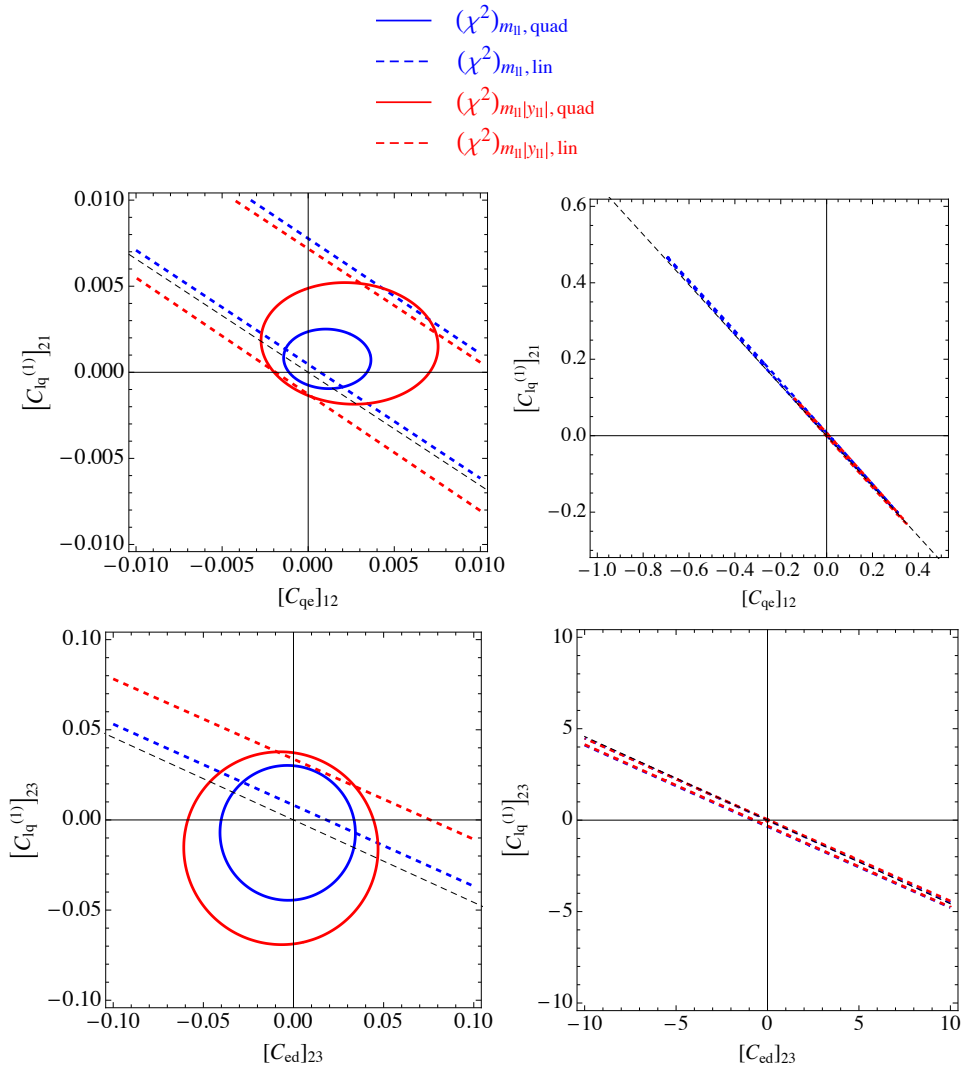
fit from the 1D distribution) with the dashed red (linear fit with including rapidity information) contours, we see that the extra information from the rapidity is able to partially alleviate the flat directions, thanks to the different dependence of different operators, as shown in Fig. 2 (left). We expect this positive effect to substantially improve with more precision.

5 Conclusions

The high-mass dilepton invariant mass distribution in Drell-Yan production $pp \rightarrow \ell^+\ell^-$ is a particularly powerful probe of New Physics at the LHC. If the scale of NP is much higher than the energy scale of the process, a model-independent approach to describe the effect of heavy states is provided by Effective Field Theories. We used ATLAS 8 TeV data with 20.3 fb^{-1} of luminosity [6] to constrain the complete set of dimension-six operators with non-vanishing

interference with the SM amplitude, listed in Tab. 1. We obtain, and make public, four likelihoods: using the differential cross section in invariant mass or in invariant mass and dilepton rapidity, and for both including or excluding the quadratic dependence of the cross section on the EFT coefficients. The four files are listed in Tab. 3 and can be downloaded at this link.

To illustrate the possible uses of these likelihoods we derive the 95%CL limits for each EFT coefficient when taken one at a time, Tab. 5, and for some examples of pairs of coefficients, Figs. 3 and 4. These examples show that the fits performed using the linear dependence provide constraints often much weaker than those obtained with the quadratic dependence, a behaviour that suggests possible issues with the EFT validity. More precise data, such as that collected at 13 TeV, is expected to alleviate this problem. We also observe that in the single-operator fits and in all the quadratic fits, using the two-dimensional distribution provides worse constraints than using only the dilepton invariant mass. This is due to the merging of $m_{\ell\ell}$ bins which is done in the 2D distribution, which washes out some of the EFT sensitivity. Again, a larger dataset with more granular binning in invariant mass should address this issue. On the other hand, the extra information coming from the rapidity distribution is able to lift part of the degeneracy of the linear fits done with pair of EFT coefficients. For these reasons we strongly advice the experimental collaborations against merging the highest invariant-mass bins in future analyses. A better solution, for the highest invariant-mass bins, could rather be to merge the angular distributions bins.

The likelihoods obtained in this work can be easily used to put constraints from the dilepton distribution in a wide class of NP models. We plan to update the results with 13 TeV data when the corresponding experimental analyses are available.

Acknowledgements

Contribution 3

LHC sensitivity to leptoquark production in τ+heavy quark final states

D. Buttazzo, D. Marzocca, M. Nardecchia, P. Pani, G. Polesello

Abstract

The anomalies observed by LHCb in flavor observables suggest the breakdown of lepton flavor universality. We study how a leptoquark solution can be tested at the LHC through final states including a the hadronic decay of a τ lepton, a heavy quark (b or t) and $E_{\mathrm{T}}^{\mathrm{miss}}$

1 INTRODUCTION

The deviations from the SM predictions observed by Babar, Belle, and LHCb in the Lepton-Flavour Universality (LFU) ratios R_D and R_{D^*} [1] are compelling hints for the presence of New Physics (NP) beyond the SM at a scale close to the TeV scale. The most successful explanations consist in scalar or vector leptoquark (LQ) states, with a larger coupling to taus than to muons.

The low scale of NP hinted by the observed deviations in flavour physics implies that direct searches at the LHC could be potentially sensible to these LQ. The processes most sensitive to such states are: i) pair-production followed by on-shell decays, ii) single production in association with a charged lepton or neutrino and iii) off-shell exchange in the t-channel of a LQ in the partonic process $pp \to \tau\nu(+j)$ or $\tau\tau(+j)$. See e.g. [22] for a review.

At present, the limits from pair-production of third-generation scalar (vector) LQ – i.e. LQ coupled mainly to third-generation fermions – range between $\sim 0.7 - 1$ TeV ($\sim 1 - 1.5$ TeV) depending on the specific decay channel considered. Single production is potentially more sensitive for larger masses and larger couplings. Experimental searches in this mode are much more limited, consisting only in a CMS search in the $b\tau$ decay channel with another associated τ [23]. It should be noted that a LQ of electric charge $Q = 1/3$, such as the S_1 introduced below, does not contribute to this process. For this reason in this work we consider the $b\nu$ (with associated τ) or the $c\tau$ (with associated ν) channels, both included in the process $pp \to \tau\nu + b-$jet.[2] We devise such an analysis for LHC searches and obtain prospects for HL-LHC with 3 ab^{-1} of luminosity. Although in a different kinematical region, corresponding to a forward b-jet, the same process is also sensitive to the same partonic transition which takes place in the anomalous flavour process: $b \to c\tau\nu$. It was shown in Ref. [5] that in several NP scenarios, LHC searches of $pp \to \tau\nu$ should probe the parameter region responsible for the anomalies. The b-tagging requirement should further increase the signal to background ratio and therefore the sensitivity to such NP compared to that work.

Due to $SU(2)_L$ gauge invariance, a coupling of a LQ to the left-handed bottom also implies a coupling to the left-handed top quark. It is thus also interesting to consider single

---

[1]See e.g. the HFLAV combination updated in the Spring of 2019 [21]
https://hflav-eos.web.cern.ch/hflav-eos/semi/spring19/html/RDsDsstar/RDRDs.html.

[2]Note that the b-tag also final states with a c-jet will be selected.

production of scalar or vector LQ in final states with one top. In the second part of this work we devise such an analysis and obtain prospects for LHC searches with 3000 fb^{-1} of luminosity.

2 THE MODELS AND SOLUTIONS TO THE $R_{D^{(*)}}$ ANOMALIES

In this work we consider a model with a pair of scalar LQs.

The scalar LQ model we implement comprise $S_1 \equiv (\overline{\mathbf{3}}, \mathbf{1}, 1/3)$ and $S_3 \equiv (\overline{\mathbf{3}}, \mathbf{3}, 1/3)$ with masses M_{S_1} and M_{S_3}, where we specify transformation properties under the SM gauge group. First (second) integer in the brackets corresponds to the dimension of the irreducible representation of $SU(3)$ ($SU(2)$) that the LQ belongs to whereas the rational number is the LQ $U(1)$ hypercharge (normalised as $Q = T_L^3 + Y$). We assume that lepton number and baryon number are conserved quantities. The interaction of the two LQs with SM fermions is described by the Lagrangian

$$\mathcal{L}_{\text{int}}^{S_1+S_3} = (\lambda_{\mathbf{R}})_{i\alpha}(\bar{u}_R^c)_i(\ell_R)_\alpha\, S_1 + (\lambda_{\mathbf{1L}})_{i\alpha}(\bar{Q}_L^c)_i\epsilon(L_L)_\alpha\, S_1 + (\lambda_{\mathbf{3L}})_{i\alpha}(\bar{Q}_L^c)_i\epsilon\sigma^a(L_L)_\alpha\, S_3^a + \text{h.c.}\,, \tag{1}$$

where ϵ is the antisymmetric matrix in $SU(2)_L$ indices and i (α) is a quark (lepton) flavor index. All gauge indices are understood for simplicity.

For the event generation we use the FEYNRULES implementation of both models from [22].

Various combination of the couplings in the two LQ model can be used to solve the $R_{D^{(*)}}$ anomalies. S_1 by itself can successfully address the anomaly with the couplings $(\lambda_{\mathbf{1L}})_{33} \lesssim 1$, $(\lambda_{\mathbf{R}})_{23} \sim \mathcal{O}(1)$, and a mass $M_{S_1} \sim 1$ TeV. This solution is considered in another Les Houches proceeding so we will not consider it in the following.

Another possibility to address the flavour anomalies is to use only the S_1 couplings to LH fermions. In this case it is necessary to also include S_3 in order to evade a strong constraint from $B \to K^*\nu\nu$ [24]. A good parameter region able to fit the anomalies in this setup is given by $M_{S_1} \sim M_{S_3} \sim 1$ TeV, $(\lambda_{\mathbf{1L}})_{33} \sim (\lambda_{\mathbf{3L}})_{33} \sim 1$, and $(\lambda_{\mathbf{1L}})_{23} \sim -(\lambda_{\mathbf{3L}})_{23} \sim 1$. This model is particularly interesting since the S_3 LQ can easily address also the flavour anomalies in neutral-current B decays via the $(\lambda_{\mathbf{3L}})_{22}$ and $(\lambda_{\mathbf{3L}})_{32}$ couplings [24].[3] Other relevant observables putting strong constraints in this setup are: $Z \to \tau\tau, \nu\nu$, τ LFU tests, and B_s mixing. The latter, in particular, is a very strong bound which puts a mild tension with $R_{D^{(*)}}$ [25]. The region in the $((\lambda_{1(3)L})_{33}, (\lambda_{1(3)L})_{23})$ plane compatible with the flavour anomalies and these other observables at 68 and 95%CL from the best fit point is shown in Fig. 1 for a simplified model comprising both S_1 and S_3, with approximately degenerate masses and equal (or opposite) couplings. In our collider analysis we focus on such a parameter region, but we include only the contribution from one LQ (e.g. S_1). This is motivated by the fact that in a more realistic scenario it is unlikely the two LQ will be exactly degenerate, but indeed a splitting of a few hundred GeV is to be expected (e.g. due to radiative EW corrections to the mass [25]) and therefore the contribution to collider searches will be dominated by whichever of the two states is the lighter.

3 SIMULATION OF LHC EVENTS.

The simulation of the LQ signal and the SM background follows the strategy introduced in Ref. [26], to which we refer for additional details.

---

[3]However, the couplings needed to fit those anomalies are too small to have an impact in the LHC searches considered here.
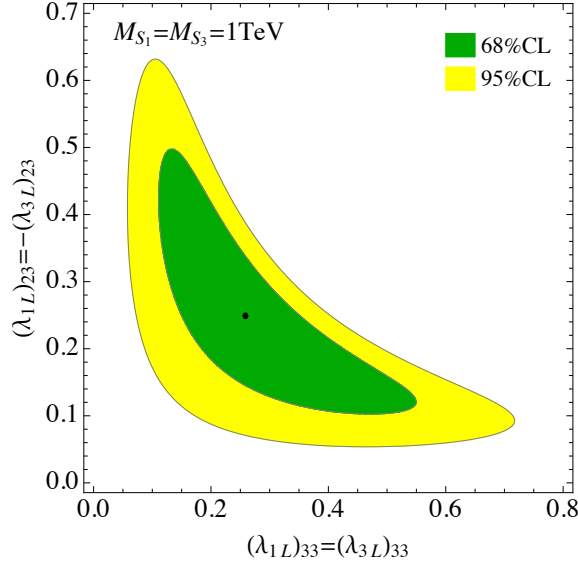
Figure 1: *Flavor fit to the $R_{D^{(*)}}$ anomalies and related observables in the $S_1 + S_3$ model.*

We simulate a full set of SM processes leading to the presence of one or two final-state leptons (e, μ, τ) originating from the decay of a W-boson, a Z-boson or a τ lepton. Events are generated within either the POWHEG BOX framework [27] or the MadGraph5_aMC@NLO platform [19], and the simulation of the QCD environment (parton showering and hadronisation) has been performed with PYTHIA 8 [28]. Hard-scattering signal events have been produced with MadGraph5_aMC@NLO on the basis of the UFO model [29] provided together with Ref. [22], and parton showering and hadronisation have been again simulated with PYTHIA 8. We finally include detector effects by smearing the properties of the final-state physics objects (*i.e.* electrons, muons, jets and $E_{\mathrm{T}}^{\mathrm{miss}}$) in a way reproducing the measured performance of the ATLAS detector. We provide here some more details on the simulation of τ-tagging and flavour-tagging, as they are of key importance for the following discussion. The parametrisation of the ATLAS b-tagging algorithm is based on the performance figures provided in Ref. [30]. For the analyses presented in the following a working point is chosen yielding a 77% efficiency for b-jets, the efficiency for c-jets will be 22%, whereas the light jets are suppressed by a factor of 140. The parametrisation of the τ-tagging performance is taken from [31]. The working point used in the analysis has an average efficiency for the identification of hadronic tau decays of approximately 80% (70%) for 1(3)-prong τ decays. The assumed rejection factor for light jets is taken as 80 (500) for 1(3)-prongs.

4 ANATOMY OF SIGNAL: τ+HEAVY QUARK+$E_{\mathrm{T}}^{\mathrm{miss}}$

Considering only the production of S_1 leptoquarks, the final state τ + heavy quark + $E_{\mathrm{T}}^{\mathrm{miss}}$ can be produced in the model described in Section 2 in three different ways:

– Through the pair production of two leptoquarks, with subsequent mixed decay:
$pp \to S_1 S_1^\dagger, S_1 \to b\nu_\tau, S_1^\dagger \to \tau t$.

– Through the single production processes with a b/c quark in final state:
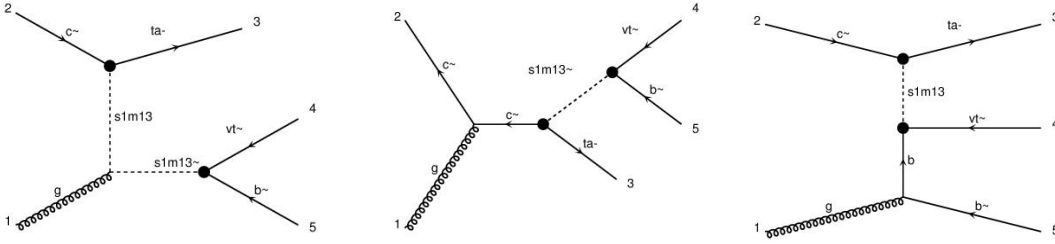
   – $gc \to \tau\nu_\tau b$

23

Figure 2: *Representative Feynman diagrams for the gc initial state.*
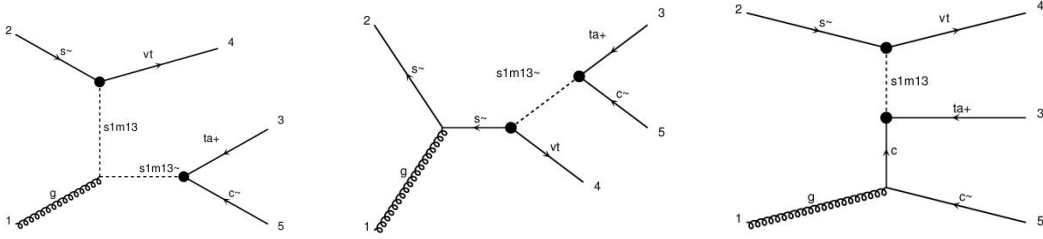

Figure 3: *Representative Feynman diagrams for the gs initial state.*

– $gs/gb \rightarrow \nu_\tau \tau c$
  as discussed above, for the implementation of the ATLAS b-tagging used in this analysis, a significant fraction of these events will pass the analysis requirement of the presence of a b-tagged jet in the event.

  The dominant signal Feynman diagrams for respectively the gc and $gs(b)$ partonic initial states are shown in Figures 2 and 3. In both cases the rightmost two diagrams correspond to associated production of a resonant leptoquark and a lepton, and the rightmost one corresponds to the t-channel exchange of a leptoquark.

– Through the single production processes with a top quark in final state:
  $gs/gb \rightarrow \nu_\tau \tau t$

The processes with a top quark in the final state contribute to searches requiring a b-tagged jet in the final state, which will be described in Section 5, but their discovery potential is optimised by searches which require an additional isolated lepton (e, μ) from the semileptonic decay of the top, and exploit the distinctive final-state kinematics of the top decay described in Section 6. The relevant Feynman diagrams are the ones of Fig. 3 with the c quark replaced by a t quark.

5 τ+b-tagged jet+$E_{\mathrm{T}}^{\mathrm{miss}}$ final state.

We produced a grid in the three-dimensional space defined by the leptoquark mass m_{S_1} (MS1 parameter in generator), and by the left-handed couplings $(\lambda_L)_{23}$ (yLL2x3) and $(\lambda_L)_{33}$ (yLL3x3). All other couplings were put to zero.

For each model point only the initial states including a gluon or a second or third generation quark were produced. Initial states including a first generation quark do not contribute to the signal, and for them the generation was performed only once with all couplings set to zero to be used as a background.

The corresponding MG5 process card is given below for reference.

```
import model LO_LQ_S1
define tau = ta+ ta-
define nutau = vt vt~
define top = t t~
define j = g u c d s b u~ c~ d~ s~ b~
define p1 = g c s b c~ s~ b~
generate p1 p1 > tau nutau j QED=4 NP=4
```

The signal thus generated also includes SM Wc-production, which in the analysis will be subtracted using a sample produced with all of the couplings set to zero to obtain a pure signal sample. In addition the final state with a top in the final state produced as:

```
generate p1 p1 > tau nutau top QED=4 NP=4
```

was incorporated in the signal sample after subtraction of the Wt background. The analysis strategy is based on requiring one and only one b-tagged jet accompanying a τ and E_T^miss. The production of a single top quark accompanied either by a W boson or a light jet will present this final state, the veto on a second b-tagged is used to reduce the very large $t\bar{t}$ background. The background from SM W production will affect this search through two main sources:

- $W \to \tau\nu$ accompanied by a light jet, where in the jet showering a b-jet is produced

- $W \to \tau\nu$ accompanied by a heavy-flavour jet (b or c). At leading order, the associated production of a W with a single b-jet does not exist, and the associated production of a W and two b-jets will be suppressed by the veto on a second b-jet in the event. The dominant contribution will thus be the case in which the W is produced with a c-jet, and the c-jet is misidentified as a b-jet.

In order to restrict the event generation to the relevant kinematic region, the following parton-level cuts were applied both on the signal and on the W+jets background at generation level in `MadGraph5_aMC@NLO`: $m_T(\tau\nu_\tau) > 150\,\text{GeV}$, where the τ is undecayed, and m_T is the transverse mass. This cut is meant to remove the bulk of the resonant $W \to \tau\nu_\tau$ production, which is the dominant background, and is peaked at 80 GeV with a long tail corresponding to the Breit-Wigner tail of the W boson. The transverse mass instead of the mass of the tau-neutrino system is chosen in order to have a selection which can be reasonably approximated with experimental cuts. Additionally we require $p_T(\tau\nu_\tau) > 150$ GeV, to define a kinematic region where the tau-neutrino system recoils against a hadronic system with high transverse momentum.

For the case where only the $(\lambda_L)_{23}$ coupling is different from zero, only the $\tau + c + \nu_\tau$ will be observable, and the invariant mass of the visible part of the hadronic τ decay and of the c-jet ($m_{\tau c}$) will approximately reconstruct the mass of the leptoquark in case of resonant production. When the $(\lambda_L)_{33}$ coupling is different from zero as well, the final state $\tau + b + \nu_\tau$ will also be available, with the transverse mass built out of the b-quark and E_T^miss (m_T^b) presenting an edge at m_{S_1}. In both cases, however, the mass peak/edge is smeared by the fact that the event includes additional undetected neutrinos from the τ decay. This feature is illustrated in Fig. 4, where the normalised distributions for $m_{\tau c}$ (left) and m_T^b (right) are shown for the Drell-Yan background and for two S_1 masses, 1000 and 1500 GeV. A clear enhancement for both distributions is
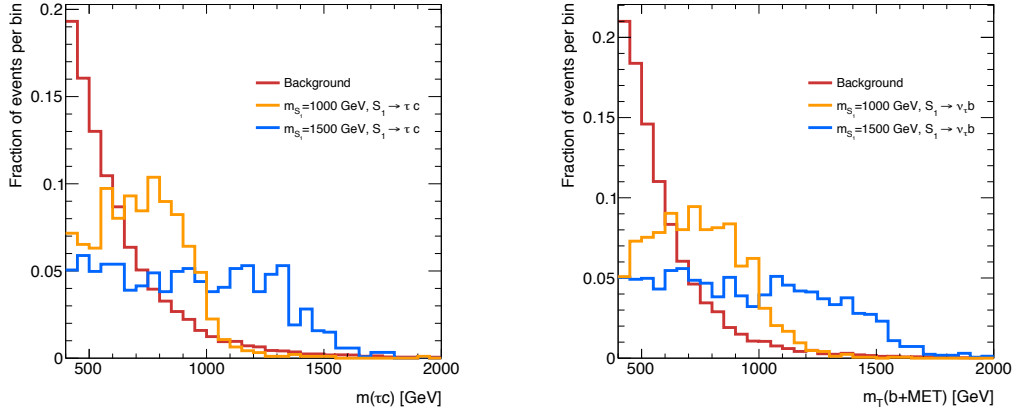
Figure 4: *Normalised distributions of the variables $m_{\tau c}$ (left) and m_T^b (right) for the Drell-Yan background and for two S_1 masses, 1000 and 1500 GeV.*

visible for the signal at values corresponding to the nominal m_{S_1}. We will therefore use these two variables as the main discriminants for the analysis.

As a first step, events with a jet tagged as the hadronic decay of a τ lepton (τ-jet) and at least one b-tagged jet and some E_T^{miss} are selected. Events are required to contain one and only one τ-jet with $p_T > 180$ GeV within $|\eta_\tau| < 2.5$, and one and only one b-tagged jet with $p_T > 250$ GeV within $|\eta| < 1.5$, and to satisfy the requirement $E_T^{\mathrm{miss}} > 150$ GeV. Events with additional b-tagged jets with $p_T > 30$ GeV or containing isolated charged leptons (e/μ) are rejected.

To match the generation-level cuts designed to reject the bulk of the Drell-Yan background we require that the transverse mass of the τ-jet with E_T^{miss}, $m_T^{\tau\nu} > 300$ GeV, and the transverse momentum of the $\tau\nu$ system is required to be $p_T^{\tau\nu} > 200$ GeV. Finally, in order to reject events where E_T^{miss} is generated by a mismeasured jet, a cut on the minimal azimuthal distance between a reconstructed jet and E_T^{miss} $\Delta\phi_{min} > 0.6$ is applied.

Based on the final discriminant variables $m_{\tau c}$ and $m_{\tau c}$ defined above, two different orthogonal signal regions are defined, requiring either $m_{\tau c} > m_T^b$ (SR1) or $m_{\tau c} > m_T^b$ (SR2), targeting the two different decays of the S_1. In each of the region a fit is performed respectively on the $m_{\tau c}$ (m_T^b) distribution for SR1 (SR2) over 4 bins starting from 600 GeV. The results of the two signal regions are then statistically combined to get the final result.

The 2-σ sensitivity of the τ+b-tagged jet analysis at the HL-LHC is shown in Fig. 5. In the left panel the sensitivity on the $(\lambda_L)_{23}$ coupling is shown as a function of m_{S_1} for two values of $(\lambda_L)_{33}$. In the right panel the value of m_{S_1} which can be excluded at the 95% level is shown in the $((\lambda_L)_{33}, (\lambda_L)_{23})$ plane.

6 Final state: τ+top+E_T^{miss}

6.1 Search for leptoquark pair production

As discussed above, the pair production of leptoquarks yields this signature in the case where one of the two leptoquarks decays $S_1 \to \tau t$ and the other decays in the channel $S_1 \to \nu_\tau b$. Given that the two decays have approximately the same branching fraction, the search for the mixed decay is in principle more powerful that the searches for the $\tau t \tau t$ and $\nu b \nu b$ existing in
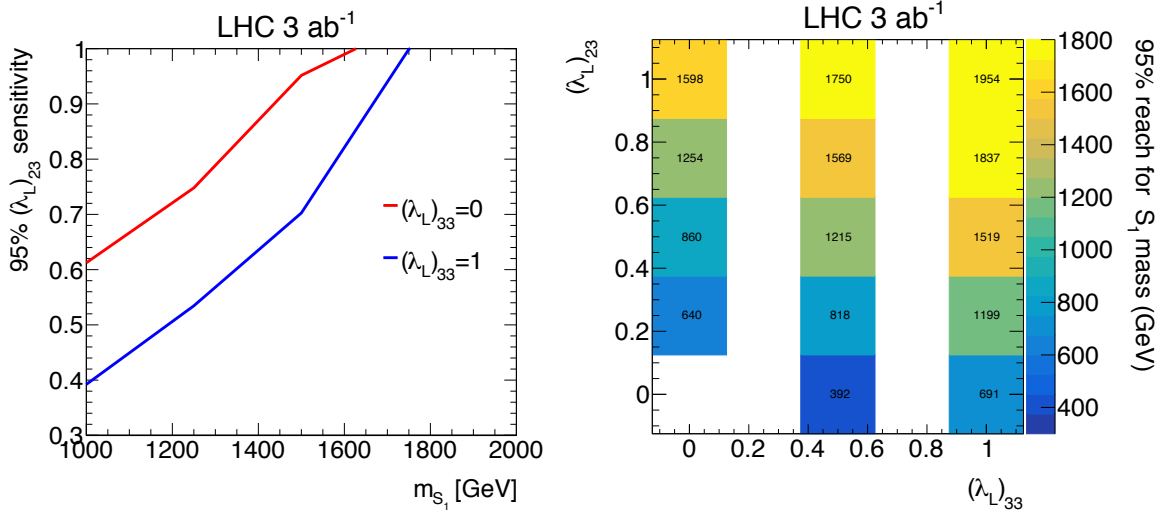
Figure 5: *Left panel: value of $(\lambda_L)_{23}$ which can be excluded at 95% CL at HL-LHC as a function of m_{S_1}. Right panel: m_{S_1} which can be excluded at 95% CL in the $((\lambda_L)_{33}, (\lambda_L)_{23})$ plane*

literature, see e.g [32]. We generated for this process the complete decay pattern of the S_1, through the card

```
define l3g = ta+ ta- vt vt~
define q23g =  c s b  c~ s~ b~ t t~
generate p p > S1m13 S1m13~, (S1m13 > l3g q23g), (S1m13~ > l3g q23g)
```

to take into account the possible contribution of all of the channels in the signal region. The generation was performed at the fixed values of yLL2x3=1 and yLL3x3=1 for a grid of S_1 masses between 750 and 2500 GeV.

We concentrate on the semileptonic decay of the top. Events are required to contain one and only one isolated lepton ℓ (e, μ) with $p_T > 20$ GeV, one τ-jet with $p_T > 30$ GeV and at least one b-tagged jet with $p_T > 30$ GeV all of them within $|\eta| < 2.5$, and to satisfy the requirement $E_T^{\text{miss}} > 200$ GeV.

The presence of at least an additional jet with $p_T > 20$ GeV is also required. The first step in the analysis is to select among the additional jets the one most likely to be a b-jet, which is taken as the second b-jet candidate. To reject the $t\bar{t}$ and $t\bar{t}Z$ backgrounds, the kinematics of the two b-jet candidates, the lepton and the τ-jet is made to be incompatible with the presence of two semileptonic top decays by requiring that $m_{b\ell}^t > 160$ GeV, where

$$m_{b\ell}^t = \min\left(\max\left(m_{\ell j_1}, m_{\tau j_2}\right)\right),\tag{2}$$

and j_1 and j_2 run over the two b-jet candidates.

Each of the two b-jet candidates is then assigned either to the decay either of the top (b_t) or of the leptoquark (b_{lq}). The jet which has invariant mass with the lepton $m_{bl} < 160$ GeV is defined as b_t. If the condition is satisfied for both jets, the softer one is defined as b_t. Based on this assignation, two variables sensitive to the mass of the leptoquark in the two decay legs are respectively $m_{b_t \ell \tau}$ and $m_T^{b_{lq}}$. These are required to be $m_{b_t \ell \tau} > 200$ GeV, $m_T^{b_{lq}} > 200$ GeV.
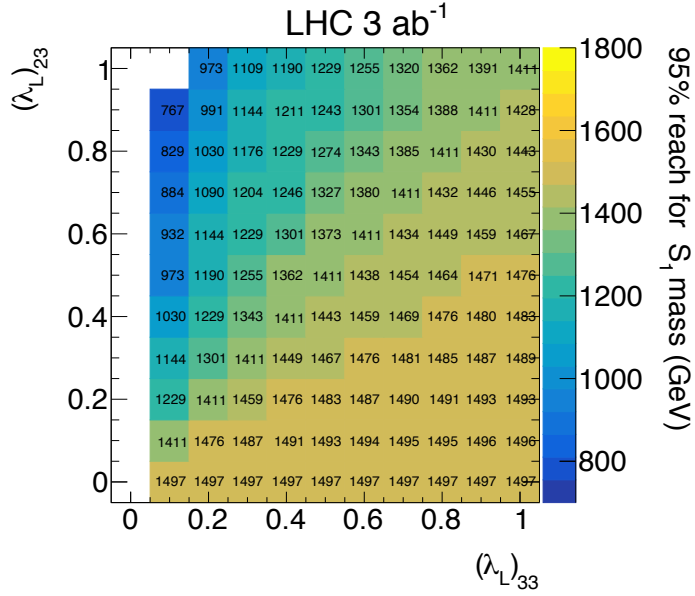
27

Figure 6: m_{S_1} *which can be excluded at 95% CL in the ((λ_L)$_{33}$,(λ_L)$_{23}$) plane on the basis of the search for pair production of S_1 described in the text.*

The final discrimination is obtained using m_{T2}^τ, which is the stranverse mass between the E_T^{miss} and the τ-lepton on one leg and the E_T^{miss} and the electron or muon on the other. This distribution has an end-point for semi-leptonic $t\bar{t}$ decays where one W boson decays into $\tau\nu$ and the other decays into $e\nu$ or $\mu\nu$, which can be then effectively suppressed with a minimal requirement of 100 GeV.

The value of m_{S_1} which can be excluded at the 95% level on the basis of this analysis is shown in the ((λ_L)$_{33}$, (λ_L)$_{23}$) plane in Fig. 6. The dependence on (λ_L)$_{23}$ is partially determined by the interplay of branching ratios, and partially by the fact that, since only one b-tagged jet is required in the analysis, the case where one leg is $S_1 \to s\nu$ is selected very efficiently.

6.2 Search for single leptoquark production

The signature studied in this case corresponds to the first two diagrams on the left of Fig. 3, where the quark in the initial state can be either a b of an s-quark, and the c in the decay of the resonant S_1 is replaced by a top quark.

The signal is generated as

```
define nutau = vt vt~
define p1 = g c s b c~ s~ b~
define LQ = S1m13 S1m13~
generate p1 p1 > nutau LQ, (LQ > top tau)
```

A grid is generated in the ((λ_L)$_{33}$, (λ_L)$_{23}$) plane for m_{S_1} between 750 GeV and 2 TeV.

The selected final state is the same as for the analysis in the previous section. The b-tagged jet is required to have $p_T > 50$ GeV, and the lepton ℓ and the tau-jet are required to have $p_T > 25$ GeV. Additionally, a minimum azimuthal separation between the direction of the missing momentum and all jets is required ($\Delta\Phi_{min}(E_T^{miss}, jets) > 0.5$).
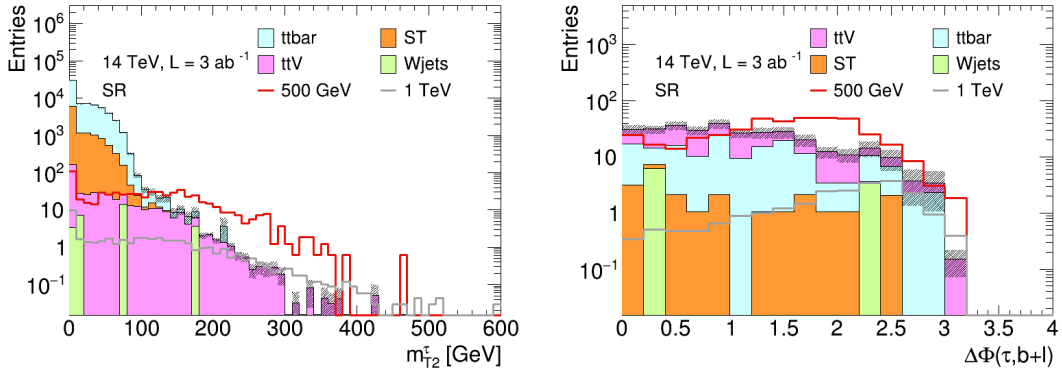
Figure 7: *Distributions after all requirements of m_{T2}^τ and $\Delta\Phi(\tau, b+\ell)$ for representative signal models and the backgrounds.*

The E_T^{miss} magnitude is required to be larger than 200 GeV. In addition, a minimal transverse invariant mass between the light lepton and the E_T^{miss}, m_T^ℓ, of at least 100 GeV.

Two variables are finally used to discriminate the residual background and the signal. One is m_{T2}^τ described above, for which we require $m_{T2}^\tau > 100$ GeV. The second variable is $\Delta\Phi(\tau, b+\ell)$, the azimuthal angle between the τ-lepton and the vectorial sum of the momenta of the b-jet and the light lepton. If you assume that the sum of the b-jet and the light lepton is a good proxy for the direction of the top-quark, this angle is a proxy for the opening angle between the decay product of the leptoquark, which tends to be larger than in the case of the background processes. See an example of these two distributions in Fig. 7. All requirements except the ones on the variables shown in the plots are applied.

The value of m_{S_1} which can be excluded at the 95% level on the basis of this analysis is shown in the $((\lambda_L)_{33}, (\lambda_L)_{23})$ plane in the left panel of Fig. 8. The reach rises with $(\lambda_L)_{23}$ because of the contribution of the gs initial state to leptoquark production. For $(\lambda_L)_{23} = 0$ the top final state has higher sensitivity than the b-tagged jet final state discussed in Sec. 5.

In the right panel of Fig. 8 the reach in the coupling $(\lambda_L)_{33}$ as a function of the leptoquark mass for $(\lambda_L)_{23} = 0$ is shown. The reach for single production (red line) is compared to the one for pair production (blue line). The single production overtakes the pair production for a coupling of approximately 3.

7 CONCLUSIONS

We studied the potential of the HL-LHC for the discovery of leptoquarks in final states involving a heavy quark (b/t), a τ lepton decaying hadronically and E_T^{miss}, produced either as the result of the pair production of two leptoquarks where the two legs decay in different final states, or of the associate production of a leptoquark with a τ or a ν_τ, with the leptoquark decaying into a heavy quark and a third generation lepton.

From the detailed simulation study involving a model with a scalar S_1 leptoquark, and only couplings of type $(\lambda_L)_{23}$ and $(\lambda_L)_{33}$ different from zero we assess the parameter space covered by three dedicated searches for the final states of interest at the HL-LHC for an integrated luminosity of 3 ab^{-1}.

Leptoquark masses above 1.5 TeV will be accessible over all of the parameter space for both couplings $(\lambda_L) < 1$. The top+τ+ν final state from leptoquark pair production dominates
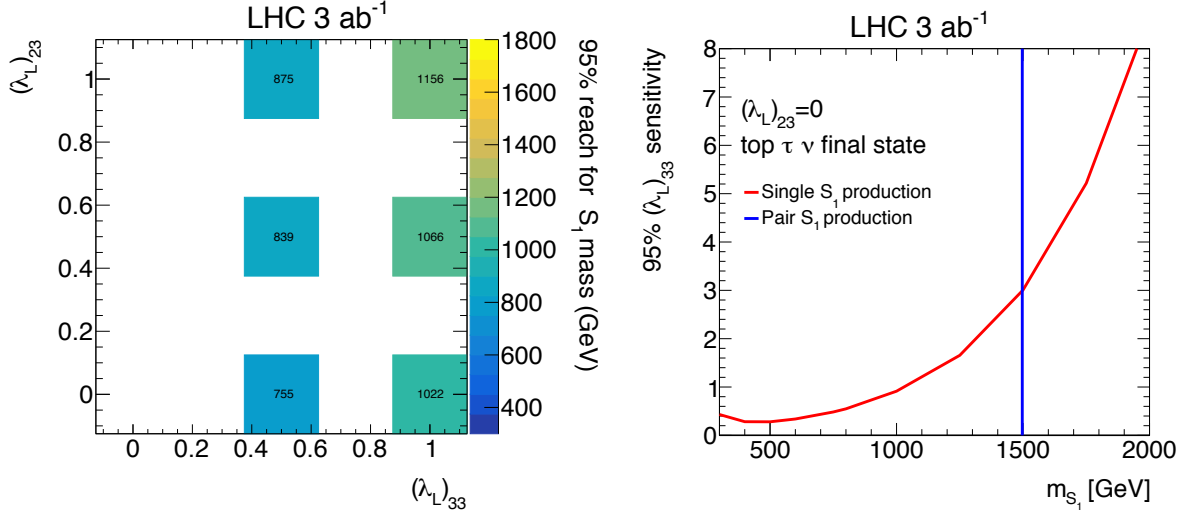
Figure 8: *Results of the search for production of S_1 in the final state top+τ+ν at the LHC with 3 ab^{-1} of integrated luminosity Left panel: m_{S_1} which can be excluded at 95% CL in the $((\lambda_L)_{33}, (\lambda_L)_{23})$ plane through the study of single production. Right panel: Value of the $(\lambda_L)_{33}$ coupling which can be excluded at 95% CL as a function of the leptoquark mass for $(\lambda_L)_{23} = 0$. The results for single (red) and pair (blue) LQ production are shown.*

the sensitivity for lower values of $(\lambda_L)_{23}$, whereas for $(\lambda_L)_{23}$ 1 the reach is dominated by the $b/c+\tau+\nu$ final state, yielding a reach up to 2 TeV. The studies were based on requiring in the final state passing the b-tagging requirements of the ATLAS experiment. It turns out that a significant part of the sensitivity is provided by final states involving the fragmentation of a c-quark mistagged as a b. A generic characteristic of the models able to explain the $R_{D(*)}$ anomalies is indeed a significant production of LHC final states involving a τ lepton and a c-quark. Analyses exploiting dedicated c-tagging algorithms will therefore significantly improve the LHC reach for this kind of models, and should be vigorously pursued by the experimental Collabirations.

ACKNOWLEDGEMENTS

Contribution 4

A common solution to the R_D anomalies and Dark Matter

*G. Bélanger, J. Bernigaud, A. Bharucha, B. Fuks, A. Goudelis, J. Heisig, A. Jueid, A. Lessa,
D. Marzocca, M. Nardecchia, G. Polesello, P. Pani, A. Pukhov, D. Sengupta and J. Zurita*

Abstract

The anomalies observed by LHCb in flavor observables suggest the breakdown of lepton flavor universality. We study how a vanilla leptoquark solution to the $R_{D^{(*)}}$ anomalies can also explain the measured relic abundance, if the leptoquark mediates between the visible sector and the dark sector.

1 Introduction

The current LHC dataset has not shown any significant deviation from the Standard Model (SM) expectations, except for the $R_{K^{(*)}}$ [33, 34] and $R_{D^{(*)}}$ [35–37] anomalies. While many models have been considered to explain these observations, the consensus is that two classes of models can accommodate these results: leptoquarks and Z' models (for a recent review see e.g [38] and references therein). It is thus interesting to consider the interplay between these solutions and dark matter (DM), which requires to allow an additional decay of the leptoquark into the dark sector, studied previously in [39, 40]. As this will reduce the branching ratios of the visible decays of the leptoquarks, it naively allows one to lower the current constraint on $m_{LQ} \gtrsim 1$ TeV with $\mathcal{O}(1)$ couplings, thus opening up novel parameter space and increasing the opportunities to probe this model at the LHC in the near future.

For our study we built a simplified model featuring the minimal ingredients to explain the charged current flavor anomalies $R_{D^{(*)}}$ and dark matter simultaneously, limiting ourselves to the couplings strictly necessary to explain the anomaly. We study how the different phenomenological constrains affect the parameter space: LHC searches for leptoquarks and dark matter, relic density, direct and indirect detection. We pay particular attention to the existing CMS search for a resonant leptoquark plus missing energy [41]: while this search might not always be the golden channel for discovery, its importance lies in the fact that this is the only channel probing the $R_{D^{(*)}}$-DM connection (RDM).

2 The model

We consider a simplified model in which we supplement the Standard Model by one scalar leptoquark field S_1 and two extra fermionic fields, a Majorana fermion χ_0 and a Dirac fermion χ_1. The S_1 and χ_1 fields are electrically-charged coloured weak singlets lying in the $(\mathbf{3}, \mathbf{1})_{-1/3}$ representation of the Standard Model gauge group. In contrast, χ_0 is a dark matter candidate and therefore a non-coloured electroweak singlet. In our FEYNRULES [18] implementation, we consider all potential interactions of the new sector with the Standard Model sector, the

corresponding Lagrangian being written as

$$\mathcal{L} = \mathcal{L}_{\text{SM}} + \mathcal{L}_{\text{kin}} + \left[\lambda_{\mathbf{R}} \, \bar{u}_R^c \, \ell_R \, S_1^\dagger + \lambda_{\mathbf{L}} \, \bar{Q}_L^c \cdot L_L \, S_1^\dagger + y_\chi \bar{\chi}_1 \chi_0 S_1 + \text{h.c.} \right] . \tag{1}$$

In this expression, all flavour indices are understood for simplicity and the dot stands for the $SU(2)$-invariant product of two fields lying in the fundamental representation. In addition, $\mathcal{L}_{\text{SM}}$ is the Standard Model Lagrangian and $\mathcal{L}_{\text{kin}}$ contains gauge-invariant kinetic and mass terms for all new fields, the χ_1 state being assumed vector-like. The Q_L and L_L spinors stand for the $SU(2)_L$ doublets of left-handed quarks and leptons respectively, whilst u_R and ℓ_R stand for the $SU(2)_L$ singlets of right-handed up-type quarks and charged leptons, respectively. The $\lambda_{\mathbf{L}}$ and $\lambda_{\mathbf{R}}$ couplings are 3×3 matrices in the flavour space, that are considered real in the following. Moreover, in our conventions, the first index i of any λ_{ij} element refers to the quark generation whilst the second one j refers to the lepton generation.

The field content of the new physics sector of our simplified model is presented in table 1, together with the corresponding representation under the gauge and Poincaré groups, the potential Majorana nature of the different particles, the adopted symbol in the FEYNRULES implementation and the PDG identifier that has been chosen for each particle. The new physics coupling parameters are collected in table 2, in which we additionally include the name used in the FEYNRULES model and the Les Houches blocks [42] in which the numerical values of the different parameters can be changed by the user when running tools like MG5_AMC [43] or MICROMEGAS [44].

Field	Spin	Repr.	Self-conj.	FEYNRULES name	PDG code
S_1	0	$(\mathbf{3}, \mathbf{1})_{-1/3}$	no	LQ	42
χ_0	1/2	$(\mathbf{1}, \mathbf{1})_0$	yes	chi0	5000521
χ_1	1/2	$(\mathbf{3}, \mathbf{1})_{-1/3}$	no	chi1	5000522

Table 1: *New particles supplementing the Standard Model, given together with the representations under $SU(3)_c \times SU(2)_L \times U(1)_Y$. We additionally indicate whether the particles are Majorana particles, their name in the FEYNRULES implementation and the associated Particle Data Group (PDG) identifier. Note that the PDG code 42 is the official PDG value for our leptoquark [45] and hence there are no issues when running showering and/or hadronizing the event sample.*

Coupling	FEYNRULES name	Les Houches block
$(\lambda_L)_{ij}$	lamL	LQLAML
$(\lambda_R)_{ij}$	lamR	LQLAMR
y_χ	yDM	DMINPUTS

Table 2: *Couplings of the new particles, given together with the associated FEYNRULES symbol and the Les Houches block of the parameter card.*

In a nutshell, our model needs three new masses and several new couplings. The R_D

anomalies can be explained with only non-zero $(\lambda_L)_{33} \equiv \lambda_L$[1] and $(\lambda_R)_{23} \equiv \lambda_R$. Finally, the dark matter phenomenology requires the coupling y_χ. Hence these 6 parameters span our parameter space. In what follows we will study how the flavor anomalies, dark matter phenomenology and collider searches constrain the parameter space of this model, showing the currently allowed regions and commenting on the future prospects.

3 Leptoquark solutions to the R_D anomalies

As mentioned in the previous chapter, a minimal solution of the $R_{D^{(*)}}$ anomalies can be obtained with just a left-handed $((\lambda_L)_{33})$ and a right-handed $((\lambda_R)_{23})$ couplings to S_1. We note that the $((\lambda_L)_{33})$ coupling is forced to be left-handed due to the presence of the neutrino[2]. The choice of having a non-vanishing $((\lambda_R)_{23})$ is due to the large contributions that $(\lambda_L)_{23}$ would generate to the $B \to X_s \nu\nu$ process, which could only be reduced by extending the model, e.g: considering a destructive interference with another leptoquark state [24, 25, 47, 48]. We perform a global fit of the model with the two couplings $(\lambda_L)_{33}$ and $(\lambda_R)_{23}$ as free parameters. The relevant observables included in the fit are: R_D, R_D^*, Br($B_c \to \tau\nu$), deviations in the Z couplings to τ_L and τ_R, effective number of neutrinos from Z decays, lepton flavour universality tests in τ decays. For more details on this fit see e.g. [24, 25, 46]. A contribution to $D^0 - \bar{D}^0$ mixing is generated at one loop, but is strongly CKM-suppressed and does not provide a relevant constraint. The results of a scan in the two parameters of the model, for $m_{S_1} = 1.5$ TeV, where all points are within 1σ of the best-fit point, is shown in the plane of the R_D and R_D^* anomalies in the left panel of figure 1. The corresponding preferred region is presented in the right panel of figure 1 in the x, y plane, with $x = \lambda_L(\text{TeV}/m_{S_1})$ and $y = \lambda_R(\text{TeV}/m_{S_1})$. [3]

From the figure we can establish two working points. We pick the first one to obtain the lowest possible $BR(S_1 \to c\tau)$, which corresponds to $(x, y) = (0.6, 0.5) = P_1$. For the second one we do not want to pick extreme values of λ_R, as we could spoil the validity of the narrow-width approximation for the leptoquark, as well as pertubativity. So we restrict ourselves to the best fit point $(0.16, 2.0) = P_2$ that already gives a negligible branching fraction into the third generation states. We thus use these working points to generate concrete benchmarks by picking two values for the leptoquark mass: $m_{S_1} = 500$ GeV and $m_{S_1} = 1000$ GeV. We show the corresponding values of the couplings and branching ratios in Table 3, where we have assumed a negligible coupling of S_1 to the dark sector. We note that the solution of the $R_{D^{(*)}}$ anomalies, being an off-shell interference with the SM amplitude, will not be affected by diluting the leptoquark visible decays, but it would rather loose the constraints coming from direct searches of S_1, which we discuss in detail in Section 4.

Before starting with the relevant collider and dark matter phenomenology, it is instructive to take a further insight into the phenomenology of our benchmarks. In figure 2 we show the branching fractions of S_1 and χ_1 for each of our working points, setting $m_{S_1} = 1$ TeV. For concreteness we fixed the dark coupling $y_{DM} = 0.2$ and $\Delta = m_{\chi_1} - m_{\chi_0} = 100$ GeV, but the phenomenology does not strongly depend on the actual values. Note that in our model the χ_1 always decays into a 3-body final state via an intermediate S_1. The phenomenology for the second case (right panel) is fairly simple: the dominant decay of S_1 is into a charm-quark

---

[1]The second index is not constrained, as the neutrino flavor is not tagged. For simplicity we restrict it here to the third generation.

[2]Alternatively one could explicitly introduce a right-handed neutrino that could serve as a dark matter candidate, see e.g [46].

[3]The $R_{D^{(*)}}$ anomalies scale with the product xy, while other constraints scale instead with x^2 or y^2.
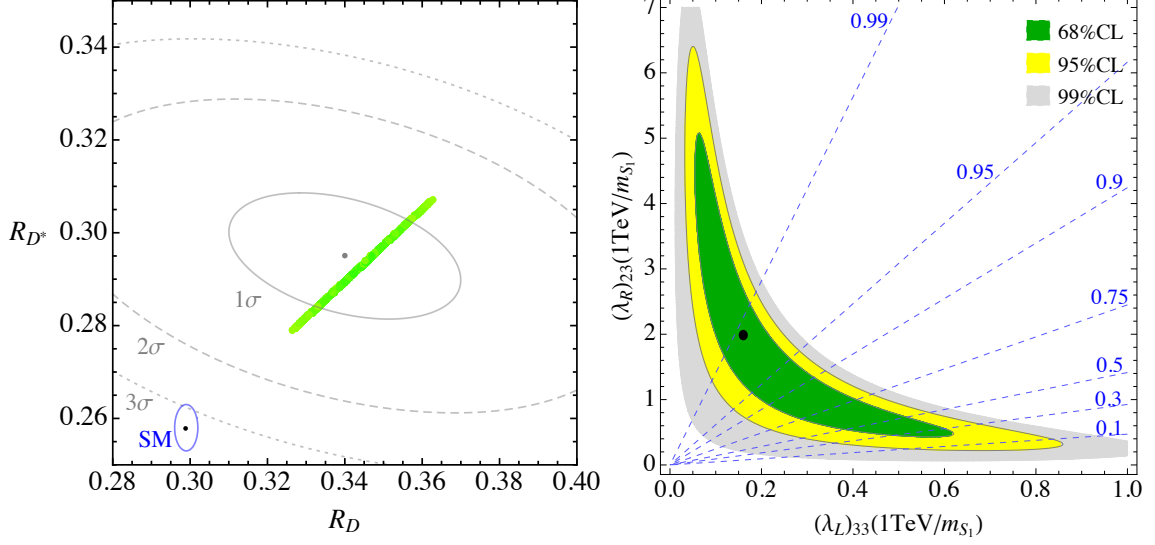
Figure 1: *Left: flavor fit to the charged current anomalies for $m_{S_1} = 1.5$ TeV (1σ region). The gray lines represent the present status in the measurements of the two observables, compared with the SM point (blue point and contour). Right: Viable parameter space from the fit of flavor and precision observables as function of λ/m_{S_1}. Blue dashed lines are iso-lines of the branching ratio $B(S_1 \to c_R \tau_R)$ assuming $y_\chi \ll (\lambda_L)_{33}, (\lambda_R)_{23}$ and $m_{S_1} \gg m_t$. The black dot represents the best-fit point.*

m_{S_1} [GeV]	λ_L	λ_R	$BR(S_1 \to b\nu)$	$BR(S_1 \to t\tau)$	$BR(S_1 \to c\tau)$	$\Gamma(S_1)/m_{S_1}$
500	0.30	0.25	0.4049	0.3139	0.2812	4.42E-3
1000	0.6	0.5	0.3794	0.3571	0.2635	1.89E-2
500	0.08	1.0	0.0063	0.0049	0.9887	3.4E-2
1000	0.16	2.0	0.0063	0.0059	0.9877	8.06E-2

Table 3: Benchmark points compatible with the flavour anomalies. Here we have assumed negligible decays into the dark sector. Note the wide range of possibilities for the $c - \tau$ channel (from 25 % to roughly 100%) while the b and top decays have an upper bound of about 40 and 30 % respectively, and can actually become at the sub-percent level.
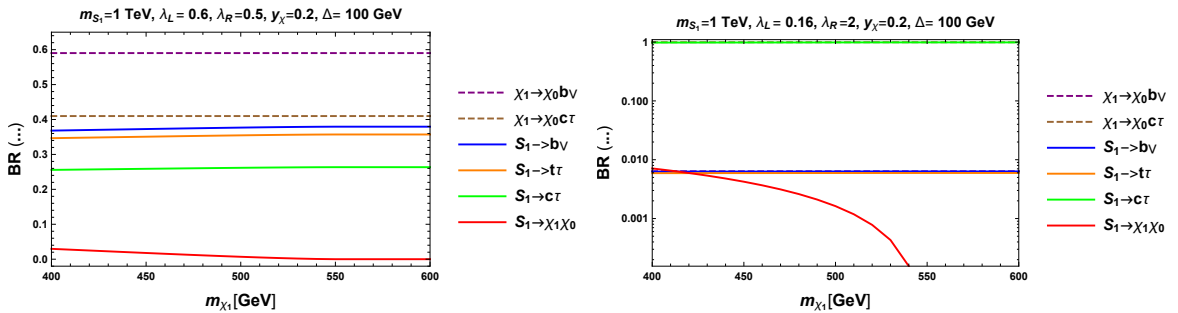
Figure 2: Branching ratios (top) for the S_1 and χ_1 as a function of the χ_1 mass. The mass difference between χ_1 and χ_0 is kept as 100 GeV, $y_\chi = 0.2$ and the other parameters correspond the second and fourth line of Table 3, called P_1 and P_2 in the main text.

and a tau-lepton, hence χ_1 decays via an off-shell S_1 almost exclusively into $c \, \tau \, \chi_0$. In the first scenario, where λ_L and λ_R are comparable, S_1 decays with appreciable ratios into both the three

34

"visible" channels and the invisible one. As a consequence, χ_1 decays into the $c\,\tau\chi_0$ and $b\nu\chi_0$ final states with similar ratios while the top final state is kinematically closed. This information is not enough to anticipate the collider phenomenology, as we will also need the production cross sections for S_1 and χ_1 states. We present the leading-order (LO) QCD cross sections as a function of m_{χ_1} and m_{S_1} in figure 3 for the three main production processes: pair production of S_1 and χ_1 via gauge interactions, and associated production of a leptoquark and a tau-lepton. We have used as a benchmark the fourth line from Table 3, hence when scanning over m_{S_1} we also vary $\lambda_{L,R}$ as to keep x and y fixed to the benchmarked values.
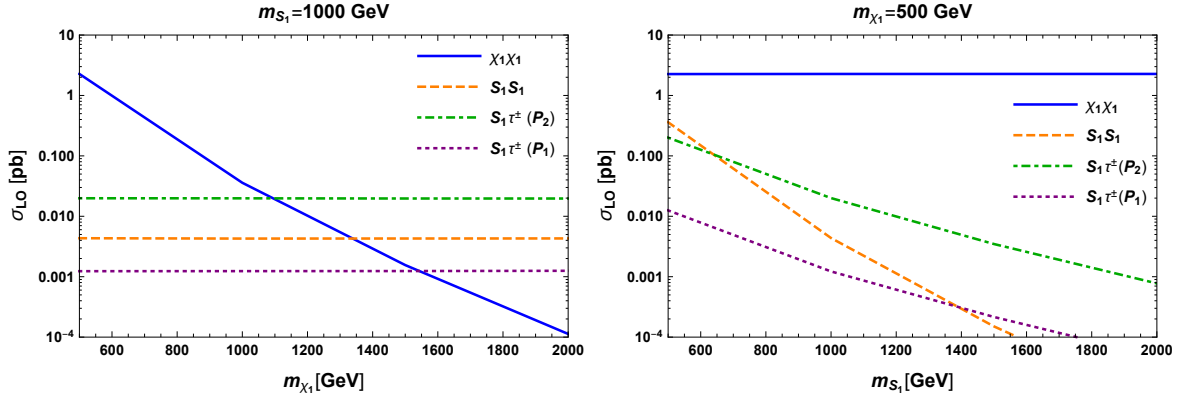

Figure 3: Cross-sections for S_1 and χ_1 production at the LHC as a function of m_{χ_1} (left panel) and m_{S_1} (right panel), for pair production of χ_1 (solid blue), pair production of S_1 (dashed orange) and associated production of S_1 and a tau lepton, which is shown for the benchmark points P_2 (dot-dashed green) and P_1 (dotted green). In the right panel we kept fixed $x = \lambda_L \mathrm{TeV}/m_{S_1}$ and $y = \lambda_R \mathrm{TeV}/m_{S_1}$ to the corresponding P_1 and P_2 values, see main text for details.

.

It comes as no surprise that the pair production of χ_1 is the process with the largest cross section, as both S_1 and χ_1 have the same colour charges but χ_1 is a fermion, and also because we are assuming that $S_1 \rightarrow \chi_1\chi_0$ occurs on-shell, hence χ_1 is lighter than S_1[4]. The single LQ cross section becomes relevant for large values of λ_R: the $S_1\tau$ cross section intercepts S_1 pair production at about 700 GeV (1.4 TeV) for $P_1(P_2)$, while the S_1 pair production cross section gets suppressed very fast by the large-x parton distribution functions. In the case of P_1, where λ_L and λ_R are comparable, then we should also include associated production of S_1 with bottom and top quarks, but these are PDF suppressed and give a negligible contribution to the total cross section at the LHC. These could however be important when considering future hadron colliders with larger energies [49].

4   LHC constraints

Our model contains three new fields that are probed by several LHC searches, which generically fall into two categories. On one hand, we have direct searches for leptoquarks (S_1), both for single and double production. On the other hand we have the full spectrum of missing transverse energy (MET) searches targeting invisible final states, in our case driven by pair production of χ_1 via gauge interactions. As a hybrid of both categories, the CMS search for leptoquark

---

[4]If we abandon this hypothesis the take-home message is exactly the same: the largest event rate corresponds to the lightest BSM colored particle in the spectrum.

plus dark matter [41], inspired by the Coannihilation Codex [40], gives not only interesting constraints on the parameter space, but moreover it would allow us to establish the connection between the flavor anomalies and dark matter, in a post-discovery scenario.

In each of the categories described above, we will consider both a) existing searches and b) novel searches (for instance, the aforementioned LQ + MET search of ref [41] only applies if the leptoquark decays to muons, but it is not applicable for e.g: electron decays). Given the large number of searches and the many processes they target, we summarize the ones we will use in this section in Table 4.

Category	Reference	Target process	Remarks
	[32]	$S_1 S_1 \to t\tau t\tau$	
	[32]	$S_1 S_1 \to b\nu b\nu$	
LQ	[50]	$S_1 S_1 \to c\tau c\tau$	Recasting of $b\tau b\tau$ study.
	Buttazzo et al. this volume	$S_1 S_1 \to b\nu t\tau$	
	[23]	$S_1 \tau \to c\tau\tau$	Rescaling of $b\tau\tau$ study
	[51, 52]	$\chi_1 \chi_1 \to bb\chi_0\chi_0$	
	[53]	$\chi_1 \chi_1 \to \tau\tau\chi_0\chi_0$	
MET	[54]	$\chi_1 \chi_1 \to \chi_0\chi_0 + nj$	$n \geq 2$ only.
	[55]	$\chi_1 \chi_1 \to \chi_0\chi_0 + nj$	$1 \leq n \leq 4$
LQ + MET	[41]	$S_1 S_1 \to lq\chi_1\chi_0$	CMS requires μ, we use $\tau \to \mu$ for interpretation

Table 4: *List of searches considered in this work. We split the studies in three categories, depending if they correspond to standard leptoquark searches, MET searches, and also the CMS search for a resonant LQ + MET, belonging to the hybrid of the two first categories.*

As anticipated in the previous section, the collider bounds will be dominated by χ_1 pair production, hence we expect the $b\bar{b}$ + MET and $\tau\tau$ + MET searches to set tight constraints on the parameter space. These would lose stem as the final state becomes inefficient (e.g: in our second working point the branching ratio of $S_1 \to b\nu$ is negligible) or if the dark sector becomes compressed, giving rise to soft decay products that would not pass the reconstruction requirements. In that case we can expect a bound from the mono-jet search, where χ_1 gives only rise to MET and one invokes initial state radiation to boost the $\chi_1\chi_1$ system while allowing for an efficient trigger. This bound should however, be looser than the one from the $b\bar{b}/\tau\tau$ + MET and hence the LQ searches become competitive in probing the parameter space. The hybrid search is necessary to fingerprint the connection between the flavour anomalies and the dark sector, but naively we would not expect it to set the leading bounds.

4.1 Leptoquark searches

There are two different production mechanisms for leptoquarks at the LHC, which are shown in figure 4: pair production (left panel) due to gauge interactions[5] and single production in association with a SM fermion (right panel). The pair production is a guaranteed mode, since its cross section is only a function of the leptoquark mass. The single production cross section depends both on the leptoquark couplings to the SM fermions and with the leptoquark masses.

---

[5]In principle also t-channel leptonic exchange can be relevant given the size of the leptoquark couplings, and would be taken into account in the next-to-leading order calculation in a future publication.

The experimental searches for leptoquarks are organized by these production mechanisms, and we will follow the same taxonomy here.
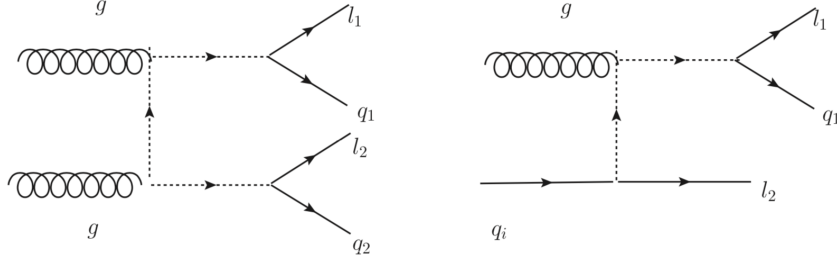

Figure 4: Representative Feynman diagrams for pair (left) and single (right) leptoquark production at hadron colliders.

4.1.1 LQ pair searches

Searches for visible decays of LQ pairs at ATLAS [32,56,57] and CMS [58–60], focus on both leptoquarks decaying in the same final state. In Ref. [32] five different searches are described. The first one is a search for LQ decaying into the $b\tau b\tau$ final state, reoptimising an existing di-Higgs search in the same final state [61], to the different final state kinematics. The other four searches are reinterpretations of existing studies of supersymmetric particles: searches for stop pair production in the zero-lepton [62] and one-lepton channel [63] ($t\bar{t}$+ MET), stop decays into staus [50] and a sbottom search [64] ($b\bar{b}$+ MET). Our model has four leptoquark decay channels, three into SM particles and one into the DM mediator, as shown in figure 2. Two of the decay channels are directly covered by the ATLAS searches, namely the decays into $t\tau$ and into $b\nu$, through the searches respectively for the $b\tau b\tau$ final states, and for $b\bar{b}$+ MET. For any choice of the coupling, and barring effects from the top mass, we would have that $BR(S_1 \rightarrow t\tau) \approx BR(S_1 \rightarrow b\nu)$, in contrast to the ATLAS study where $BR(S_1 \rightarrow b\nu) = 1 - BR(S_1 \rightarrow t\tau)$ is assumed.

We note that even if this search is restricted to the third generation final states, there is no search for the "mixed" final state, namely $b\nu t\tau$. In order to achieve an optimal coverage this channel should be included, and we have indeed carried out a preliminary simulation study. A detailed analysis of this final state for a 14 TeV LHC based on a parametrised simulation of the ATLAS detector, with full consideration of all relevant backgrounds is described elsewhere[6]. In this study a dedicated selection is developed to separate the final state of interest from the overwhelming $t\bar{t}$ background through novel variables which optimally exploit the kinematical features of leptoquark pair production, and its difference from the $t\bar{t}$ kinematics.

In addition we also try to address the $c\tau c\tau$ final state through a rough rescaling of the existing ATLAS $b\tau b\tau$ limits. [7]

---

[6]See Buttazzo et al. in the same proceedings volume.

[7]To be fully comprehensive one should also consider the mixed final states $c\tau b\nu$ and $c\tau t\tau$, but these are beyond the scope of this work. We expect them to be subdominant: given the lesser quality of c-tagging with respect to bottom- and top-tagging, c final states will only matter when the 3rd generation branching fraction is very small, $\mathcal{O}(5\%)$. In that case the largest branching fraction would occur in the $c\tau c\tau$ channel, which would be at least about an order of magnitude above the "mixed" rate.

In the model under consideration this decay is dominant over a large part of the parameter space allowed by the consideration of the flavour anomalies, as shown in figure 1, where dashed blue lines represent the isovalues of $BR(S_1 \to c\tau)$ in the $\lambda_L - \lambda_R$ plane. This final state is not targeted by the ATLAS searches which are focused on the third generation.

In absence of a dedicated analysis, a rough evaluation of the coverage for the $c\tau c\tau$ final state can be obtained by the consideration of the ATLAS results for the $b\tau b\tau$ final state. The experimental algorithm for tagging the b-jets used in Ref. [32] has an average efficiency for tagging a jet from the fragmentation of a b-quark of 70%. The same algorithm tags the jet from the fragmentation of a c-quark with an efficiency of $\sim 8\%$ ([65]). Therefore the results for the $b\tau b\tau$ final can be recasted for the $c\tau c\tau$ final state by scaling down the excluded branching fraction by a factor ~ 8.5. This scaling is conservative, as it assumes that the analysis requires two b-tagged jets in the event, whereas both events with 1 and 2 b-tags are considered in [32]. A dedicated analysis, based on e.g. the c-tagging algorithms recently developed by ATLAS [66] should provide a much better coverage for the $c\tau$-dominated region and the inclusion of such a study within the leptoquark search programme should be high in the list of priorities of the experimental collaborations.

Both for the proposed mixed analysis and for the $c\tau c\tau$ rescaling of the ATLAS $b\tau b\tau$ analysis we evaluated, for each point in the $\lambda_L - \lambda_R$ plane the excluded mass based on the considerations above. The result is shown in figure 5, where the results for the mixed ($c\tau c\tau$) analyses are shown in the left (right) panel. For the uncovered points in the two panels the exclusion on the S_1 mass is below 400 GeV, which is the lowest mass for which the two considered analyses provide an exclusion.
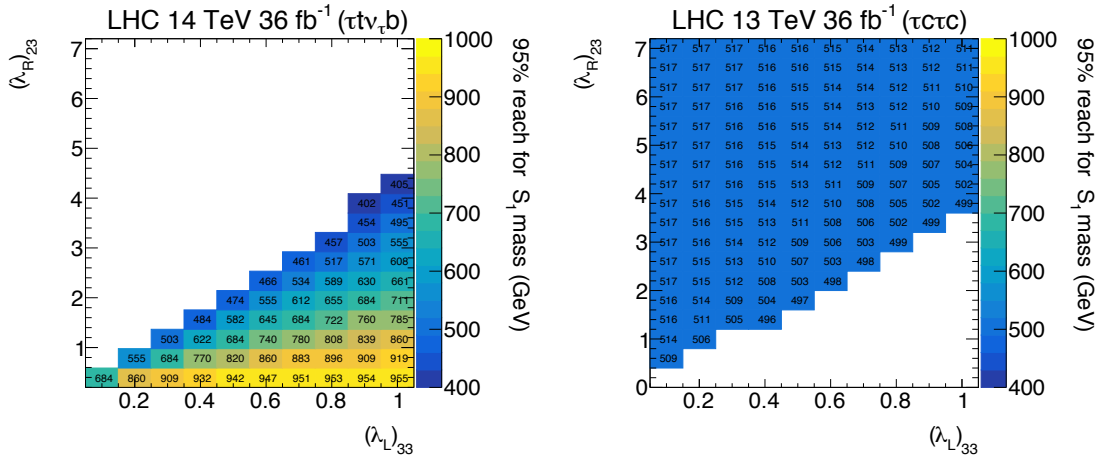
Figure 5: *Excluded values of m_{S_1} at 95% CL in the plane defined by the $(\lambda_L)_{33} - (\lambda_R)_{23}$ couplings for an integrated luminosity of 36 fb^{-1}. In the right panel the 14 TeV mixed-decay $b\nu_\tau t\tau$ analysis (described in Buttazzo et al within this proceeding volume) and on the right the rescaling of the ATLAS $b\tau b\tau$ analysis (described in the main text).*

By combining the results from the two recasts, with the currently published LHC statistics of 36 fb^{-1} a value of m_{S_1} of at least 500 GeV is (or can be) excluded at 95% CL, but significantly larger discovery potential can be expected with a dedicated $c\tau c\tau$ analysis.

To summarize, we compare in figure 6 the leptoquark mass coverage as a function of the BR for the four final states defined above for 36 fb^{-1}, where for the mixed decay $BR(S_1 \to$

$t\tau) \approx BR(S_1 \to b\nu)$ is assumed. In the searches where both leptoquarks decay in the same manner what is usually reported is the leptoquark branching fraction into a given channel, but the event rate scales with the squared of this value. Hence, for the mixed decay we plot the square of $2BR(S_1 \to b\nu)BR(S_1 \to t\tau)$. The solid lines correspond to the mass reach from the experiments and our two proposed searches, while the dashed lines correspond to our second benchmark[8]. Over most of the leptoquark mass range considered, the mixed decay $b\nu t\tau$ (dashed green) search has a higher sensitivity than the $b\nu b\nu$ (dashed blue) and the $b\tau b\tau$ (dashed red) searches. The $c\tau$ final state is only relevant for the case where the branching fraction of S_1 to other states is below about 5 %. As shown in our first benchmark, branching fractions even smaller into $b\nu$ and $t\tau$ do occur near the best fit point.
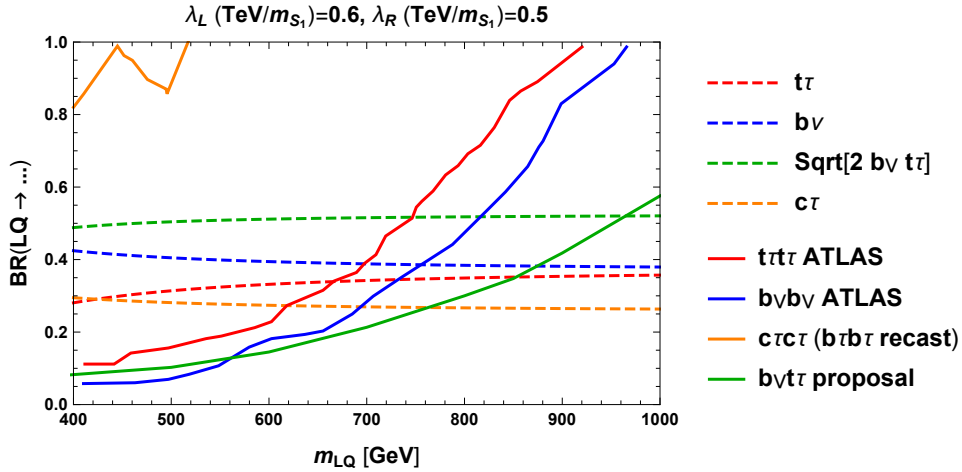

Figure 6: *Coverage of the different LQ pair searches with decays into third generation fermions. We show in dashed lines the branching ratios for the case where $x = 0.5$ and $y = 0.6$ (see main text for definition), while solid lines denote the branching ratio reach as a function of the leptoquark mass, for the $t\tau t\tau$ (red), $b\nu b\nu$ (blue), and $c\tau c\tau$ taken directly or rescaled from [32], as well as our proposed search in the $t\tau b\nu$ channel (green). For the mixed decay we plot the square of $2BR(S_1 \to b\nu)BR(S_1 \to t\tau)$, see main text for details.*

4.1.2   LQ associated production with a lepton

A single leptoquark can also be produced in association with a SM fermion, as shown in the right panel of figure 4. For our particular choice of couplings and of leptoquark charge, two single leptoquark production processes will contribute: $bg \to \nu_\tau S_1$ and $cg \to \tau S_1$. Combining with the three possible decays into SM particles shown in figure 2, one has a final state with a single b+MET (mono-b), states with a single τ + heavy quark + MET, and states with two taus and a c or a t quark.

Searches exist for the mono-b final state, but, due to the large backgrounds, and the lack of kinematic handles, we expect the sensitivity to be lower than the other channels.

The final states with a single tau and a heavy quark are addressed elsewhere in these proceedings, and will be relevant for the case where $\lambda_R \sim \lambda_L$. Given the relatively low values of λ_L compatible with the explanation of the flavour anomalies, we expect the reach in mass to

---

[8]In our first benchmark we only can constrain the model using the $c\tau$ analysis, hence the mass reach is about 500 GeV.

be comparable with the one from the mixed decay in pair production discussed in the previous section.

The $\tau\tau c$ final state will be the dominant channel for the case in which $\lambda_R > \lambda_L$, as the event rate scales as $\lambda_R^2 \times BR(S_1 \to c\tau)$. No search for this channel exists in the literature, but the CMS Collaboration has published a search for single leptoquark production in the $\tau\tau b$ channel [23]. As is the case for the ATLAS $b\tau b\tau$ analysis in the previous subsection, the algorithm used to tag jets from the fragmentation of b-quarks has a certain sensitivity also for jets from the fragmentation of c-quarks. Under the assumption that the kinematic acceptance of the analysis is the same for the $\tau\tau b$ and for the $\tau\tau c$ final states, the results for the $\tau\tau c$ may be obtained by a simple rescaling of the heavy-flavour tagging efficiency. In Ref. [23] they declare that they are using the combined secondary vertex algorithm at a working point with an efficiency for b-jets of approximately 60%. For this algorithm they define in Ref. [67] a medium working point with efficiency of 63% for b-jets and 12% for c-jets. We will assume the ratio of these numbers for our rescaling. The result is shown in figure 7, where the value of m_{S_1} excluded at 95% CL is shown in the plane defined by the $(\lambda_L)_{33} - (\lambda_R)_{23}$ couplings.
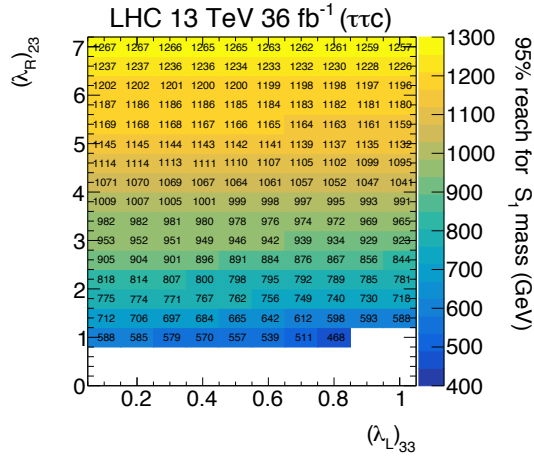
LHC 13 TeV 36 fb^{-1} ($\tau\tau c$)

$(\lambda_R)_{23}$ (vertical axis, 0–7) — 95% reach for S_1 mass (GeV) (colour scale 400–1300)

1267	1267	1266	1265	1265	1263	1262	1261	1259	1257
1237	1237	1236	1236	1234	1233	1232	1230	1228	1226
1202	1202	1201	1200	1200	1199	1198	1198	1197	1196
1187	1186	1186	1186	1185	1184	1183	1182	1181	1180
1169	1168	1168	1167	1166	1165	1164	1163	1161	1159
1145	1145	1144	1143	1142	1141	1139	1137	1135	1132
1114	1114	1113	1111	1110	1107	1105	1102	1099	1095
1071	1070	1069	1067	1064	1061	1057	1052	1047	1041
1009	1007	1005	1001	999	998	997	995	993	991
982	982	981	980	978	976	974	972	969	965
953	952	951	949	946	942	939	934	929	923
905	904	901	896	891	884	876	867	856	844
818	814	807	800	798	795	792	789	785	781
775	774	771	767	762	756	749	740	730	718
712	706	697	684	665	642	612	598	593	588
588	585	579	570	557	539	511	468		

$(\lambda_L)_{33}$ (horizontal axis: 0.2, 0.4, 0.6, 0.8, 1)

Figure 7: *Excluded values of m_{S_1} at 95% CL in the plane defined by the $(\lambda_L)_{33} - (\lambda_R)_{23}$ couplings for an integrated luminosity of 36 fb^{-1} for the CMS $\tau\tau c$ analysis as described in the text.*

Finally we compare in figure 8 the interplay of exclusions arising from pair and single leptoquark studies, where we show the 95 % C.L exclusion on λ_R as a function of m_{S_1}. For concreteness we included here only the proposed "mixed" search $b\nu t\tau$ (in red) and the $c\tau\tau$ result obtained via a recasting of the CMS study (green), and present curves using two representative values of λ_L: 0.5 (solid) and 1.0 (dashed). As previously discussed, we clearly see that the mixed search is optimal for lower values of λ_R (where the $c\tau$ final state has a comparable branching fraction with the other visible decays), while the single leptoquark search is optimal for high values of λ_R, where $c\tau$ is by far the dominant decay mode. As our benchmark points show that the flavor anomalies can be solved with either $\lambda_R \sim \lambda_L$ or $\lambda_R \gg \lambda_L$, both kind of searches are a necessary ingredient of a comprehensive campaign to probe the "leptoquark solution" of the $R_{D^{(*)}}$ anomalies.

4.2 Dark matter (missing energy) searches

Since the χ_1 particle is the lightest new particle with non-trivial SM quantum numbers, its production is strongly constrained by LHC searches, and it can only be "hidden" if χ_1 and χ_0
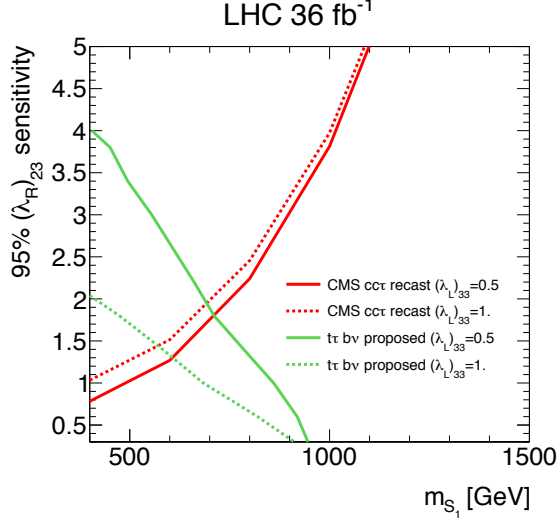
Figure 8: *Comparison of the excluded λ_R for the "mixed" $b\nu t\tau$ proposed search (green) and the $c\tau\tau$ recasting of the CMS $b\tau\tau$ study. Solid (dashed) lines denote $\lambda_L = 0.5(1.0)$.*

are close in mass. The LHC production is depicted in figure 11. Since we always assume $m_{\chi_1} < m_{S_1}$, the decay of χ_1 is entirely determined by the LQ branching ratios and the only decay channel is $\chi_1 \to S_1^*(\to lq) + \chi_0$. As shown in figure 2, χ_1 dominantly decays to $\chi_0 + c\tau$ for $\lambda_R > \lambda_L$ (third and fourth benchmarks in Table 3) or has similar BRs to $\chi_0 + c\tau$, $\chi_0 + b\nu$ and $\chi_0 + t\tau$ (first and second benchmarks) if $\lambda_R \lesssim \lambda_L$. Therefore searches for missing energy associated with jets, b-jets, tops or taus can be used to test our model.

4.2.1   b-jets plus MET searches

If $\lambda_L \gtrsim \lambda_R$ a sizeable fraction of the χ_1s produced at the LHC decay to $b\nu$ or $t\tau$. In order to constrain this scenario we re-interpret the CMS results for the sbottom simplified model $pp \to \tilde{b} + \tilde{b} \to b\tilde{\chi}_1^0 + b\tilde{\chi}_1^0$. For simplicity we assume that the decay $\chi_1 \to \chi_0 b\nu$ has similar efficiencies and the same cross-section upper limits obtained by CMS for the sbottom scenario can be applied to our model. We have used the SMODELS [68] implementation of the CMS searches at 13 TeV and 35.9 fb^{-1} from Refs. [51, 52] and used it to recast the CMS bounds. The cross-sections were computed using MG5_AMC and we have applied a K-factor of 1.5 to the χ_1 pair production cross-section. The results are shown in figure 9, where we have assumed the second benchmark of Table 3 and varied m_{χ_1} and m_{χ_0}. As we can see, χ_1 masses up to 900 GeV can be excluded for sufficiently large mass gaps. However, once $m_{\chi_1} - m_{\chi_0}$ drops below 25 GeV the b-jets originating from the χ_1 decay become too soft and the search looses its sensitivity.

4.2.2 τ plus MET searches

Once $\lambda_L \lesssim \lambda_R$, the χ_1 decays are dominated by $\chi_1 \to \chi_0 + c\tau$. Although there is no LHC search which targets this final state, searches for taus plus missing energy can still be sensitive to this decay mode. Here we consider the 13 TeV ATLAS search at 139 fb^{-1} from Ref. [53], which targets final states with two taus plus missing energy and has been used to constrain the $pp \to \tilde{\tau} + \tilde{\tau} \to \tau\tilde{\chi}_1^0 + \tau\tilde{\chi}_1^0$ simplified model. Since in our model χ_1 is colored, its production cross-section is much larger than for pair production of staus and much higher masses can be
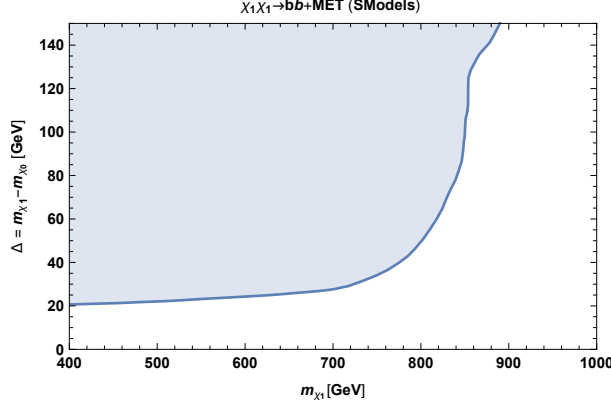
Figure 9: Region in the $m_{\chi_1} - m_{\chi_0}$ vs m_{χ_1} plane excluded by LHC searches for b-jets plus MET. The remaining model parameters are $y_\chi = 0.2$, $\lambda_L = 0.6$, $\lambda_R = 0.5$ and $m_{S_1} = 1$ TeV. The shaded region corresponds to the parameter space excluded by CMS searches for final states containing one or more b-jets and missing energy [51, 52].

tested by the analysis. The upper limits presented by ATLAS, however, are limited to $m_{\tilde{\tau}} < 450$ GeV and do not extend to the region of interest ($m_{\tilde{\chi}_1} \sim$ TeV). Therefore a full recasting was done using the tools provided by CHECKMATE2 [69].[9] We also point out that since the final state considered here contains c-jets and the ATLAS analysis has a veto on b-jets, about 50% of our signal will be lost due to mis-tagging of c-jets.

Using MG5_AMC, PYTHIA 8.2 [28] and our analysis implementation in CHECKMATE2 2.0.26 we compute the 95% C.L. exclusion for the fourth benchmark model in Table 3. Once again we apply a K-factor of 1.5 for the $\chi_1 \chi_1$ cross-section and vary m_{χ_1} and m_{χ_0}. The result is shown in figure 10, where we see that only points with a mass gap above 80 GeV can be excluded.
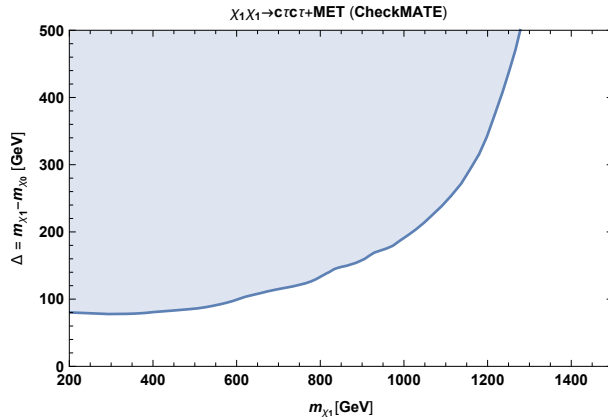

Figure 10: Region in the $m_{\chi_1} - m_{\chi_0}$ vs m_{χ_1} plane excluded by LHC searches for τ leptons plus MET. The remaining model parameters are $y_\chi = 0.2$, $\lambda_L = 0.16$, $\lambda_R = 2.0$ and $m_{S_1} = 1$ TeV. The shaded region corresponds to the parameter space excluded by ATLAS search for final states containing two hadronically decaying tau-jets and missing energy [53].

---

[9]The working point for the tau-tagging efficiency implemented in CHECKMATE seems to be slightly different from the one reported in Ref. [53]. Nonetheless the efficiencies obtained with our implementation are within 20%-50% of the ones obtained by ATLAS for the stau simplified model.

4.2.3 jets plut MET searches

As can be seen from figures 9 and 10, these searches lose steam once the mass gap between the parent and the daughter particle becomes small (compressed spectra). The usual strategy against a compressed spectra is to boost the system with additional radiation, leading to the mono-X (typically jet) signals. However, if the SM decay products in the $\chi_1 \to \chi_0$ are hard enough to be reconstructed (but probably not to be triggered on) the LHC sensitivity gets greatly enhanced, as shown in e.g. [70] for MSSM electroweakinos and soft-leptons. In our model this is shown in figure 11. However, the mass gap can be small enough such that the soft decay products fail to pass the reconstruction thresholds, in which case the pair production of χ particles can only be constrained by jet + MET searches. We stress that this is an unavoidable bound, that, for a given Δ, sets a lower mass on the dark sector masses. We will thus ignore here the MET searches that also include resolved (soft or hard) leptons.
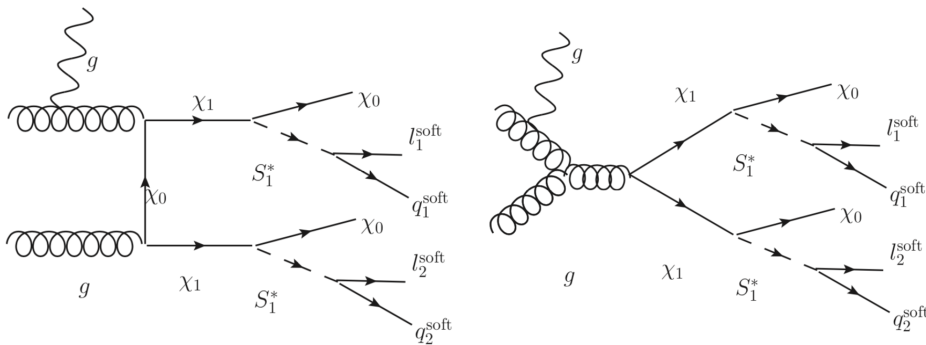

Figure 11: *Feynman diagram for monojet (plus soft leptons and quarks) signatures.*

In figure 12 we show the corresponding constraints in the $m_{\chi_1} - \Delta$ plane. In blue we show the region excluded by [55] (obtained via the MADANALYSIS 5 [71,72] implementation of said study) and in orange we show the region covered by the ATLAS search of two (or more) hard jets and MET [54]. As anticipated the excluded cross section is independent of m_{χ_1} unless the spectra is compressed: the mono-jet (multi-jet) study can exclude up to 650 (750) GeV if $\Delta \gtrsim 30(10)$ GeV.

4.3 Resonant lepto-quark + MET search

The model under consideration can also be constrained by reinterpreting the results of the CMS analysis [41] specifically searching, in 77.4 fb^{-1} of LHC data, signatures of dark matter that originate from the decay of a heavy leptoquark. In this search, the signal is assumed to arise from the production of a pair of heavy scalar leptoquarks that decay differently. The first leptoquark is hence considered to decay into a muon and a jet while the second one decays into dark matter and mostly soft Standard Model states. Consequently, the searched for signal is comprised of a significant amount of missing energy, jets and a high-p_T muon.

More specifically, preselected events are required to feature at least 100 GeV of missing transverse energy and one isolated central muon candidate with a transverse momentum $p_T > 60$ GeV and a pseudorapidity $|\eta| < 2.4$. [10] The analysis then restricts the properties of the hadronic activity in the events by constraining the centrally reconstructed jets ($|\eta| < 2.4$). The

---

[10]We note that our interest lies in the search with one τ lepton instead of one muon. We can, however, expect similar acceptances in the case of a leptonically decaying τ. A detailed study by the experimental collaborations
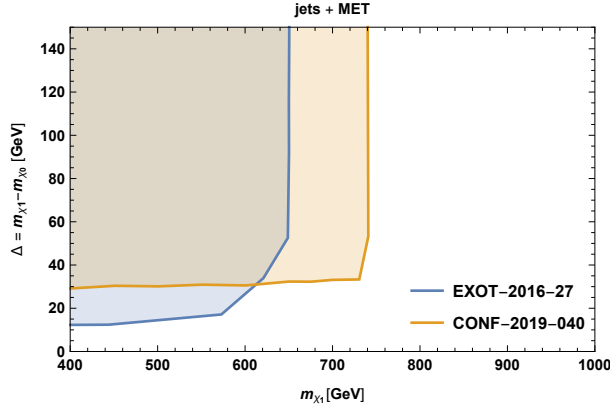
Figure 12: Region in the $m_{\chi_1} - m_{\chi_0}$ vs m_{χ_1} plane excluded by LHC studies for jets plus MET for a) more than one hard jet [54] (orange region) and b) a mono-jet search [55] (blue region) . Note that the additional model parameters ($y_\chi, \lambda_{L,R}, m_{S_1}$) do not play any relevant role here.

leading jet is hence enforced to have a transverse momentum $p_T > 100$ GeV and to be well separated, in the transverse plane, from the leading muon (by $\Delta R > 0.5$). The leading jet and leading muon are further considered to arise from the decay of a first leptoquark.

The selection then vetoes events featuring b-tagged jets, hadronic taus and electrons, as well as those featuring a second muon of electric charge opposite to the leading muon one, in which the muon pair made of these two muons is compatible with a Z-boson. Finally, the missing transverse momentum, being considered to stem from the decay of a second leptoquark, is required to be well separated in azimuth ($\Delta\phi > 0.5$) from the leading jet and muon, and the transverse mass of the system comprised of the muon and the missing energy is required to be larger than 500 GeV.

We have reimplemented this search in the MADANALYSIS 5 framework [20, 72, 73], and are currently validating our reimplementation by trying to reproduce detailed cutflows kindly provided by the CMS collaboration.

With the help of our (unvalidated) reimplementation, we considering two benchmark points for which the LQ mass if fixed to 1 TeV,

$$\begin{align}
\text{BP1}: \ & m_{\chi_1} = 400 \text{ GeV}, \ m_{\chi_0} = 380 \text{ GeV}, \\
\text{BP2}: \ & m_{\chi_1} = 600 \text{ GeV}, \ m_{\chi_0} = 200 \text{ GeV}, \tag{2}
\end{align}$$

and where the new physics couplings are given by $\lambda_R = 2$, and $\lambda_L = 0.16$. This choice affects the LQ pair branching ratios and is motivated as to maximize the sensitivity of the CMS search. For $m_{S_1} = 1$ TeV, the total production cross section is about 3.4 fb. In table 5, we show the expected, and the observed limits on the visible cross sections at 95% CL along with the acceptance times the efficiency ($A \times \epsilon$) of the selection in the signal region The investigated scenarios are out of reach of the LHC, at least in in the channel under consideration and there is very little hope to catch up such a huge gain in sensitivity even at the HL-LHC. This is not surprising as tau-enriched final states are more relevant than muon-enriched ones in our benchmarks. This should motivate the design, by the ATLAS and/or CMS collaborations, of a similar analysis targeting the tau channel.

---

including also electrons and τ-leptons would be an important contribution to both the leptoquark and DM LHC search programmes.

Benchmark Point	$\sigma_{\text{exp}}^{95\%}$	$\sigma_{\text{obs}}^{95\%}$	$A \times \epsilon\ [\%]$
BP1	62.24	58.25	0.00225
BP2	112.01	104.53	0.00125

Table 5: The values of the expected, and observed visible cross sections at the 95% CL along with the acceptance times the efficiency for the two benchmark points BP1 and BP2.
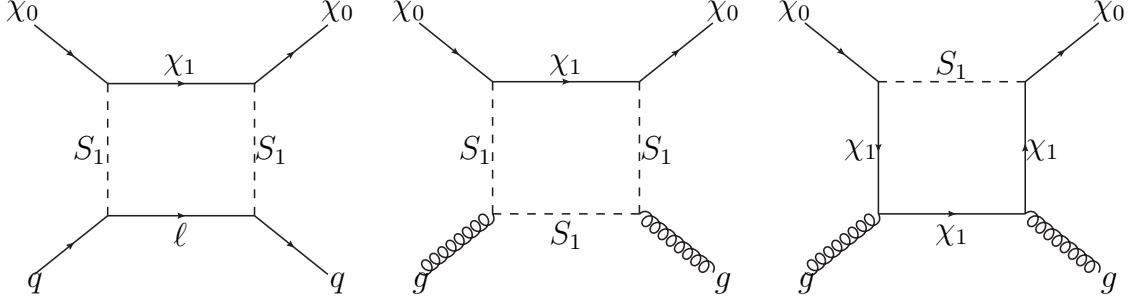

Figure 13: Feynman diagrams for the direct detection of dark matter in our model at the lowest order in perturbation theory.

5 Dark Matter constraints

In this section we study how the measured relic density and the null results of direct detection impact our model. We start by noting that the direct detection rate is one-loop suppressed (see figure 13), however given the current σ_{SI} exclusions this suppression might not be enough to discard this observable. For the relic density we consider two distinct scenarios. On one hand we study the (co)-annihilation case, as done in [40], while on the other hand we also consider the conversion-driven freeze-out (CDFO) scenario [74], also known as co-scattering [75]. The main idea behind this mechanism is that the self-annihilation of the DM candidate is negligible: the DM abundance arises instead from conversion processes within the dark sector. Hence, this scenario requires small/tiny interactions between the SM and the DM candidate (y_{DM} in our case), thus rendering the $BR(S_1 \rightarrow \chi_1\chi_0)$ negligible. This will thus affect the relevance of the collider signatures, that are discussed in detail in section 4.

5.1 Direct Detection

The scattering of χ_0 on a nucleon proceeds via 1-loop diagrams, which we show in figure 13. In the first diagram the loop include two leptoquark masses and the χ_1 mass, which are already heavy enough compared with the typical momentum transfer, so that would naively induce a mass suppression. In the second diagram one would have three leptoquark masses and a χ_1 mass, so that would be more suppressed than the diagram with three χ_1 and one S_1 in the loop.

Integrating out the heavy degrees of freedom χ_1 and S_1, we can obtain a rough estimate for the Wilson coefficient of the rightmost diagram, finding that $y_x \lesssim 1$. This result implies that direct detection constraints have an impact on our parameter space, and hence a complete 1-loop calculation taking into account all possible diagrams and interference effects is incumbent and is left for future work [11].

---

[11] Such a calculation was carried out for a similar model [76], however in that case S_1 is a t-channel mediator
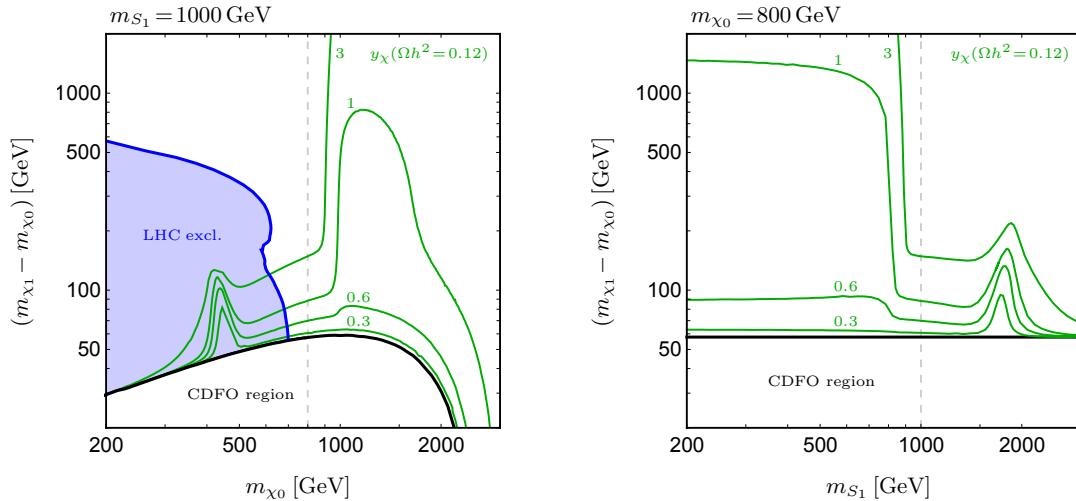
5.2 Relic Density

Figure 14: Parameter space satisfying $\Omega h^2 = 0.12$. The solid black line denotes the boundary between the standard freeze-out and conversion-driven freeze-out (CDFO) regime. The thin green curves denote contours of constant coupling y_χ. We also overlay the envelope of the missing energy searches (blue region) discussed in the previous section.). *Left panel:* Plane spanned by m_{χ_0} and $(m_{\chi_1} - m_{\chi_0})$ while fixing $m_{S_1} = 1000\,\text{GeV}$. *Right panel:* Plane spanned by m_{S_1} and $(m_{\chi_1} - m_{\chi_0})$ while fixing $m_{\chi_0} = 800\,\text{GeV}$. We choose $\lambda_L = 0.6\,m_{S_1}/\text{TeV}$ and $\lambda_L = 0.5\,m_{S_1}/\text{TeV}$. The vertical grey dashed line in the left panel indicates the fixed mass value in the right panel and vice versa.

In figure 14 we display contours of constant y_χ satisfying the correct relic abundance, $\Omega h^2 \simeq 0.12$ [77], computed with MICROMEGAS [44]. We consider two slices of the parameter space. In the left panel we fix $m_{S_1} = 1000\,\text{GeV}$ and $\lambda_L = 0.6, \lambda_L = 0.5$ (second benchmark point in table 3), which renders it safe from the leptoquark searches described in section 4. In the right panel we fix $m_{\chi_0} = 800\,\text{GeV}$ and m_{S_1} while keeping $\lambda_L = 0.6\,m_{S_1}/\text{TeV}$ and $\lambda_L = 0.5\,m_{S_1}/\text{TeV}$ consistent with the flavour anomalies.

As mentioned above, cosmologically allowed parameter space falls into two main classes: The standard thermal freeze-out regime with $y_\chi \sim \mathcal{O}(1)$ and the CDFO regime, residing above and below the thick black curve, respectively. For the latter the required couplings are small such that the decay of coannihilating partner is typically non-prompt [74]. In the standard freeze-out regime co-annihilations are important. The y_χ contours show two prominent features. The one at $m_{\chi_0} \sim m_{S_1}/2$ arises from resonantly enhanced coannihilation via an s-channel LQ, while the one at $m_{\chi_0} \sim m_{S_1}$ is due to the opening of DM pair-annihilation into a pair of LQs. Qualitatively, the phenomenology is very similar to the one of the top-philic charge parent model as studied in [78]. Note that for $m_{\chi_0} < m_{S_1}/2$ loop-induced DM annihilation into gluons can become important [78] which is, however, neglected here.

We overlay on top of these curves the "envelope" of the missing energy searches, which clearly disfavors low masses except for small mass splittings, where solutions in the CDFO regime can be found. Here, the applicability of LHC searches depends on the lifetime of the metastable χ_1 and is investigated elsewhere. For non-compressed mass spectra limits from the LHC require $m_{\chi_1} \gtrsim 750$ GeV.

(instead of s-channel), and there is no χ_1 particle.

Note that in the CDFO region the S_1 branching fractions into the dark sector would be negligible, and the invisible decay of S_1 would not be seen at colliders. The only handle into the dark world are the χ_1 searches (note that this is also true for the low m_{χ_1} region with compression). In the thermal freeze-out case one can have, besides the LQ, missing energy and direct detection searches, also information from the resonant leptoquark plus missing energy searches, thus allowing to firmly establish a connection between the flavor anomalies and the dark sector.

5.3 Indirect Detection

In general indirect detection constitutes an important probe of the self-annihilating nature of DM. In the considered model annihilation today dominantly takes place either via the $2 \to 2$ process $\chi_0 \chi_0 \to S_1 S_1$, if $m_{S_1} < m_{\chi_0}$, or via $2 \to 4$ or loop-induced $2 \to 2$ processes otherwise. In the first case the leading contribution is p-wave suppressed and hence the corresponding cross sections are small. The same is true for the $2 \to 4$ process which is suppressed by the off-shell S_1 propagator. Points where annihilation dominantly proceeds via these processes are, hence, not expected to be challenged by current or upcoming indirect detection searches.[12] If, in contrast, annihilation in the early Universe proceeds predominantly via the loop-induced $2 \to 2$ processes, requiring large y_χ, the situation might change and the corresponding cross section today might be sizeable. In particular, the signature of mono-chromatic gamma lines, appearing at the same loop-level, can be a promising search strategy given higher sensitivity [82, 83]. However, as the region $m_{S_1} < m_{\chi_0}$ is not the prime focus of this study, we leave a detailed study of this case for future work.

6 Conclusions and Outlook

The charged-current flavor anomalies hint at the present of leptoquarks near or at the TeV scale. Here we have studied the connection between these models and dark matter, which necessarily requires to add new particles and couplings. Employing a simplified model with only 6 parameters we have scanned the parameter space vis-a-vis the aforementioned flavor anomalies, relic density, direct detection and LHC constraints.

We have seen that when taken all these constraints simultaneously one is left with two possible scenarios: either the dark sector couples to the leptoquark mediator with a similar strength than the one required from taking the $R_{D^{(*)}}$ anomaly at face-value, which then implies a traditional freeze-out scenario to account for the current abundance of dark matter, or the leptoquark couples faintly to the dark sector, which in turn implies that the dark matter abundance arises from the conversion-driven freeze-out (co-scattering) mechanism. In the second scenario the leptoquark branching fraction into the dark sector is negligible, and thus the phenomenology will consist of seemingly disconnected leptoquark "anomaly-inspired" and traditional missing energy + X signatures. In the latter case, depending on the "compression" between the dark sector particles, one can resolve the leptons and quarks from the $S_1 \to \chi_1 \chi_0 \to l q \chi_0 \chi_0$ decay chain, which would then allow to establish a firm connection between both new physics signals. In the case where the branching fraction into the dark sector is non-negligible, then the strongest indication of the leptoquark-dark matter connection is through the pair production of

---

[12]For instance, choosing $m_{\chi_0} = 800\,\text{GeV}$, $m_{\chi_1} = 1000\,\text{GeV}$, $y_\chi = 0.71$ (obeying $\Omega h^2 \simeq 0.12$) and $m_{S_1} = 500$ GeV, (according to benchmark point 1) yields a annihilation cross section $\langle \sigma v \rangle_0 \simeq 3 \times 10^{31}\,\text{cm}^3/\text{s}$, way below current limits from gamma rays [79] or cosmic rays [80]. Note that the corresponding spectra (computed with MADDM [81]) are similar to the one for annihilation into $b\bar{b}$ considered as a benchmark in these analyses.

leptoquarks with one decaying into the dark sector and another one into hard leptons and quarks. Since this search is only being conducted currently by the CMS collaboration, we encourage the ATLAS collaboration to undertake this key study for a comprehensive dark matter program going beyond the mere annihilation into singlet final states.

Along this work we have pointed out the existence of three important holes in the campaign to optimally cover the leptoquark parameter space. On one side we have noted that for leptoquarks decaying into the third generation fermions (almost) exclusively, a search in the $b\nu t\tau$ should be added to the existing ones looking into $b\nu b\nu$ and $t\tau t\tau$, where one can benefit from a larger branching fraction, and devise cuts to keep the background under control, which we have demonstrated with a simple analysis. On the other side, noting that the solutions to the $R_{D^{(*)}}$ anomalies involve larger couplings connecting second generation quarks with third generation leptons, we advocate to study the $c\tau c\tau$ final state, and if possible and depending on the c-tagging efficiencies, also include the mixed cases, e.g $c\tau t\tau$ or $b\nu c\tau$ final states. Finally, it is also important to include single leptoquark searches decaying largely into $c\tau$, namely study the $c\tau\tau$ final state.

Our results show that the exploration of common solution to the $R_{D^{(*)}}$ anomalies and the dark matter puzzle is an interesting research avenue, and we thus plan to expand the preliminary results presented here into a comprehensive study of this model, vis-a-vis current constraints and also considering future projections of LHC and direct detection coverage.

Acknowledgements

Contribution 5

Non-standard VLQ and LQ signatures from cascade decays

J. Butterworth, G. Cacciapaglia, L. Corpe, T. Flacke, B. Fuks, L. Panizzi, W. Porod, D. Yallup

Abstract

Many Standard Model extensions contain vector-like-quarks (VLQs) as well as potentially lighter additional particles, *e.g.* leptoquarks (LQs), vector-like leptons (VLLs), or additional scalars, through which the VLQs can cascade decay. Searches for vector-like quarks do not straightforwardly apply to the resulting new final states, bounds on VLQ masses can thus be altered, and Standard Model mesurements can provide valuable constraints on exotic VLQ or LQ decays. We consider several sample models in which VLQ or LQ cascade decays are present, and determine bounds from Standard Model measurements, using the CONTUR package.

1 Introduction

Searches for new physics at the LHC based on simplified models representing the essential features of classes of theoretical scenarios have so far considered minimal extensions of the SM, where only one new state is added and allowed to decay directly into SM states. Underlying models however often predict chain decays with several new states which can lead to final states with many SM particles with peculiar kinematics. A recasting of direct searches might thus not be sensitive to the different properties of final states originated by their decays, and can in some cases only yield weak bounds on BSM state masses. On the other hand, SM measurements contain a plethora of information due to the large range of final states and distributions which have been experimentally tested, and can thus contribute to fill gaps in searches.

This contribution focuses on extensions of the SM featuring vector-like quarks (VLQs) with exotic decays, either into a neutral new scalar and a SM quark, or through chains involving leptoquarks (LQs) and vector-like leptons (VLLs). Current VLQ searches consider processes of pair and single production and assume that VLQs interact exclusively with SM quarks (mostly third generation) and electroweak bosons. Under such hypotheses the bounds on the masses of the VLQs have been already pushed to $1 - 1.4$ TeV, with the precise bound depending on the VLQ charge and its branching ratios (see *e.g.* [84, 85]). Scenarios with LQs have also been widely considered in experimental searches (see *e.g.* [32, 59]). VLLs on the other hand have received less attention, due to the fact that in a hadron collider their production cross-section is generally lower and more dependent on their interaction with the SM particles [86].

The two scenarios analysed in this contribution are motivated by underlying models (*c.f.* Sec. 2), and serve as working examples to assess the potential of current SM searches in setting new limits on the masses of the new states when exotic decays are included. A generic and model-independent simplified model describing the interactions of VLQs, LQs and VLLs between them, with exotic scalars and with SM states has been produced and used (isolating the

relevant interactions) to simulate their process of production and decay at the LHC. The simulated events have then been tested against various searches and SM measurements (available in RIVET [87]) made at the LHC at various beam energies by both ATLAS and CMS through the CONTUR framework [88].

2 Models

2.1 Model for VLQ interacting with a colour-singlet, electrically neutral scalar S_1^0 (VLQ-S_1^0)

As a first simple extension with VLQ cascade decays, we consider a model with a charge $2/3$ vector like quark T and a colour-singlet, electrically neutral scalar or pseudo-scalar S_1^0, which (for example) is commonly present in Standard Model extensions with VLQs and a composite Higgs [89]. Bounds from cascade decays $T \to t S_1^0$ from LHC BSM searches in various S_1^0 decay channels have been studied [90–96]. In particular the cascade decays to tops and (especially b) jets have been shown to be less severely constrained than canonically studied VLQ decays [93, 94]. Here, we therefore focus on QCD pair production of $T\bar{T}$ with the subsequent decay $T \to t S_1^0 \to t b\bar{b}$ or $T \to t S_1^0 \to t g g$.

The interaction part of the effective Lagrangian relevant for the cascade decay reads[1]

$$\mathcal{L}_{\text{VLQS}} = \left(S_1^0 \bar{T} \left(\Gamma_T^L P_L + \Gamma_T^R P_R \right) t + \text{h.c.} \right) + \frac{g_s^2}{16\pi^2 v} S_1^0 G_{\mu\nu}^a \left(\kappa_G^0 G_{\mu\nu}^a + \tilde{\kappa}_G^0 \tilde{G}_{\mu\nu}^a \right) + S_1^0 \bar{b} \left(\Gamma_b + i \tilde{\Gamma}_b \right) b,$$

where the parameters κ_G^0 ($\tilde{\kappa}_G^0$) and Γ_b ($\tilde{\Gamma}_b$) correspond to the scalar (pseudo-scalar) case. The mass scale in the denominator of the effective interaction of S_1^0 with the gluons has been arbitrarily set to the vacuum expectation value v of the Higgs boson to factorise all the new physics in the κ parameters.

2.2 Model including interactions between VLQs, LQs and VLLs (VLQ-LQ-VLL)

As a second example model, we extend the Standard Model by three species of scalar leptoquarks S_1, R_2 and S_3 that are coloured weak singlet, doublet and triplet fields whose representation under the SM gauge group is $(\mathbf{3}, \mathbf{1})_{-1/3}$, $(\mathbf{3}, \mathbf{2})_{7/6}$ and $(\mathbf{3}, \mathbf{3})_{-1/3}$ respectively[2]. These states can either arise as composite states or as remnants of breaking a larger group, see e.g. [97, 98] and references therein for various possibilitities.

Expanding those gauge fields in terms of their component fields, we define

$$S_1 = \Delta^{(-1/3)}, \qquad R_2 = \begin{pmatrix} \Delta^{(5/3)} \\ \Delta^{(2/3)} \end{pmatrix}, \qquad S_3 = \begin{pmatrix} \frac{1}{\sqrt{2}} \Delta'^{(-1/3)} & \Delta'^{(+2/3)} \\ \Delta^{(-4/3)} & -\frac{1}{\sqrt{2}} \Delta'^{(-1/3)} \end{pmatrix},$$

where the subscripts refer to the electric charges of the various component fields. We consider a minimal set of interactions whose Lagrangian is given by

$$\mathcal{L}_{\text{LQ}} = \lambda_{\mathbf{R}}^{(\mathbf{1})} \bar{u}_R^c \, \ell_R \, S_1^\dagger + \lambda_{\mathbf{L}}^{(\mathbf{1})} (\bar{Q}_L^c \cdot L_L) \, S_1^\dagger + \lambda_{\mathbf{R}}^{(\mathbf{2})} \bar{Q}_L \, \ell_R \, R_2 + \lambda_{\mathbf{L}}^{(\mathbf{2})} \bar{u}_R \, (L_L \cdot R_2)$$
$$+ \lambda_{\mathbf{L}}^{(\mathbf{3})} \left(\bar{Q}_L^c \cdot \frac{\sigma_a}{2} L_L \right) S_3^{a\dagger} + \text{h.c.} \, .$$

---

[1]A much more general implementation of the model will be made publicly available on the FEYNRULES Model website https://feynrules.irmp.ucl.ac.be/wiki.

[2]In principle there is also $\tilde{R}_2$ ($(\mathbf{3}, \mathbf{2})_{1/6}$) which however cannot be used to explain the B-physics anomalies. It corresponds essentially to $\tilde{Q}$ in supersymmetric models with broken R-parity. We omit it here for the moment being as we do not expect any additional features. Other representations for the weak singlet leptoquarks are also possible, but will be ignored for similar reasons.

Here, all flavour indices are understood and the dot stands for the $SU(2)$-invariant product of two $SU(2)_L$ doublets. In addition, $\mathcal{L}_{\text{kin}}$ contains gauge-invariant kinetic and mass terms for all new fields. The λ_{L} and λ_{R} couplings are 3×3 matrices in the flavour space, that we considered real for simplicity. In our conventions, we associate the first index i of any λ_{ij} element with the corresponding quark generation whilst the second one j refers to the lepton generation.

We then supplement the model by four species of physical extra quarks X, T, B and Y of electric charges of 5/3, 2/3, $-1/3$ and $-4/3$ respectively. A model-independent effective parameterisation suitable for the phenomenology related to these quarks has been developed in [99, 100].

Next, we consider a pair of vector-like leptons E and N. As for their vector-like quark counterparts, we keep their couplings to the Higgs and gauge bosons as free parameters, so that the corresponding interaction Lagrangian reads[3]

$$
\mathcal{L}_{\text{VLL}} = -h\left[\bar{E}\left(\hat{\kappa}_L^E P_L + \hat{\kappa}_R^E P_R\right)\ell + \bar{N}\left(\hat{\kappa}_L^N P_L\right)\nu_\ell\right] + \frac{g}{2c_W}\left[\bar{E}\cancel{Z}\left(\tilde{\kappa}_L^E P_L + \tilde{\kappa}_R^E P_R\right)\ell + \bar{N}\cancel{Z}\left(\tilde{\kappa}_L^N P_L\right)\nu_\ell\right]
$$
$$
+ \frac{g}{\sqrt{2}}\left[+\bar{E}\cancel{W}\left(\kappa_L^E P_L\right)\nu_\ell + \bar{N}\cancel{W}\left(\kappa_L^N P_L + \kappa_R^N P_R\right)\ell\right] + \text{h.c.} ,
$$

using the same conventions as for $\mathcal{L}_{\text{VLQ}}$ of [99, 100]. We assume the couplings $W - N - L$ to be suppressed as otherwise there are strong contraints on the masses of vectorlike leptons close to the TeV range [86].

Finally, all possible interactions involving one leptoquark and one vector-like-fermion (and one SM fermion), are

$$
\mathcal{L}_{\text{LQVL}} = \Delta^{(-4/3)\dagger}\left[\bar{B}^c\left(\tilde{\Gamma}_L^B P_L + \tilde{\Gamma}_R^B P_R\right)\ell + \bar{q}_d^c\left(\tilde{\Gamma}_L^E P_L + \tilde{\Gamma}_R^E P_R\right)L + \bar{Y}^c\left(\tilde{\Gamma}_L^Y P_L\right)\nu_\ell\right]
$$
$$
+ \Delta^{(-1/3)\dagger}\left[\bar{T}^c\left(\Gamma_L^T P_L + \Gamma_R^T P_R\right)\ell + \bar{q}_u^c\left(\Gamma_L^E P_R + \Gamma_R^E P_L\right)L + \bar{B}^c\left(\Gamma_L^B P_L\right)\nu_\ell + \bar{q}_d^c\left(\Gamma_L^N P_R + \Gamma_R^N P_L\right)N\right]
$$
$$
+ \Delta^{(+2/3)}\left[\bar{B}\left(\hat{\Gamma}_L^B P_L + \hat{\Gamma}_R^B P_R\right)\ell + \bar{q}_d\left(\hat{\Gamma}_L^E P_R + \hat{\Gamma}_R^E P_L\right)L + \bar{T}\left(\hat{\Gamma}_L^T P_L\right)\nu_\ell + +\bar{q}_u\left(\hat{\Gamma}_L^N P_R + \hat{\Gamma}_R^N P_L\right)N\right]
$$
$$
+ \Delta^{(+5/3)}\left[\bar{T}\left(\bar{\Gamma}_L^T P_L + \bar{\Gamma}_R^T P_R\right)\ell + \bar{q}_u\left(\bar{\Gamma}_L^E P_R + \bar{\Gamma}_R^E P_L\right)L + \bar{X}\left(\bar{\Gamma}_L^X P_L\right)\nu_\ell\right] + \text{h.c.} .
$$

The corresponding couplings, Γ, $\hat{\Gamma}$, $\tilde{\Gamma}$ and $\bar{\Gamma}$ are all three-dimensional vectors in flavour space.

For simplicity we only take one VLQ, one VLL and one LQ at a time and evaluate the bounds in two steps:

1. We consider the production processes $pp \to \Delta\,\Delta^\dagger \to L^+ L^- q\bar{q}$ and $pp \to \Delta\,\Delta^\dagger \to N\bar{N}q\bar{q}$ where Δ is any of the leptoquarks listed in eq. (2.2). In more detail we focus on the LQ decays

$$
\Delta^{(5/3)} \to l^+\, t , \; E^+\, t
$$
$$
\Delta^{(2/3)} \to l^+\, b , \; E^+\, b , \; \nu\, t , \; N\, t
$$
$$
\Delta^{(-1/3)} \to l^-\, t , \; E^-\, t , \; \nu\, b , \; N\, b
$$

---

[3] We constrain ourselves here to leptons which are either singlets, doublets or triplets with respect to $SU(2)_L$. In the latter case we set the hypercharge to 0 as in case of seesaw type III.

$$\Delta^{(-4/3)} \to l^- \, b \; , \; E^- \, b$$

and the VLL decays

$$E \to Z \, l \; , \; h \, l \; , \; W \, \nu$$
$$N \to Z \, \nu \; , \; h \, \nu \; , \; W \, l$$

2. We then move on with the production processes $pp \to Q\bar{Q} \to \Delta\Delta^\dagger l^+ l^-$ and $pp \to Q\bar{Q} \to \Delta\Delta^\dagger \nu\bar{\nu}$, where Q is any of the VLQ X, T, B or Y. In more detail

$$X \to \Delta^{(5/3)} \, \nu \; , \; \Delta^{(2/3)} \, l^+$$
$$T \to \Delta^{(5/3)} \, l^- \; , \; \Delta^{(2/3)} \, \nu \; , \; \Delta^{(-1/3)} \, l^+$$
$$B \to \Delta^{(2/3)} \, l^- \; , \; \Delta^{(-1/3)} \, \nu \; , \; \Delta^{(-4/3)} \, l^+$$
$$Y \to \Delta^{(-1/3)} \, l^- \; , \; \Delta^{(-4/3)} \, \nu$$

Moreover, the Δ decay to the final states above.

For simplicity we assume here that the decays into third generation SM-fermions dominate (except maybe the leptons). We use CONTUR to get a first idea of the underlying bounds due to existing LHC data. However, we expect that final states containing at least one top quark which decays semileptonically will lead to sizable missing transverse energy E_T^{miss}. Moreover, also the decays of the VLL contain final states with sizable E_T^{miss}. Consequently, we expect that part of the parameter space will be constrained by supersymmetry searches which we plan to evaluated using MADANALYSIS 5 in the future.

3 Results

3.1 Results for the VLQ-S_1^0 model

The model discussed in Sec. 2.1 is implemented in FEYNRULES 2.3 [18] at leading order. For simplicity we assume a pseudo-scalar S_1^0 ($\kappa_G^0 = 0 = \Gamma_b$) with 100 % decay rate to either $b\bar{b}$ or gg and narrow width. Events are generated with HERWIG++ v.7.2 [101] and compared to LHC measurements using CONTUR v1.0.[4] The CONTUR scan took into account a range of measurements from 7, 8 and 13 TeV data from both ATLAS and CMS.

Fig.1 shows the obtained constraints on $T\bar{T}$ pair production with subsequent decay $T \to tS_1^0 \to tb\bar{b}$ (top) or $T \to tS_1^0 \to tjj$ (bottom) in the S_1^0 vs. T mass plane. As can be seen, the bounds from LHC search recasts are comparable to the bounds obtained with CONTUR in the case of $S_1^0 \to b\bar{b}$ decays, where `ATLAS_13_LMETJET` [102–104], `CMS_13_LMETJET` [105–107], and `ATLAS_13_TTHAD` [108] contribute most. For $S_1^0 \to jj$, CONTUR yields stronger bounds than current recasts, with bounds arising mainly from `ATLAS_13_LMETJET` and `CMS_13_LMETJET`. This provides an example of the exclusion power of Standard Model measurements on BSM.

3.2 Results for the VLQ-LQ-VLL model

In the spirit of simplified models we investigate a bench-mark scenario where T, $\Delta^{(-1/3)}$, L and N are all present at the same time. Moreover, we here assumed that decays into final states

---

[4]See Sec. 18 of these proceedings for more details on the CONTUR methodology.

containing third generation fermions dominate. To obtain a conservative bound we switch off all couplings to fermions of the first two generations. For definiteness, we set $\hat{\kappa}_X^F = \tilde{\kappa}_X^F = \kappa_X^F = 0.2$ with $x = L, R$ and $F = E, N$. We have checked that we can reproduce the results of the ATLAS searches [56, 109] for leptoquarks within a few percents for several mass and branching ratio combinations using the CONTUR package. In a first step we have investigated to which extent the masses of L and $\Delta^{(-1/3)}$ are constrained. As can be seen in Fig. 2 the bounds from the direct production of these particles are relatively mild. We have checked that the cross section for the L^+L^- pair production is below the bounds given in [86]. As second step we have fixed $M_L = M_N = 250$ GeV and varied M_T and $M_{\Delta^{(-1/3)}}$. The corresponding exclusion-limits are presented in Fig. 3. Here we allowed for the simultaneous pair production of both species, where
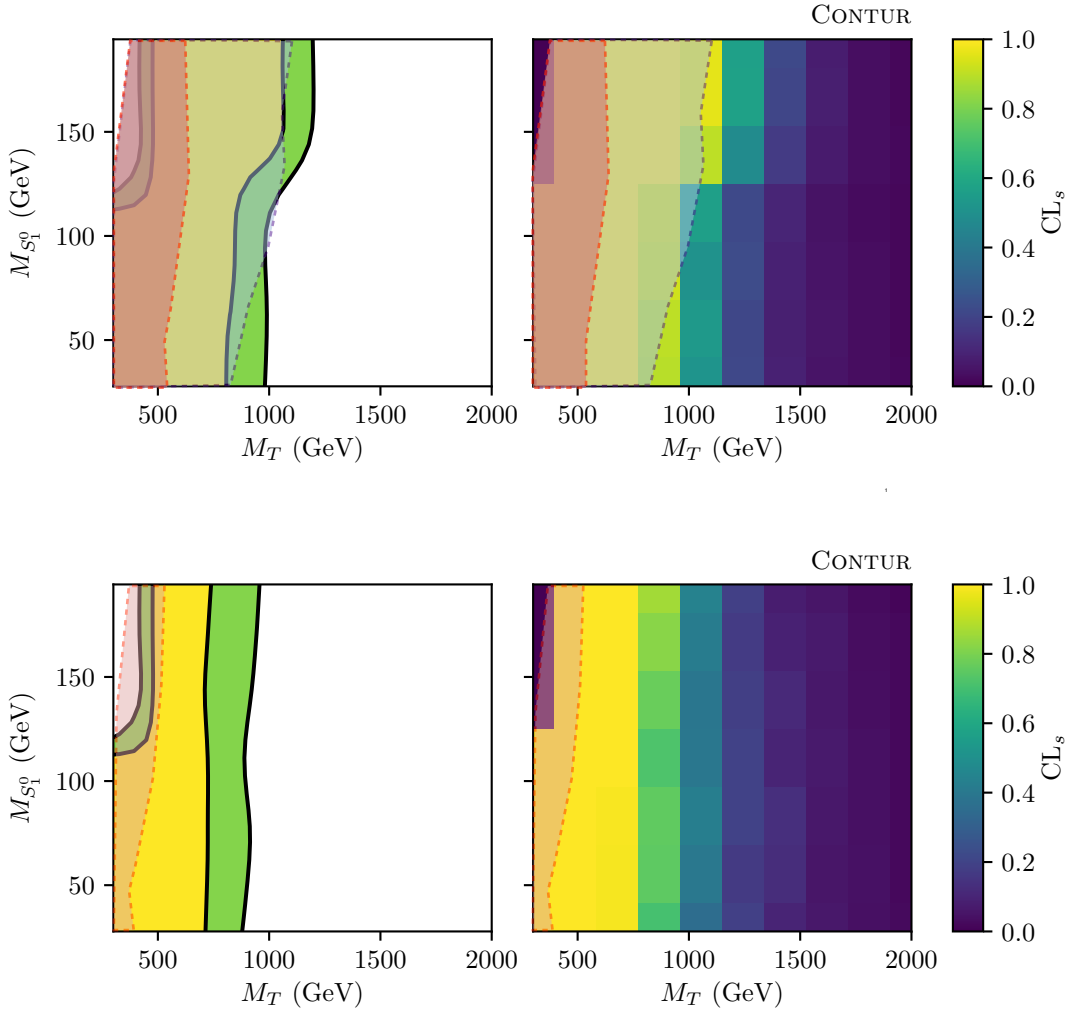

Figure 1: Exclusion on the $M_{S_1^0}$ vs. M_T mass plane by CONTUR for $T\bar{T}$ production with subsequent cascade decay $T \rightarrow tS_1^0 \rightarrow tb\bar{b}$ (top) or $T \rightarrow tS_1^0 \rightarrow tjj$ (bottom). The right-hand figures show the heatmap of the obtained CL_s values at each point. The left-hand figures show the areas which are excluded at 1 (2) σ level in green (yellow). For comparison, red and blue areas show 2 σ exclusions from a recast of several LHC searches [93].
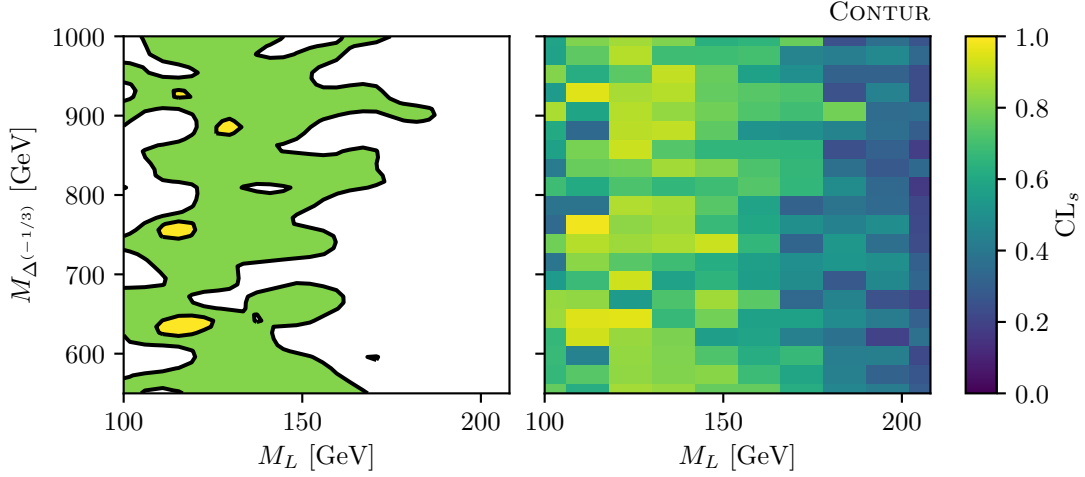
Figure 2: Exclusion on the M_L vs. $M_{\Delta^{(-1/3)}}$ mass plane by CONTUR for $L\bar{L}$ and $\Delta^{(-1/3)}\Delta^{(+1/3)}$ pair production with subsequent cascade decays. The underlying parameters are given in the text.

Figure 3: Exclusion on the $M_{\Delta^{(-1/3)}}$ vs. M_T mass plane by CONTUR for $T\bar{T}$ and $\Delta^{(-1/3)}\Delta^{(+1/3)}$ pair production with subsequent cascade decays. The underlying parameters are given in the text and we have fixed $M_L = M_N = 250$ GeV.
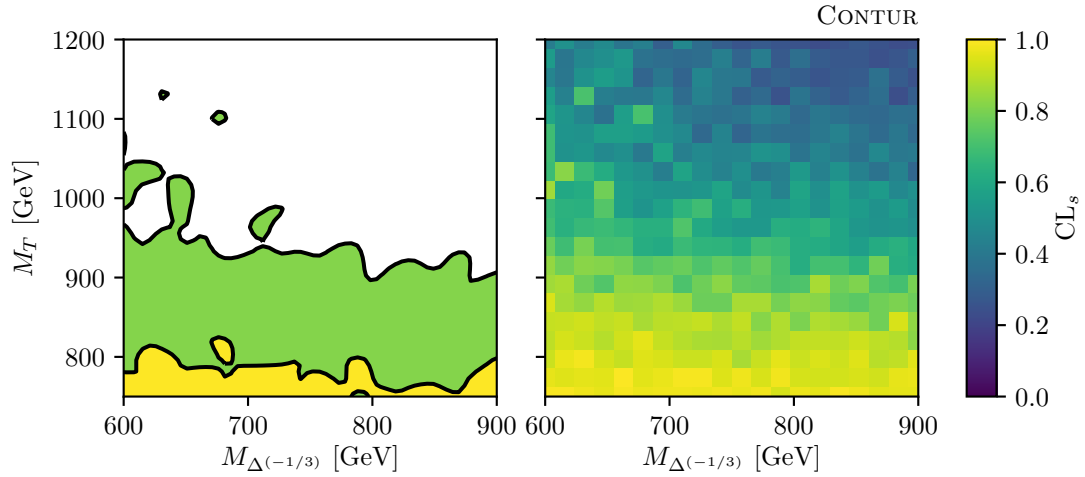
the one for $T\bar{T}$ is significantly larger than the one for leptoquarks if both have the same mass. We see that the bound on M_T is well below a TeV with a mild dependence on $M_{\Delta^{(-1/3)}}$. The analyses which contribute most are `ATLAS_13_JETS` [110, 111] followed by `CMS_13_LMETJET` [105–107] Similar to the example in the previous section this shows again the exclusion power of SM measurements on BSM models.

4 Conclusions

We studied two theoretically motivated sample models in which VLQ or LQ cascade decays are present, and determined bounds from Standard Model measurements, using the CONTUR package.

The first sample model features the decay $T \to tS_1^0$ with $S_1^0 \to jj$ or $b\bar{b}$. For top partner pair-production and T-decay into tjj we find 95% c.l. bounds of $M_T \gtrsim 700$ GeV with a very mild dependence on $M_{S_1^0}$, which exceeds bounds from previous search recasts. For the decay to $tb\bar{b}$ we find bounds $M_T \gtrsim 800 - 1050$ GeV, depending on $M_{S_1^0}$, which are comparable to bounds from previous search recasts.

The second sample model features a more complex scenario, namely we allow in addition to the standard decays of T also for the decay $T \to \tau^+ \Delta^{(-1/3)}$. The $\Delta^{(-1/3)}$ decays further into τt, $b\nu$, Lt or bN. Fixing the mass of the heavy leptons to 250 GeV and including the pair production of both, the top partners and the leptoquarks, we find 95% c.l. bounds of $M_T \gtrsim 850$ GeV with a very mild dependence on $M_{\Delta^{(-1/3)}}$.

The above (theoretically motivated) physics cases and first benchmarks are examples for a much broader class of studies of "visible cascade decays" and the importance of SM measurements for constraining them. We provide examples of simplified models describing the interactions of VLQs, LQs, VLLs and exotic scalars, and plan to provide publicly available model implementations in the near future.

Acknowledgements

Contribution 6

Freeze-in with large couplings at the LHC

G. Bélanger, A. Bharucha, N. Desai, B. Fuks, A. Goudelis, J. Heisig, A. Lessa, A. Mjallal, S. Sekmen, D. Sengupta, J. Zurita

Abstract

We study freeze-in scenarios in which the interactions of dark matter with the Standard Model are mediated by a heavy vector-like fermion with a mass that is higher than the reheating temperature of the Universe. In such scenarios freeze-in requires sizeable interactions between the two sectors which, in turn, implies that prompt LHC dark matter searches become relevant, unlike in conventional scenarios of freeze-in. We examine the interplay of long-lived and prompt searches and show that their role is highly complementary in constraining different regions of the parameter space.

1 Introduction

In order to establish a thermodynamical explanation for the observed dark matter (DM) abundance in the Universe an extension of the Standard Model (SM) by new particles, possibly with new interactions, appears to be necessary. While the freeze-out of a weakly interacting massive particle (WIMP) has been the most widely studied scenario of dark-matter genesis during recent decades, other possibilities exist, such as dark matter freeze-in[1]. In most well-studied freeze-in scenarios DM interacts only extremely weakly, or *feebly* [120], with the SM particles. This feature renders most DM searches targeting the WIMP scenario (direct, indirect detection and prompt LHC searches for missing energy events) inefficient, although a few exceptions do exist (*e.g.* direct detection via light mediators [121]).

Among the most phenomenologically interesting freeze-in scenarios are those in which DM is one (typically the lightest) of several states belonging to some 'dark' $\mathcal{Z}_2$-odd sector under which the SM particles are even. In such configurations, the heavier particles in the dark sector may even interact strongly with the SM. Then, they may be copiously pair-produced at high-energy colliders and subsequently decay into DM along with visible particles, typically with a macroscopic lifetime. In other words, the visible signals of most usual freeze-in scenarios fall into the realm of searches for long-lived particles. The situation becomes substantially more challenging if DM is the *only* $\mathcal{Z}_2$-odd particle in the spectrum. In this case, DM is essentially inaccessible at colliders [122], and the only handle on the corresponding models are traditional ($\mathcal{Z}_2$-even) mediator searches.

There are, however, situations in which the previous picture breaks down. For instance, DM can be overproduced in the early Universe and subsequently diluted by injection of entropy

---

[1]The production rates of non-thermalized dark matter through occasional scatterings or decays of thermal bath particles were first computed in [112–117] (UV-dominated production) and [118–120] (IR-dominated production). The name 'freeze-in' was introduced in [120].

in the primordial plasma [123]. In this work we investigate yet another possibility, in which DM production is suppressed due to relatively small reheating temperatures (T_R). We will assume that the interactions between DM and the SM are mediated by some heavy particle (F) and $m_{DM} < T_R \lesssim m_F$. In this case DM is mostly produced through higher-dimensional operators which scale with T_R/m_F[2].

Such a scenario is, arguably, less predictive than standard IR-dominated freeze-in (or freeze-out, for that matter) due to the presence of an additional free parameter entering the calculations: the reheating temperature. However, it is by no means excluded or disfavoured from a cosmological standpoint. Moreover, as we will see it allows for a fair amount of freedom in choosing the interaction strength between the DM and SM particles. In a sense, this scenario bridges the gap that exists between thermal freeze-out and freeze-in by requiring intermediate values for the DM-SM or DM-mediator coupling strength[3]. This freedom has twofold consequences: first, microscopic models in which the thermal freeze-out or standard (*i.e.* with a large T_R) freeze-in regimes are excluded may now become viable. Secondly, the scenario we consider here provides motivation to continue and intensify all existing or planned DM searches at the LHC and beyond since it constitutes a class of freeze-in configurations which can, indeed, be probed at DM detection experiments.

The remainder of this contribution is structured as follows: in Sec. 2 we present some general features of the freeze-in mechanism and the concrete microscopic model we will study. In Sec. 3 we study the various constraints that our model is subject to, stemming from cosmology, flavour and collider observations. Finally, in Sec. 4 we summarise our main findings and conclude.

2 Theoretical framework

2.1 Freeze-in

Let us consider a simple "dark" (*i.e.* $\mathcal{Z}_2$-odd) sector containing just the DM particle s along with a charged parent F (we will present a concrete such model in Sec. 2.2). Dark matter freeze-in can proceed either via decays of the heavier particle or from scattering processes involving bath particles in the initial state. Scattering processes can further fall into two classes: *(i)* conversions, which (similarly to the case of freeze-in from decays) involve at least one charged parent in the initial state and *(ii)* production of two DM particles from annihilation of two SM particles. In the standard freeze-in scenario where $T_R \gg m_F > m_s$, class *(ii)* is usually not considered as in many models it is of higher order in the feeble coupling and, hence, negligible. If, however, $m_F > T_R > m_s$ the situation can change as the DM yield of both the decays and the conversions is proportional to the charged parent abundance which can be very small after reheating, whereas pair-production of DM is proportional to the abundances of the – potentially unsuppressed – (light) SM degrees of freedom. Note that in everything that follows we will consider very light dark matter, namely $m_s \sim 12$ keV, the lowest value compatible with Lyman-α forest bounds for the model considered here [124].

In order to quantify the abundance of F we consider instantaneous reheating, assuming that the SM sector is reheated and thermalized at T_R while the abundance of the parent is zero at this point in time. This is, of course, a rather unrealistic approximation. However, it constitutes

---

[2]This scenario is similar to the production of gravitinos in supersymmetric models, except that in the gravitino case the suppression scale is related to the supersymmetry-breaking or the Planck scale.

[3]Other such scenarios exist like conversion-driven freeze-out/co-scattering [74,75].

a framework sufficient for the subsequent discussion. In this setup the (comoving) abundance of F, Y_F, is governed by the usual Boltzmann equation, which describes thermal freeze-out [125, 126]:

$$\frac{\mathrm{d}Y_F}{\mathrm{d}x} = \frac{1}{3H}\frac{\mathrm{d}s}{\mathrm{d}x}\langle\sigma v\rangle\left(Y_F^2 - Y_{F,\mathrm{eq}}^2\right)\,, \tag{1}$$

with the initial condition $Y_F^2(x_\mathrm{R}) = 0$. Here $x = m_F/T$, H is the Hubble parameter and s the entropy density.

Let us define T_fo to be the freeze-out temperature where $\langle\sigma v\rangle Y_{F,\mathrm{eq}}/s \simeq H$, *i.e.* where Y_F departs from its equilibrium density in standard freeze-out. If the reheating temperature is above the freeze-out temperature of the mediator, $T_\mathrm{R} > T_\mathrm{fo}$, the production of F from the thermal bath is efficient and it quickly thermalizes. In this case the DM abundance is essentially equal to the freeze-out abundance for $T_\mathrm{R} \gg m_F$. If, however, $T_\mathrm{R} \lesssim T_\mathrm{fo}$ the mediator abundance becomes smaller than its (would-be) freeze-out abundance. In the limit $T_\mathrm{R} \ll T_\mathrm{fo}$ it is:

$$Y_{F,0} \simeq \int_{x_\mathrm{R}}^{x_0} Y_{F,\mathrm{eq}}^2 \frac{s}{Hx}\langle\sigma v\rangle dx \simeq 1.6\times 10^{31}\,\frac{g_{*s}}{\sqrt{g_*}}\,\frac{m_F}{\mathrm{GeV}}\,\frac{\langle\sigma v\rangle(x_\mathrm{R})}{\mathrm{cm}^3/\mathrm{s}}\,x_\mathrm{R}\,\mathrm{e}^{-2x_\mathrm{R}} \tag{2}$$

provided that $\langle\sigma v\rangle$ is a sufficiently slowly varying function of x. This means that Y_F decreases very fast with x_R (faster than $Y_{F,\mathrm{eq}}(x_\mathrm{R})$). This consideration shows that decay and conversion processes become irrelevant relatively quickly if $T_\mathrm{R} < T_\mathrm{fo}$ is chosen. Once this happens, DM is mostly (pair-) produced through scattering of SM particles. In passing, let us point out that as the DM production process is mediated by the heavy charged parent F appearing in the t-channel, the corresponding higher-dimensional effective operator leads to UV-dominated freeze-in and, hence, to a dependence of the DM abundance on T_R.

2.2 A simple charged parent model

In order to render the previous discussion more concrete, we consider an extension of the SM by a real scalar DM candidate s that is neutral under the SM gauge group along with a vector-like fermion F which we take to be an $SU(3)_c \times SU(2)_L$ singlet but to carry a hypercharge of -1. Both s and F are taken to be odd under a $\mathbf{Z}_2$ symmetry which, provided $m_s < m_F$, renders s completely stable. The SM particles are taken to be even under the same discrete symmetry.

The most general Lagrangian compatible with these symmetries reads

$$\begin{aligned}
\mathcal{L} = \mathcal{L}_\mathrm{SM} + \partial_\mu s\,\partial^\mu s - \frac{\mu_s^2}{2}s^2 + \frac{\lambda_s}{4}s^4 + \lambda_{sh}s^2\left(H^\dagger H\right) \\
+ i\bar{F}\slashed{D}F - m_F\bar{F}F - \sum_f y_s^f\left(s\bar{F}\left(\frac{1+\gamma^5}{2}\right)f + \mathrm{h.c.}\right),
\end{aligned} \tag{3}$$

where $f = \{e, \mu, \tau\}$. This model, as well as variants thereof assuming other gauge quantum number and spin assignments, has been studied in the context of IR-dominated freeze-in in [124, 127]. For simplicity, we assume flavor universal y_s^f couplings, so that the model has a total of five free parameters,

$$m_s, m_F, \lambda_{sh}, \lambda_s, y_s\,, \tag{4}$$

i.e. the DM mass, the vector-like fermion mass, the DM-Higgs quartic coupling, the DM quartic self-coupling and the universal Yukawa-type couplings between DM, the vector-like lepton and

the right-handed SM leptons. The dark scalar mass is related to the μ_s parameter entering Eq. (3) through

$$\mu_s^2 = m_s^2 + \lambda_{sh}v^2 , \tag{5}$$

and the two λ couplings are irrelevant for our purposes. We will thus set them to zero during the remainder of our analysis[4].

The parent particle lifetime spans a wide range of values depending on the magnitude of y_s, which strongly affects the LHC phenomenology of our model as we will see in Sec. 3.3. In Fig. 1 we illustrate this dependence in the (m_F, y_s) plane assuming $m_s = 12$ keV and
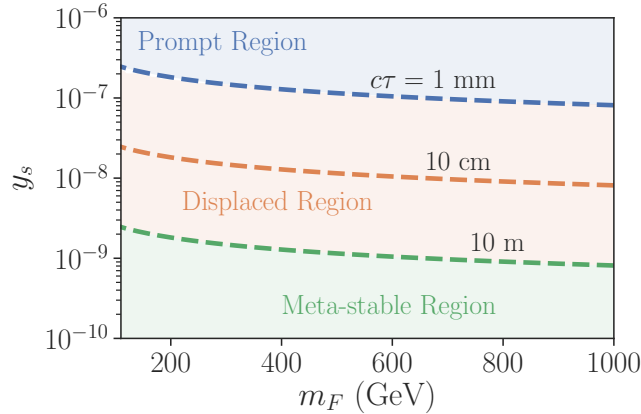

Figure 1: Contours of $c\tau$ for the mediator F in the y_s- m_F plane. The dark matter mass is assumed to be much smaller than m_F. The shaded regions approximately display the distinct regimes relevant for collider searches.

highlighting in different colours regions of parameter space in which F decays mostly promptly ($c\tau \lesssim 1$ cm, blue region), through displaced vertices but within the LHC detectors ($c\tau \lesssim 10$ cm, red region) or outside the detector ($c\tau \lesssim 1$ m, green region). Needless to say that in reality, these regions are not as sharply separated as one might infer from Fig. 1. The decay length of F is a statistically distributed quantity which also depends on the boost of F which, in turn, varies from one event to another. In this respect, Fig. 1 should be taken as a ballpark illustration of the proper lifetimes (and, hence, (m_F, y_s) combinations) for which most of the decays occur promptly, displaced or outside the LHC detectors.

In order to perform our phenomenological analysis we have used the FEYNRULES [18] model implementation that was developed in the framework of [124], along with the corresponding UFO [29] and CALCHEP [130] model files for use with MADGRAPH5_AMC@NLO [19] (for the collider part of our analysis) and MICROMEGAS 5 [131] (for the computation of the freeze-in DM abundance).

3 Experimental constraints

We now move on to discuss the constraints that the model presented in Sec. 2.2 is subject to. At first we discuss bounds from dark matter phenomenology, we then move on to flavour observables and, finally, LHC searches that affect our parameter space.

---

[4]We refer to, *e.g.*, Refs. [118, 128] and [129] for examples in which λ_{sh} and λ_s become relevant respectively.

3.1 Dark matter constraints

3.1.0.1 The dark matter abundance

In Fig. 2 we show contours of $\Omega h^2 = 0.118$ [77] for four different (low) values of the reheating temperature, namely $T_R = 5, 10, 25$ and 50 GeV (green lines) in the (m_F, y_s) (left panel) and (m_F, y_s) (right panel) planes. For comparison, we also include the result obtained assuming a high value of $T_R = 10^5$ GeV, which corresponds to conventional (IR-dominated) freeze-in. We observe that for decreasing T_R increasingly large values of y_s are required to reproduce the observed DM abundance in the Universe. This behaviour can be understood in light of the comments made in Sec. 2.1. In conventional (*i.e.* high T_R) freeze-in scenarios the relic density is usually dominated by DM production through F decays, while the coupling y_s required to reproduce the PLANCK observations is feeble. However, as the reheating temperature decreases the parent particle abundance becomes suppressed, DM production through scattering of SM particles can dominate, and larger values of y_s are required.
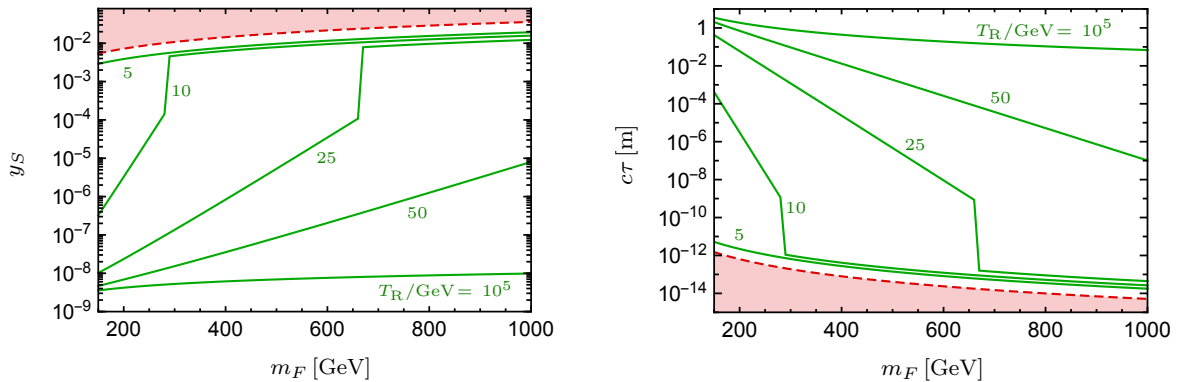

Figure 2: Contours of $\Omega h^2 = 0.118$ in the $y_s - m_F$ plane (left) and $c\tau - m_F$ plane (right) for different reheating temperatures and $m_s = 12$ keV. The red shaded region represents the constraint from $\mu \to e\gamma$.

Concretely, DM production through F decays becomes subleading with respect to (F-mediated) annihilation processes $f\bar{f} \to ss$ once T_R drops below the freeze-out temperature of F, $T_{\rm fo}$, which is roughly given by $m_F/30$. This occurs for $m_F > 680(290)$ GeV for $T_R = 25(10)$ GeV and for all considered masses of F when $T_R = 5$ GeV. It is seen as a sharp transition in two of the curves in Fig. 2. Note also that in all cases of scattering-dominated freeze-in, the couplings involved $y_s \approx 10^{-3} - 10^{-2}$ are weak rather than feeble, thus clearly leading to prompt decays of F, whereas long-lived signatures (corresponding roughly to $c\tau > 10^{-3}$ m) are relevant only for $T_R > 50(10)$ GeV when $m_F = 550(150)$ GeV. If we considered higher values of the reheating temperature and/or the DM mass, long-lived signatures would be much more relevant, as *e.g.* discussed in [124].

A few remarks are in order. In our calculations we assume a sharp transition of the initial conditions at $T_{\rm fo} \approx T_R$ between the decay-dominated and the scattering-dominated regimes. More specifically, we assume that for $T_R > T_{\rm fo}$ the parent particle F follows its equilibrium distribution, whereas in the opposite regime we assume that its initial abundance is zero and it is produced through freeze-in. Moreover, for $T_R > T_{\rm fo}$ we should also take into account the freeze-out of F, *i.e.* the fact that below roughly $m_F/30$ the equilibrium distribution constitutes

an underestimation of its true abundance. This component contributes to the DM density as

$$\Omega_s h^2 = \frac{m_s}{m_F} \Omega_F^{\text{fo}} h^2 \qquad (6)$$

where Ω_F^{fo} is the density of F from the freeze-out mechanism. However, since F is a charged particle, its relic abundance is rather small (and independent of y_s), while we are also considering a large mass hierarchy between F and s. We have numerically checked that the combination of these two factors renders the post-freeze-out contribution of F to the total DM density completely negligible. Lastly, note that although the sharp transition approximation is a rough one, it does not impact our conclusion that F decay is prompt both before and after the transition. It simply means that for $m_F \simeq T_{\text{fo}}$, our estimates should be taken with a pinch of salt.

3.1.0.2 Direct detection through electron scattering

The tree-level interaction between our DM candidate and the SM leptons opens up possibilities for direct detection through s scattering off electrons. This interaction can be parameterized in a model-independent way with respect to a reference cross section $\bar{\sigma}_e$, and a form factor $F_{DM}(q)$ [132],

$$\bar{\sigma}_e \equiv \frac{\mu_{se}^2}{16\pi m_s^2 m_e^2} |\overline{M_{se}(q)}|^2_{q^2=(\alpha m_e)^2} \qquad (7)$$

$$|\overline{M_{se}(q)}|^2 = |\overline{M_{se}(q)}|^2_{q^2=(\alpha m_e)^2} \times F_{DM}(q)^2 \qquad (8)$$

The reference cross section $\bar{\sigma}$, is the non-relativistic DM-electron scattering cross section with the momentum transfer q set to the reference value αm_e. $|\overline{M_{se}(q)}|^2$ is the spin-averaged squared matrix element for the dark matter-electron scattering. Electron scattering experiments are typically sensitive to light dark matter interacting through ultra light mediators via either electron ionization or excitation. For the model considered in this work, the reference cross section $\bar{\sigma}_e$ is proportional to y_s^4/m_F^4. Then, even in the case of relatively large, $\mathcal{O}(10^{-4})$ couplings an extremely light mediator (~ 1 MeV) is required to give rise to observable signals. Since in what follows the heavy fermion mass will be taken to lie in the $\mathcal{O}(10^2)$ GeV region, the resulting reference cross section is significantly below the threshold required to excite electrons. Hence, constraints from direct detection experiments relying on DM-electron scattering are negligible.

3.2 Constraints from flavour observables

In the absence of any flavour protection mechanism, and for sufficiently low values of m_s, the model described by the Lagrangian of Eq. (3) gives rise to tree-level exotic contributions to the charged lepton decay widths, through processes of the type $l_1 \to l_2 ss$, as well as to contributions to radiative (three-body) decays such as $l_1 \to l_2 \gamma$ ($l_1 \to l_2 l_2 l_2$). For our choice $m_s = 12$ keV, the leading constraints stem from the very well-measured muon observables, in particular the measurement of the muon lifetime and, more importantly, the decay $\mu \to e\gamma$.

The muon lifetime has been measured extemely accurately, with a relative precision of 10^{-6} [45]. In practice, in order to ensure that the decay mode $\mu \to ess$ does not spoil the successful prediction of the Standard Model, we impose that the corresponding partial width should not exceed the 1σ uncertainty of the measured total muon width, $\Gamma_{\mu\to ess} \lesssim 3 \times 10^{-25}$ GeV. For a heavy fermion mass of 100 GeV, we find that this condition can be satisfied as long as $y_s \lesssim 2 \times 10^{-2}$, with the bound scaling as $1/m_F^4$.

The radiative muon decay $\mu \to e\gamma$ turns out to provide the most stringent constraint on our parameter space. Using the general expressions that can be found in [133], neglecting the muon and electron masses in the loop integrals and keeping only the leading terms in m_F^2/m_s^2, the $\mu \to e\gamma$ partial width can be approximated as

$$\Gamma_{\mu \to e\gamma} \simeq \frac{16 m_\mu^5 y_s^4}{9 m_F^4 (16\pi)^5}. \tag{9}$$

At the same time, assuming that the muon decay width is dominated by the Standard Model contribution, we have as usual

$$\Gamma_{\mu \to e\gamma} = \frac{G_F^2 m_\mu^5}{192\pi^3} \tag{10}$$

where G_F is the Fermi constant, the most precise determination of which comes exactly from the muon lifetime measurement. The branching ratio for $\mu \to e\gamma$, then, reads

$$Br(\mu \to e\gamma) \simeq \frac{y_s^4}{12 G_F^2 m_F^4 (16\pi)^2}. \tag{11}$$

Given the latest constraint $Br(\mu \to e\gamma) < 4.2 \times 10^{-13}$ [134], we obtain the bound:

$$\frac{y_s}{m_F} \lesssim 3.6 \times 10^{-5} \ \text{GeV}^{-1} \tag{12}$$

which, as we can see in Fig. 2 (red shaded region), approaches our phenomenologically interesting parameter space without affecting it substantially.

3.3 Constraints from searches at the LHC

Our model contains a scalar dark matter field s and a vector-like fermionic mediator F. Since s is a singlet under the SM gauge symmetries and we have chosen to neglect the Higgs portal interaction appearing in the Lagrangian of Eq. (3), it can only be produced through the mediator F. The main process relevant for production of s at the LHC is illustrated in Fig. 3, which leads
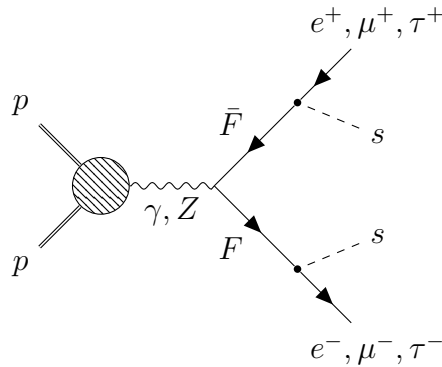

Figure 3: *Diagram for the main production mode of the mediator (F) and its decay to dark matter (s) at the LHC. Since we assume universal couplings to leptons, all decay modes (including mixed flavor) have the same branching ratio.*

us to typically expect for a signal to emerge in searches for two (OS) leptons accompanied by missing energy (MET). However, as illustrated by Figs.1 and 2, in most regions of parameter

space the decay length of F can vary over many orders of magnitude and F can decay promptly, inside the detector with a macroscopic decay length or even outside the detector. The searches for F can, therefore, be regrouped into three classes:

1. Prompt decays ($c\tau \lesssim 1$ mm): the main signature in this case consists of 2 leptons and MET. In order to test this regime, we will use the corresponding ATLAS search from Ref. [135].

2. Displaced decays (10 mm $\lesssim c\tau \lesssim 1$ m): in this scenario F can either decay inside the tracker or in the calorimeter. Hence, the signal can either consist of displaced leptons (which can be searched for with or without missing energy) or of disappearing tracks (DT) if the leptons from the F decay are not associated to their parent track. In the former case we will consider the CMS displaced lepton + MET search of Ref. [136] whereas in the latter case we will rely on the ATLAS disappearing track search peformed in Ref. [137].

3. Meta-stable decays ($c\tau \gtrsim 1$ m): if the F decay length is of the order of a meter or larger, a fraction of the produced F's can decay outside the detector. In this case the main signature is a charged track, corresponding to a heavy stable charged particle (HSCP). In order to constrain this scenario we will consider the 13 TeV ATLAS search for HSCPs [138].

In Table 1 we present a summary of the searches we consider, their phenomenological signature and the approximate lifetime interval for which they apply.

Lifetime range	Signature	Reference
Prompt Decays ($c\tau \lesssim 1$ mm)	2 OS leptons + MET	ATLAS-SUSY-2018-32 [135]
Displaced Decays (10 mm $\lesssim c\tau \lesssim 1$ m)	displaced leptons plus MET	CMS-PAS-EXO-16-022 [136]
	disappearing track	CMS-EXO-16-044 [137]
Meta-stable decays ($c\tau \gtrsim 1$ m)	HSCPs	ATLAS-SUSY-2016-32 [138]

Table 1: *List of LHC searches used to test the final state illustrated in Fig. 3. The searches are split in three groups, corresponding to distinct lifetime ranges.*

3.3.0.1 Searches for prompt leptons + MET

If the mediator lifetime is of the order of a few mm or below, it will mostly decay promptly and prompt searches for leptons accompanied by MET apply. Since the topology in Fig. 3 is similar to slepton pair-production and decay, we employ the 139 fb^{-1} ATLAS search [135] which looked for an excess in the two leptons (electrons and muons) plus missing energy channel. This search requires the leptons to be produced within $|z_0 \sin\theta| = 0.5$ mm of the primary vertex, where θ is the azimuthal angle of the lepton 3-momentum and z_0 its longitudinal impact parameter relative to the primary vertex. Therefore, this search is only relevant for lifetimes $c\tau \lesssim \mathcal{O}(1$ mm). In order to apply the search results to constrain our model, we make use of the upper limits on the total production cross-section of the simplified slepton model ($pp \rightarrow \tilde{l}_{L,R} + \tilde{l}_{L,R} \rightarrow l^- l^+ \chi_1^0 \chi_1^0$) provided by ATLAS. Although F is a vector-like fermion, we do not expect its spin to significantly change the signal efficiencies when compared to the slepton scenario. It is, therefore, a good approximation to apply the ATLAS cross-section upper limits to the process $pp \rightarrow F + \bar{F} \rightarrow l^- l^+ s s$. In the near future we intend to properly re-implement this search in the MADANALYSIS 5 framework [20, 72, 73] for a more accurate recasting. However,

even within our level of approximation there are two differences between the decay of F and the simplified model considered by ATLAS that *do* need to be accounted for:

– first, since we assume universal couplings to leptons, about 55% of the signal will contain at least one τ-lepton. Here we make the conservative assumption that the search has zero sensitivity to these events. Therefore we rescale the F production cross-section by 45%.

– Second, for lifetimes larger than a few mm, some events will contain leptons with impact parameter above the value required by ATLAS. In order to take this effect into account we generate parton level events with MADGRAPH5_AMC@NLO and apply the $|z_0 \sin\theta| < 0.5$ mm requirement to the leptons originating from F decays in order to compute the fraction of events that contain prompt leptons. We then rescale the cross-section by this factor.

Taking into account the above considerations, we compute the 95% C.L. limit on m_F as a function of lifetime, comparing the rescaled production cross-section for F with the upper limit provided by ATLAS for the corresponding slepton mass and a massless neutralino. The F production cross-section is computed at LO using MADGRAPH5_AMC@NLO, but a K-factor value of 1.2, typical of Drell-Yan-like processes at 13 TeV, is applied. The results are shown in the top-left panel of Fig. 4, in the $(m_F, c\tau)$ plane. As expected, the constraints are strongest for $c\tau < 1$ mm, excluding masses up to $m_F = 700$ GeV. However, once the lifetime is larger then 1 cm, the search loses all its sensitivity. Let us also point out that although masses below 200 GeV are not considered by the analysis, they are excluded by searches at 8 TeV.

3.3.0.2 Searches for displaced leptons + MET

In the analysis performed in Ref. [136], long-lived particles have been searched for using 2.6 fb^{-1} of LHC data at a center-of-mass energy of 13 TeV. This search especially targeted long-lived particles that decay into leptons within the volume of the tracker, a signature which is typical of specific R-parity-violating supersymmetric scenarios in which the stop squark is long-lived and decays into a b-jet and an electron or a muon. The three search signal regions are populated by events featuring two isolated leptons of different flavors[5]. The properties of the two selected lepton candidates are such that they are hard (with a transverse momentum $p_T \gtrsim 40$ and 42 GeV for muons and electrons respectively), central (with a pseudorapidity $|\eta| < 2.4$) and with a transverse impact parameter d_0 lying between 0.2 mm and 10 cm. Moreover, the two leptons are constrained to be well separated in the transverse plane, with a ΔR distance of at least 0.5. The analysis then includes three signal regions relevant for important displacements ($d_0 > 1$ mm), moderate displacements ($d_0 \in [0.5, 1]$ mm) and smaller displacements ($d_0 \in [0.2, 0.5]$ mm).

We compute exclusion limits by using the combined log likelihood ratio of all three signal regions. The corresponding results are shown in the top-right panel of Fig. 4. We see that the constraints reach peak sensitivity for displacements of the order of a few cm, excluding heavy lepton masses up to $m_F \sim 500$ GeV.

3.3.0.3 Searches for disappearing tracks

The CMS search for disappearing tracks at 13 TeV [137] selects events with at least one track with $p_T > 55$ GeV and $|\eta| < 2.1$, having at least three missing hits in the outer calorimeter

---

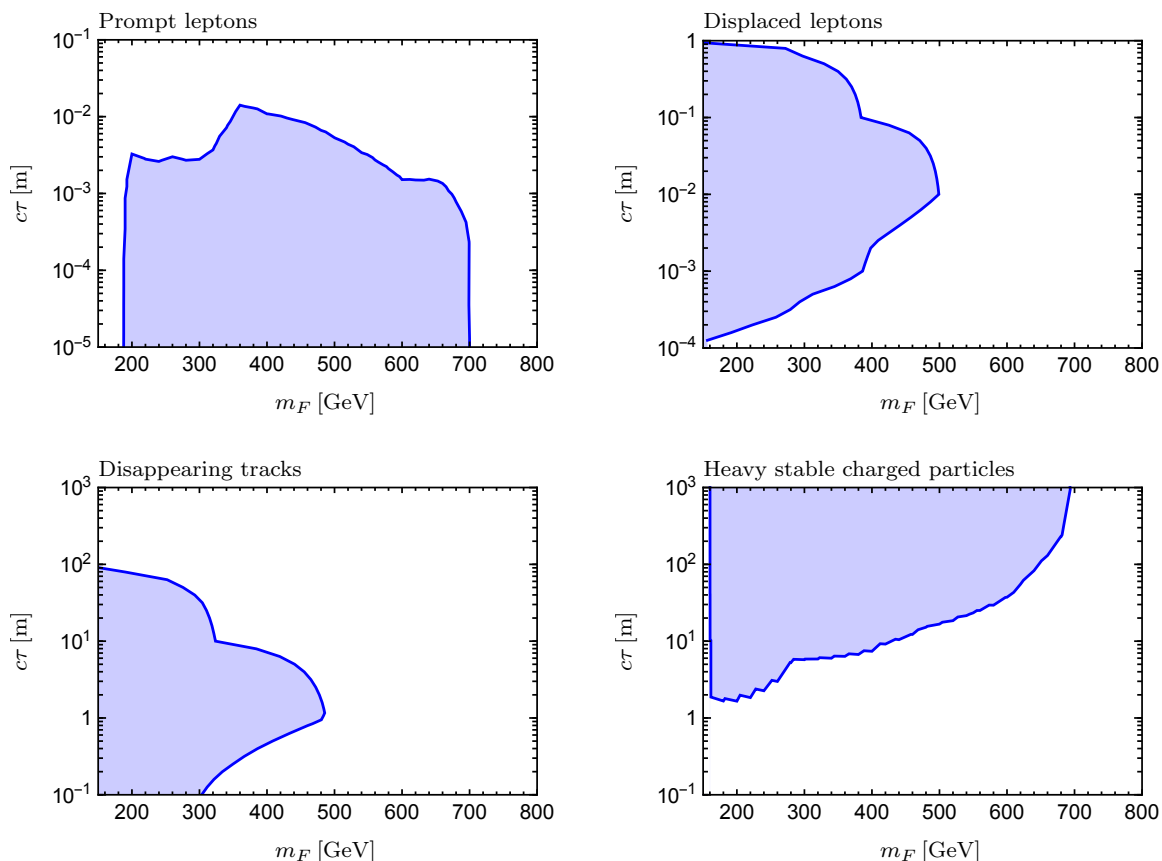[5]In the following, the term 'leptons' solely refers to electrons and muons.

Figure 4: 95% CL collider limits in the m_F-$c\tau$ plane. *Upper left:* Prompt ATLAS 2 leptons plus missing energy search from Ref. [135]. *Upper right:* CMS displaced lepton search from Ref. [136]. *Lower left:* Disappearing track search from Ref. [137]. *Lower right:* Heavy Stable Charged Particle (HSCP) search from Ref. [138]. In all cases, the dark matter mass is assumed to be much smaller than m_F.

layer and small energy deposit in the electromagnetic calorimeter (< 10 GeV). While the full detector simulation is rather involved, the acceptances for a supersymmetric chargino model have been provided for the mass range between $100 - 900$ GeV and lifetimes between $\tau_0 = 0.3 - 333$ ns. Since we do not expect a significant difference in the angular distributions of Drell-Yan production between the chargino and our heavy lepton, we assume the same acceptances but weighted by the Drell-Yan production of F instead.

The caveat here is that we have assumed that the leptons from F decay will not be correctly identified (which would have caused the event to be vetoed). Clearly, the leptons from F decay are likely to be hard whereas the pions from chargino decay are too soft to be detected. However, given that $m_{e,\mu,s} \ll m_F$, we expect both the lepton and the DM candidate to carry equal p_T, and therefore form a large cone around the direction of the original track. Thus any leptons from this decay will be seen as having a large impact parameter d_0 and not as coming from the primary vertex. We postpone a more detailed study of the lepton veto-induced loss of acceptance in our model for the future.

The exclusion bounds obtained using these assumptions are shown in the bottom-left panel of Fig. 4. The highest excluded mass is roughly 480 GeV for a lifetime of 1 m, whereas masses of 200 GeV are excluded for lifetimes between $0.1 - 100$ m. It should also be mentioned

that the published acceptance grid is not fine enough to allow for a smooth interpolation and the kinks in the exclusion curve are likely to constitute an artifact.

3.3.0.4 Searches for Heavy Stable Charged Particles

When the proper decay length of the mediator F is of the order of a few meters or longer, a sizeable fraction of its decays will take place outside the detector. In this case searches for heavy stable charged particles are relevant. Here we consider the ATLAS search at 13 TeV with and integrated luminosity of 36.1 fb^{-1}, which looked for charged particles decaying inside the calorimeter or outside the detector [138]. In particular, colour-neutral HSCPs are required to decay outside the ATLAS detector: $R > 12$ m and $|z| > 23$ m, where R (z) is the transverse (longitudinal) distance between the decay point and the primary vertex. Limits on the signal yield are provided for 8 distinct signal regions which differ by the number of HSCP candidates reconstructed in each event (one or two) and the minimum value for the reconstructed HSCP mass.

Trigger and HSCP reconstruction efficiencies have been made publicly available by ATLAS, which allows us to recast the search using truth level events at the hadron level[6]. Using MADGRAPH5_AMC@NLO for the generation of parton level events and PYTHIA 8.2 [28] for showering and hadronization, we compute the signal efficiencies for the model considered here as a function of the mediator mass and lifetime. Once again, we apply a constant K-factor of 1.2 to the F production cross-section and compute the 95% C.L. exclusion using the best signal region for the given mediator mass. The results are shown in the bottom-right panel of Fig. 4. Since the search requires all F decays to take place outside the ATLAS detector, it is only sensitive to decay lengths larger than a few meters and is not relevant for the small $T_{\rm R}$ scenario discussed in Sec. 3.1.

4 Summary and discussion

The results obtained in the previous sections are summarised in Fig. 5, in which we overlay the (m_f, y_s) (left panel) and $(m_f, c\tau)$ (right panel) values for which the model described in Sec. 2.2 can explain the observed dark matter abundance in the Universe (green contours) for different values of the reheating temperature $T_{\rm R}$ and assuming a DM mass $m_s = 12$ keV, along with the flavour (red shaded regions) and collider (blue shaded regions) constraints discussed in Sec. 3.3.

We observe that the combination of the various constraints offers an almost complete parameter space coverage up to heavy fermion masses of roughly 700 GeV, and the role of prompt searches is crucial in order to complete this picture. The largest sensitivity is reached in the prompt and detector-stable limit, while the constraints for intermediate decay lengths of $0.1-1$ m turn out to be weaker. It is also interesting that the flavour constraints, and in particular $\mu \to e\gamma$ are only a factor of a few away from actually probing part of the cosmologically interesting parameter space. Limits on $\mu \to e\gamma$, which are expected to improve during the next few years, can provide an extremely interesting handle on some freeze-in scenarios with a heavier parent particle, which are kinematically inaccessible at the LHC.

Our results show that, as we already mentioned in the Introduction, conventional LHC dark matter searches are of vital importance, not only in order to assess the viability of tradi-

---

[6]Information about the recasting and its validation as well as a sample code can be found in https://github.com/llprecasting/recastingCodes.
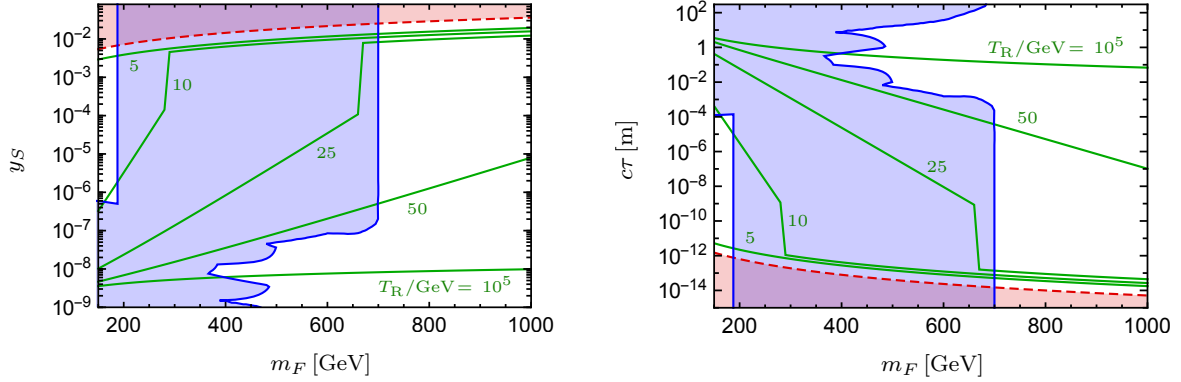
Figure 5: Summary of the results obtained in this work in the (m_f, y_s) (left panel) and $(m_f, c\tau)$ (right panel) planes, assuming a dark matter mass $m_s = 12$ keV: Contours along which the cosmic DM abundance as measured by Planck can be explained through freeze-in of s (green lines) along with global constraints from searches for prompt dileptons plus MET, displaced leptons plus MET, disappearing tracks and Heavy Stable Charged Particles (blue shaded region) and parameter space region disfavoured by $\mu \to e\gamma$ (red shaded region).

tional freeze-out scenarios, but also in order to probe more exotic ones such as freeze-in with a low reheating temperature. In this respect, they probe regions of the "freeze-in parameter space" which are inaccessible to long-lived particle searches. Our analysis illustrates, hence, the fact that there are indeed interesting freeze-in scenarios which can be probed at the LHC and that different LHC dark matter searches are complementary with each other.

Acknowldgements

Contribution 7

Long-lived signatures of conversion-driven freeze-out

B. Fuks, J. Heisig, A. Lessa, J. M. No, S. Sekmen, D. Sengupta, J. Zurita

Abstract

We consider a dark matter model where the relic density is set by conversion-driven feeze-out. This mechanism predicts long-lived particles at the LHC requiring small couplings and a relatively small mass splitting in the dark sector. As such it falls somewhat in between the typical targets of currently performed long-lived particle searches either considering extreme mass compressions or very small couplings, but lack their combinations. We study various search strategies covering the whole range of possible decay lengths $\mathcal{O}(1\,\mathrm{mm}-1\,\mathrm{m})$, pointing out blind spots in the experimental search programme and estimating the corresponding potential for improvement.

1 Introduction

The existence of dark matter (DM) is one of the prime motivations for physics beyond the standard model (SM) and hence its detection consists in an important scientific goal of the LHC experiments. While the weakly interacting massive particle (WIMP) paradigm has mainly guided our DM search strategies in the past, other possibilities exist and have now come into focus. In this work we compare various search strategies for DM models containing long-lived particles with decay length $\mathcal{O}(1\,\mathrm{mm}-1\,\mathrm{m})$, and small mass splittings $\mathcal{O}(10)$ GeV, as predicted by conversion-driven freeze-out [74, 75, 139]. As a benchmark model we take the one studied in [74] supplementing the SM by a Majorana fermion DM candidate and a scalar bottom partner, both odd under a new Z_2 symmetry under which all SM particles are even.

This example is interesting as it reveals blind spots in the performed LHC analyses targeted to other benchmark scenarios, where the long lifetime is typically considered to arise either from an extreme mass compression (long-lived chargino scenario) or a very small (effective) coupling (*e.g.* split supersymmetry or gravitino scenarios). However, the case in-between, as it occurs here, is often not explicitly considered.

We study various different searches aiming at covering as much of the model parameter space as possible. For very small decay lengths, common DM searches requiring missing energy plus jets can be applied [140, 141]. These searches typically assume direct DM production, or its production via the prompt decays of a parent particle. Depending on the inclusiveness of the search, the latter could also be sensitive to intermediate decay lengths. However, as the corresponding SM backgrounds are sizeable, missing energy searches are typically outperformed by dedicated searches towards large decay lengths.

For very large decay lengths $\gtrsim 1\,\mathrm{m}$, searches for heavy stable charged particles (in this case R-hadrons) [138, 142–144] can be applied and provide great prospects while being extremely inclusive. However, the sensitivity drops quickly for smaller decay length due to the

exponentially suppressed number of R-hadrons passing through the whole detector. Therefore, intermediate lifetimes can only be sensitively searched for when exploiting the displaced decay of the parent particle. In this respect we consider searches for disappearing tracks [145], displaced jets [146] and delayed jets [147]. However, these searches are less inclusive than the two cases mentioned above. Furthermore, displaced and delayed jets searches are not targeted to small mass splittings, and hence soft visible decays of the long-lived parent particle.

2 The dark matter model

We extend the SM by a singlet Majorana fermion DM candidate χ and a colored scalar bottom partner $\widetilde{b}$ both transforming odd under a new Z_2 symmetry (while SM particles are even). The new physics interactions are described by

$$\mathcal{L}_{\text{int}} \subset D_\mu \tilde{b}^\dagger D^\mu \tilde{b} - \left(\lambda_\chi \widetilde{b} \bar{b} \frac{1 - \gamma_5}{2} \chi + \text{h.c.} \right), \tag{1}$$

where b is the b-quark field, D_μ the covariant derivative and λ_χ the DM coupling. The model resembles a supersymmetric simplified model with a bino-like neutralino and a right-handed sbottom, except for the coupling λ_χ, being considered a free parameter here. Within the model, conversion-driven freeze-out allows one to explain the measured relic density for small couplings, $\lambda_\chi = \mathcal{O}(10^{-7} - 10^{-6})$ and relatively small mass splittings, $\Delta m_{\chi \widetilde{b}} = m_{\widetilde{b}} - m_\chi \lesssim 35\,\text{GeV}$ [74]. The respective parameter space resides below the thick black curve in Fig. 1. The thin green and grey dotted curves denote contours of constant coupling and decay length, respectively, predicting the measured relic density, $\Omega h^2 \simeq 0.12$ [77]. A qualitatively similar phenomenology is obtained for a model with a top partner [78] or a leptonic partner [148].

3 Search strategies

As the bottom partner $\widetilde{b}$ is strongly interacting, its pair-production cross section at the LHC is large. In the regime of non-prompt decays considered here, it hadronizes and forms R-hadron bound states before decaying into a b-quark and DM. The corresponding process is sketched in Fig. 2. In the following we study and discuss various search strategies in the context of this signature.

3.1 Missing energy searches

Among the most inclusive search strategies are missing energy searches. In Ref. [74], the results of an early Run 2 ATLAS monojet search for new physics in 3.2 fb^{-1} of LHC data [140] have been reinterpreted. The red curve in Fig. 1 shows the boundary of the corresponding 95% confidence level (CL) exclusion (the red shaded area being excluded), as taken from [74]. In the experimental analysis, a signal is selected by requiring events to feature a large amount of missing transverse energy ($E_T^{\text{miss}} > 250$ GeV) and a hard central leading jet with a transverse momentum p_T larger than 250 GeV and pseudorapidity $|\eta| < 2.4$. Moreover, a charged lepton veto is applied and the search strategy allows for a subleading jet activity provided it is well separated from the missing energy, the number of jets with $p_T > 30$ GeV, $|\eta| < 2.8$ and with an angular separation from the missing transverse momentum in azimuth $\Delta\phi$ of at least 0.4, being constrained to be at most 4. The selection is then divided into several exclusive and inclusive signal regions with different E_T^{miss} requirements. Whereas not directly targeting long-lived
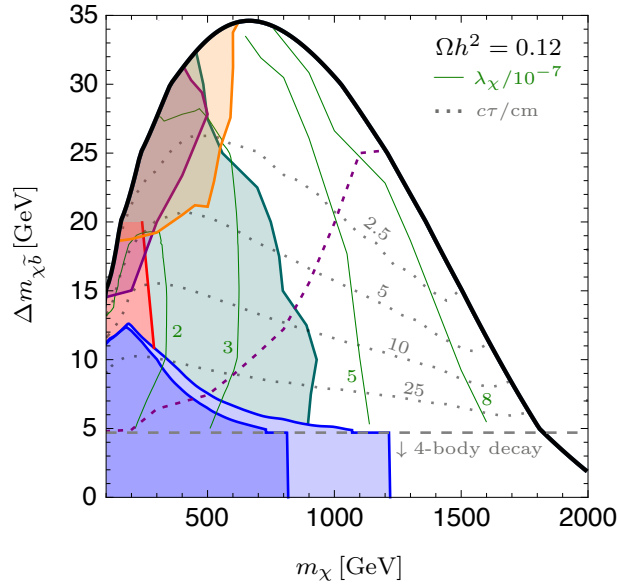
Figure 1: Allowed parameter space in the considered conversion-driven freeze-out scenario in the DM-mass vs. mass-splitting plane. The thin green and dotted grey curves denote contours of constant DM coupling and decay length, respectively (taken from [74]). We show 95% CL exclusion limits derived from the following analyses. The dark and light blue regions are excluded from R-hadron searches at the 8 [142] and 13 TeV LHC [143], respectively, as reinterpreted in [74]. The red and orange regions are excluded by the monojet [140] and multijet plus missing energy [141] analyses, respectively, while the teal and purple regions represent the limits obtained from the disappearing track [145] and displaced jet [146] searches, respectively. Finally, the purple dotted curve illustrates the limit that would be obtained after dropping the invariant mass cut of the last search (see the text for details).
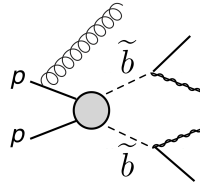

Figure 2: Production and decay diagram at LHC (in this case with ISR).

new physics, this search is able to constrain sbottom-neutralino configurations featuring a not too heavy neutralino $m_\chi \lesssim 300$ GeV for moderate mass splittings of about 10–20 GeV.

Here, we additionally update those bounds by including the impact of a recent ATLAS search for supersymmetry in a multijet plus missing energy final state [141]. As for the early Run 2 analysis, events exhibiting a large amount of missing energy ($E_T^{\text{miss}} > 300$ GeV), a hard central leading jet ($p_T > 200$ GeV and $|\eta| < 2.8$), and no reconstructed electron or muon are preselected. However, in contrast, there is no limit on the number of subleading jets of $p_T > 50$ GeV, provided that the first three jets are well separated from the missing transverse momentum in azimuth ($\Delta\phi > 0.4$), and that the effective mass defined as the sum of the p_T of all reconstructed jets and the missing transverse energy satisfy $m_{\text{eff}} > 800$ GeV. Different signal regions are then defined depending on the jet multiplicity and properties, the missing energy significance and the exact value of the effective mass. This analysis has been recast

and validated within the MADANALYSIS 5 framework [20, 71–73] with details of validation provided in the url [149], and the recast code available in [150].

We reinterpret this search, within the context of the simplified model described in this work. To this end, we generate Monte Carlo samples of 100000 parton-level events describing the production and decay of a pair of scalar bottom partners, possibly together with up to two additional QCD partons. Event generation is achieved with MADGRAPH5_AMC@NLO [19] and we use the MLM prescription to merge events featuring different jet multiplicities at the hard-scattering level [151]. Parton showering and hadronization are achieved with PYTHIA 8.2 [28] and event reconstruction is performed using the anti-k_T algorithm [152], as implemented in FASTJET [153]. Detector simulation with parameters set to match the performance of the reinterpreted search has been performed with DELPHES 3 [154]. The results of the reinterpretation are presented in Fig. 1, where the orange curve delineates the constraint on the parameter space in question, as an exclusion at 95 % using the CLs prescription. The constraint is dominated by the two jet bin with the lowest values of m_{eff} and missing transverse momentum criteria. This is understandable as we predominantly rely on radiation jets to pass the analysis selection, the new physics spectra being too compressed to lead to hard objects. The difference in the behaviour of the constrained region between the monojet analysis and the multijet plus missing energy analysis can be understood as stemming from two factors. The first one consists in the increased luminosity used in the multijet search. Secondly, the multijet search prioritizes larger mass gaps, while the monojet targets more compressed regions. Overall, we observe that up to $m_\chi \sim 500$ GeV is ruled for $\Delta m_{\widetilde{\chi}b} \sim 35$ GeV.

Those typical searches for supersymmetry through the production of a large amount of missing energy in association with an important hadronic activity are however unsensitive to more compressed new physics spectra. In order to circumvent this issue, the CMS collaboration has performed a traditional search [155] for squarks and gluino using the M_{T2} kinematic variable [156] and extended it by including a signal region specifically focusing on events featuring a disappearing track that could be interpreted as the impact of a long-lived particle. In the standard search region, the selection vetoes the presence of leptons and either requires the presence of one central jet ($p_T > 30$ GeV and $|\eta| < 2.4$) or a low hadronic activity ($H_T < 1.2$ TeV) together with $E_T^{\text{miss}} > 250$ GeV, or of a larger hadronic activity and $E_T^{\text{miss}} > 30$ GeV. Once again, the missing transverse momentum is imposed to be well separated from the four leading jets, the missing transverse energy to be mainly originating from the jet activity and one finally requires $M_{T2} > 200$ GeV if $H_T < 1.5$ TeV, or $M_{T2} > 400$ GeV otherwise. The M_{T2} cut is lowered to 200 GeV in all cases if the event features a disappearing track. The implementation of such an analysis in the MADANALYSS 5 framework [20, 71–73] is ongoing.

3.2 Heavy stable charged particles

Towards large lifetimes, searches for heavy stable chareged particles become sensitive (see *e.g.* [138, 142–144]). These searches make use of observables related to large ionization energy loss and time of flight, typical for heavy charged particles traveling at low velocity through the detector. In this case, events are selected if they feature a well reconstructed track candidates with a large transverse momentum and a large amount of missing transverse momentum or a isolated muon candidate. In Fig. 1 we show the 95% CL exclusion from an reinterpretation of the 8 TeV [142] and early 13 TeV [143] CMS analysis for finite lifetimes performed in [74] as the dark and light blue curve (shaded area), respectively. The latter excludes the region of very small mass splittings $\Delta m_{\widetilde{\chi}\widetilde{b}} \lesssim 5$ GeV up to around 1.2 TeV. However, it quickly loses

constraining power towards larger values of $\Delta m_{\chi \widetilde{b}}$.

3.3 Disappearing tracks

Searches for disappearing tracks by the ATLAS [145] and CMS [137] collaborations also have the potential to constrain the scenario considered here, particularly for $\widetilde{b}$ decay lengths in the range $c\tau \in [0.1 - 1]$ m. In the following, we analyze the sensitivity of the disappearing track ATLAS analysis using 36.1 fb^{-1} of 13 TeV LHC data [145]. We use the electroweak production event selection from the ATLAS analysis (despite our signal being produced via strong interactions), since the ATLAS strong production selection requires, besides the leading-p_T jet, several jets with a transverse momentum $p_T > 50$ GeV in the event. Such an option is usually not featured by our signal, due to the small mass splitting $\Delta m_{\chi \widetilde{b}}$ between the new physics states.

The kinematic event selection for electroweak production requires the presence of at least one jet with $p_T > 140$ GeV, a large amount of missing transvers energy ($E_T^{\mathrm{miss}} > 140$ GeV) that must be well separated in azimuth (with $\Delta\phi > 1$) from the four leading jets with $p_T > 50$ GeV. In addition, the selection vetoes the presence of reconstructed electron and muon, and events passing the kinematic selection so far are imposed to exhibit *tracklets* (short isolated tracks reconstructed solely from hits in the pixel detector, with no requirements from the SCT and TRT detectors [145]), with four specific properties. The corresponding requirements are:

1. *p_T and isolation*: The p_T of the candidate tracklet must be greater that 20 GeV, and the separation ΔR between the tracklet and any jet with $p_T > 50$ GeV must be greater than 0.4. Furthermore, the tracklet is required to be isolated (see [145] for details).

2. *Geometrical acceptance*: The tracklet properties must satisfy $0.1 < |\eta| < 1.9$.

3. *Quality requirements*: The tracklet is required to have hits in all four pixel layers (located at a radial distance $R \in [33.25, \, 122.5]$ mm from the interaction point).

4. *Disappearance condition*: The number of SCT hits associated with the tracklet must be zero.

The last two requirements may be satisfied if the $\widetilde{b}$ decays outside the pixel detector and before the first SCT layer. Besides, the track hits on the first SCT layer from the jets coming out of the $\widetilde{b}$ decay are required to have a minimal distance (d_{min}) from the would-be hit of the extrapolated tracklet in this layer. This minimal distance is such that, taken the resolution $\sigma_{\mathrm{SCT}} \simeq 17$ μm of the SCT from [157], the χ^2 for matching the tracks is at least 15. That is,

$$d_{\mathrm{min}} > \sqrt{15}\,\sigma_{\mathrm{SCT}}\,. \tag{2}$$

Among the candidate tracklets (if more than one) passing all the above requirements, the one with the largest p_T is selected, and the analysis defines its signal region for tracklets with $p_T > 100$ GeV.

In order to estimate the sensitivity of this search to the present model, we generate $pp \to \widetilde{b}\widetilde{b}j$ (with $\widetilde{b} \to \chi b$ decays) hard-scattering signal events with MADGRAPH5_AMC@NLO, imposing that the additional hard-jet satisfies $p_T > 140$ GeV[1] and the two $\widetilde{b}$ states as yielding potential tracklets. We compute the fraction of events that pass the kinematic selection and the

---

[1]This allows for a preliminary estimate of the sensitivity. A full recasting of the ATLAS analysis including multipartonic matrix element merging, parton shower and hadronization is left for the future.

$\widetilde{b}$ tracklet selection at generator level. Furthermore, since $\widetilde{b}$ states form R-hadrons, we need to multiply the resulting efficiencies by the probability that the R-hadron ends up in a state with charge ± 1 (given approximately by 0.5, which we obtain from [138]). The *quality requirement* for the candidate tracklet is interpreted here as the $\widetilde{b}$ decaying outside the pixel detector volume (the ATLAS inner detector configuration measures are taken from Fig. 2 of [158]), and together with the tracklet *disappearance condition* ($\widetilde{b}$ decay before the first ATLAS SCT layer, together with its visible decay product satisfying the inequality (2)) mainly dictates the signal selection acceptance $\times$ efficiency. We also include in our analysis the efficiency for a generator level tracklet candidate to be identified as a tracklet at the reconstruction level, estimated approximately as 0.45 from the auxiliary material from [145].

The resulting excluded region is illustrated by the solid teal curve in Fig. 1, that shows that the analysis is sensitive to bottom partner masses ranging up to $m_{\widetilde{b}} \sim 900$ GeV and to splittings $\Delta m_{\chi \widetilde{b}} \sim 10$ GeV (corresponding to decay lengths $c\tau \sim 20$ cm, in the "sweet-spot" of the ATLAS disappearing track search). Due to the high resolution of the ATLAS tracker, the condition (2) on the visible decay product does not have a significant effect even though the mass splitting here ($\mathcal{O}(10)$ GeV) is much larger than in the long-lived chargino model ($\mathcal{O}(100)$ MeV) targeted by the analysis. We expect this to also hold in a refined analysis performed at hadron level which is, however, left for future work.

3.4 Displaced jets

For decay lengths between a few millimeters and a few centimeters, the long-lived particle dominantly decays within the inner tracker, resulting in displaced b-jets and missing energy. A few ATLAS and CMS searches targeting this topology exist [146, 159, 160].

We consider here the ATLAS search for displaced vertices and missing energy using 32.8 fb^{-1} of 13 TeV LHC data [146]. This search is dedicated to final states exhibiting a large amount of missing energy and vertices containing at least five charged tracks displaced from the primary vertex by a distance between 4 mm and 30 cm. The benchmark scenario considered by the ATLAS analysis is a long-lived gluino simplified model, where the gluino decays into two jets and a neutralino. In this scenario, gluino masses of 1.5–2.5 TeV are excluded, the precise exclusion depending on the neutralino mass and gluino lifetime. The signal region considered by ATLAS requires the presence of a large amount of missing transverse energy ($E_T^{\mathrm{miss}} > 250$ GeV), either one jet with $p_T > 70$ GeV or two jets with $p_T > 25$ GeV, and one or more displaced vertices containing at least 5 charged tracks and of invariant mass (m_{DV}) larger than 10 GeV.

Although the model considered here can produce events with large missing energy and sufficiently hard jets, the small mass gap between the long-lived parent and its daughter results in displaced vertices with invariant masses typically much smaller than 10 GeV. In Fig. 3, we compare the m_{DV} distribution for the gluino simplified model considered by ATLAS with masses $m_{\widetilde{g}} = 625$ GeV and $m_{\widetilde{\chi}_1^0} = 100$ GeV, and the model considered here with and without a large mass gap. For cases with a large mass gap, a sizeable fraction of the events contains vertices with large invariant masses. However, in the compressed case almost all events fail the $m_{\mathrm{DV}} > 10$ GeV requirement.

In order to estimate the sensitivity of the search, we recast it by making use of the trigger and DV reconstruction efficiencies provided by ATLAS in the auxiliary material of Ref. [146]. We then use MADGRAPH5_AMC@NLO and PYTHIA 8.2 to generate hadron-level events and compute the signal efficiency for the model described in Sec. 2. Events are normalized to cross
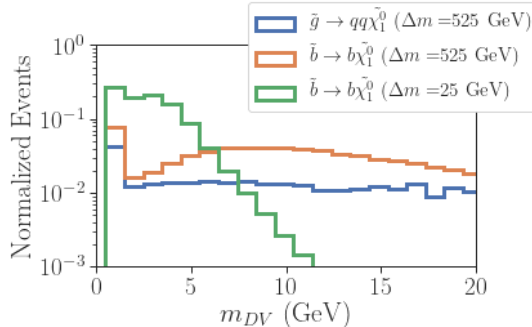
Figure 3: The invariant mass distribution for candidate displaced vertices. The blue histogram shows the distribution for a gluino simplified model with a large mass gap: $(m_{\tilde{g}}, m_{\tilde{\chi}_1^0}) = (625\,\text{GeV}, 100\,\text{GeV})$. The orange histogram shows the distribution for the model considered here with masses $(m_{\tilde{b}}, m_\chi) = (625\,\text{GeV}, 100\,\text{GeV})$, while the green histogram shows the same distribution but for the compressed scenario: $(m_{\tilde{b}}, m_\chi) = (625\,\text{GeV}, 600\,\text{GeV})$.

sections matching next-to-leading order calculations with the resummation of the next-to-next-to-leading threshold logarithms, as obtained from NNLL-FAST [161, 162].

As expected, most of the events fail the m_{DV} cut, suppressing the signal yield. The resulting 95% CL exclusion is illustrated by the solid purple curve in Fig. 1 that shows that only points with very large cross sections (small $\tilde{b}$ masses) and a mass gap larger than 15 GeV are excluded. Since the main loss in sensitivity is due to the invariant mass requirement for the displaced vertices, we try to estimate what could be the reach resulting from relaxing this cut. In order to achieve this, we assume that the SM background remains unchanged and the DV reconstruction efficiency for vertices with $m_{\text{DV}} < 10\,\text{GeV}$ is the same as the one for $m_{\text{DV}} = 15\,\text{GeV}$. Although these certainly are optimistic assumptions, it allows us to use the efficiencies provided by the ATLAS collaboration when smaller mass cuts are used. The result is shown by the purple dashed line in Fig. 1, the excluded region being now significantly enhanced, extending up to 1 TeV bottom partner masses for small lifetimes (large mass splittings within the considered scenario).

Once again we stress that this is an optimistic and probably unrealistic projection. Nevertheless, it illustrates the impact of the invariant mass cut on the sensitivity to models with small mass gaps and reveals the potential gain of relaxing this cut. To achieve this, the background might be reduced by other means, *e.g.* by requiring a larger displacement. In fact, Fig. 1 shows a significant region where the displaced jets without a m_{DV} cut would outperform the disappearing track search (*e.g.* for $c\tau > 2.5\,\text{cm}$).

3.5 Delayed jets

Another option for distinguishing the long lifetime of some particles is to measure the timing information of their decay products, and search for delays with respect to the collision time. This method was exploited in a recent CMS analysis [147], where timing capabilities of the CMS electromagnetic calorimeter (ECAL) were used to identify non-prompt or "delayed" jets. The analysis is sensitive to long-lived particles decaying within the ECAL barrel volume extending up to 1.79 m and covering $|\eta| < 1.48$. The analysis uses only calorimetric information to reconstruct jets and imposes a set of quality criteria on the ECAL cells and energy fractions. Jet timing is calculated from the median of the times of ECAL cells associated with the jet,

and is required to be at least 3 ns to discriminate from detector, beam, pileup and cosmic ray backgrounds. Events are imposed to have at least one delayed central jet with $p_T > 30$ GeV and $|\eta| < 1.48$. Additionally, one imposes that $E_T^{\mathrm{miss}} > 300$ GeV to eliminate SM multijet backgrounds and other beam-related backgrounds.

The analysis was interpreted using a gauge-mediated supersymmetry breaking model, where a 1–3 TeV long-lived gluino decays into a gluon and a 10 GeV gravitino. The large gluon-gravitino mass difference leads to high-p_T jets and a high signal efficiency. In the DM models considered here, the small $\widetilde{b}$-χ mass difference typically results in a much softer jet p_T spectrum. However, a preliminary study of events generated with MADGRAPH5_AMC@NLO (hard-scattering), PYTHIA 8.2 (parton showering and hadronization) and DELPHES 3 (detector simulation) leads to a sizable fraction of events passing the jet p_T and E_T^{miss} selection, especially for points with a relatively high mass difference. The larger cross sections for lower masses would further improve the signal significance in this very low background analysis. Where the simulation of delayed jet selection criteria is non-trivial in existing public tools, delayed jet selection efficiencies depending on the jet transverse momentum and pseudorapidity would be a fundamental requirement for obtaining reliable estimates of the sensitivity of this analysis.

4 Conclusions

In this contribution, we considered a conversion-driven feeze-out DM scenario predicting long-lived particles with decay length $\mathcal{O}(1\,\mathrm{mm} - 1\,\mathrm{m})$ at the LHC. The scenario is characterized by small DM couplings and relatively small mass splittings ($\mathcal{O}(10)\,\mathrm{GeV}$) in the dark sector, *i.e.* between the parent particle pair-produced at the LHC and the DM particle it decays into. We considered searches for heavy stable charged particles (R-hadrons), disappearing tracks, displaced (and delayed) jets as well as prompt missing energy searches covering the whole range of possible decay lengths. The strongest constraint can be reached towards the upper edge of the occurring decay lengths within the model, $c\tau \sim 1\,\mathrm{m}$, by searches for heavy stable charged particles, reaching DM masses around 1.2 TeV. For intermediate lifetimes, searches for disappearing tracks are most sensitive and constrain DM masses up to $\sim 900\,\mathrm{GeV}$ for $\Delta m_{\chi\widetilde{b}} \sim 10$ GeV (which corresponds to a decay length of around 20 cm). Towards smaller lifetimes the search loses sensitivity. Finally, for $c\tau \lesssim 2.5\,\mathrm{cm}$ ($\Delta m_{\chi\widetilde{b}} \gtrsim 25\,\mathrm{GeV}$), the considered multijet plus missing energy search the most sensitive, constraining DM masses ranging up to around 600 GeV.

The search for displaced jets is only sensitive to a very small region of the parameter space, with masses below $m_\chi = 500\,\mathrm{GeV}$ – a region being already excluded by the disappearing tracks and missing energy search. This is mainly due to the lower invariant mass cut on the tracks arising from the displaced vertex which is affordable in the scenario considered in the experimental analysis with a large mass gap, but that rejects most of the signal for the considered model with small mass splittings. Relaxing this cut potentially has a very large effect and would render the displaced jet search to be the most sensitive for $\Delta m_{\chi\widetilde{b}} \gtrsim 15\,\mathrm{GeV}$ ($c\tau \lesssim 10\,\mathrm{cm}$). Determining whether this is possible (above a certain minimal displacement) requires further studies considering the relevant backgrounds.

Acknowledgements

The Higgs Boson

Contribution 8

Confronting Gildener-Weinberg Higgs bosons with LHC measurements

J. M. Butterworth, K. Lane, D. Sperka

Abstract

Gildener-Weinberg (GW) models of electroweak symmetry breaking solve two fundamental problems of the Standard Model: (1) What _natural_ mechanism makes the 125 GeV Higgs boson H light? (2) Given that most proposed answers to (1) require multiple Higgs multiplets, generally doublets, what can _naturally_ explain the apparently SM couplings of H to gauge bosons and fermions [163, 164]? The GW mechanism of approximate scale invariance answers both questions, but at a price. The masses of extra Higgs bosons $\mathcal{H}$ in these models satisfy a sum rule: $(\sum_{\mathcal{H}} M_{\mathcal{H}}^4)^{1/4} = 540\,\text{GeV}$. This is a powerful constraint which we probe with LHC data in this report.

1 Overview of the Gildener-Weinberg 2HDM

In 1976, E. Gildener and S. Weinberg (GW) [165] proposed a scheme, based on broken scale symmetry, to generate a light Higgs boson H in multi-scalar models of electroweak symmetry breaking. What GW did not appreciate then, for there was no reason for them to, was that that H was also aligned [166]. That is, of all the scalars, its couplings to gauge bosons and fermions were exactly those of the single Higgs boson of the Standard Model (SM) [167]. Like the Higgs boson's mass, its alignment is protected by the approximate scale symmetry [168].

Generalizing the work of S. Coleman and E. Weinberg [169], GW assumed a multi-Higgs multiplet potential V_0 with only quartic interaction terms. Assuming that all gauge boson and fermion masses arise from their couplings to Higgs bosons, such a theory is scale-invariant at the classical level. This V_0 has a trivial minimum, the one at which all scalar fields $\Phi = 0$ so that $(V_0)_{\min} = 0$. This Lagrangian also has a nontrivial extremum. It occurs along a ray in scalar-field space and it is a *flat minimum* if the quartic couplings satisfy certain positivity conditions. This flat minimum corresponds to spontaneously broken scale symmetry, so there is a massless Goldstone boson, a "dilaton", and it is H. Higgs alignment is then a simple consequence of the linear combination of fields composing H having the *same form* as the Goldstone bosons $w^{\pm}$ and z that become the longitudinal components of the $W^{\pm}$ and Z bosons.

This classically-exact scale symmetry is explicitly broken by the first-order term V_1 in the Coleman-Weinberg loop expansion of the effective scalar potential [169]: $V_0 + V_1$ has a deeper minimum than the trivial one at zero fields. It occurs at a specific vacuum expectation value $\langle H \rangle = v$, an explicit breaking of scale invariance. Then M_H and all other masses in the theory are proportional to v.

In 2012, Lee and Pilaftsis [170] proposed a simple model of the GW mechanism using

the two Higgs doublets

$$\Phi_i = \frac{1}{\sqrt{2}} \begin{pmatrix} \sqrt{2}\phi_i^+ \\ \rho_i + i a_i \end{pmatrix}, \quad i = 1, 2. \tag{1}$$

Here, ρ_i and a_i are neutral CP-even and odd fields, respectively. The potential V_0 is

$$\begin{aligned} V_0(\Phi_1, \Phi_2) &= \lambda_1 (\Phi_1^\dagger \Phi_1)^2 + \lambda_2 (\Phi_2^\dagger \Phi_2)^2 + \lambda_3 (\Phi_1^\dagger \Phi_1)(\Phi_2^\dagger \Phi_2) \\ &+ \lambda_4 (\Phi_1^\dagger \Phi_2)(\Phi_2^\dagger \Phi_1) + \tfrac{1}{2}\lambda_5 \left((\Phi_1^\dagger \Phi_2)^2 + (\Phi_2^\dagger \Phi_1)^2 \right). \end{aligned} \tag{2}$$

All five quartic couplings are real so that V_0 is CP-invariant.

In 2018, Lane and Shepherd studied this model and, *inter alia*, updated its consistency with LHC data of the previous six years [168]. For this, the following $\mathcal{Z}_2$ symmetry was imposed to prevent tree-level flavor-changing interactions among fermions, ψ, induced by neutral scalar exchange [171]:

$$\Phi_1 \to -\Phi_1, \ \Phi_2 \to \Phi_2, \quad \psi_L \to -\psi_L, \ \psi_{uR} \to \psi_{uR}, \ \psi_{dR} \to \psi_{dR}. \tag{3}$$

This is the usual type-I 2HDM [172], but with Φ_1 and Φ_2 interchanged. In type-I, all Yukawa couplings of the new, heavier Higgs bosons are proportional to $\tan\beta$ in the alignment limit. It was chosen to remain consistent with limits from CMS [173] and ATLAS [174] on charged Higgs decay into $t\bar{b}$; also see Ref. [175]. The limits from these papers are consistent with $\tan\beta \lesssim 0.5$ for $M_{H^\pm} \simeq 200\text{–}500\,\text{GeV}$. Type-I couplings also suppress gluon fusion of A, H' by $\tan^2\beta$, where A and H' are the massive CP-odd and CP-even Higgs of the 2HDM. We refer to this version of the model as GW-2HDM.[1]

The flat minimum of the potential V_0 occurs along the ray

$$\Phi_{1\beta} = \frac{1}{\sqrt{2}} \begin{pmatrix} 0 \\ \phi \cos\beta \end{pmatrix}, \quad \Phi_{2\beta} = \frac{1}{\sqrt{2}} \begin{pmatrix} 0 \\ \phi \sin\beta \end{pmatrix}. \tag{4}$$

Here $\phi > 0$ is any real mass scale and $0 < \beta < \pi/2$. The massless CP-even dilaton H and its massive orthogonal combination H' are

$$\begin{aligned} H &= \rho_1 \cos\beta + \rho_2 \sin\beta, \\ H' &= -\rho_1 \sin\beta + \rho_2 \cos\beta. \end{aligned} \tag{5}$$

This H is the <u>same</u> linear combination of ρ_1 and ρ_2 as the electroweak Goldstone bosons $z = a_1 \cos\beta + a_2 \sin\beta$ and $w^\pm = \phi_1^\pm \cos\beta + \phi_2^\pm \sin\beta$ that are eaten by Z^0 and $W^\pm$. <u>This</u> is the origin of H being perfectly aligned.

The one-loop potential, V_1, explicitly breaks scale symmetry but, of course, not electroweak symmetry. This picks out a particular value $v = \langle H \rangle$ of ϕ at which $V_0 + V_1$ has a deeper minimum than the trivial one for V_0, and it mixes H and H' to become the mass eigenstates

$$\begin{aligned} H_1 &= \cos\delta H - \sin\delta H' = \cos\beta' \rho_1 + \sin\beta' \rho_2, \\ H_2 &= \sin\delta H + \cos\delta H' = -\sin\beta' \rho_1 + \cos\beta' \rho_2, \end{aligned} \tag{6}$$

---

[1]**Experimentalists beware!** Because of the Φ_1–Φ_2 interchange relative to the type-I definition in Ref. [172], experimental limits on $\tan\beta$ for the usual type-I are limits on $\cot\beta$ for the GW-2HDM.

where $\beta' = \beta - \delta$.[2] The angle δ measures the departure of the Higgs boson H_1 from perfect alignment. Being one-loop corrections, δ and δ/β are only a few percent and, so, $H_1 \cong H$ is very nearly an aligned Higgs boson [168]. The decays $A, H_2 \to W^+W^-$, ZZ, ZH_1 and $H^\pm \to W^\pm Z$, $W^\pm H_1$ are highly suppressed by $\sin^2 \delta$; observing them from a new, heavier spinless boson would be significant, if not fatal, blows to GW models. As noted earlier, all couplings of $H^\pm$, A and H_2 are proportional to $\tan\beta$ up to a correction of $\mathcal{O}(\delta^2)$ [168]. From now on, we refer interchangeably to the 125 GeV Higgs boson as H_1 or H, as clarity requires.

The nonzero one-loop mass of the Higgs boson H is given by [165], [170], [168]

$$M_H^2 = \frac{1}{8\pi^2 v^2}\left(6M_W^4 + 3M_Z^4 + M_{H'}^4 + M_A^4 + 2M_{H^\pm}^4 - 12m_t^4\right). \tag{7}$$

In accord with first-order perturbation theory, all the masses on the right side of this formula are obtained from zeroth-order perturbation theory, i.e., from V_0 plus gauge and Yukawa interactions; see Refs. [165,168]. As v is the only mass scale in the theory, all masses in Eq. (7) are proportional to v; e.g., $M_W = \frac{1}{2}gv = M_Z/\cos\theta_W$, so that $v = 246\,\mathrm{GeV}$ and $\tan\beta = v_2/v_1$.

Eq. (7) implies a remarkable sum rule for the masses of the new Higgs bosons in the GW-2HDM [168,170,176]:

$$\left(M_{H'}^4 + M_A^4 + 2M_{H^\pm}^4\right)^{1/4} = 540\,\mathrm{GeV}. \tag{8}$$

With appropriate modification of the left side to allow for different Higgs sectors, this sum rule holds in *any* GW model of electroweak breaking in which the only weak bosons are W and Z and the only heavy fermion is the top quark. The second-order loop correction will modify the right side, but we would be surprised if it were more than $\mathcal{O}(100\,\mathrm{GeV})$. Thus, in GW models, new Higgs bosons should be found at surprisingly low masses. Furthermore, the larger the Higgs sector in a GW model, the lighter will be the masses of at least some of the new Higgs bosons.

Beyond this observation, Eq. (8) has a significant impact on searching for the new GW Higgses. Figure 1 shows the CP-even masses M_H (from Eq. (7), with initial input Higgs mass $M_H = 125\,\mathrm{GeV}$), $M_{H'}$ (from Eq. (8)), and the corresponding eigenvalues M_{H_1} and M_{H_2} of the CP-even mass matrix at one-loop order. They are calculated as a function of $M_{H^\pm} = M_A = 200$–$410\,\mathrm{GeV}$. (The constraint $M_{H^\pm} = M_A$ is important; it makes the contribution to the T-parameter from the new scalars vanish identically [177,178].) Three observations:

– 1) M_H and M_{H_1} are very close along the entire range of $M_{H^\pm}$; their ratio is 1.004–1.012. This is not surprising since Eq. (7) and diagonalizing the CP-even mass matrix should be equivalent.

– 2) $M_{H'} \to 0$ at $M_{H^\pm} = 410.22\,\mathrm{GeV}$, the boundary of the sum rule for $M_{H^\pm} = M_A$. This is both unphysical and in conflict with LHC (but not LEP) limits on light Higgses decaying to $b\bar{b}$ and $\gamma\gamma$.

– 3) $M_{H'} \cong M_{H_2}$ up to $M_{H^\pm} \simeq 370\,\mathrm{GeV}$; beyond that $M_{H'}$ starts to dive rapidly to zero while $M_{H_2} \to 214\,\mathrm{GeV}$ at $M_{H^\pm} = 410\,\mathrm{GeV}$.

---

[2]Because $H^\pm$ and A must remain orthogonal to the combinations defining $w^\pm$ and z, their masses are unchanged by V_1.
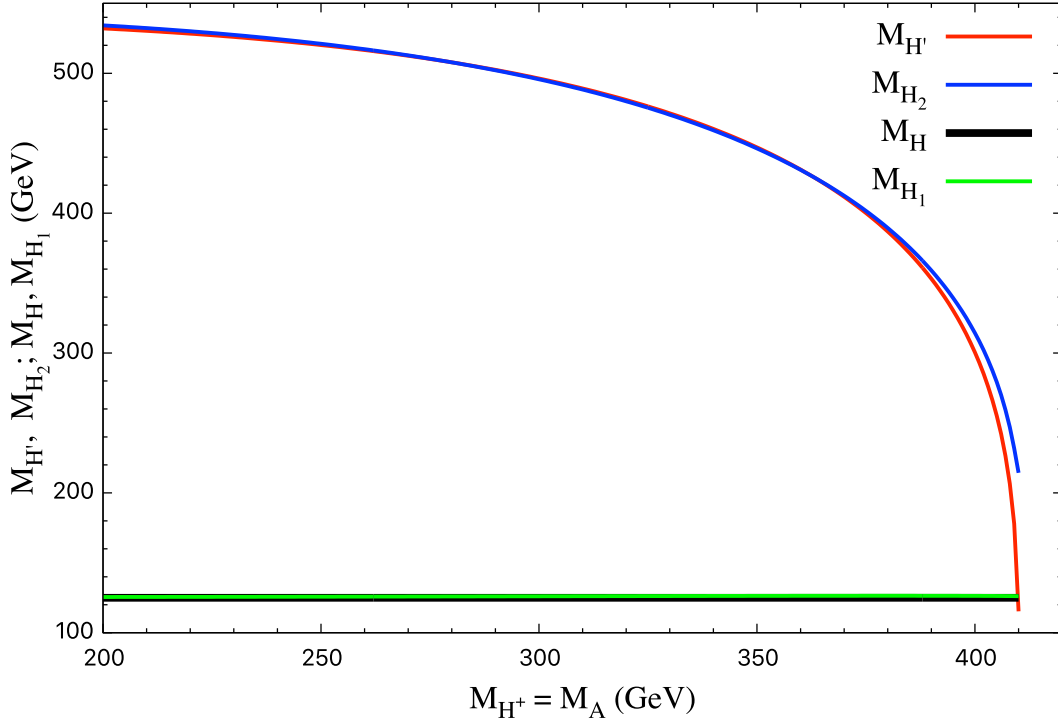
Figure 1: The CP-even masses in tree (M_H and $M_{H'}$) and 1-loop (M_{H_1} and M_{H_2}) approximations, calculated as a function of $M_{H^\pm} = M_A$ and using the sum rule (8).

To remedy this, we propose using M_{H_2} over the entire range of $M_{H^\pm} = M_A$ for estimates of production cross sections and decay branching ratios of the GW Higgs bosons. We recommend this approach for searches by ATLAS and CMS. For example, in a search involving all three GW Higgs bosons (say, $pp \to A \to ZH_2$ and $pp \to H^\pm \to W^\pm H_2$, with $H_2 \to b\bar{b}$), one could use ellipsoidal search regions in $(M_{H^\pm}, M_A, M_{H_2})$-space, roughly consistent with $M_{H^\pm} = M_A$ and the sum rule, and then calculate the model's predicted $\sigma \cdot$ BR's accordingly.

The sum rule (8) makes searches for the new Higgs bosons lying below about $500\,\mathrm{GeV}$ the most promising tests of GW models. In the GW-2HDM, the new scalars are just $H^\pm$, A and H_2. Their main production cross sections at the LHC are $gg \to A$, H_2 and $g\bar{b} \to H^+\bar{t}(b)$. Assuming as we have that $M_{H^\pm} = M_A$, the principal search modes are via the decays [179]:

$$H^\pm \;\to\; t\bar{b}\,(b\bar{t}) \text{ and } W^\pm H_2; \tag{9}$$

$$A \;\to\; b\bar{b}, \; t\bar{t} \text{ and } ZH_2; \tag{10}$$

$$H_2 \;\to\; b\bar{b}, \; t\bar{t} \text{ and } ZA, \; W^\pm H^\mp. \tag{11}$$

Searches by CMS [173, 175] and ATLAS [174] for $H^\pm \to t\bar{b}$ were noted above. CMS has posted a search for A or $H_2 \to t\bar{t}$ that actually showed a $1.9\,\sigma$ global ($3.5\,\sigma$ local) excess in $A \to t\bar{t}$ at $M_A \simeq 400\,\mathrm{GeV}$ [180]. Searches for $A(H_2) \to ZH_2(A) \to \ell^+\ell^- b\bar{b}$ have been reported by ATLAS [181] and CMS [182]. Their 95% C.L. limits cross sections are well above GW-2HDM expectations [179].

From Fig. 1, the decays $H^\pm \to W^\pm H_2$ and $A \to ZH_2$ require $M_{A,H^\pm} \geq 400\,\mathrm{GeV}$. Then, the rapid decrease of M_{H_2} to $214\,\mathrm{GeV}$ at $M_{A,H^\pm} = 410\,\mathrm{GeV}$ implies that these decays are quickly dominated by the emission of longitudinally-polarized W, Z. Thus, their rates grow

as $p_{W,Z}^3$, and they quickly overcome $A \to t\bar{t}$ and $H^\pm \to t\bar{b}$. This behavior is illustrated in Table 1 where CONTUR was used to compare the GW-2HDM prediction for $\sigma(pp \to A \to ZH_2)B(Z \to \ell^+\ell^-)B(H_2 \to b\bar{b})$ to $\ell^+\ell^- +$ jets production at the 8-TeV LHC; here $\ell = e$ or μ. For $M_A = M_{H^\pm}$, similar behavior of $H_2 \to ZA$ and $W^\pm H^\mp$ occurs above $M_{H_2} = 450\,\text{GeV}$.[3,4]

Confronting these signals with LHC data is the subject of Sec. 2.

M_A (GeV)	M_{H_2} (GeV)	$B(A \to ZH_2)$	8-TeV data exclusion
400	314.3	0.0%	26.6%
403	295.1	9.8%	55.7%
407	259.4	42%	97.9%
410	214.4	63%	99.9%

Table 1: The rapid onset of the branching ratio for $A \to ZH_2$ and its exclusion at the LHC for $\sqrt{s} = 8\,\text{TeV}$ and $ZH_2 \to \ell^+\ell^- b\bar{b}$ ($\ell = e, \mu$). As discussed in the text, this due to the growing dominance of the decay by emission longitudinally polarized Z-bosons and the corresponding growth of the decay rate as p_Z^3. The 26.6% exclusion at $M_A = 400\,\text{GeV}$ is due to decay of top quarks produced in $A \to t\bar{t}$ and $H^\pm \to t\bar{b}$.
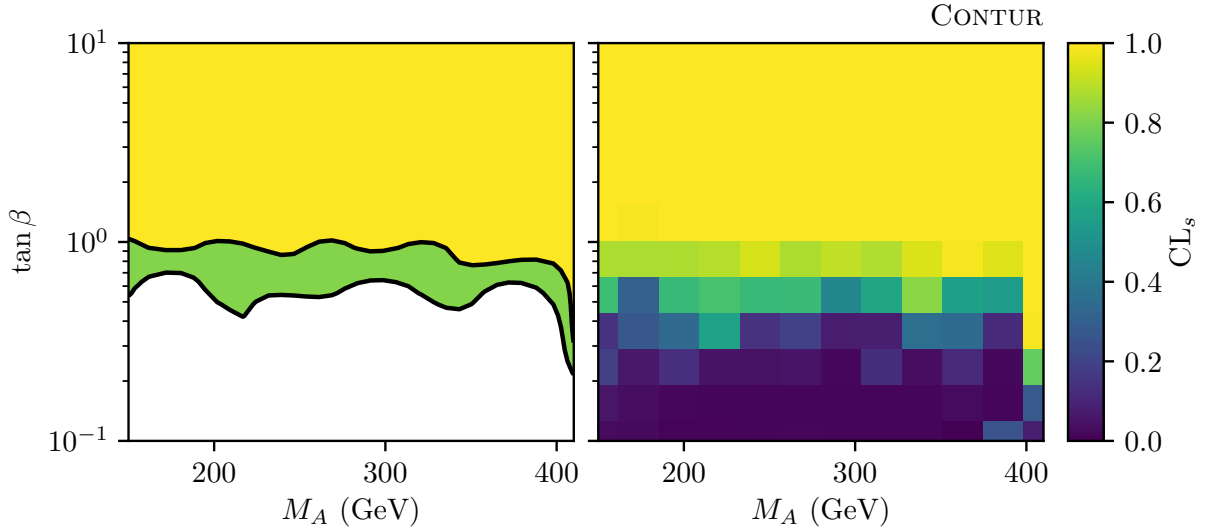
2 Confronting GW with CONTUR

Figure 2: Left: Sensitivity plot for the GW-2HDM of $\tan\beta$ vs. $M_A = M_{H^\pm}$ over the range allowed by the sum rule Eq. (8). Yellow areas signify exclusion at $\geq 95\%$ C.L.; green areas are 68–95%. Right: The same exclusion shown on a continuous scale by the bar on the right, with 1.0 being fully excluded and 0.0 being zero sensitivity.

In this section we use CONTUR [88] to determine whether and where the GW-2HDM model is in conflict from LHC measurements. In a nutshell, BSM processes are generated by

---

[3]The specific masses in these statements should be taken *cum grano salis* because of the distinct possibility of some modification of the right side of Eq. (8) by higher-order corrections.

[4]Given the large $b\bar{b}$ SM production rate, $gg \to H_2$, $A \to b\bar{b}$ is likely to be background limited for $\tan\beta \lesssim 0.5$; e.g., see Ref. [183].

HERWIG [101] and CONTUR compares these particle-level simulations with existing measurements contained in the RIVET library of analyses [87]. Since, with the exception of relatively few isolated excursions, all these measurements agree with SM predictions, these comparisons provide a "health check" on new physics models. Currently, most analyses in RIVET use data from the 8-TeV run of the LHC. This may not be much of a disadvantage for probing the GW-2HDM. The sensitivity to its signals — the new Higgs bosons below about 500 GeV — is generally not better with $36\,\mathrm{fb}^{-1}$ at $13\,\mathrm{TeV}$ than with $25\,\mathrm{fb}^{-1}$ at 7 and $8\,\mathrm{TeV}$ because SM background rates often increase faster than signal rates, especially for low-mass signals. See, e.g., the expected significances for observing $H_1 \to b\bar{b}$ with the Run 1 and $36\,\mathrm{fb}^{-1}$ Run 2 datasets in Ref. [184]. For more information on CONTUR in this document, see 18.

Figure 2 shows the sensitivity of LHC data to the decay signals in Eqs. (9–11) as a function of $\tan\beta$. Signal events were generated assuming $M_A = M_{H^\pm}$ as explained in Sec. 1.[5] Generally, the GW-2HDM is fully excluded for $\tan\beta > 1$. The 1-σ and 2-σ excluded regions are consistent with the finding in Ref. [168] that limits on $\sigma(pp \to H^\pm \to t\bar{b})$ from CMS [173] and ATLAS [174] require $\tan\beta \lesssim 0.5$. The exception to this in Fig. 2 (right) is at $M_A \gtrsim 403\,\mathrm{GeV}$ where the 95% C.L. upper limit is $\tan\beta = 0.3$; also see Table 1. This sensitivity comes from data on $\ell^+\ell^- + \mathrm{jets}$ and $\ell^\pm \not{E}_T + \mathrm{jets}$ and it is due to the rapid turn-on of the decays $A \to ZH_2$ and $H^\pm \to W^\pm H_2$ discussed above. The production cross sections for both processes are proportional to $\tan^2\beta$.

The sensitivity plot Fig. 3 of M_{H_2} vs. $M_A = M_{H^\pm}$ treats them as independent variables, but (1) they are restricted to their ranges allowed by the sum rule Eq. (8) and (2) $\tan\beta$ is fixed at 0.5, approximately its largest value allowed by data. So, this figure allows a much wider range of masses to be probed by LHC data than does Fig. 2. There is a sizable fully excluded region in the lower right corner. Again, it is due to the conflict between the model and data on $\ell^+\ell^- + \mathrm{jets}$ and $\ell^\pm + \not{E}_T + \mathrm{jets}$. A sliver of this contains the masses consistent with $M_A = M_{H^\pm}$ and the sum rule, depicted in Fig. 1. It is shown as the purple band in this figure, whose lower edge is $M_{H'}$ and upper edge is M_{H_2}. The separation between the two masses above $M_A = 370\,\mathrm{GeV}$ accounts for the band's thickening at the high end. The excluded portion of the band corresponds exactly to the one in Fig. 2

3 Summary

In this report we described the Gildener-Weinberg mechanism which naturally accounts for and stabilizes the low mass of the Higgs boson H and its apparently SM couplings to fermions and gauge bosons. We illustrated the mechanism in the simple 2HDM proposed by Lee and Pilaftsis in 2012, just before the announcement of the discovery of $125\,\mathrm{GeV}$ Higgs at the LHC. In 2018, Lane and Shepherd modified this model with type-I Higgs couplings to fermions to make it consistent CMS and ATLAS searches for $H^\pm \to t\bar{b}$; they determined that $\tan\beta = v_2/v_1 \lesssim 0.5$ at $\leq 95\%$ C.L.

A remarkable feature of this GW-2HDM is the sum rule (8) limiting the masses of the new Higgs bosons $H^\pm$, A, and H_2 to be less than about $500\,\mathrm{GeV}$. Thus, searching for and finding — or excluding — these new Higgses at the LHC is far and away the best way to test GW models _in this decade_.

This paper is a start on that program. We outlined a simplified scheme for such searches, based on the sum rule and the equality, $M_{H^\pm} = M_A$, that makes the contribution to the T-

---

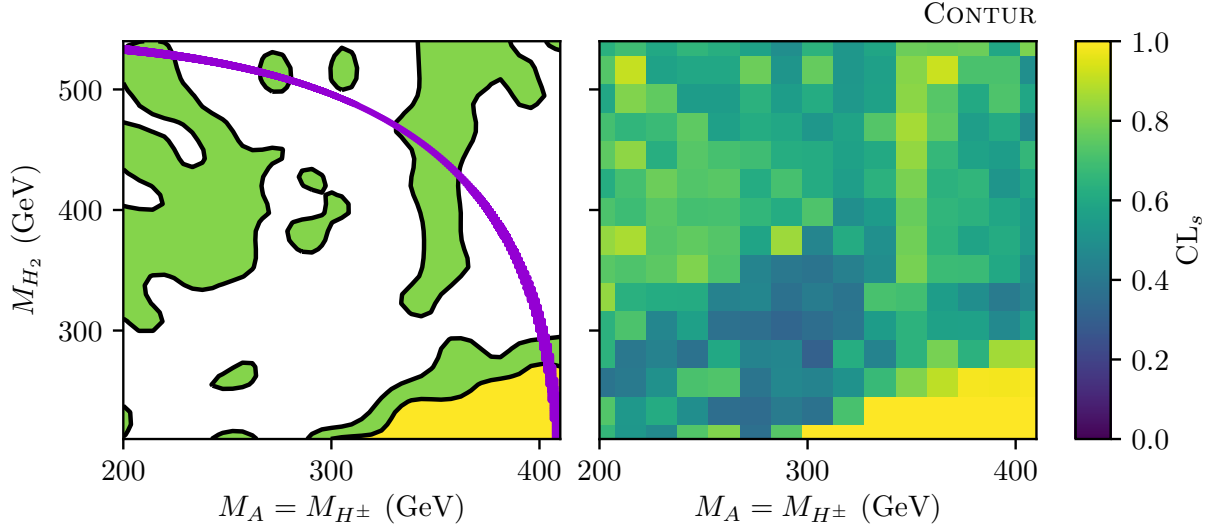[5]The endpoint $M_A = 410\,\mathrm{GeV}$ is the boundary of the sum rule (8) when $M_A = M_{H^\pm}$.

Figure 3: Left: Excluded regions in a plot of M_{H_2} vs. $M_A = M_{H\pm}$, treated as independent variables, for fixed $\tan\beta = 0.50$. The purple band shows the masses $M_{H'}$ (lower edge) and M_{H_2} (upper edge) determined by the sum rule (8) and the one-loop CP-even mass matrix in Fig. 1. The color scheme is as in Fig. 2. Right: The corresponding continuous scale of exclusions with 1.0 being fully excluded and 0.0 being zero sensitivity.

parameter from the new scalars vanish. And we put the GW-2HDM to a wide-ranging test using CONTUR to compare its major signals, Eqs. (9–11), with LHC measurements. This powerful tool did its job. It turned up the one instance that the GW-2HDM with $\tan\beta \simeq 0.5$ is in conflict with LHC data: For $M_A = M_{H\pm} \gtrsim 403\,\mathrm{GeV}$ and $M_{H_2} \lesssim 295\,\mathrm{GeV}$, the rates for $pp \to A \to ZH_2 \to \ell^+\ell^- b\bar{b}$ and $pp \to H^\pm \to W^\pm H_2 \to \ell^\pm \not{E}_T\, b\bar{b}$ exceed the measured rates of these final states at greater than the 95% C.L. for $\tan\beta > 0.3$.

Acknowledgments

Contribution 9

Sensitivity of LHC measurements to a two-Higgs-doublet plus pseudoscalar DM model

J. M. Butterworth, M. Habedank, P. Pani

1 Introduction

In this short contribution we use CONTUR [88] to examine the sensitivity of ATLAS, CMS and LHCb measurements available in RIVET 3.1 [87] to a Dark Matter model involving two Higgs doublets and an additional pseudoscalar mediator [185]. This model has been the subject of several searches at the LHC [186, 187] and in particular was studied using a combination of ATLAS searches, which we will compare with in the following.

We focus on two parameter scans, those of Fig. 19 in Reference [187], shown for convenience in Fig. 1. In these scans, which follow the recommendations of the LPCC DMWG [188], the masses of all the exotic Higgs bosons $(A, H, H^\pm)$ are set to be degenerate, the mass of the DM candidate $\chi = 10$ GeV, the coupling of the pseudoscalar mediator a to χ is unity, $\sin\theta = 0.35$ where θ is the mixing between the two neutral CP-odd weak eigenstates, and we set $\sin(\beta - \alpha)$, the sine of the difference of the mixing angles in the scalar potential containing only the Higgs doublets, to unity, meaning we are in the aligned limit so that the lightest mass eigenstate has SM Higgs couplings.
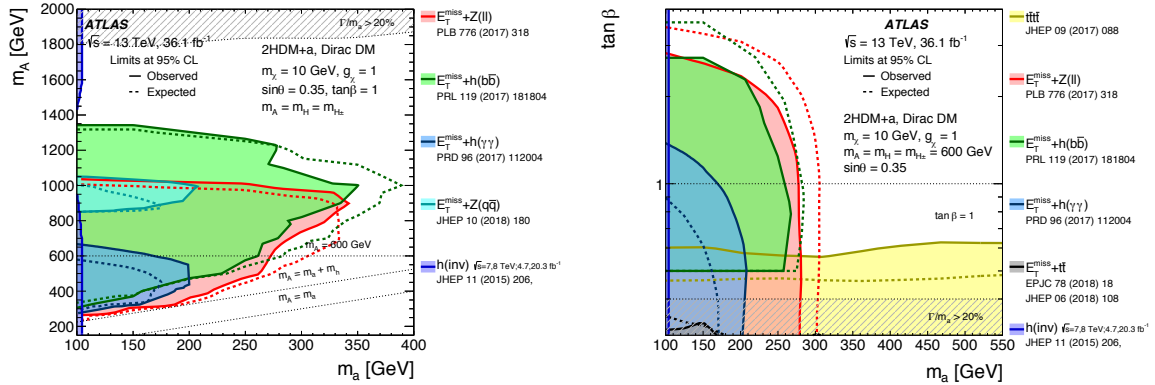

Figure 1: Figure 19 from Ref. [187], showing ATLAS exclusion limits from a combination of searches.

This model is characterised by a particularly rich phenomenology, dominated by the production of the lightest pseudoscalar or the heavier Higgs boson partners, via loop-induced gluon fusion, associated production with heavy-flavour quarks or associated production with a SM Higgs or Z boson. Very diverse characteristic signatures can be produced by various decay chains of these bosons. Many of these signatures remain largely unexplored.

For this reason, the use of CONTUR with its wide range of analysis signatures, coupled with the inclusive approach of Herwig in generating all processes leading to BSM particle pro-

duction, is of particular interest, as a contribution to a systematic identification of all signatures that can potentially constrain the model.

2 Results

We use CONTUR to scan over the same parameter plane as ATLAS, generating the BSM events with HERWIG [101] and looking for parameter points where an observably significant number of events would have entered the fiducial phase space of the measurements. The results are shown in Fig. 2 (see Section 18 of these proceedings for more detail on the CONTUR methodology).
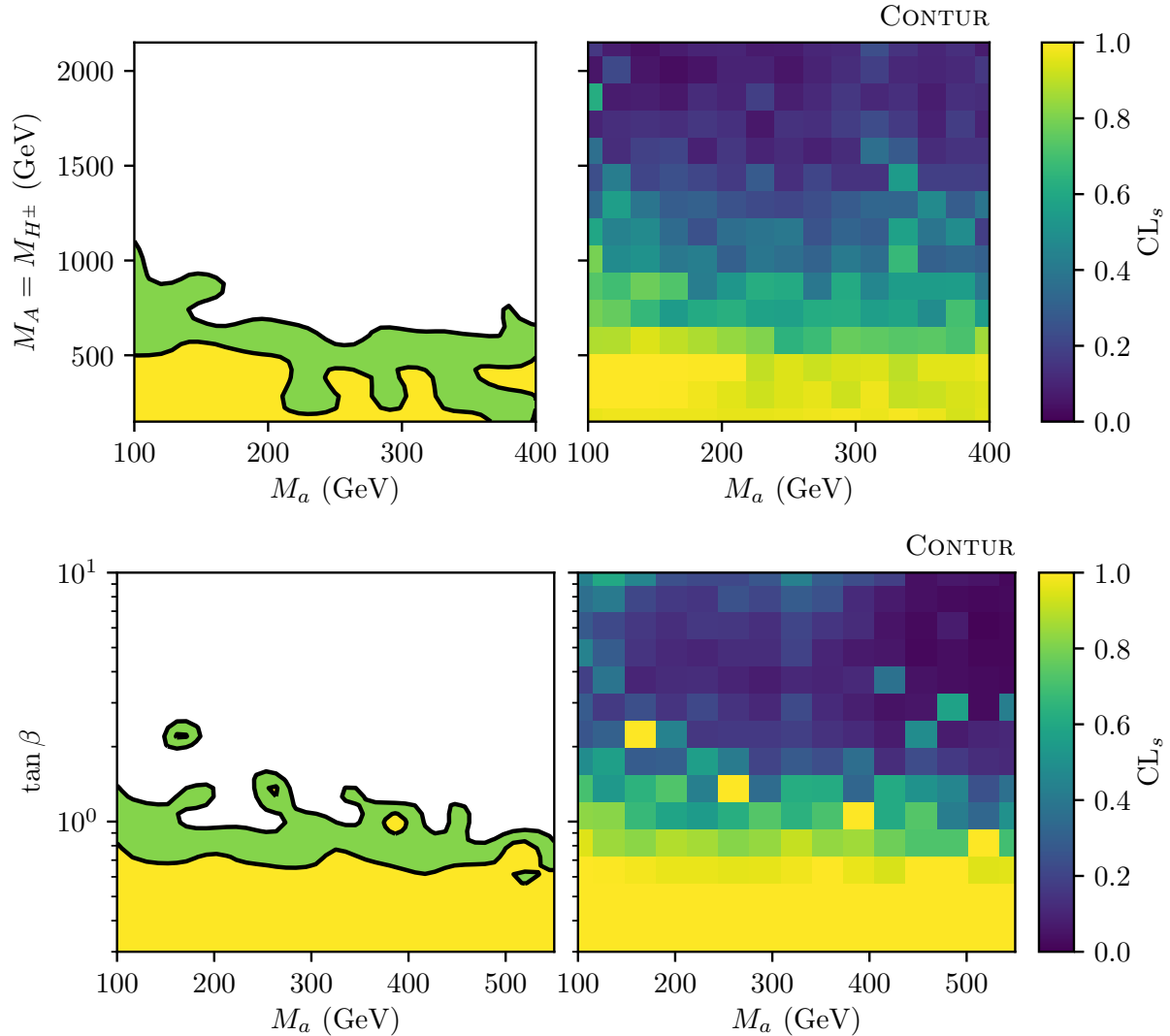

Figure 2: CONTUR scans over the parameter planes shown in Fig. 1 in the M_a–M_A (top) and M_a–$\tan\beta$ plane (bottom). Left: 95% (68%) excluded contours in yellow (green). Right: Underlying heatmap of exclusion at each investigated parameter space point.

The overall sensitivity is mostly the combined result of what would be 1-2 σ contributions to a wide range of cross-section measurements. Fig. 3 shows exemplary heatmaps of analyses contributing to the sensitivity in the M_a–M_A scan. Especially analyses involving W boson

production and leptonic decay (i.e. lepton-plus-missing-energy final states) contribute to the sensitivity. It generally arises from the production of all the exotic Higgs bosons, with subsequent decays either to top or directly to W bosons. For example for $m_A = m_H = m_{H^\pm} = 435$ GeV and $m_a = 250$ GeV, the production cross-section for the CP-odd Higgs boson A is about 6 pb and its dominant decay channels are in $t\bar{t}$ (85%) and $\chi\bar{\chi}$ (15%). In addition, the production cross section for the CP-even Higgs boson H is 3 pb, and it decays into a top-pair with a branching ratio of 88%, while the second dominant decay mode is $H \to aZ$ (10%). For lower pseudoscalar mediator masses as $m_a = 100$ GeV, the $H \to aZ$ branching ratio increases to 30% and this final state dominates the sensitivity to this model (Fig 3 left). All cross sections have been calculated with Herwig 7 [189,190] and with Madgraph5_aMC@NLO [19] and were found in good agreement.
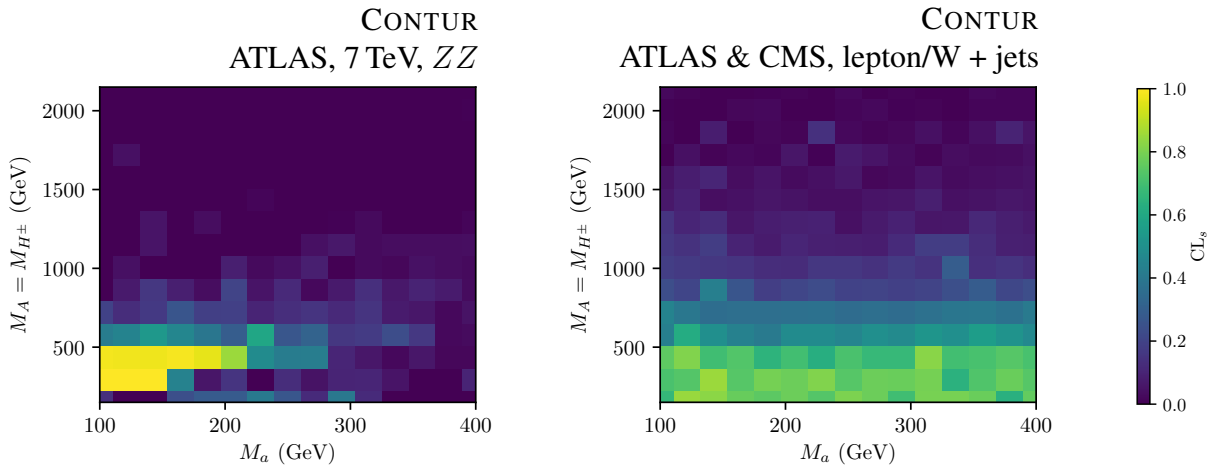

Figure 3: Heatmaps of exclusion at each considered parameter space point in the M_a–M_A plane for the ZZ measurement at $\sqrt{s} = 7\,\text{TeV}$ [191] by ATLAS (left) and the combination of various ATLAS and CMS analyses with signatures comprising a lepton or vector boson and jets [104, 105, 192, 193] (right) as used by CONTUR.

Because CONTUR takes the SM as being identical to the data, the absolute sensitivity should be treated with caution. In addition, correlated systematic uncertainties between different measurements are not accounted for, as the information is not provided by the experiments. Nevertheless, the conclusion that there is sensitivity in these final states, even with current data, is robust.

In passing we note that naively, there is apparent strong sensitivity in the $H \to WW$ fiducial cross section measurements. However, these measurements typically apply a b-jet veto, or use a b-jet control region, to suppress the large background from $t\bar{t}$. In the case of CMS [194], this is applied at detector level and is not included as part of the fiducial cross section definition (and thus not applied in the Rivet routine). Therefore, the analysis cannot be used here, as in reality many of our signal events would fail the veto, but we cannot evaluate how many. The same applies to the CMS W+jet measurements. In the case of ATLAS [195], the cross section is measured as a function of jet multiplicity and is consistently implemented in Rivet, so in principle the analysis could be used. However, there is a large data-driven background subtraction, and our signal would most likely contribute in both the control region and signal

region of the analysis, so simply counting the contribution to the signal region is likely to overestimate our sensitivity. For these reasons we also exclude the ATLAS measurement from the current study.

3 Conclusion

There is interesting sensitivity to the two-Higgs-doublet plus pseudoscalar DM model, across several measured final states, due to the quite complex phenomenology of the model. This phenomenology can change a lot when the parameters change, and a wider set of parameter scans would be of interest, relaxing some of the current assumptions imposed on the parameters.

Future searches for this model should also consider final states involving top and/or W production, even in the absence of a large missing energy signature.

Of course, the full run 2, coming run 3, and HL-LHC measurements can be expected to have a substantial impact. If future $H \rightarrow WW$ measurements can be made less model-dependent, they may also make a significant contribution.

Contribution 10

Looking for exotic Higgs decays via $h \rightarrow Za$

A. Bharucha, J. M. Butterworth, N. Desai, S. Gascon-Shotkin, S. Jain, A. Lesauvage, G. Moreau, S. Mutzel, J. M. No, J. Quevillon, C. Smith, K. Tobioka, N. Vignaroli, S. L. Williamson, J. Zurita

Abstract

We study the exotic decay of the 125 GeV Higgs boson into a Z boson and a light pseudoscalar a beyond the Standard Model, $h \rightarrow Za$. Such decay is well-motivated in a variety of new physics scenarios, ranging from axion-like particles to extended Higgs sectors. We analyse the LHC sensitivity to this Higgs decay mode in several decay modes $a \rightarrow xx$ of the light pseudoscalar, namely $xx = \gamma\gamma$, $\mu^+\mu^-$, $\tau^+\tau^-$. Besides deriving model-independent LHC sensitivity estimates on BR($h \rightarrow Za$) $\times$ BR($a \rightarrow xx$), we interpret our results in terms of axion-like particles with masses $m_a < 35$ GeV, showing that this search would provide a powerful window to discover such states at the LHC.

1 Introduction

Exploring the possible existence of exotic decays of the 125 GeV Higgs boson h constitutes a primary avenue to search for new physics beyond the Standard Model (SM) at the LHC (see [196] for a review). Current data from ATLAS and CMS measurements of Higgs signal strengths are compatible with the existence of a 125 GeV Higgs boson branching fraction into beyond the SM (BSM) states as large as $\mathcal{O}(20\%)$ [164]. Direct searches targeting specific BSM decay modes of the 125 GeV Higgs boson have the potential to probe much smaller branching fractions, and thus they may provide a unique window into new BSM light states.

In this work we focus on exotic decays of h into light pseudoscalars via $h \rightarrow Za$. Such decays arise naturally in well-motivated extensions of the SM, e.g. via the presence of axion-like particles (ALPs) [197–201] or in the context of non-minimal Higgs sectors featuring a light scalar/pseudoscalar [202–204]. Decays of the 125 GeV Higgs boson into a Z boson plus a BSM state may also occur in other SM extensions (e.g. $h \rightarrow ZZ_D$ with Z_D a hidden gauge boson, see [205–207]). The LHC potential to probe the decay $h \rightarrow Za$ has been recently highlighted by Bauer et al. in [199], considering a to be an ALP decaying to di-photon or di-electron final states. In this work we perform for the first time a detailed analysis of the LHC sensitivity to the exotic decay $h \rightarrow Za$ in the $Z \rightarrow \mu\mu$, $a \rightarrow \gamma\gamma$ final state, for which no present ATLAS or CMS search exists (although we note that this final state was measured in 8 TeV collisions [208], without a Higgs mass constraint). In addition, we consider the leptonic decays $a \rightarrow \mu\mu$ and $a \rightarrow \tau\tau$ and derive approximate limits on the corresponding branching fractions by reinterpreting existing ATLAS and CMS analyses. In all cases, we restrict ourselves to the mass range $m_a < 34$ GeV, for which the Higgs boson decays into two on-shell states. We derive limits on the branching fractions BR($h \rightarrow Za$) $\times$ BR($a \rightarrow \gamma\gamma$), BR($h \rightarrow Za$) $\times$ BR($a \rightarrow \mu\mu$) and BR($h \rightarrow Za$) $\times$ BR($a \rightarrow \tau\tau$) respectively in sections 2.1, 2.2 and 2.3, and in section 3

we interpret our results in terms of the ALP effective field theory (EFT) extension of the SM (see [198, 199] and references therein).

2 LHC searches for $h \to Za$

2.1 $a \to \gamma\gamma$

The decay of the state a into two photons provides a very clean final state in combination with the leptonic decay of the Z boson coming from the Higgs decay. Depending on the mass m_a of the light pseudoscalar state and on the event kinematics, the two photons may be resolved in the detector or appear as one reconstructed object (as noted in [199]), the latter occuring for strongly boosted ALPs. The minimal angular separation ΔR the two photons need to have to be resolved in the detector is dictated by the resolution of the Electromagnetic Calorimeter (ECAL) barrel and endcap: for CMS, individual crystals in the ECAL span $d\eta/d\phi \sim 0.0175$ for the barrel (for the endcap, this can be up to 0.05 depending on η), with most of the photon energy ($\sim 97\%$) captured by a 5×5 array of crystals [209, 210], spanning a $\Delta R \sim 5 \times 0.0175 \simeq 0.09$. As a result, for $\Delta R_{\gamma\gamma} < 0.1$ photon energy deposits in the CMS ECAL start overlapping and are likely to be reconstructed as one single photon. For converted photons, this $\Delta R_{\gamma\gamma}$ may be slightly larger. A similar minimal angular separation to resolve the two photons is found for ATLAS (see e.g. [211]). Below this angular separation, it is still viable to differentiate between single and multiple photons by means of shower-shape analyses [211], a possibility we do not discuss further here.
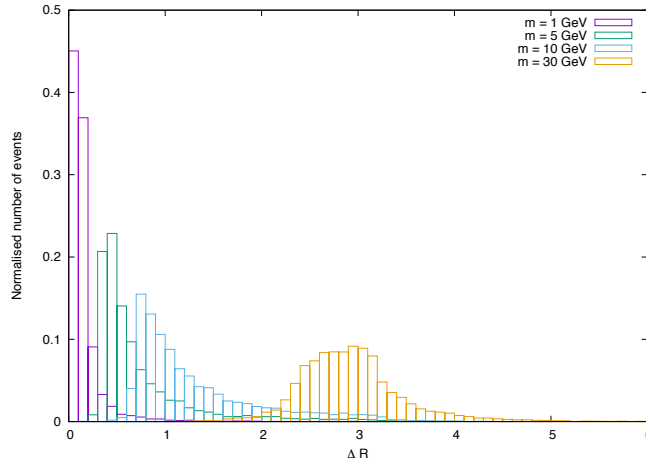

Figure 1: Kinematic event distribution for the $\Delta R_{\gamma\gamma}$ separation between the two photons in $pp \to h \to Za$, $a \to \gamma\gamma$ for various values of m_a.

We thus begin our analysis by studying the $\gamma\gamma$ angular separation for the process $pp \to h \to Za$ (the Higgs boson produced via gluon-fusion) at LHC 13 TeV, followed by the decay $a \to \gamma\gamma$, as a function of m_a. The $\Delta R_{\gamma\gamma}$ distribution is shown in Fig. 1 for masses in the range $m_a \in [1, 30]$ GeV. For $m_a \lesssim 1$ GeV, a very large fraction of the events has $\Delta R_{\gamma\gamma} < 0.1$, and thus would fail a resolved analysis. For $m_a \ll 1$ GeV it is safe to assume the two photons are reconstructed as one, and thus possible to reinterpret the current LHC 13 TeV upper bounds on the $h \to Z\gamma$ branching fraction [212,213] to yield a constraint $\mathrm{BR}(h \to Za) \times \mathrm{BR}(a \to \gamma\gamma) < 0.01$ at 95% C.L.[1]. Whether this limit can be extrapolated to masses close to and above 1 GeV

---

[1]We use here the ATLAS analysis [212] with 36.1 fb^{-1} of integrated luminosity.

strongly depends on the details of the ATLAS and CMS photon identification and reconstruction algorithms (see e.g. [214]). Here we simply consider the fraction of signal events that satisfy $\Delta R_{\gamma\gamma} < 0.1$ as a measure of the degrading of the limit for increasing m_a (e.g. for $m_a = 500$ MeV this fraction is 0.83, while it drops to 0.008 for $m_a = 2$ GeV).

Turning now to the analysis of $pp \to h \to Za$, $a \to \gamma\gamma$ with two resolved photons, we simulate the signal[2] at LHC 13 TeV with MADGRAPH_MC@NLO [19], PYTHIA 8.2 (parton showering and hadronization) [28] and DELPHES 3 (detector simulation) [154]. We adopt the N^{3}LO results from [215] for the single Higgs production cross section, which quotes a value of 48.58 pb for $\sigma(pp \to h)$ in gluon-fusion. For the photon isolation in DELPHES 3 we use a standard isolation cone $\Delta R = 0.5$, which we note causes a strong degrading of the signal efficiency for $m_a \lesssim 5$ GeV (as is apparent from Fig. 1 and the discussion above). We thus consider pseudoscalar masses in the range $m_a \in [5, 34]$ GeV. The event selection is performed as follows:

- We require two isolated photons with $p_T^\gamma > 10$ GeV and $|\eta_\gamma| < 2.5$, and two oppositely charged muons with $p_T^\mu > 10$ GeV and $|\eta_\mu| < 2.4$.

- The two muons must satisfy $m_{\mu\mu} \in [75, 105]$ GeV. Similarly, the combination of the two muons and two photons must reconstruct the Higgs boson mass, $m_{\mu\mu\gamma\gamma} \in [115, 135]$ GeV.

- The two photons must satisfy $m_{\gamma\gamma} + p_T^{\gamma\gamma} < m_h/2$. This condition is effective in suppressing the reducible $Z+$ jets SM background (see below), while maintaining a high efficiency for the signal for all m_a.

For events that pass the event selection, a signal region is defined in the $m_{\gamma\gamma}$ variable, where we look for an excess over the background in a ± 5 GeV mass window centered in the m_a mass hypothesis.

The main SM backgrounds are $pp \to \mu\mu\gamma\gamma$ (with an inclusive cross section at LHC 13 TeV of 0.109 pb) and the reducible, but very large $pp \to jj\mu\mu$ background coming dominantly from $Z+$ jets, with the two jets faking photons. We obtain the approximate $j \to \gamma$ fake rates in the detector barrel and endcap as a function of the jet p_T from [216] (see also [217])[3]. We then compute the expected number of 13 TeV LHC SM background and signal (for BR($h \to Za$) $\times$ BR($a \to \gamma\gamma$) $= 1$) events, with an integrated luminosity of 36.1 fb^{-1}, in the $m_{\gamma\gamma}$ signal region as a function of the m_a hypothesis. From these expectations, we derive the 95% C.L. expected exclusion sensitivity for BR($h \to Za$) $\times$ BR($a \to \gamma\gamma$) as a function of m_a from the present resolved di-photon analysis, using a simple likelihood ratio of signal + background and background only as the test statistic. The CLs method [218] is used to quote the 95% C.L. upper limits. The resulting (expected) limits are shown in Fig. 2. These limits however do not take into account any potential systematic uncertainties, particularly from our simulation of the reducible $Z+$ jets background and the lack of sufficient statistics in our Monte Carlo event sample given the very large cross section for this process, as well as from the $j \to \gamma$ fake rate (see above). As a result, our derived 95% C.L. exclusion sensitivity may be regarded as a first

---

[2]We use an in-house tune of the UFO model developed in [199].

[3]We stress that for low jet transverse momentum, $p_T \lesssim 30$ GeV, the uncertainty on the $j \to \gamma$ fake rate becomes rather large. Since this is precisely the most important kinematical region in our analysis (the two photons from the $a \to \gamma\gamma$ decay have fairly low p_T in general), the aforementioned uncertainty may somewhat degrade the sensitivity of the analysis. We leave a detailed investigation of this issue for future work.

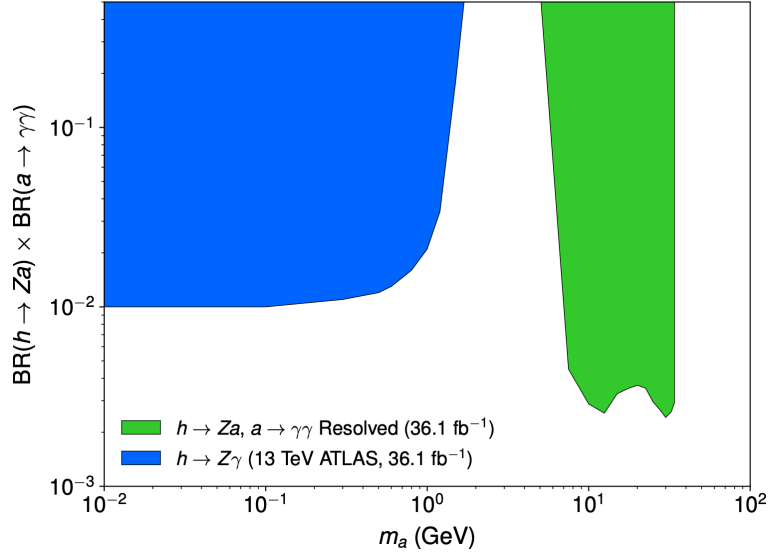approximation, until a more detailed analysis of the reducible SM backgrounds for this process is granted.

Figure 2: 95% C.L. upper limits for $\mathrm{BR}(h \to Za) \times \mathrm{BR}(a \to \gamma\gamma)$ in our resolved di-photon analysis (green) and via $h \to Z\gamma$ when the two photons are too collimated to be resolved by the detector (blue) at LHC 13 TeV with 36.1 fb^{-1}.

Fig. 2 also shows the expected 95% C.L. exclusion sensitivity on $\mathrm{BR}(h \to Za) \times \mathrm{BR}(a \to \gamma\gamma)$ as a function of m_a from the reinterpretation of the ATLAS $h \to Z\gamma$ analysis [212] (when the two photons are too collimated to be resolved by the detector). Altogether, we find that for $\mathrm{BR}(a \to \gamma\gamma) = 1$, values of the exotic Higgs branching fraction $\mathrm{BR}(h \to Za) \sim 0.01$ are probed with present LHC data for $m_a < 1$ GeV, whereas in the region of the resolved analysis, $10\,\mathrm{GeV} \lesssim m_a \lesssim 35$ GeV, the sensitivity approaches the per-mille level, reaching values $\mathrm{BR}(h \to Za) \sim 0.003$. We also emphasize that it would be possible to significantly close the gap between the $h \to Z\gamma$ limits and our resolved analysis, corresponding to masses $m_a \in [1, 10]$ GeV, by lowering the ΔR photon isolation cone used in our analysis down to $\Delta R \sim 0.2$, a study we leave for the future.

2.2 $a \to \mu\mu$

Contrary to the case of the previous section, for leptonic decays $a \to \ell\ell$ ($\ell = e, \mu$) there exist ATLAS and CMS searches that target the corresponding final state, and so it becomes possible to reinterpret existing LHC searches to obtain limits on $\mathrm{BR}(h \to Za) \times \mathrm{BR}(a \to \ell\ell)$. In this section we concentrate on the decay $a \to \mu\mu$. Among the suite of LHC searches targeting final states with four leptons, the ATLAS 13 TeV search for exotic Higgs decays via $h \to ZZ_D \to 4\ell$ (with Z_D a BSM gauge boson) [219] provides the most comprehensive coverage of our signal, having two key advantages w.r.t. other analyses: *(i)* the analysis considers both electrons and muons (as opposed to [220, 221] which employ only muons); *(ii)* the analysis requires a reconstructed Z boson together with a varying mass resonance, as opposed to other analyses which typically consider the decay of the Higgs boson to two resonances of the same mass (see e.g. [220]) and whose di-lepton invariant mass selection requirements discard our signal.

We then reinterpret in this work the ATLAS analysis [219] to derive the present LHC sensitivity to $pp \to h \to Za\,(Z \to \ell\ell, a \to \mu\mu)$. We have validated our analysis by first considering a parton level[4] sample of the largest SM background, $h \to ZZ^* \to 4\ell$, and comparing the acceptance of our Monte Carlo sample generated with MADGRAPH_MC@NLO with the m_{34} kinematical distribution published by ATLAS (Fig. 2 of [219]). The event selection requires

– Two pairs of same-flavour (SF), opposite-sign (OS) leptons, ℓ_i.

– $p_T(\ell_1, \ell_2, \ell_3) > 20, 15, 10$ GeV.

– $\Delta R(\ell, \ell') > 0.1\,(0.2)$ for SF (OF).

– 115 GeV $< m_{4\ell} < 130$ GeV.

– $m_{i,j} > 5$ GeV.

– 50 GeV $< m_{1,2} < 106$ GeV and 12 GeV $< m_{3,4} < 115$ GeV.

with $i, j = 1, 2, 3, 4$ indexing the leptons. After these cuts the ATLAS collaboration displays the m_{34} mass distribution (namely, the pair of leptons that do not reconstruct the Z mass) in the range $m_{34} \in [11, 59]$ GeV. In order to account for the detector effects not included in the parton level generation we have assumed a flat lepton reconstruction efficiency of ~ 0.9. The results of our validation are shown in the left panel of Fig. 3, and are in reasonable agreement with each other.

After validation, we proceed to derive the limits on $\mathrm{BR}(h \to Za) \times \mathrm{BR}(a \to \mu\mu)$ as a function of the pseudoscalar mass m_a. We use MADGRAPH_MC@NLO for the signal event generation (with the same UFO model as in section 2.1, and the same N^{3}LO value for the single Higgs production cross section from [215]). In order to derive a 95% C.L. exclusion for our model, we compare the 2σ upper limits quoted by ATLAS with our expected signal rate as a function of $\mathrm{BR}(h \to Za) \times \mathrm{BR}(a \to \mu\mu)$. For each mass point, we consider for this purpose the most constraining individual bin of the m_{34} distribution. The resulting LHC 13 TeV 95% C.L. exclusion for $\mathrm{BR}(h \to Za) \times \mathrm{BR}(a \to \mu\mu)$ with 36.1 fb^{-1} is shown in the right panel of Fig. 3 as a function of m_a. While this search can in principle provide sensitivity to masses $m_a > 35$ GeV (up to around 50 GeV) for an $h \to Z^*a$ decay, we concentrate here in the region $m_a < 35$ GeV for which the Higgs boson can decay into on-shell Z and a states.

---

[4]A full-fledged analysis including parton shower, hadronization and detector simulation is warranted, but outside of the scope of this work and will be presented elsewhere.
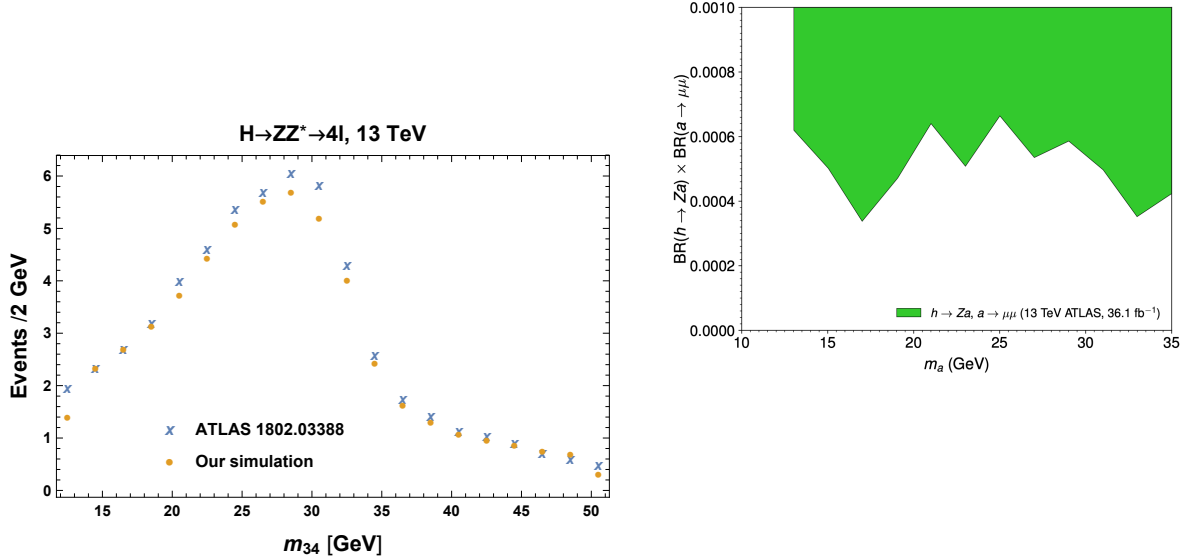
Figure 3: Left: Comparison of the reported $H \to ZZ^* \to 4\ell$ SM background distribution in the m_{34} variables of the ATLAS collaboration (orange circles) versus our simulation with a flat 0.9 lepton reconstruction efficiency (blue crosses), for the 13 TeV ATLAS analysis [219]. Right: 95% C.L. excluded values of $\mathrm{BR}(h \to Za) \times \mathrm{BR}(a \to \mu\mu)$ as a function of m_a.

2.3 $a \to \tau\tau$

As in section 2.2 for the $a \to \mu\mu$ decay mode, existing 8 TeV and 13 TeV ATLAS and CMS searches may be used to probe the $pp \to h \to Za$ ($Z \to \mu\mu$, $a \to \tau\tau$) signature at the LHC. However, for the $\mu\mu\tau\tau$ final state all the available searches target the decay $h \to aa \to \mu\mu\tau\tau$ [222–224], whereas in our case the invariant masses for the di-muon and the di-tau systems will be rather different for on-shell decays $h \to Za$. In particular, the 8 TeV ATLAS analysis [224] requires a reconstructed di-muon mass $m_{\mu\mu} \in [2.8, 70]$ GeV, and the 13 TeV CMS analysis [223] requires a reconstructed di-muon mass $m_{\mu\mu} \in [14, 64]$ GeV. Thus, both analyses discard[5] our signal events $h \to Z(\to \mu\mu)\, a$.

Fortunately, the signal event selection from the 8 TeV CMS search [222] for $h \to aa \to \mu\mu\tau\tau$ events provides coverage to pseudoscalar masses in the approximate range $m_a \in [18, 34]$ GeV for our $h \to Za$ signal. The CMS analysis is divided according to the various decay modes of the τ leptons: leptonic (into an electron, τ_e, or a muon, τ_μ) or hadronic (τ_h), with the following final states considered: $\mu\mu\, \tau_e\tau_e$, $\mu\mu\, \tau_e\tau_\mu$, $\mu\mu\, \tau_e\tau_h$, $\mu\mu\, \tau_\mu\tau_h$ and $\mu\mu\, \tau_h\tau_h$. The two reconstructed muons are required to satisfy $|\eta| < 2.4$ and $p_T > 18$ GeV ($p_T > 9$ GeV)[6] for the leading (subleading) muon, together with certain isolation criteria. For the tau leptons,

---

[5]These searches may nevertheless be sensitive to $h \to Z^*(\to \mu\mu)\, a$, for $m_a \gtrsim 50$ GeV. We defer a study of this region of parameter space for the future.

[6]For the $\mu\mu\, \tau_\mu\tau_e$ and $\mu\mu\, \tau_\mu\tau_h$ final states, the subleading muon from the $a \to \mu\mu$ decay may be selected with $p_T > 5$ GeV provided that the muon from the τ decay satisfies $p_T > 9$ GeV, in order for the event to be triggered upon.

a reconstructed τ_e is required to satisfy $|\eta| < 2.5$ and $p_T > 7$ GeV, a reconstructed τ_μ is required to satisfy $|\eta| < 2.4$ and $p_T > 5$ GeV (see however footnote 8) and a reconstructed τ_h is required to satisfy $|\eta| < 2.3$ and $p_T > 15$ GeV. In all cases, there are further isolation and reconstruction criteria which must be satisfied (see [222] for details). In addition, the distance between any pair of leptons in the event is required to be $\Delta R_{\ell\ell} > 0.4$, and the reconstructed invariant masses for the $\mu\mu$, $\tau\tau$ and $\mu\mu\tau\tau$ systems need to satisfy $|m_{\mu\mu\tau\tau} - 125\,\text{GeV}| < 25\,\text{GeV}$ and $|m_{\mu\mu} - m_{\tau\tau}|/m_{\mu\mu} < 0.8$. Under the assumption of perfect $m_{\mu\mu}$ and $m_{\tau\tau}$ reconstruction for our $h \to Za \to \mu\mu\tau\tau$ signal, satisfying the latter cut would require $m_{\tau\tau} = m_a > 18$ GeV (since $m_{\mu\mu} = m_Z = 91$ GeV). Due to the presence of neutrinos in the decay of the τ-leptons, the invariant mass reconstruction for di-tau resonances generally involves the use of likelihood algorithms [225, 226]. From the public information of the performance of these methods in the reconstruction of SM Higgs and Z bosons in $h \to \tau\tau$ and $Z \to \tau\tau$ decays [225], we assume here that $m_{\tau\tau}$ and $m_{\ell\ell\tau\tau}$ are smeared compared to their true values with a Gaussian with RMS width $\sigma = 0.15\,m_a$ (incidentally, this makes the analysis sensitive to pseudoscalar masses slightly below 18 GeV).

We perform a validation of our analysis by generating $pp \to h \to aa \to \mu\mu\tau\tau$ signal events with MADGRAPH_MC@NLO and PYTHIA 8.2 for the two mass points $m_a = 20$ GeV and $m_a = 60$ GeV detailed in the CMS analysis [222], obtaining the expected number of signal events in each of the possible di-tau decay modes considered: $\tau_e\tau_e$, $\tau_e\tau_\mu$, $\tau_e\tau_h$ $\tau_\mu\tau_h$ and $\tau_h\tau_h$. Our results tend to overestimate the number of expected events for categories including τ_e (by a factor $\sim 1.5-2$), and particularly τ_h, while for categories with τ_μ we agree better with the CMS expected number of signal events (or slightly underestimate it). We then define a fudge factor (which we define for each category from a linear interpolation between our validation results for $m_a = 20$ GeV and $m_a = 60$ GeV) to approximately account for the mismatch between the CMS expected number of signal events and ours (typically larger) due to features of the CMS selection which we do not capture, such as particle isolation and the precise performance of the $m_{\tau\tau}$ reconstruction algorithm at low invariant masses.

We then generate 8 TeV LHC signal events for $pp \to h \to Z(\to \mu\mu)a$, $a \to \tau\tau$ with MADGRAPH_MC@NLO and PYTHIA 8.2 in the mass range $m_a \in [15, 33]$ GeV, and compute the expected number of events after selection (for $\text{BR}(h \to Za) \times \text{BR}(a \to \tau\tau) = 1$) with an integrated luminosity of 19.7 fb^{-1}. From these expectations, we derive the 95% C.L. exclusion sensitivity on $\text{BR}(h \to Za) \times \text{BR}(a \to \tau\tau)$ as a function of m_a using the same likelihood method as in section 2.1. The resulting limits are shown in Fig. 4 for each of the five search categories, as well as the combined limit.

3 Model interpretation: Axion-like particles

While the previous LHC sensitivity studies of the exotic Higgs boson decay $h \to Za$ ($a \to \gamma\gamma, \ell\ell$) are model independent, it is also useful to cast the results into specific, well-motivated BSM theories. This also allows to explore the complementarity with other probes of the parameter space of such theories, an aspect we leave for a future study. In this work we consider the EFT for the SM extended by an axion-like particle, a [197–199, 201]. This ALP extension is inspired by axion models which aim, amongst other potential motivations, to solve the strong CP problem, and at the same time provides a flexible phenomenological framework to interpret the constraints from the LHC.

In full generality, ALPs are assumed to couple both to SM gauge bosons and fermions.
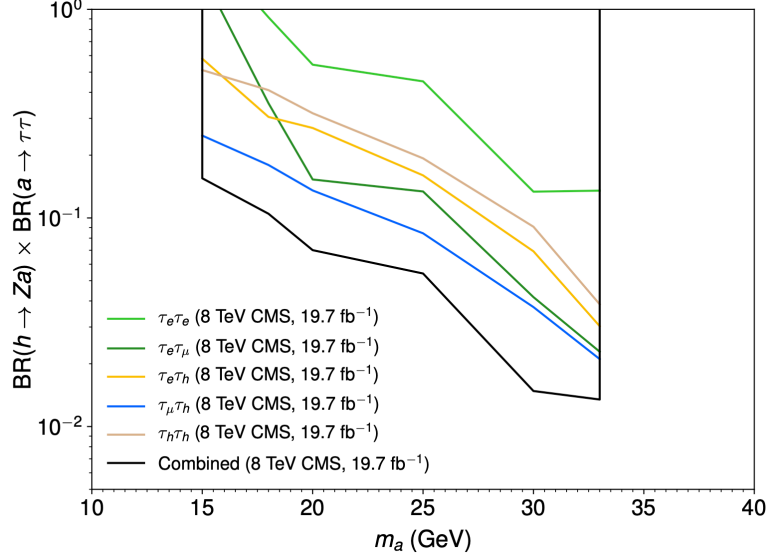
Figure 4: 95% C.L. excluded values of $\mathrm{BR}(h \rightarrow Za) \times \mathrm{BR}(a \rightarrow \tau\tau)$ as a function of m_a from the reinterpretation of the 8 TeV CMS analysis [222]. We show separately the limits from the $\mu\mu\,\tau_e\tau_e$ (light green), $\mu\mu\,\tau_e\tau_\mu$ (dark green), $\mu\mu\,\tau_e\tau_h$ (yellow), $\mu\mu\,\tau_\mu\tau_h$ (blue) and $\mu\mu\,\tau_h\tau_h$ (brown), as well as the combination (black).

Only including terms up to dimension-5 in a linear EFT expansion, we therefore modify the SM Lagrangian as follows:

$$\mathcal{L}_{\mathrm{eff}}^{d \leq 5} \supset \mathcal{L}_{\mathrm{SM}} + \frac{1}{2}\partial_\mu a \partial^\mu a - \frac{1}{2}m_a^2 a^2 + \sum_f \frac{m_f}{\Lambda}C_f\, a\bar{f}\gamma_5 f - \frac{e^2}{4\Lambda}\,C_\gamma\, a\, F_{\mu\nu}\tilde{F}_{\mu\nu}. \tag{1}$$

where the coupling of the ALP to the photon is given by C_γ and the coupling to the fermion f (of mass m_f) is given by C_f. The ALP could couple to the other gauge bosons (see e.g. the discussion in [227]) but this is not relevant to our analysis. Note that in this Lagrangian the ALP couplings to the Higgs boson are not present. In the linear EFT expansion, the dimension-5 coupling of the Higgs boson h to a Z boson and the ALP vanishes [197–199], as the operator can be rewritten in terms of the ALP-fermion operators using the equations of motion. There are

two possible sources[7] for the decay $h \to Za$. The first is from higher-dimensional terms, which can be incorporated in a straightforward way by including the following effective interaction in our Lagrangian:

$$\mathcal{L}_{\text{eff}}^{d=7} \supset \frac{1}{\Lambda^3} C_{Zh}^{(7)} (\partial^\mu a) \left(\phi^\dagger i \overset{\leftrightarrow}{D}_\mu \phi + \text{h.c.} \right) \phi^\dagger \phi + \dots , \tag{2}$$

where $C_{Zh}^{(7)}$ is the effective coupling between the ALP and the Higgs and Z bosons [200]. The second source of this coupling is loop effects, notably from the top quark, as detailed in Ref. [200]. The full effective coupling between the Higgs, the Z boson and the ALP can then be written as:

$$C_{Zh}^{\text{eff}} = -\frac{N_c y_t^2}{8\pi^2} T_3^t C_t F + \frac{v^2}{2\Lambda^2} C_{Zh}^{(7)} . \tag{3}$$

where F is defined in Ref. [200] via

$$F = \int_0^1 d[xyz] \frac{2m_t^2 - x m_h^2 - z m_Z^2}{m_t^2 - xy m_h^2 - yz m_Z^2 - xz m_a^2} , \tag{4}$$

using the abbreviation $d[xyz] \equiv dx\, dy\, dz\, \delta(1 - x - y - z)$. Note that the numerical size of the coefficients of C_t and $C_{Zh}^{(7)}$ is comparable for an EFT cut-off scale $\Lambda = 1$ TeV. In terms of this effective coupling C_{Zh}^{eff}, the Higgs partial decay width into Za, for $m_a < m_h - m_Z$, can be expressed as

$$\Gamma_{h \to Za} = \frac{m_h^3}{16\pi \Lambda^2} \left| C_{Zh}^{\text{eff}} \right|^2 \lambda^{3/2} \left(\frac{m_Z^2}{m_h^2}, \frac{m_a^2}{m_h^2} \right) . \tag{5}$$

with $\lambda(x,y) = (1 - x - y)^2 - 4xy$.

Having established the expression for the decay width of $h \to Za$, we now determine the different possibilities for the decay of the ALP in this model. As we are focusing on ALPs below the electroweak scale (in fact, lighter than the Z boson), clearly ALP decays into (on-shell) massive electroweak bosons are not possible, leaving fermion pairs, photons and gluons as potential decay signatures. In the following we define two model benchmarks for which we analyse the LHC sensitivity discussed in the previous sections. In the first, we neglect the ALP-fermion couplings, setting $C_f = 0$. In the second, we choose the opposite situation where all the ALP coupling to photons vanishes ($C_\gamma = 0$), and consider *i)* all C_f to be equal and *ii)* only C_μ or C_τ to be non-zero.

3.1 $C_f = 0$

In such a case, the decay rate of the ALP into photons is given by [200]

$$\Gamma(a \to \gamma\gamma) = \frac{4\pi \alpha^2 m_a^3}{\Lambda^2} \left| C_\gamma \right|^2 . \tag{6}$$

For this benchmark point, in the kinematic range that we are considering, the branching fraction to photons will be 100%. Therefore limits on the $h \to Za \to \gamma\gamma$ final state will provide a bound on the Wilson coefficient $C_{Zh}^{\text{eff}} (= v^2/(2\Lambda^2) C_{Zh}^{(7)})$. Note that we do not make any assumption about C_γ other than that it is sufficiently large that the ALP decays within the detector. The

---

[7]This is so in the context of a linear EFT that we are considering here. For a *chiral* EFT expansion the ALP-h-Z coupling is present at the lowest (leading) order in the expansion, see [198] for details.

results are presented in Fig. 5. We find that the exclusion on C_{Zh}^{eff} goes down to $\sim 10^{-1}$ for small values of m_a where the photons are unresolved, and down to $\sim 5 \cdot 10^{-2}$ at $m_a = 10$ GeV for the case that the photons are resolved, assuming that $\Lambda = 1$ TeV. Note that the difference from Ref. [200] in the blue region corresponding to the limits from $h \to Z\gamma$ arises due to the fact that we allow C_γ to vary such that the ALP always decays within the detector.
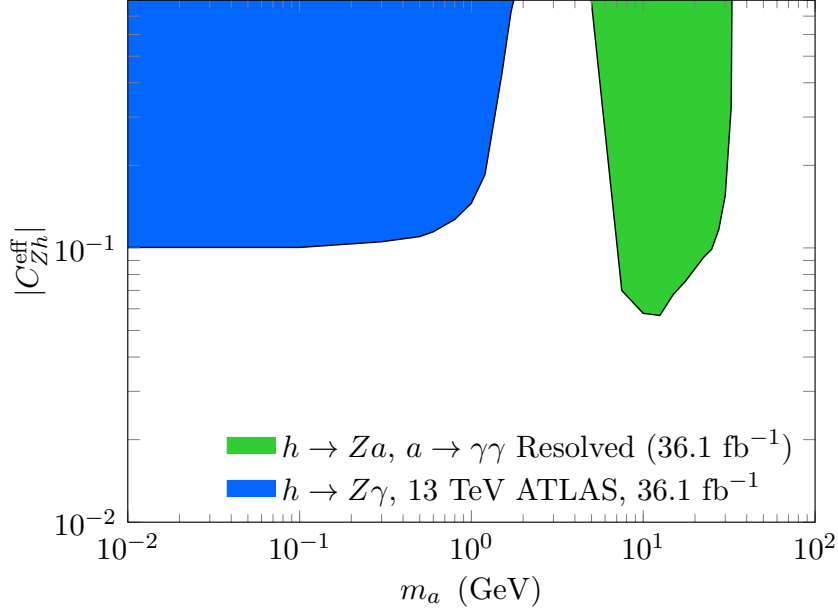

Figure 5: 95% C.L. upper limits on the Wilson coefficient $|C_{Zh}^{\text{eff}}|$ for $C_f = 0$ from bounds on BR($h \to Za$) $\times$ BR($a \to \gamma\gamma$) where the photons are resolved (green) and from bounds on $h \to Z\gamma$ when the two photons are too collimated to be resolved by the detector (blue) at LHC 13 TeV with 36.1 fb^{-1}. We have assumed that the ALP does not couple to fermions, and $\Lambda = 1$ TeV.

3.2 $\; C_\gamma = 0$

The second benchmark point is the case where all couplings to gauge bosons vanish. In this case, the decay rate into charged leptons is given by [200]

$$\Gamma(a \to \ell^+\ell^-) = \frac{m_a m_\ell^2}{8\pi\Lambda^2} \left|C_\ell^{\text{eff}}\right|^2 \sqrt{1 - \frac{4m_\ell^2}{m_a^2}}\,. \tag{7}$$

We consider two possibilities: a) the case where all C_f are equal and b) the case where only the muon or tau lepton coupling is present, and all other fermion couplings to the ALP vanish. In scenario a), for the $h \to Za$ decay we assume that $C_{Zh}^{(7)} = 0$, and that this decay is mediated by the top loop. For the ALP decay, in order to calculate the branching fraction several decay modes need to be accounted for, i.e. decays into hadrons and into heavy quarks. The necessary decay rates are [200]:

$$\Gamma(a \to \text{hadrons}) = \frac{\alpha_s^2(m_a) n_q^2 m_a^3}{32\pi^3\Lambda^2} \left[1 + \left(\frac{97}{4} - \frac{7n_q}{6}\right)\frac{\alpha_s(m_a)}{\pi}\right] |C_f|^2, \tag{8}$$

$$\Gamma(a \to Q\bar{Q}) = \frac{3m_a \overline{m}_Q^2(m_a)}{8\pi\Lambda^2} \sqrt{1 - \frac{4m_Q^2}{m_a^2}}\; |C_f|^2\,, \tag{9}$$

98

Figure 6: 95% C.L. upper limits on: the Wilson coefficient C_f assuming a universal coupling of the ALP to fermions and that $C_{Zh}^{(7)} = 0$ (left); the Wilson coefficient $|C_{Zh}^{\text{eff}}|$ assuming that the ALP decays 100% to muons (right). These limits are taken from the bounds obtained in Sec. 2.2 on $\mathrm{BR}(h \to Za) \times \mathrm{BR}(a \to \mu\mu)$ in the case that $C_\gamma = 0$, assuming $\Lambda = 1$ TeV.
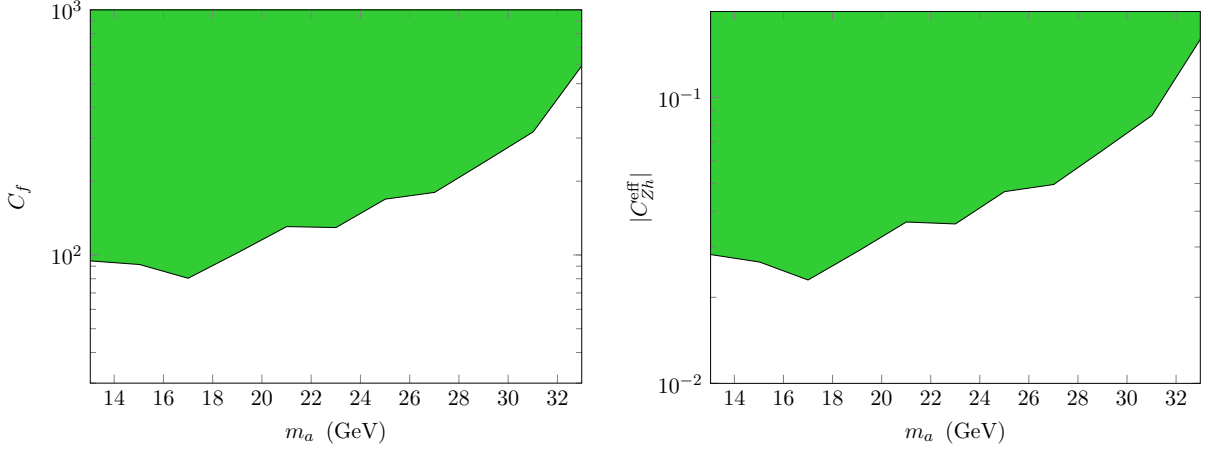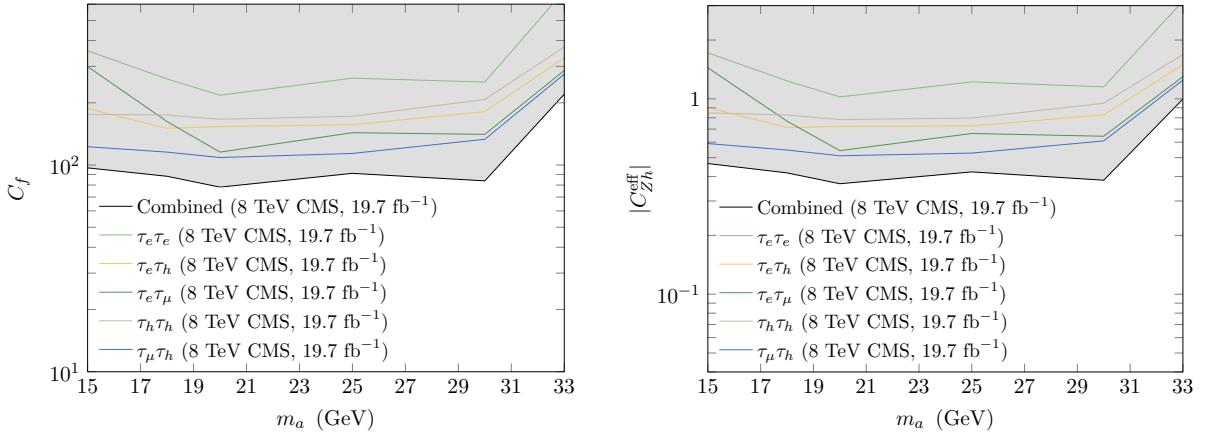

Figure 7: 95% C.L. upper limits on: the Wilson coefficient C_f assuming a universal coupling of the ALP to fermions and that $C_{Zh}^{(7)} = 0$ (left); the Wilson coefficient $|C_{Zh}^{\text{eff}}|$ assuming that the ALP decays 100% to tau leptons (right). These limits are taken from the bounds obtained in Sec. 2.3 on $\mathrm{BR}(h \to Za) \times \mathrm{BR}(a \to \tau\tau)$ in the case that $C_\gamma = 0$, assuming $\Lambda = 1$ TeV.

where the number of light quarks, n_q, is equal to 3 and $\overline{m}_Q$ is the MS-bar mass of the heavy quark Q. In scenario b), we assume that the contribution of C_{Zh}^{eff} to the $h \to Za$ decay width dominates, and that the branching ratio of the ALP to muons or taus is 100% respectively. Again we do not make any assumption about the size of C_μ or C_τ beyond that it is large enough such that the ALP decays within the detector. The results are presented in Fig. 6 and in Fig. 7. We see that for the case a) the lowest bound on C_f in the $\sim 15 - 30$ GeV region is ~ 80 for both the muon and tau lepton searches, when $\Lambda = 1$ TeV. In the case b) the constraint on C_{Zh}^{eff} from the muon final state ($\sim 2 \cdot 10^{-2}$) is stronger than that from tau leptons ($\sim 4 \cdot 10^{-1}$). Clearly very large values of the coupling C_f or conversely low scales are still allowed.

4 Conclusions

In this contribution, we have considered the exotic decay of the 125 GeV Higgs boson h into a Z boson and a BSM pseudoscalar state a. This Higgs decay mode may occur in many BSM scenarios, such as axion-like particle extensions of the SM or theories with non-minimal Higgs sectors. The corresponding branching fraction of the Higgs is currently allowed at the $\mathcal{O}(20\%)$ level by LHC measurements of Higgs signal strengths, and could be probed much more efficiently via dedicated searches. Here we study specific final states where the pseudoscalar a decays into photons, muons or τ-leptons. In the former, we perform an analysis of the 13 TeV LHC sensitivity with 36.1 fb^{-1} integrated luminosity, in the mass range $m_a \in [5, 34]$ GeV, where the two photons from the $a \to \gamma\gamma$ decay are isolated/resolved. In this region we reach a sensitivity to BR$(h \to Za) \times$ BR$(a \to \gamma\gamma) \sim 0.003$. Using ATLAS searches for the $h \to Z\gamma$ Higgs decay mode we also derive limits for pseudoscalar states lighter that 1 GeV, when the two photons are very collimated and appear as one in the detector, constraining in this case BR$(h \to Za) \times$ BR$(a \to \gamma\gamma) \sim 0.01$.

For the leptonic decays of a we reinterpret existing ATLAS and CMS searches: to probe the $a \to \mu\mu$ decay mode, we use the 13 TeV ATLAS search (with 36.1 fb^{-1} integrated luminosity) for exotic Higgs decays into four leptons via $h \to ZZ_D$ [219], constraining values of BR$(h \to Za) \times$ BR$(a \to \mu\mu)$ in the range $\sim (4-6) \times 10^{-4}$ for $m_a \in [10, 35]$ GeV. For the $a \to \tau\tau$ decay mode, despite the existence of 13 TeV LHC searches targeting the decay mode $h \to \mu\mu\tau\tau$, these are not sensitive to the kinematic region of our $h \to Za$, $Z \to \mu\mu \, a \to \tau\tau$ signal. However, we find the 8 TeV CMS search for exotic Higgs decays $h \to aa \to \mu\mu\tau\tau$ with 19.7 fb^{-1} integrated luminosity [222] provides sensitivity to our signal in the mass range $m_a \in [15, 33]$ GeV, reaching values BR$(h \to Za) \times$ BR$(a \to \tau\tau) \sim 0.02$ in the upper end of that mass range.

Finally, we cast our limits into the linear EFT extension of the SM by an axion-like particle, considering two simple benchmarks where respectively the coupling of the ALP to SM fermions C_f or to photons C_γ vanishes. In the former, the $a \to \gamma\gamma$ search from section 2.1 would allow values of $C_{Zh}^{\text{eff}} \lesssim 0.1$ TeV^{-1} to be probed with 36.1 fb^{-1} of LHC 13 TeV data. In the latter, existing ATLAS and CMS analyses are sensitive to $C_{Zh}^{\text{eff}} \lesssim 0.03$ TeV^{-1} (0.4 TeV^{-1}) when the decay $a \to \mu\mu$ ($a \to \tau\tau$) is the dominant ALP decay mode. These searches also allow the ALP-fermion coupling C_f to be probed when it is universal (all SM fermions having the same C_f) and responsible for the decay $h \to Za$ via loop effects.

Acknowledgements

id: 084011- 550- 042584).

Contribution 11

Extra Scalar Boson Searches at the LHC through Vector Boson Fusion

S. Fichet, S. Gascon-Shotkin, A. Lesauvage, G. Moreau

Abstract

Extra scalar bosons predicted in several scenarios beyond the Standard Model (SM) might have been missed so far by the present experimental searches based on the Large Hadron Collider (LHC) data. We study the Vector Boson Fusion (VBF) mode of production of a such a scalar which has the generic possibility to be comparable in rate with the main gluon-gluon Fusion (ggF) mechanism. The VBF presents a different final state from the ggF, with two additional jets that can optimise the sensitivity reach of the signal and prove to be particularly helpful for the tagging of final state when the diphotons from the decays of a too light scalar field do not allow an efficient triggering. We show that the VBF productions of generic neutral CP-odd or CP-even scalar fields exhibit specific kinematical distributions which could indeed allow to distinguish between their signatures at LHC and the SM background. In order to reach this conclusion, we have used a theoretical framework based on an effective field theory including various types of interactions, and, run Monte Carlo simulations for the signal and background in order to confront them with each other.

1 Introduction

Many extensions of the Standard Model (SM) of elementary particle physics include an electrically neutral scalar boson in their field content with a mass below a hundred GeV: light Higgs bosons, the radion, the dilaton, the axion... Although in 2012 the Large Hadron Collider (LHC) discovered a particle compatible with the SM Higgs boson as a 125 GeV resonance, one should thus consider the possibility that some lighter or heavier scalar particles might have been missed so far in the LHC data analyses.

Regarding the SM Higgs boson rates, the second production mechanism at a proton beam machine of 14 TeV – after the gluon-gluon Fusion (ggF) – is the Vector Boson Fusion (VBF), over an hypothetical mass range between 100 GeV and 1 TeV. Hence one could expect that the VBF is crucial as well for an extra (pseudo)scalar field production. Furthermore, depending on the scenario where the scalar field is arising, the photon contribution to the VBF might be competitive with the Z^0 and $W^\pm$ boson exchanges since both the extra scalar couplings to the photons and to the ElectroWeak (EW) fields $[Z^0, W^\pm]$ might appear at the tree-level [1] – in contrast with the Higgs boson interaction configuration. Such a new contribution tends to increase

---

[1] See for instance Ref. [228, 229] for the radion field of warped extra dimensions.

the VBF cross section relatively to the ggF one. Moreover, there is the generic possibility that the new scalar coupling to the top quark is reduced compared to the corresponding Yukawa interaction so that the VBF amplitude would be enhanced with respect to the ggF one.

For establishing the LHC potential reach for VBF productions of generic neutral CP-odd/even (under the combined Charge Parity symmetry) scalar fields in an effective parameter space, one has to find selective kinematical cuts possibly taking possibly benefit of the two characteristic VBF jets of the final state, in particular for scalar boson masses below typically ~ 65 GeV where the golden scalar decay into a pair of on-shell Z bosons is kinematically closed while their decay into diphoton is extremely difficult to detect experimentally (as the LHC diphoton triggers are bandwidth-limited for such soft photon productions) [2].

For this purpose we have performed Monte Carlo simulations of the events for the signal, using the `Feynrules` code [29], and the SM Background, with `MadGraph5_aMC@NLO` [43] interfaced with `Pythia8` [230] for hadronisation as well as `FastJet` [153, 231] and `Delphes` [154] for detector reconstruction.

2 The effective model

Diagrammatically, the studied scalar boson production via VBF occurs through the double radiation off quarks of photons or electroweak gauge bosons then merging to create the new scalar field. Hence, these processes involve only the new scalar coupling to two photons γ, two Z^0 bosons or two $W^\pm$ bosons. We use an effective theory approach to describe the scalar interaction with SM EW gauge bosons. The scalar mass can be smaller than the EW symmetry breaking scale. When it is the case, we make the extra assumption that the scalar has large tree-level $SU(2)_L \times U(1)_Y$ couplings, so that the loop-induced EW breaking contributions are subleading. Under this condition, the interactions of a neutral CP-even or CP-odd scalar ϕ with the EW gauge bosons are respectively described by the following dimension-5 effective gauge invariant Lagrangians

$$\mathcal{L}_{\text{eff}} \supset \phi \left(\frac{1}{f_G} G^{\mu\nu\,a} G^a_{\mu\nu} + \frac{1}{f_W} W^{\mu\nu\,b} W^b_{\mu\nu} + \frac{1}{f_B} B^{\mu\nu} B_{\mu\nu} + \frac{1}{f_H} |D^\mu H|^2 \right) \tag{1}$$

$$\mathcal{L}_{\text{eff}} \supset \phi \left(\frac{1}{\tilde{f}_G} G^{\mu\nu\,a} \tilde{G}^a_{\mu\nu} + \frac{1}{\tilde{f}_W} W^{\mu\nu\,b} \tilde{W}^b_{\mu\nu} + \frac{1}{\tilde{f}_B} B^{\mu\nu} \tilde{B}_{\mu\nu} \right) \tag{2}$$

where $\tilde{V}^{\mu\nu} = \frac{1}{2}\epsilon^{\mu\nu\rho\sigma}V_{\rho\sigma}$, H represents the SM Higgs doublet, D^μ the covariant derivative, the f's denote high-energy scales of new physics, a, b are summed group generator indices whereas μ, ν stand for summed Lorentz indices and the rank-2 tensors are the field strengths for all the SM gauge bosons before EW symmetry breaking (using standard notations). After this breaking, the effective Lagrangian, for example in the CP-even case, contains the ϕZZ interactions

$$\mathcal{L}_{\text{eff}} \supset \frac{1}{f_Z} \phi (Z_{\mu\nu})^2 + \frac{m_Z^2}{2f_H} \phi (Z_\mu)^2 \,, \tag{3}$$

where $f_Z^{-1} = s_w^2 f_B^{-1} + c_w^2 f_W^{-1}$ and $s_w^2 \equiv \sin^2(\theta_w) \approx 0.23$. The effective theory is valid as long as the f's (related to Kaluza-Klein mass scales for instance) are larger than the typical energies going through the vertices. The ϕ scalar mixing with the SM Higgs boson is assumed

---

[2]At low diphoton invariant masses, boosted diphoton events with high p_T transverse momentum can still be triggered, but at the price of a weaker selection efficiency.

to be small to ensure that the SM Higgs field has SM-like couplings compatible with the LHC signal strength measurements. The scalar fields entering Eq. (1)-(2) are taken to be the mass eigenstates.

The CP-even couplings might be those of a radion in a model with a warped extra dimension along which matter is propagating. Notice that if EW brane kinetic terms are negligible in such models, one has $f_W = f_B$ [232, 233] which implies that the $\phi F^{\mu\nu} Z_{\mu\nu}$ coupling vanishes, a property which can be used for model discrimination [234].

The CP-odd scalar field can be a pseudo Nambu-Goldstone boson from an approximate global symmetry, just like those appearing in composite Higgs models. The couplings to gauge fields are then induced by the many fermion resonances populating the TeV scale (see e.g Ref. [235] or Ref. [236]).

3 Numerical analyses

3.1 Cross sections

First we present the cross sections, obtained with the `Feynrules` code, for the VBF production of a light scalar, $pp \to \phi qq$ (q denoting light quarks), at the 13 TeV LHC. The results are shown in Fig. 1 for a typical scale value $f_H = f_B = f_W = 1$ TeV ($\tilde{f}_B = \tilde{f}_W = 1$ TeV) in case of a CP even (odd) scalar field. For instance, we see that with $m_\phi = 200$ GeV, the number of events with an integrated luminosity of 36.1 fb^{-1} (100 fb^{-1}) would be around 7 10^8 (2 10^9) which could be promising for detection even after a signal suppression by a small branching ratio of the scalar field decay. Any model builder can use the result presented in Fig. 1 to deduce the rate values in a specific scenario using the present generic parametrisation.
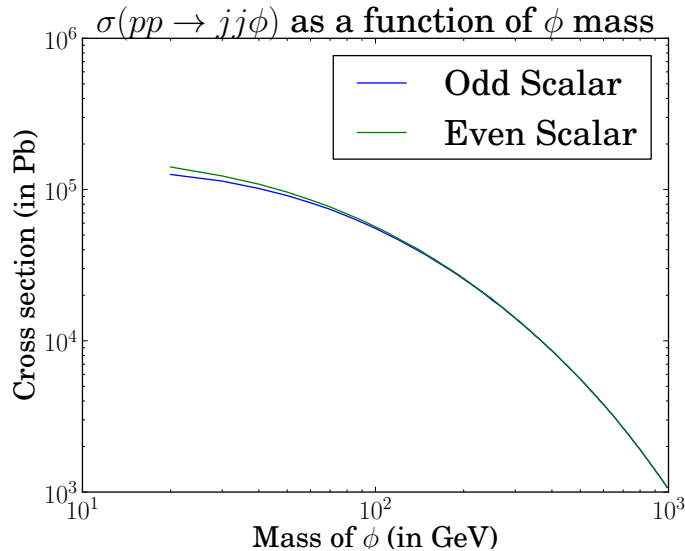

Figure 1: Cross section (in Pb) for the VBF production of a generic light scalar, $pp \to \phi qq$, at the 13 TeV LHC as a function of the scalar mass m_ϕ (in GeV). Both odd and even scalar field cases are considered. A typical scale value $f_H = f_B = f_W = 1$ TeV ($\tilde{f}_B = \tilde{f}_W = 1$ TeV) is used in case of a CP even (odd) scalar field.

3.2 Kinematical distributions

Following the preliminary analysis of Ref. [237], in order to investigate the capability of such an analysis to be able to distinguish the production of a CP-even from a CP-odd scalar particle as defined in the above effective model, and from SM background processes, we constructed both CP-even and CP-odd instances of the model with the `Feynrules` code in the form of Universal FeynRules Output (UFO) files. These were then propagated to the `MadGraph5_aMC@NLO_v2_5_5` program for generation of parton-level events then to `Pythia8` for showering and to `Delphes` (using 'CMS flavor') for a detector reconstruction at $\sqrt{s} = 13$ TeV of the process $pp \to \phi qq$, $\phi \to \gamma\gamma$, for each of $m_\phi = 20$ and 70 GeV, as well as for generation of events from the process $pp \to \gamma\gamma + 2$ jets within the SM. The event generations were performed for the following three choices of parameters.

- Two different cases of a CP-even scalar boson:
    - $f_B = f_W = 1$ TeV and $f_H \to \infty$, corresponding to the case of a CP-even scalar boson coupling to two Z^0 bosons via the $(Z_{\mu\nu})^2$ Lorentz structure, to two photons γ via $(F_{\mu\nu})^2$ and to two $W^\pm$ bosons via $(W_{\mu\nu})^2$; case called CP-even$_{1/f_V}$,
    - $f_H = 1$ TeV and $f_{B,W} \to \infty$, corresponding to the case of a CP-even scalar boson coupling to two Z^0 bosons via the $(Z_\mu)^2$ Lorentz structure, to two photons γ via $(A_\mu)^2$ and to two $W^\pm$ bosons via $(W_\mu)^2$; case called CP-even$_{1/f_H}$.

- The case of a CP-odd$_{1/\tilde{f}_V}$ scalar field with $\tilde{f}_B = \tilde{f}_W = 1$ TeV, in which the coupling to two Z^0 bosons always occurs via the $Z_{\mu\nu}\tilde{Z}^{\mu\nu}$ Lorentz structure, to two photons γ via $F_{\mu\nu}\tilde{F}^{\mu\nu}$ and to two $W^\pm$ bosons via $W_{\mu\nu}\tilde{W}^{\mu\nu}$.

Fig. 2-5 show kinematical distributions for $m_\phi = 20$ and 70 GeV without selection or acceptance criteria and for each of the above three cases of light scalar: CP-even$_{1/f_V}$, CP-even$_{1/f_H}$ and CP-odd$_{1/\tilde{f}_V}$, as well as for the SM background. The areas of all distributions have been normalized to unity. We see that it is difficult to discriminate between the CP odd and CP even scalar fields or among the two different CP even types of coupling. In contrast, there exist kinematical distributions allowing to reduce significantly the SM background, using some relevant cuts. Since the distributions shown are at parton level, further precise studies must be undertaken in order to determine whether the differences in shape are as marked after parton showering/hadronisation, reflecting only partly the influence of the underlying event.

4 Conclusion

Hence, for two examples of low scalar masses at 20 GeV and 70 GeV, we have shown that some kinematical distribution shapes should allow for a reasonable discrimination of the extra scalar
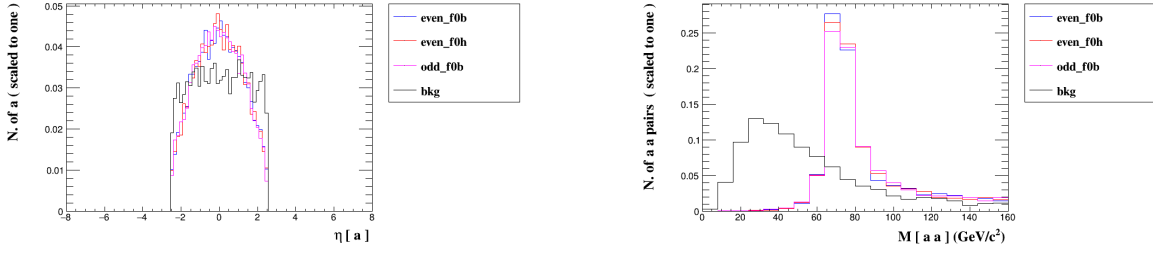
Figure 2: Left-hand side: Normalised distribution of η for a photon (denoted a on the figure) which can be approximated by $-ln\tan(\theta/2)$, θ and ϕ here being the polar and azimuthal angles. Right-hand side: Normalised distribution of the invariant mass (in GeV) of the diphoton system. We consider a scalar mass $m_\phi = 70$ GeV. The signal and SM background (black) are superimposed over each other. A typical scale value $f_B = f_W = 1$ TeV, $f_H = 1$ TeV and $\tilde{f}_B = \tilde{f}_W = 1$ TeV is used respectively in the case CP-even$_{1/f_V}$ (blue), CP-even$_{1/f_H}$ (red) and CP-odd$_{1/\tilde{f}_V}$ (purple).
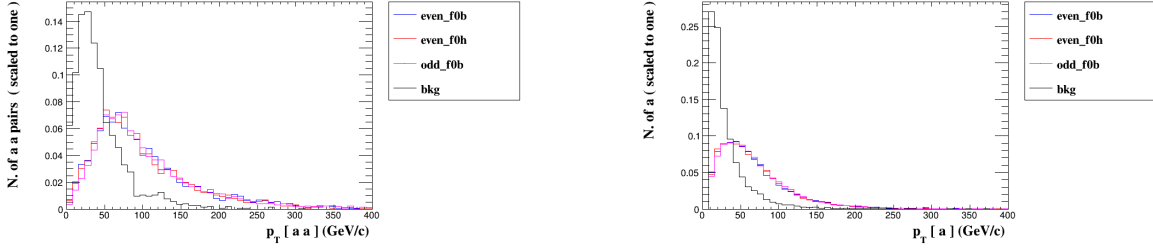
Figure 3: Left-hand side: Normalised distribution of the diphoton system transverse momentum, $p_{T_{\gamma\gamma}}$ (in GeV). Right-hand side: Normalised distribution of the photon system transverse momentum, p_{T_γ} (in GeV). We consider a scalar mass $m_\phi = 20$ GeV. The signal and SM background (black) are superimposed over each other. A typical scale value $f_B = f_W = 1$ TeV, $f_H = 1$ TeV and $\tilde{f}_B = \tilde{f}_W = 1$ TeV is used respectively in the case CP-even$_{1/f_V}$ (blue), CP-even$_{1/f_H}$ (red) and CP-odd$_{1/\tilde{f}_V}$ (purple).

boson VBF production against the SM background. This result combined with the obtained potentially large number of VBF events makes the VBF production process at LHC a promising channel of search for physics beyond the SM. It also turns out to be more challenging to distinguish among the CP even and CP odd scalar bosons so those two kinds of production would sum up to increase the signal.

ACKNOWLEDGEMENTS
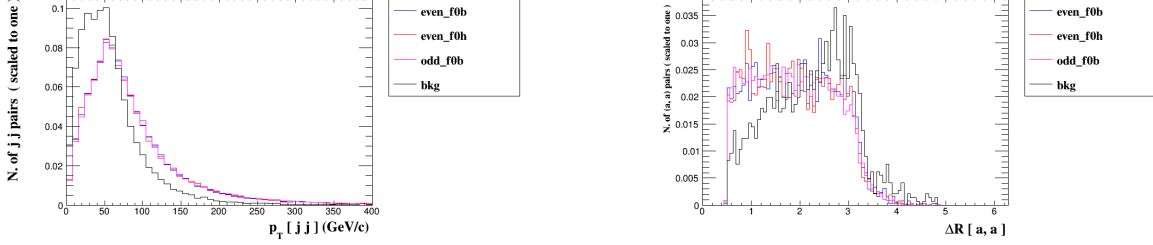
Figure 4: Left-hand side: Normalised distribution of the dijet system transverse momentum, $p_{T_{jj}}$ (in GeV). Right-hand side: Normalised distribution of the diphoton system quantity: $\Delta R^2 = \sqrt{\Delta\theta^2 + \Delta\phi^2}$ (θ and ϕ denoting the polar and azimuthal angles, respectively). We consider a scalar mass $m_\phi = 20$ GeV. The signal and SM background (black) are superimposed over each other. A typical scale value $f_B = f_W = 1$ TeV, $f_H = 1$ TeV and $\tilde{f}_B = \tilde{f}_W = 1$ TeV is used respectively in the case CP-even$_{1/f_V}$ (blue), CP-even$_{1/f_H}$ (red) and CP-odd$_{1/\tilde{f}_V}$ (purple).
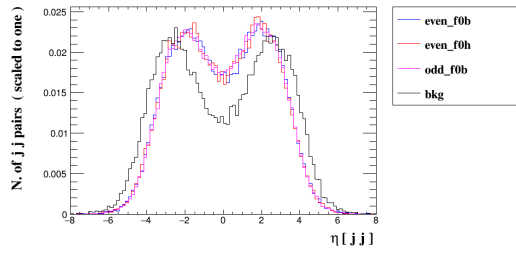
Figure 5: Normalised distribution of the same quantity η as above, but now for the dijet system. We consider a scalar mass $m_\phi = 20$ GeV. The signal and SM background (black) are superimposed over each other. A typical scale value $f_B = f_W = 1$ TeV, $f_H = 1$ TeV and $\tilde{f}_B = \tilde{f}_W = 1$ TeV is used respectively in the case CP-even$_{1/f_V}$ (blue), CP-even$_{1/f_H}$ (red) and CP-odd$_{1/\tilde{f}_V}$ (purple).

Contribution 12

Probing the Top and Charm Yukawa Couplings in $pp \rightarrow VV + t/c + j$

A. Falkowski, S. Ganguly, P. Gras, J. M. No, K. Tobioka, E. Venturini, N. Vignaroli, T. You

Abstract

The top and charm Yukawa couplings of the Higgs boson are important measurements to target in the Standard Model. They can be probed in complementary ways to on-shell Higgs decays through processes involving an off-shell Higgs. We estimate the sensitivity of the HL-LHC in the $pp \rightarrow VV + q + j$ channel to modifications of the Yukawa δy_q, where $q = t, c$ and $V = W^{\pm}, Z$. We find a rough 95% CL sensitivity of around $|\delta y_t| \sim 0.2 - 0.3$ and $|\delta y_c| \sim 1 - 3$ assuming an amount of reducible background a factor 1 to 10 of the irreducible SM signal. This preliminary study can serve as a baseline for more refined future projections.

1 Introduction

Almost a decade after its discovery, the Higgs boson remains a mysterious lynchpin of the Standard Model (SM). Its apparent simplicity as an elementary scalar belies an undesired arbitrariness in its properties – from the unexplained pattern of Yukawa couplings to the precarious nature of the electroweak symmetry-breaking potential. This makes it all the more important to probe the Higgs experimentally in every way possible. Such a program of measurements of the Higgs sector will benefit from the upcoming high-luminosity LHC (HL-LHC) upgrade enabling new types of analyses to become competitive [238].

Recently, it has been suggested by Ref. [239] to measure the Higgs couplings without the Higgs; in other words, to consider processes with an off-shell Higgs. While many such studies have already been performed and are being pursued, others remain to be investigated. The relation of processes involving longitudinal gauge bosons to those with an on-shell Higgs can be categorised systematically by considering higher-dimensional operators in the SM effective field theory (SMEFT). The conclusions also follow more generally from the energy-growing behaviour that arises when breaking delicate cancellations in the electroweak sector.

Here we follow up on the top Yukawa study of the $pp \rightarrow VV + t + j$ channel in Ref. [239] and make first projections also for the charm Yukawa. In Fig. 1 we show the Feynman diagram for our target process that is modified by the SMEFT dimension 6 operator

$$\mathcal{L}_{\text{SMEFT}} \supset \frac{Y_q}{v^2}|H|^2 \bar{Q}_L H q_R \,, \tag{1}$$

where $q = t, c$. On the left of Fig. 1 is the diagram "without the Higgs" in a non-unitary gauge in which the longitudinal degrees of freedom of the vector bosons appear explicitly; on the right is the corresponding unitary gauge picture with a virtual off-shell Higgs. By setting

$|H|^2 \sim v^2$ in the effective operator (1), we see that this induces a modification of the top Yukawa coupling that can be probed through precision measurements of the Higgs couplings in on-shell decays or constrained in global SMEFT fits (see e.g. Refs. [240–246] for some recent such fits). However, this operator also contains $|H|^2 \sim \phi^+\phi^-$ corresponding to the longitudinal gauge boson components in the non-unitary gauge. The operator will therefore necessarily modify correlated processes such as the one in Fig. 1. It benefits moreover from an energy-growing behaviour $\sim E^2/\Lambda^2$ as one probes higher energies closer to the new physics threshold Λ. This may compensate somewhat for the limited precision of these measurements.
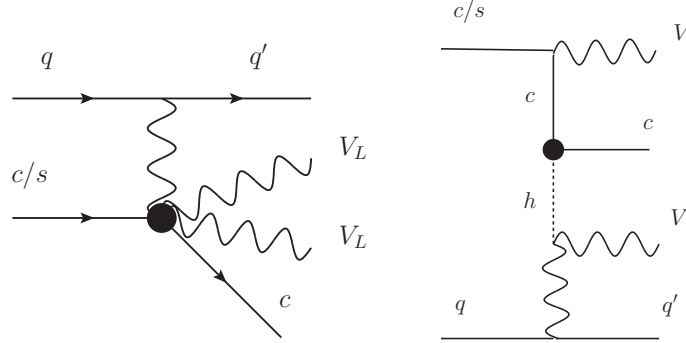
Figure 1: Feynman diagrams for the signal of modification to y_c as seen in the Feynman gauge (left) or in the unitary gauge (right).

In the next Section we study first the top Yukawa's signal sensitivity and estimate the top background. In Section 3 we consider the charm Yukawa, before concluding in Section 4.

2 Top Yukawa

As the heaviest particle in the SM, the top quark and its coupling to the Higgs may be particularly sensitive to new physics. The projected reach of the HL-LHC from on-shell Higgs measurements is reviewed in Ref. [238]. Here we estimate the HL-LHC sensitivity of the complementary off-shell process following the analysis of Ref. [239] (see also the related process with linear growth in Refs. [247, 248]) starting with a calculation of the signal expectation with a naive sensitivity estimate before describing our $t\bar{t}$ background simulations.

2.1 Signal

In the presence of the dimension 6 operator (1) the cross-section for $pp \rightarrow VV + t + j$ can be expanded as

$$\sigma \sim \sigma_{SM} + Y_t \frac{1}{v^2} \sigma_{int} + Y_t^2 \frac{1}{v^4} \sigma_{BSM^2} \,. \tag{2}$$

We illustrate the quadratic dependence on the Wilson coefficient, for example, in the $W^\pm W^\pm$ channel in Fig. 2, which is non-negligible. We apply the following cuts:

$$cut\ 1\ (2)\text{:}\quad p_T^t > 250\,(500)\,\text{GeV}\,, \ |\eta_j| > 2.5\,, \ p_T^j > 30\,\text{GeV}\,, \ E_j > 300\,\text{GeV}\,. \tag{3}$$

For reference we report here the dependence of each channel on both the looser and tighter cuts 1 and 2 respectively. We use MadGraph [19] with a model implementing the operator (1) to simulate events and calculate the dependence on the Yukawa modification.
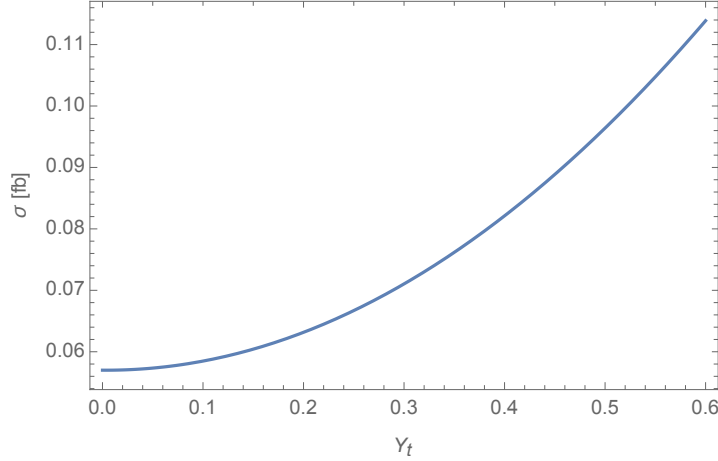
Figure 2: Cross section (in fb) for $W^{\pm}W^{\pm}$ production, with *cuts 2* applied, as a function of Y_t.

The number of SM signal events with the cuts above applied are given in Table 1. For the WW channels with cut 1 we find good agreement with Ref. [239] in each decay sub-channel (we include leptonic decays of the τ's in the leptonic categories), though we find discrepancies in the WZ and ZZ estimates for cut 1 and obtain more suppression when applying cut 2, which warrants further study.

In Tables 2, 3 and 4, the cross sections and their dependence on Y_t in each decay channel are indicated, with *cut 2* applied (as used to estimate the sensitivity of our search).

	0ℓ	1ℓ	$\ell^{\pm}\ell^{\mp}$	$\ell^{\pm}\ell^{\pm}$	3ℓ (4ℓ)
$W^{\pm}W^{\mp}$	1.277/0.0682	0.9034/0.04826	0.1598/0.008538	0	0
$W^{\pm}W^{\pm}$	1.102/0.03656	0.7799/0.02587	0	0.1380/0.004576	0
WZ	6.329/0.4799	2.239/0.1698	0.7089/0.05375	0	0.2508/0.01902
ZZ	0.1810/0.01387	0	0.04054/0.003106	0	0.002270/0.0001740

Table 1: $Y_t = 0$ (SM) and cut 1/cut 2 on p_T^t. Cross sections are in fb

	0ℓ	1ℓ
$W^{\pm}W^{\mp}$	$0.06820 + 0.007311\,Y_t + 0.2783\,Y_t^2$	$0.04826 + 0.005174\,Y_t + 0.1969\,Y_t^2$
$W^{\pm}W^{\pm}$	$0.03656 - 0.0004092\,Y_t + 0.1233\,Y_t^2$	$0.02587 - 0.0002896\,Y_t + 0.08726\,Y_t^2$
WZ	$0.4800 + 0.001319\,Y_t + 0.05116\,Y_t^2$	$0.1698 + 0.0004665\,Y_t + 0.01810\,Y_t^2$
ZZ	$0.01387 + 0.002090\,Y_t + 0.04232\,Y_t^2$	0

Table 2: Channels without leptons and with a single lepton; cut 2 on p_T^t. Cross sections are in fb.

We may make a rough sensitivity projections based on the signal dependence on the Yukawa modification due to Y_t relative to the SM value y_t,

$$\delta y_t \equiv \frac{3}{2}\frac{Y_t}{y_t} \, . \tag{4}$$

110

	$\ell^{\pm}\ell^{\mp}$	$\ell^{\pm}\ell^{\pm}$
$W^{\pm}W^{\mp}$	$0.008538 + 0.0009152\,Y_t + 0.03483\,Y_t^2$	0
$W^{\pm}W^{\pm}$	0	$0.004576 - 0.00005123\,Y_t + 0.01544\,Y_t^2$
WZ	$0.05375 + 0.0001477\,Y_t + 0.005730\,Y_t^2$	0
ZZ	$0.003106 + 0.0004682\,Y_t + 0.009479\,Y_t^2$	0

Table 3: Channels with 2 leptons; cut 2 on p_T^t. Cross sections are in fb.

	$3\ell\ (4\ell)$
$W^{\pm}W^{\mp}$	0
$W^{\pm}W^{\pm}$	0
WZ	$0.01902 + 0.00005225\,Y_t + 0.002027\,Y_t^2$
ZZ	$0.0001740 + 0.00002622\,Y_t + 0.0005308\,Y_t^2$

Table 4: Channels with 3 and 4 leptons; cut 2 on p_T^t. Cross sections are in fb.
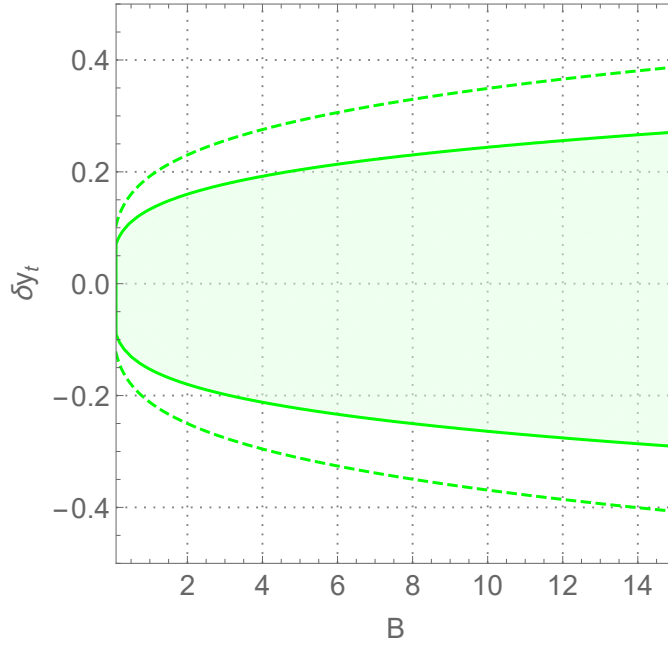
Figure 3: Projection of the 1- and 2-σ sensitivity, in solid and dashed lines respectively, at the 3ab^{-1} HL-LHC to modifications of the top Yukawa δy_t.

The significance σ is estimated by applying a naive background rescaling factor B that parametrises the number of background events as a ratio of the SM signal events:

$$\sigma = \frac{N_{SM+BSM} - N_{SM}}{\sqrt{B \times N_{SM}}}. \tag{5}$$

The resulting sensitivity at HL-LHC with 3ab^{-1} is shown in Fig. 3. Cut 2 has been applied as this led to increased sensitivity, though we note that optimal choices of cuts will rely on a detailed study of individual sub-channels together with their background estimates that we leave

Table 5: Event categories. Here leptons refer to muons, electrons and their antipaticles. The letter V_h refers to a vector boson, indifferently W or Z.

Category name	Selection	Selected signal
$0\,\ell + 2\,V_h$	No isolated lepton and two tagged vector bosons	$\overset{(-)}{t}\,V(\to jj)V(\to jj)$
$1\,\ell + 1\,V_h$	One isolated lepton and one tagged vector boson	$\overset{(-)}{t}\,W(\to \ell\nu)V(\to jj)$
$\ell^{\pm}\ell^{\pm}$	Two same-sign isolated leptons	$\overset{(-)}{t}\,W^{\pm}(\to \ell^{\pm}\overset{(-)}{\nu})W^{\pm}(\to \ell^{\pm}\overset{(-)}{\nu})$
$\ell^{\pm}\ell^{\mp}$	Two opposite-sign leptons	$\overset{(-)}{t}\,W^{\pm}(\to \ell^{\pm}\overset{(-)}{\nu})W^{\mp}(\to \ell^{\mp}\overset{(-)}{\nu})$
$\ell^{\pm}\ell^{\mp} + 1\,V_h$	Two opposite-sign isolated leptons and one tagged vector boson	$\overset{(-)}{t}\,Z(\to \ell^{\pm}\ell^{\mp})V(\to jj))$
$3\,\ell$	Three isolated leptons	$\overset{(-)}{t}\,Z(\to \ell^{\pm}\ell^{\mp})W^{\pm}(\to \ell^{\pm}\overset{(-)}{\nu})$
$4\,\ell$	At least four isolated leptons	$\overset{(-)}{t}\,Z(\to \ell^{\pm}\ell^{\mp})Z(\to \ell^{\pm}\ell^{\mp})$

to future work. In the next Section we describe in detail our analysis to estimate the dominant $t\bar{t}$ background.

2.2 Backgrounds

2.2.1 Introduction

We restrict the study to the final state with one boosted hadronic top ($p_T > 250\,\text{GeV}$) that can be identified with a top tagging technique [249–253]. A rejection factor of $\gtrsim 10$ is obtained for working point with a 80% top quark selection efficiency. We now review background processes with one top quark that decays hadronically.

2.2.2 Event selection and classification

Vector bosons that decay hadronically can be identified if they are boosted enough, $p_T \gtrsim 200\,\text{GeV}$. The boson is reconstructed as a jet with a large radius parameter, and a discriminator as the jet mass is used for the identification [251, 252]. Events are classified according to the number of leptons as in the previous sections (only electrons and muons are considered). The category with two opposite-sign leptons is split into two categories, with and without a tagged vector boson. The leptons are required to fulfill the following isolation criteria: the sum of the transverse momentum of particle within a R distance, $R = \sqrt{\Delta\eta^2 + \Delta\varphi^2}$ of 0.4 must be smaller than 15% of the lepton transverse momentum. The vector boson tagging is applied for all the categories covering a signal final state with one or two hadronic vector boson. Table 5 lists the categories with the respective targeted signal processes. When vector boson tagging is applied, a threshold of $200\,\text{GeV}$ is applied on the transverse momentum of the jet. The $t\bar{t}$ background is further suppressed by rejecting events with one b-tagged jet or more whose R distance from the reconstructed top quark is larger than 0.8 are rejected. If several top quarks are reconstructed, the one with the highest transverse momentum is considered. For the category $\ell^{\pm}\ell^{\mp} + 1\,V_h$ it is also required that the two reconstructed leptons have the same flavour and that their four-momentum sum has a mass of $\pm 20\,\text{GeV}$ around 91 GeV.

Table 6: Contribution from the $t\bar{t}jj$ process. The event yields are given for an integrated luminosity $3000\,\mathrm{fb}^{-1}$ at $\sqrt{s} = 14\,\mathrm{TeV}$. The quoted uncertainties are the statistical uncertainty

Category	$t\bar{t}jj$ event yield
$0\,\ell\,2\,\mathrm{V}_h$	$10\,200. \pm 4.5\mathrm{e}{+}03$
$1\,\ell\,1\,\mathrm{V}_h$	$175\,000. \pm 1.9\mathrm{e}{+}04$
$\ell^{\pm}\ell^{\pm}$	-
$\ell^{\pm}\ell^{\mp}$	$42\,600. \pm 9.3\mathrm{e}{+}03$
$\ell^{\pm}\ell^{\mp}\,1\,\mathrm{V}_h$	$12\,200. \pm 5.0\mathrm{e}{+}03$
$3\,\ell$	-
$4\,\ell$	-

2.2.3 Event yield estimation

To estimate the background process event yields, samples are generated at leading order with Madraph5_aMC@NLO [19]. Madspin [254] is used for the top quarks and the vector boson decays. The parton distribution function (PDF) NNPDF 2.3 NLO [255] is used and the strong coupling is set to $\alpha_s(m_Z) = 0.119$ at the Z boson mass. Parton showering is performed with PYTHIA 8. A 250 GeV threshold is applied on the top quark (at parton level). Particles are clustered in jets using the anti-k_T algorithm implemented in fastjet with a distance parameter of 0.4. One jet with energy above 300 GeV and pseudorapidity $|\eta| > 2.5$ is required. Quark and gluons are required to be within the pseudorapidity range $|\eta| < 5$ to account for the calorimeter acceptance.

A factor of 80% is applied on the event yields to account for the top tagging efficiency. For the b-jet veto the efficiency parametrization of the loose working point given in [67] is used, assuming similar performance for HL-LHC. The acceptance for b-tagging is extended to $|\eta| = 4$ to account for the larger coverage of the trackers of the experiment Phase II upgrade [256, 257]. The vector boson tagging is emulated by reconstructing anti-k_T jets with a distance parameter $R = 0.8$ and applying an efficiency of 80% for a jet from a vector boson decay and 0.04% for a jet from a prompt quark or gluon. The event yield estimate from the pp $\rightarrow t\bar{t}jj$ process is provided in Table 6.

The cross section of the pp $\rightarrow t\bar{t}Wj$ process, that will contribute to the categories with one or more leptons, has been estimated at leading order. After requiring one top or antitop quark with $p_T > 250$ GeV and a forward jet, with $|\eta| > 2.5$ and $E > 300\,GeV$, the cross section is, leading to less than one event for $3000\,\mathrm{fb}^{-1}$. The contribution from pp $\rightarrow t\bar{t}W$ with one hadronic top quark with $p_T > 250$ GeV and one leptonic top quark from which the b-jet passes the forward jet requirement ($|\eta| > 2.5$ and $E > 300$ GeV) is also smaller than one event before the b-jet veto.

The background from the processes with a top pair in the final state is substantial for the hadronic and semi-leptonic channels, while it is negligible for the fully leptonic channels. We expect that the background for leptonic channels will mainly come from events where a QCD jet was misidentified as a top quark, e.g. from the production of two W bosons with two jets. Such contribution remains to be estimated.

3 Charm Yukawa

We now study the process with two gauge bosons plus a jet plus a tagged charm in the final state [1]. In this way we can directly probe the modification to the Yukawa coupling of the charm due to the operator (1),

$$\delta y_c \equiv \frac{y_c^{BSM}}{y_c} = \frac{3}{2}\frac{Y_c}{y_c}, .$$ (6)
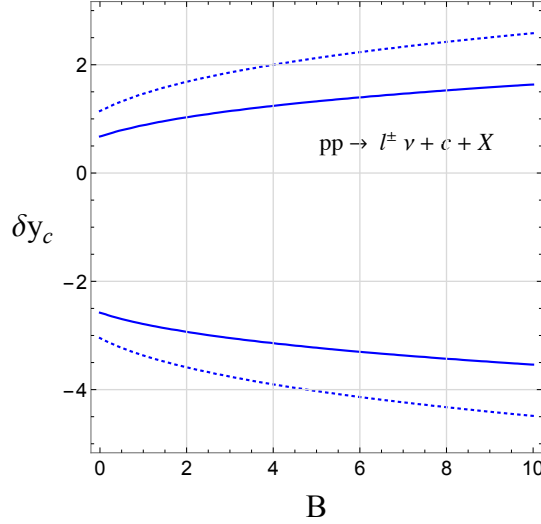
Figure 4: 1σ (continuous curve) and 2σ (dotted curve) HL-LHC (14 TeV, 3 ab^{-1}) sensitivity on δy_c, as a function of an arbitrary amount of reducible background, calculated as a factor B of the irreducible background given by the SM signal.

We can estimate the BSM contribution to the inclusive cross section by expanding it in the SM ($Y_c = 0$) plus the SM-BSM interference term ($\propto Y_c$) plus the pure BSM term ($\propto Y_c^2$):

$$\sigma \approx \sigma^{SM}(Y_c = 0) + Y_c\,\sigma^{INT}(Y_c = 1) + Y_c^2\,\sigma^{BSM}(Y_c = 1)\,.$$ (7)

We find the following cross sections in the different $VVcj$ channels:

	SM ($Y_c = 0$)	INT ($Y_c = 1$)	BSM ($Y_c = 1$)
W^+W^-cj	2.3 pb	0.58 pb	63 pb
W^+Zcj	0.86 pb	0.17 pb	17 pb
W^-Zcj	0.79 pb	0.09 pb	9.1 pb
$ZZcj$	0.19 pb	0.14 pb	15 pb
W^+W^+cj	29 fb	0.42 fb	94 fb
W^-W^-cj	23 fb	0.31 fb	90 fb

The significance can be estimated using the rescaling factor B as for the top case in Eq. 5. By considering the results in the semileptonic channel, $\ell^\pm\nu+c+X$, and considering a 25% c-

---

[1]See e.g. Refs [258–260] for some recent studies on probing the charm Yukawa.

tagging efficiency (see e.g. Refs. [259, 260]), we find a rough estimate of the background-free sensitivity as

$$\delta y_c \lesssim \quad 0.7\,(1\sigma)\;-\;1.1\,(2\sigma) \qquad \text{(HL-LHC, 3 ab}^{-1}) \tag{8}$$

Note that in this estimate we do not include the contribution of reducible backgrounds, for example the $t\bar{t}$ background estimated in the previous section. It is important to evaluate the contribution of this background to obtain a realistic estimate, though we consider an idealised estimate of the sensitivity in the absence of backgrounds to be a useful starting point for more realistic studies to aim towards. Fig. 4 shows the 1σ (continuous curve) and the 2σ (dotted curve) HL-LHC sensitivity on δy_c, as a function of an arbitrary amount of reducible background, calculated as a factor B of the irreducible background given by the SM signal.

4 Conclusion

In this Proceedings note we made sensitivity projections for the top Yukawa at the HL-LHC and analysed its $t\bar{t}$ background, also considering for the first time the charm Yukawa, in the off-shell Higgs process $pp \to VV + t/c + j$. For the top Yukawa we find a comparable sensitivity to Ref. [239] of $|\delta y_t| \sim 0.2-0.3$. The charm Yukawa sensitivity is $\delta y_c \sim \mathcal{O}(1)$ in the semileptonic channel, though this will depend in large part on improvements in charm tagging and controlling backgrounds sufficiently.

In future work we aim to incorporate detailed background estimates in each sub-channel and identify optimal cuts and channels for a more realistic analysis. Furthermore several other related processes remain to be investigated in the off-shell Higgs program; the development of these measurements could complement the on-shell Higgs ones and provide a useful input to global fits of the SMEFT. As the HL-LHC will enable more sensitive EFT measurements in the next decade, we have focused on those projections here. In the longer term off-shell Higgs measurements could form an important part of Higgs studies at the 100 TeV FCC-hh.

Acknowledgements

Contribution 13

Constraining the $t\bar{t}hZ$ vertex from $t\bar{t}hZ$ and $t\bar{t}hj$ production channels

S. Banerjee, R. S. Gupta, S. Jain, E. Venturini

Abstract

In this chapter, we consider two processes through which operator generating the $Zt_R\bar{t}_R$ and $hZt_R\bar{t}_R$ interactions can be probed. These interaction is uncorrelated to Z-decays to bottom quarks and thus unconstrained by LEP data. With the objective of constraining these couplings we specifically study the energy growth of the cross-sections in the processes $pp \to t\bar{t}hZ$ and $pp \to t\bar{t}hj$. A first analysis for the future 27 TeV and 100 TeV machines yield a percent to permille level level bound on this coupling.

1 Introduction

Colliders such as the Large Hadron Collider and other proposed future machines would study the interactions of elementary particles at the multi-TeV scale for the first time ever. As this will correspond to the fundamental scale ever probed, the data collected by these machines would be valuable whether or not any new physics beyond the Standard Model (SM) is directly discovered.

Of particular interest are the interactions of the top quark with the electroweak and Higgs bosons. From a purely experimental point of view many of the interactions of the top quark are still unconstrained. For example, the $Zt_R\bar{t}_R$ and $hZt_R\bar{t}_R$ couplings, the focus of this chapter, are still poorly constrained compared to the analogous couplings to lighter quarks which were precisely measured by LEP in Z-boson decays.

Studying the top couplings to electroweak bosons is also very well motivated theoretically. This is because the top quark and its BSM partners often play a crucial role in electroweak symmetry breaking, for instance by radiatively contributing to the Higgs potential. The mass scale of the top partners is not expected to be much larger than the TeV scale due to naturalness considerations and thus this sector might lead to sizeable indirect effects. In composite models [261, 262] for example, integrating out the top partners generates all the dimension-6 operators that can lead to deviations of the coupling of the Z-boson to the top ,

$$\mathcal{O}_{HQ_L}^{(1)} = iH^\dagger \overleftrightarrow{D}_\mu H \bar{Q}_L \gamma^\mu Q_L \quad \mathcal{O}_{HQ_L}^{(3)} = iH^\dagger \sigma^a \overleftrightarrow{D}_\mu H \bar{Q}_L \sigma^a \gamma^\mu Q_L \quad \mathcal{O}_{Ht_R} = iH^\dagger \overleftrightarrow{D}_\mu H \bar{t}_R \gamma^\mu t_R \tag{1}$$

While the operators involving the left-chiral fermions deform both the SM $Zb\bar{b}$ and $Zt\bar{t}$ couplings and are thus constrained by LEP measurements (specifically Z-pole and anomalous triple gauge coupling measurements), the operator $\mathcal{O}_{Ht_R}$ is completely unconstrained.[1] This operator

---

[1]Note that there is a linear combination of $\mathcal{O}_{HQ_L}^{(1)}$ and $\mathcal{O}_{HQ_L}^{(3)}$ that generates only a $Zt_L\bar{t}_L$ deformation but not a

when expanded in the unitary gauge yields,

$$\frac{\mathcal{O}_{Ht_R}}{\Lambda^2} = -\frac{gv^2}{2c_{\theta_W}\Lambda^2}(1 + \frac{2h}{v} + \frac{h^2}{v^2})Z_\mu\bar{t}_R\gamma^\mu t_R, \tag{2}$$

where Λ is the scale of new physics. In this work we will compute the bounds on the coefficient of $(h/v)Z_\mu\bar{t}_R\gamma^\mu t_R$,

$$g_{hZt_R} = -\frac{g}{c_{\theta_W}}\frac{v^2}{\Lambda^2}c_{Ht_R} \tag{3}$$

where c_{Ht_R} is the Wilson coefficient of the operator $\mathcal{O}_{Ht_R}$. In composite models we expect $c_{Ht_R} \sim g_*^2$ [262] where, $1 \lesssim g_* \lesssim 4\pi$, is the coupling characterising the strong sector.

At the LHC, the $Zt\bar{t}$ coupling can be constrained in $t\bar{t}Z$ production. Contribution of $\mathcal{O}_{Ht_R}$ to $t\bar{t}Z$ production however does not grow with energy and thus only $\mathcal{O}(1)$ constraints on deviations of the Z coupling from its SM value are expected from this process at the LHC [263, 264]. In this note, we explore the feasibility of probing the contribution of this operator to the $t\bar{t} \rightarrow hZ$ and $tZ \rightarrow th$ processes in pp collisions. These contributions grow quadratically with energy with respect to the SM (energy growth in the analogous process for light quarks was studied in [265–267]) and hence stronger constraints may be possible. This operator also generates contributions to $tW \rightarrow tW$ process that grow quadratically in energy with respect to the SM but this has already been studied in Ref. [264]. An analogous channel involving $t\bar{t} \rightarrow W^+W^-$ in pp collisions can also be interesting to look into.

This chapter is divided as follows. In Section 2, we discuss the $t\bar{t} \rightarrow hZ$ scattering and show the energy growth of the interference piece as a function of the Zh invariant mass. In Section 3, we show the energy growth in the $tZ \rightarrow th$ scattering as a function of the th invariant mass. Finally we conclude in Section 4.

2 $pp \rightarrow t\bar{t}hZ$

In this first analysis, we consider the process $pp \rightarrow t\bar{t}hZ$. Apart from the SM processes, we encounter the gg initiated diagram with the effective $t\bar{t}hZ$ vertex. At 14 TeV, the SM cross-section is ~ 1.5 fb without including the branching ratios of the various particles. Hence, even upon considering a semi-leptonic channel comprising $h/Z \rightarrow b\bar{b}$, we end up with 110 events at 3 ab^{-1}. However, various detector effects will need to be folded in including b-tagging efficiencies. Upon demanding a flat 70% b-tagging efficiency, one obtains ~ 15 events. Owing to this reason, we reconsider this channel for the planned future hadron colliders at 27 TeV (HE-LHC) and 100 TeV (FCC-hh). The respective SM cross-sections for these two colliders with the default scale choices in MG5_aMCNLO [19] are 8 fb and 130 fb without the decays. Hence, we can see that going to higher energy colliders have strong advantages in probing this coupling. Because we want to look into the higher energy effects, it is important to mention the cross-sections with cuts on m_{Zh}, *i.e.*, on the Zh invariant mass. With $m_{Zh} > 500$ GeV, 1000 GeV and 1500 GeV, the respective SM cross-sections at 27 TeV (100 TeV) colliders are 2.2 fb (47 fb), 0.3 fb (10.7 fb) and 0.07 fb (3.6 fb) without including the branching ratios. It is thus more feasible to consider the semi-leptonic channel for the 27 TeV collider (yielding ~ 70 events) and the fully leptonic channel (yielding ~ 160 events) for the 100 TeV collider. Now, upon considering $g_{hZt_R} = 0.1$, one obtains the respective interference cross-section values as

---

$Zb_L\bar{b}_L$ deformation. This linear combination is also not constrained by LEP. As in the case of $\mathcal{O}_{Ht_R}$, to constrain this direction in EFT space we need to analyse the other processes mentioned in the discussion.

-0.2 fb (3.2 fb), 0.08 fb (8.2 fb) and 0.06 fb (6.4 pb) for $m_{Zh} > 500$ GeV, 1000 GeV and 1500 GeV for the 27 TeV (100 TeV) machine. Thus, we can clearly see the interference term growing quadratically in energy with respect to the SM cross-section in Figure 1. The dominant backgrounds (that we do not consider in this proceeding) ensue from $t\bar{t}hh, t\bar{t}ZZ, t\bar{t}hb\bar{b}, t\bar{t}Zb\bar{b}$ and fake backgrounds involving c-jets and light jets [268]. We leave the full analysis for a future work.
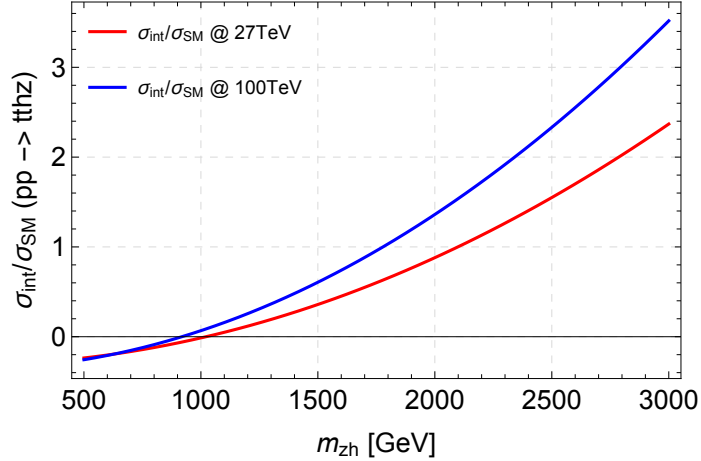
Figure 1: Results from `MG5_aMCNLO` simulation of the $pp \to t\bar{t}hZ$ process: ratio $\sigma_{int}^{(g_{hZt_R}=1)}/\sigma_{SM}$ for $g_{hZt_R} = 0.1$. The `UFO` [29] model implementation of the Standard Model Effective Field Theory (SMEFT) is done within the `FeynRules` [18] framework.

Upon treating the SM $t\bar{t}hZ$ production as the background, our first estimates for the allowed coupling range at 95% C.L. are

$$-0.007 \, (-0.0006) \lesssim g_{hZt_R} \lesssim 0.007 \, (0.00045) \tag{4}$$

for the 27 TeV @ 3 ab^{-1} (100 TeV @ 30 ab^{-1}) machine. Using $c_{Ht_R} \sim g_*^2$ and Eq. 3 this corresponds to a scale $\Lambda \gtrsim 4$ TeV for any $g_* \gtrsim 1.6$ ($g_* \gtrsim 0.5$). As there are no events beyond this energy in both our 27 TeV and 100 TeV studies, our bounds respect EFT validity requirements. A plot showing the exclusion (μ) as a function g_{hZt_R} is shown in Figure 2. The limits are quoted using a simple likelihood ratio of signal + background and a background only hypothesis as the test statistic. We employ the CLs method [218] to quote the 95% C.L. upper limits.

3 $pp \to t\bar{t}hj$

An alternative process that can be used to constrain $\mathcal{O}_{Ht_R}$ is $pp \to t\bar{t}hj$. In particular, for the quark-gluon initiated scenario, one encounters the $tZ \to th$ scattering which gives a contribution to the amplitude that grows with $\hat{s}$, with respect to the SM process. Upon exploiting this energy growth and analysing the m_{th} distribution, one can improve the sensitivity to the g_{hZt_R} parameter.

The cross-section for $pp \to t\bar{t}hj$ is more than two order of magnitudes larger than the process studied in Section 2. For this channel, the cross-section is ~ 0.64 pb at 14 TeV. The cross-section is enhanced to ~ 3.5 pb for a 27 TeV machine. Hence it is feasible to study the fully leptonic channel and obtain constraints on g_{hZt_R}, even without going to the FCC-hh.
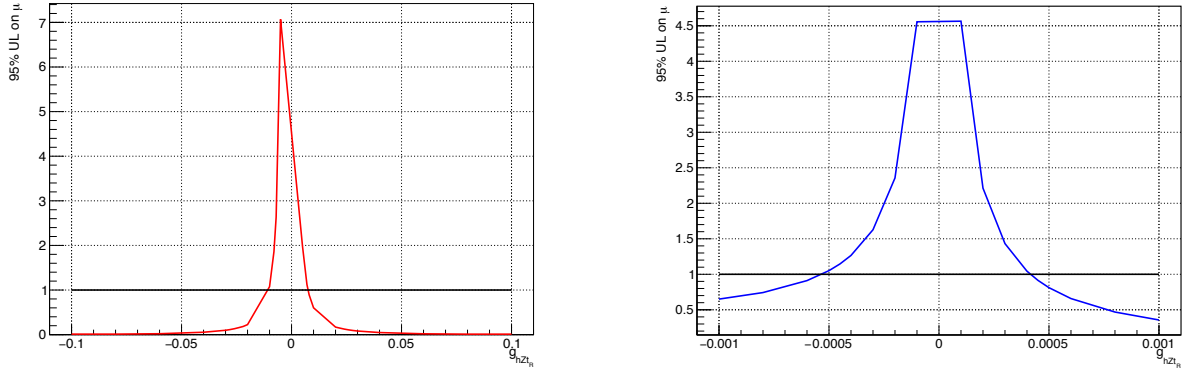
Figure 2: μ as a function of g_{hZt_R} for the 27 TeV (100 TeV) machine in the left (right) panel. All the values below the black line are excluded.

However, the cross-section is dominated by gluon-gluon induced processes, which do not receive contributions from $\mathcal{O}_{Ht_R}$ and thus do not interfere with the diagrams involving this effective vertex. At 14 TeV (27 TeV) the gg initiated channels constitute $\sim 68\%$ (74%) of the total σ_{SM}. The gq initiated subprocesses, which are relevant for this analysis, comprise $\sim 74\%$ ($\sim 80\%$) of the remaining cross-section. The qq scattering provides an even smaller contribution; in this case there can be amplitudes involving the aforementioned effective vertex. However, these diagrams do not grow in energy with respect to SM.

As a consequence, despite the huge difference in the total cross-section with respect to the $pp \to t\bar{t}hZ$ process, the interference term is not as much enhanced in comparison to what we found in Section 2. Upon expanding in powers of g_{hZt_R},

$$\sigma = \sigma_{SM} + g_{tht_R}\sigma_{int} + g_{tht_R}^2\sigma_{BSM^2} \tag{5}$$

one has $\sigma_{int} \sim -4\,\text{fb}$ ($\sim -7\text{fb}$) at 14 TeV (27 TeV) and, therefore, for $g_{hZt_R} = 0.1$, $\sigma_{int}^{(g_{hZt_R}=1)} \sim -0.4\,\text{fb}$ ($\sim -0.7\text{fb}$) at 14 TeV (27 TeV). This is of the same order of magnitude larger as the interference cross-section for the process $pp \to t\bar{t}hZ$. Besides, the interference for the present process only corresponds to $< 1\%$ of the total cross-section. Furthermore, only a fraction of the $gq \to t\bar{t}hq$ interference cross-section is affected by $\mathcal{O}_{Ht_R}$ and shows energy growth. Thus, it is difficult to observe the energy growing information from the full $pp \to t\bar{t}hj$ process. In order to see the energy growth, we first rely on the $tZ \to th$ scattering process.

The 4-point amplitude for $tZ \to th$, $A_{tZ\to th}^{BSM}$, can receive contributions from the contact interactions induced by $\mathcal{O}_{Ht_R}$. This scales as $A_{tZ\to th}^{BSM}/A_{tZ\to th}^{SM} \sim m_{th}^2/\Lambda^2$. Therefore, since the SM cross-section falls off as $1/\hat{s}$, we expect a leading $\sim \hat{s}$ growth for the cross-section in presence of non-zero values for g_{hZt_R} owing to the fact that in the large energy regime it is dominated by the σ_{BSM^2} term (see Eq. 5). On the other hand, the interference σ_{int} should behave as a constant in $\hat{s}$. These expectations are indeed consistent with the results of our simulations for $tZ \to th$ as shown in Figure 3. A pseudorapidity cut $|\eta| < 2$ has been applied on the final state objects in order to remove the forward singularity. In Figure 4, the ratio between the interference and the SM terms of the cross-section is shown. It is evident that the m_{th} distribution is consistent with the expected quadratic growth. We must also mention here that the $tZ \to th$ process is complementary to the $tW \to tW$ scattering studied in Ref. [264], which yields similar results.

119
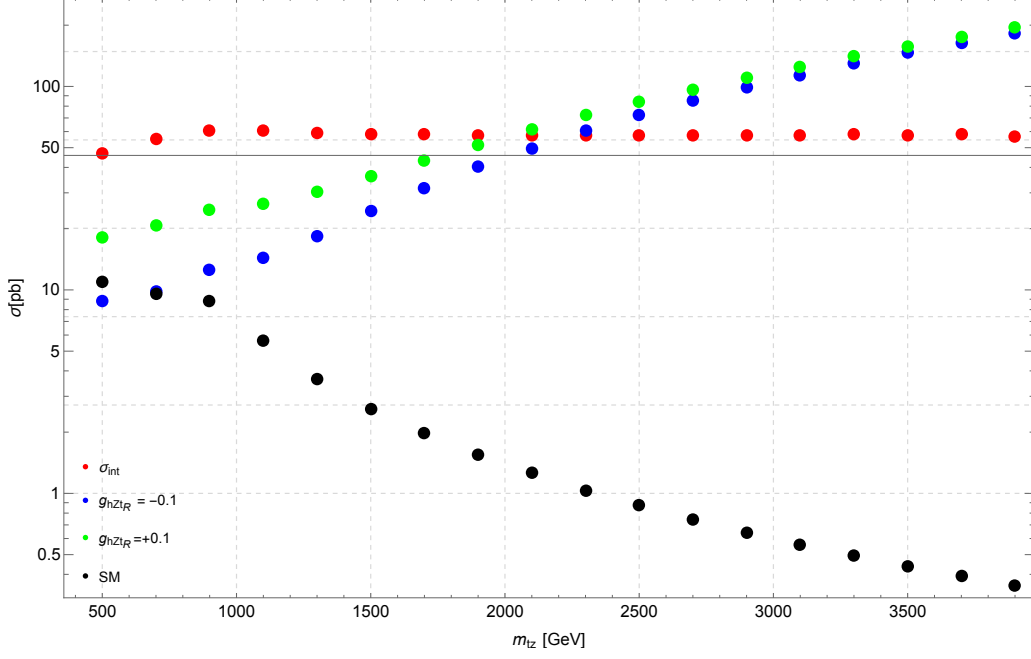
Figure 3: Results from a `MG5_aMCNLO` simulation for the $tZ \to th$ process: cross sections within SM, with $g_{hzt_R} = \pm 0.1$ and interference term σ_{int}.
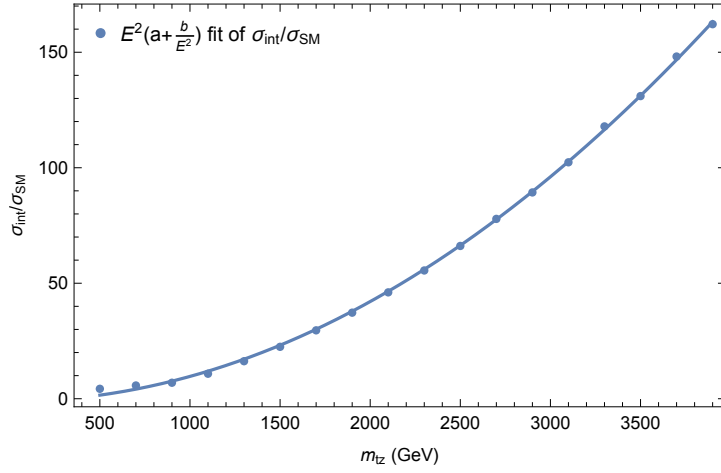
**Figure 4:** Results from a `MG5_aMCNLO` simulation of the $tZ \to th$ process: ratio σ_{int}/σ_{SM}.

4 Conclusions and Outlook

In this work we have explored the possibility of constraining the $hZt_R\bar{t}_R$ coupling by studying the $pp \to t\bar{t}hZ$ and $pp \to t\bar{t}hj$ processes where the EFT contributions grow quadratically in energy with respect to the SM. Probing this coupling is important as it is unconstrained by LEP unlike the corresponding couplings involving lighter quarks. Furthermore measuring this coupling can be a probe of naturalness in many interesting BSM theories, such as composite Higgs models, where they are generated upon integrating out the top partners. We find $pp \to t\bar{t}hZ$ to be the more sensitive of the two processes. Our preliminary estimates indicate that the $(h/v)Zt_R\bar{t}_R$ coupling can be measured at the percent to permille level (see Eq. 4) which

translates to a bound $\Lambda >$ few TeV for the new physics scale.

Acknowledgements

Tools and Methods

Contribution 14

EFT parametrization of Higgs observables

A. Gilbert, J. Langford, N. Wardle

1 Introduction

Effective field theories (EFTs) provide a consistent set of perturbations of the standard model (SM) Lagrangian [269, 270] in which new physics enters at some higher energy scale Λ, assumed to be much larger than the electroweak scale and beyond our current direct detection reach. The SM EFT is constructed by the addition of higher-dimensional operators to the SM Lagrangian,

$$\mathcal{L}_{\text{EFT}} = \mathcal{L}_{\text{SM}} + \sum_i \frac{C_i^{(6)}}{\Lambda^2} \mathcal{O}_i^{(6)} + \sum_i \frac{C_i^{(8)}}{\Lambda^4} \mathcal{O}_i^{(8)} + \cdots, \tag{1}$$

where (D) denotes an operator of dimension D and $C_i^{(D)}/\Lambda^{D-4}$ are Wilson coefficients which take non-zero values in the presence of new physics. The leading deviations from the SM are generally expected to occur at $D = 6$.

The study of EFT effects in Higgs boson production and decay is of growing interest due to the large $\sqrt{s} = 13\,\text{TeV}$ data set accumulated during LHC Run 2, and the increased sensitivity to kinematic information this provides. The ATLAS and CMS Collaborations have produced EFT constraints via interpretations of Simplified Template Cross Section (STXS) measurements [271, 272]. The STXS framework [273] defines a set of fiducial region for each Higgs boson production mode that are chosen to cover a broad range in relevant observables, for example the Higgs boson p_T and additional jet multiplicity for gluon fusion production, and the p_T of the vector boson in W and Z associated production.

One approach to constrain EFT coefficients is to start from an analysis which measures a set of unfolded fiducial cross sections of sensitive observables, such as the STXS. Each cross section is then parametrized by the coefficients, and the best-fit values and associated confidence intervals can be determined. The parametrization of the cross sections could come from known analytic expressions, or via Monte Carlo simulation which incorporates an EFT Lagrangian model. This approach has the advantage of not requiring a full detector simulation of the events, and means new models can readily be applied to existing analyses. Conversely, a limitation is that it assumes there is no change of experimental acceptance due to the non-SM kinematics. Methods based on full simulation, for example Ref. [274], can incorporate this information and utilise more optimal observables. This report focusses on the former approach, and is based on the procedure outlined in Refs. [275, 276].

A software package has been developed, EFT2Obs [1], that aims to facilitate the process of deriving an EFT parametrization. It utilises MADGRAPH v2.6.6 [19] for simulation, interfaced to PYTHIA v8.2 [28] for hadronisation and showering. The fiducial selection and histograms

---

[1] https://github.com/ajgilbert/EFT2Obs

of observables are defined in the RIVET v3.0.1 [87] framework. While this report focusses on the EFT parametrization of Higgs boson production, the tool is generic and can be applied to arbitrary observables for any model with new couplings implemented in MADGRAPH via FEYNRULES [18], subject to the limitations described in Section 5.

2 Method

This section outlines the main features of EFT2Obs. As input, the user must define the process to simulate using the standard MADGRAPH syntax, as well as the FEYNRULES model to import which defines the EFT Lagrangian. The subset of N model parameters that will be included in the cross section parametrization, denoted c_j, where $j = 1 \dots N$ are also specified. Finally, one or more RIVET routines should be provided, defining histograms of observables to be parametrized, with each fiducial bin labelled with an index i in the following.

The cross section for bin i can be expressed as the sum shown in Eq. 2, where σ_i^{int} is the leading term in the EFT expansion ($\propto 1/\Lambda^2$), and accounts for the interference with the SM amplitude. The SM-independent term is labelled as σ_i^{BSM} ($\propto 1/\Lambda^4$).

$$\sigma_i^{\text{EFT}}(c_j) = \sigma_i^{\text{SM}} + \sigma_i^{\text{int}}(c_j) + \sigma_i^{\text{BSM}}(c_j) \tag{2}$$

Dividing through by the SM cross section, σ_i^{SM}, provides a scaling function for each bin, $\mu_i(c_j)$, which parametrizes deviations in the cross section in terms of the c_j parameters. The general form of the scaling function is given in Eq. 3.

$$\mu_i(c_j) = 1 + \sum_j A_j^i c_j + \sum_{jk} B_{jk}^i c_j c_k \tag{3}$$

The tool then automates running MADGRAPH to generate events, passing them through PYTHIA before running RIVET on the output. It handles splitting these steps into several independent parallel jobs, supporting both multi-process running on a single machine as well as a number of commonly used batch computing systems.

In order to determine the A_j and B_{jk} coefficients the cross sections in each bin, $\sigma_i^{\text{EFT}}(c_j)$, is sampled at a series of points in c_j. One approach is to generate multiple samples, each with varied c_j values. There are however some drawbacks to this approach: the minimum number of independent samples needed is $2N + (N^2 - N)/2$, which may become computationally prohibitive if N is large. In addition, the statistical uncertainties in each sample must be propagated to the extracted coefficients, which may have a large impact if the C_j for each sample are not well-chosen. For example, the precision on σ_{int}, calculated from the difference between two samples giving σ_{SM} and $\sigma_{\text{SM}} + \sigma_{\text{int}}$ will be limited if the C_j are chosen such that $\sigma_{\text{int}} << \sigma_{\text{SM}}$.

A more efficient approach, and the one utilised in EFT2Obs, is to generate a single sample in which a set of weights is calculated for each event, using the reweighting module in MADGRAPH [277]. Each weight W corresponds to the original event weight W_{orig} multiplied by the ratio of LO squared matrix elements: $|M_{\text{new}}|^2/|M_{\text{orig}}|^2$, with the numerator evaluated at the specified values of c_j and the denominator giving the matrix element used for the event generation. The tool will automatically generate the reweighting configuration for MADGRAPH. For this it uses the set of parameters requested by the user and corresponding set of non-zero values, denoted D_i. Considering a simple case where only two operators are considered, c_1 and c_2, Table 1 gives the set of parameter configurations that will be evaluated. The generalisation

to any number of operators is straightforward: two weights are needs to calculate the linear and squared terms for each parameter in turn, and an additional weight is needed for each $c_j c_k$ combination where $j \neq k$.

Table 1: The set of weights for the two parameter case. The values of c_1 and c_2 for each weight are given, along with expressions for the weights in terms of the A_j and B_{jk} factors which are sampled in each event. The final column gives the expression for the weights after a transformation is applied.

Label	c_1	c_2	Weight	Transformed weight
W_1	0	0	1	1
W_2	$0.5D_1$	0	$1 + 0.5D_1 A_1 + 0.25{D_1}^2 B_{11}$	$D_1 A_1$
W_3	D_1	0	$1 + D_1 A_1 + {D_1}^2 B_{11}$	${D_1}^2 B_{11}$
W_4	0	$0.5D_2$	$1 + 0.5D_2 A_2 + 0.25{D_2}^2 B_{22}$	$D_2 A_2$
W_5	0	D_2	$1 + D_2 A_2 + {D_2}^2 B_{22}$	${D_2}^2 B_{22}$
W_6	D_1	D_2	$1 + D_1 A_1 + D_2 A_2 + {D_1}^2 B_{11} + {D_2}^2 B_{22} + D_1 D_2 B_{12}$	$D_1 D_2 B_{12}$

The final output from RIVET is a set of histograms for each observable, one per event weight configuration. In each histogram the sum of the weights and sum of squared weights is stored, allowing the mean weight and associated standard error to be determined. From these the averages $\overline{A_j}$ and $\overline{B_{jk}}$ can be extracted. However it is important to note that as shown in Table 1 the A_j and B_{jk} distributions are not sampled directly. For example in W_3 the distribution of $1 + D_1 A_1 + D_{(1)}^2 B_{11}$ is sampled when $c_1 = D_1$, since both the interference and SM-independent contributions are included by default. While the $\overline{A_j}$ and $\overline{B_{jk}}$ can be determined via linear algebra from the set of $\overline{W_i}$, it is generally not possible to isolate their standard errors given only the standard errors on the $\overline{W_i}$. As a solution, an event-by-event transformation of the weights is performed before the events are passed through RIVET, in order to isolate the A_j and B_{jk} distributions. The transformed weights are given in the final column of Table 1.

3 Example

This section gives an example of parametrizing the ZH production process using the Higgs Effective Lagrangian (HEL) model [278, 279], and using the STXS RIVET routine to study the effect on the $p_T(Z)$ distribution. The HEL model introduces 39 flavour independent dimension-6 operators, $\mathcal{O}_j$. Table 2 summarises the relevant operators considered in this example, and the normalisation convention used for each of the corresponding parameters c_j.

Within EFT2Obs a `proc_card.dat` file is specified which imports the HEL model and defines the leading order ZH process, limited to at most one vertex that depends on an EFT parameter using the `NP<=1` syntax.

```
import model HEL_UFO
define ell+ = e+ mu+ ta+
define ell- = e- mu- ta-
define j2 = g u c d s u~ c~ d~ s~
generate p p > h ell+ ell- / j2 ell+ ell- vl vl~ a h w+ w- NP<=1 @0
output zh
```

Table 2: The HEL operators and the corresponding parameters considered in this example. Also given are the relevant vertices which are modified by these operators.

Operator	Expression	Parameter	Relevant vertices
$\mathcal{O}_A$	$|H^2|B_{\mu\nu}B^{\mu\nu}$	$c_A = \frac{m_W^2}{g'^2}\frac{f_A}{\Lambda^2}$	H$\gamma\gamma$
$\mathcal{O}_{HW}$	$i(D^\mu H)^\dagger \sigma^a (D^\nu H)W^a_{\mu\nu}$	$c_{HW} = \frac{m_W^2}{2g}\frac{f_{HW}}{\Lambda^2}$	HWW, HZZ
$\mathcal{O}_{HB}$	$i(D^\mu H)^\dagger (D^\nu H)B_{\mu\nu}$	$c_{HB} = \frac{m_W^2}{g'}\frac{f_{HB}}{\Lambda^2}$	HZZ
$\mathcal{O}_W$	$i(H^\dagger \sigma^a \overleftrightarrow{D}^\mu H)D^\nu W^a_{\mu\nu}$	$c_{WW} = \frac{m_W^2}{g}\frac{f_{WW}}{\Lambda^2}$	HWW, HZZ
$\mathcal{O}_B$	$i(H^\dagger \overleftrightarrow{D}^\mu H)\partial^\nu B_{\mu\nu}$	$c_B = \frac{2m_W^2}{g'}\frac{f_B}{\Lambda^2}$	HZZ

Using this file as input, the MADGRAPH directory structure for the process is then created. A configuration file in JSON format is also needed, which in this case specifies that c_A, c_{HW}, c_{HB}, c_{WW} and c_B are the parameters of interest, that $D_i = 0.01$ should be used in the reweighting, and that all other parameters should be set to zero throughout. It should be noted that the choices of D_i are in principle arbitrary, but should be chosen such that the resulting weights are not so large or small as to cause issues with numerical precision. From this configuration file a reweighting card is created automatically which specifies the 20 points in c_i that will be evaluated.

A sample of events is then generated and the reweighting and weight transformation described in the previous section are performed. The events are hadronised and showered with PYTHIA and passed through the RIVET routine. From the output histograms the scaling terms for each bin of the $p_T(Z)$ distribution are calculated, along with the associated statistical uncertainty. An example of the output for a single bin and just two parameters is given below.

```
-------------------------------------------------------------------
Bin 0    numEntries: 77325      mean: 1.25e-10   stderr: 2.95e-15
-------------------------------------------------------------------
Term                 |      Value |      Uncert | Rel. uncert.
-------------------------------------------------------------------
chw                  |     4.7348 |      0.0083 |       0.0018
chb                  |     1.4179 |      0.0025 |       0.0018
chw^2                |     7.5364 |      0.1640 |       0.0218
chb^2                |     0.6758 |      0.0147 |       0.0218
chw * chb            |     4.5137 |      0.0982 |       0.0218
```

The uncertainty on each term can be useful in estimating the additional number of events needed to reduce the uncertainty to a particular level. The full parametrisation in four coarse bins of $p_T(Z)$ is given in Table 3. Figure 1 shows the distribution expected in the SM along with a few examples for non-zero values of the c_j. The statistical uncertainty on the A_j and B_{jk} is propagated to these distributions.

4 Investigating acceptance corrections

As previously mentioned, the approach documented in this section is limited by assuming the introduction of non-SM kinematics has a negligible effect on the experimental acceptance. By

Table 3: The scaling functions produced by the EFT2Obs tool for four bins of $p_{\mathrm{T}}(\mathrm{Z})$ in ZH production.

$p_{\mathrm{T}}(\mathrm{Z})$ bin [GeV]	Scaling
0–50	$1 + 24.9\,c_{WW} + 6.9\,c_B + 4.7\,c_{HW} + 1.4\,c_{HB} + 4.7\,c_A + 160.2\,c_{WW}{}^2 + 12.9\,c_B{}^2 + 7.5\,c_{HW}{}^2 + 0.7\,c_{HB}{}^2 + 7.2\,c_A{}^2 + 88.8\,c_{WW}\,c_B + 60.9\,c_{WW}\,c_{HW} + 18.2\,c_{WW}\,c_{HB} + 59.9\,c_{WW}\,c_A + 17.1\,c_B\,c_{HW} + 5.1\,c_B\,c_{HB} + 18.5\,c_B\,c_A + 4.5\,c_{HW}\,c_{HB} + 10.7\,c_{HW}\,c_A + 3.2\,c_{HB}\,c_A$
50–100	$1 + 29.4\,c_{WW} + 8.3\,c_B + 8.1\,c_{HW} + 2.4\,c_{HB} + 5.1\,c_A + 227.6\,c_{WW}{}^2 + 18.6\,c_B{}^2 + 25.2\,c_{HW}{}^2 + 2.3\,c_{HB}{}^2 + 8.6\,c_A{}^2 + 127.9\,c_{WW}\,c_B + 126.5\,c_{WW}\,c_{HW} + 37.9\,c_{WW}\,c_{HB} + 77.1\,c_{WW}\,c_A + 35.9\,c_B\,c_{HW} + 10.7\,c_B\,c_{HB} + 23.6\,c_B\,c_A + 15.1\,c_{HW}\,c_{HB} + 17.7\,c_{HW}\,c_A + 5.3\,c_{HB}\,c_A$
100–200	$1 + 43.3\,c_{WW} + 12.5\,c_B + 20.0\,c_{HW} + 6.0\,c_{HB} + 5.6\,c_A + 518.6\,c_{WW}{}^2 + 43.5\,c_B{}^2 + 160.6\,c_{HW}{}^2 + 14.4\,c_{HB}{}^2 + 12.1\,c_A{}^2 + 298.2\,c_{WW}\,c_B + 503.6\,c_{WW}\,c_{HW} + 150.8\,c_{WW}\,c_{HB} + 127.1\,c_{WW}\,c_A + 145.6\,c_B\,c_{HW} + 43.6\,c_B\,c_{HB} + 38.5\,c_B\,c_A + 96.2\,c_{HW}\,c_{HB} + 41.9\,c_{HW}\,c_A + 12.6\,c_{HB}\,c_A$
200–400	$1 + 91.4\,c_{WW} + 26.9\,c_B + 66.4\,c_{HW} + 19.9\,c_{HB} + 6.1\,c_A + 2521.2\,c_{WW}{}^2 + 219.5\,c_B{}^2 + 1630.0\,c_{HW}{}^2 + 146.2\,c_{HB}{}^2 + 23.6\,c_A{}^2 + 1485.2\,c_{WW}\,c_B + 3825.9\,c_{WW}\,c_{HW} + 1145.7\,c_{WW}\,c_{HB} + 295.3\,c_{WW}\,c_A + 1128.2\,c_B\,c_{HW} + 337.8\,c_B\,c_{HB} + 89.0\,c_B\,c_A + 976.2\,c_{HW}\,c_{HB} + 127.6\,c_{HW}\,c_A + 38.2\,c_{HB}\,c_A$

including acceptance cuts in the RIVET routine, it becomes possible to study EFT corrections to this acceptance.

Figure 2 shows the dilepton invariant mass, $m_{\ell\ell}$, distribution for the ZH process in the SM and for a non-zero value of c_{HW}. Experimental acceptance ensures events at low $m_{\ell\ell}$ do not enter current analyses and the effects of such selections can be studied with the EFT2Obs tool. In this particular case, the c_{HW} dependency varies by at most a few per cent across the entire $m_{\ell\ell}$ spectrum.

5 Summary

This report has described the main features of a software tool, EFT2Obs, to assist in the parametrization of observables by EFT parameters. The current implementation features several limitations that will be addressed in future developments. In particular, the tool requires there is at most one vertex containing the new operators in each diagrams produced. In the example of the Higgs processes given here this means that new physics contributions can be studied in either Higgs boson production or decay, but not both simultaneously. This restriction can be lifted by sampling an expanded set of points in the reweighting step, such that terms at more than second order in the c_i can be evaluated. In addition, the parametrization of processes at next-to-leading order in QCD is not currently supported, but can implemented following a conceptually similar approach to the leading-order case presented here.
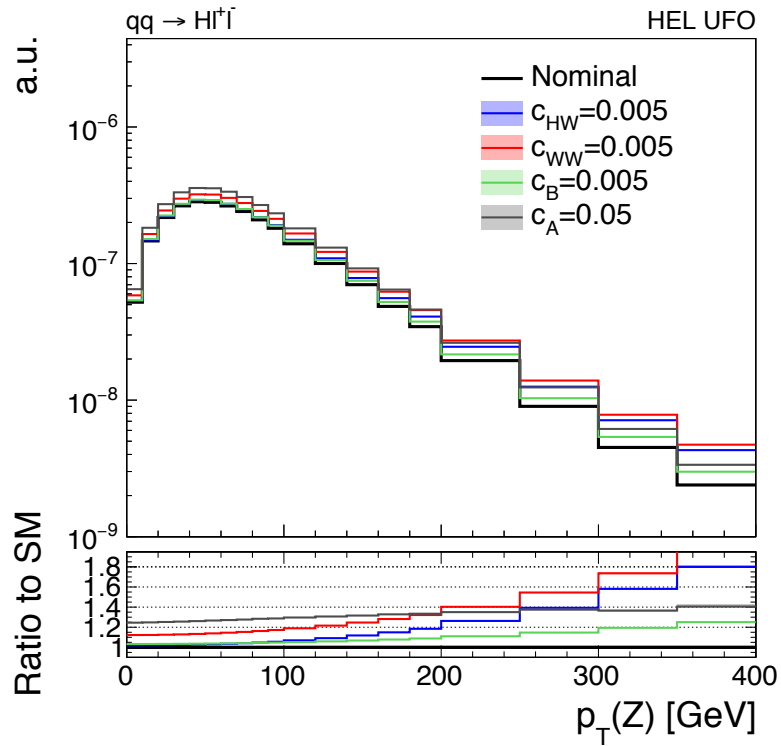
Figure 1: Distribution of $p_T(Z)$ comparing the SM expectation (black) to the SM with the inclusion of non-zero EFT coefficients in the Higgs Effective Lagrangian.
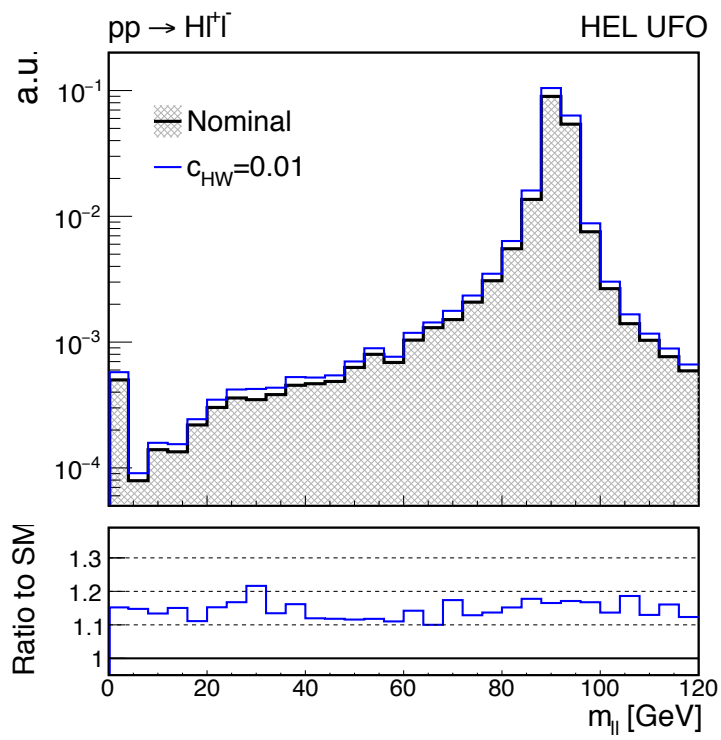
Figure 2: Distribution of $m_{\ell\ell}$ comparing the SM expectation (black hatched) to the SM with the inclusion of contributions from the HEL parameter, c_{HW} (0.01).

Contribution 15

On the use of likelihood information for reinterpreting LHC results

G. Alguero, J. Araz, B. Fuks, S. Kraml, W. Waltenberger

Abstract

Both the ATLAS and CMS collaborations have started to provide information on background correlations for some of their searches. This is extremely useful for re-interpretation purposes, as it allows one to construct a proper likelihood from the combination of signal regions (SRs) of a given search. The two collaborations follow quasi-ortogonal approaches: while CMS provides the linear correlations between the background contributions as simple covariance matrices, ATLAS recently released the full likelihood model for two analyses. We discuss the usage of this (simplified or full) likelihood information in two public re-interpretation tools, MADANALYSIS 5 [72] and SMODELS [68].

1 CMS simplified likelihoods

For most of its Run 2 analyses of $36\,\mathrm{fb}^{-1}$ of data, the CMS SUSY group made available approximate covariance matrices for the background estimates in various search regions, or a reduced set thereof. These covariance matrices can be used to build a simplified likelihood [280] for any signal model. The underlying assumptions are that systematic uncertainties in the signal modeling can be neglected, and that uncertainties on the background contributions are Gaussian such that the distribution of the number of background events is symmetric around the expectation. Although approximate, the combination of SRs through this simplified likelihood scheme greatly improves the constraining power of analysis recasts.

The combination of SRs via the simplified likelihood approach has been available in SMODELS since v1.2.0 (Aug 2018) [68]. We adopt this implementation in SMODELS, *i.e.* the relevant python module for use in MADANALYSIS 5 (v1.8 onwards). In order to comply with the MADANALYSIS 5 framework [72], the covariance information has to be included in the `.info` file associated with the studied analysis. For each region, the covariance with every other region must be supplied. There is thus a list of covariances with two entries: the paired region and the value of the covariance. The standard syntax of the `.info` file

```
<analysis id="analysis name">
    <region type="signal" id="region name">
        <nobs> ... </nobs>
        <nb> ... </nb>
        <deltanb> ... </deltanb>
    </region>
    ...
</analysis>
```

specifying, for each SR, the number of observed events `<nobs>`, expected background events `<nb>` and their uncertainty `<deltanb>`, is therefore extended as follows:

```
<analysis id="analysis name" cov_subset="combined SRs">
    <region type="signal" id="region name">
        <nobs> ... </nobs>
        <nb> ... </nb>
        <deltanb> ... </deltanb>
        <covariance region="first SR name">...</covariance>
        <covariance region="second SR name">...</covariance>
        ...
        <covariance region="last SR name">...</covariance>
    </region>
    ...
</analysis>
```

If a covariance is not supplied, it will be considered as zero in the covariance matrix. However, if a region does not contain any covariance field, it will not be included in the SR combination. This feature can be useful if the covariance matrix is available only for a subset of SRs, like for example in the CMS multilepton plus missing transverse energy (E_T^{miss}) search `CMS-SUS-16-039` [281] which provides covariances only for SRs of type A. In order to keep trace of which subset of SRs is combined, we introduce a `cov_subset` attribute in the `<analysis>` tag, in which one can give a brief description of the subset of SRs for which the covariance is available. For the `CMS-SUS-16-039` example, this is

```
<analysis id="cms_sus_16_039" cov_subset="SRs_A">
```

This description will be printed in the output file (`CLs_output_summary.dat`) with the result from the simplified likelihood combination, just after the usual exclusion information under the format

```
<set> <tag> <cov_subset> <exp> <obs> <CLs> ||
```

The successive elements consist of the dataset name, the analysis name, the description of the subset of combined SRs, the expected and observed cross section upper limits at 95% confidence level (CL), and finally the exclusion level, $1 - \mathrm{CL}_s$. A concrete example reads

```
defaultset  cms_sus_16_039  [SL]-SRs_A  10.4851515  11.1534040  0.9997  ||
```

where 'SL' stands for 'simplified likelihood'. The statistical error, usually provided after the double bar, is not printed here as it is already encoded in the simplified likelihood calculation.

To illustrate the gain in constraining power, we stay with the example of the `CMS-SUS-16-039` analysis, which is available as recast code [282] in the MADANALYSIS 5 PAD (Public Analysis Database), and whose `.info` file we extended by the covariance information provided by CMS for the SRs of class A. The analysis is searching for supersymmetry through multilepton plus E_T^{miss} final states, and the set of SRs class A specifically concerns final states with three electrons or muons comprising at least one opposite-sign-same-flavour pair.

The targeted process is chargino/neutralino associated production, $pp \rightarrow \tilde{\chi}_1^{\pm} \tilde{\chi}_2^0$, with $\tilde{\chi}_1^{\pm} \rightarrow W^{\pm} \tilde{\chi}_1^0$ and $\tilde{\chi}_2^0 \rightarrow Z^0 \tilde{\chi}_1^0$ decays. Focusing on such a signal, we simulate events with
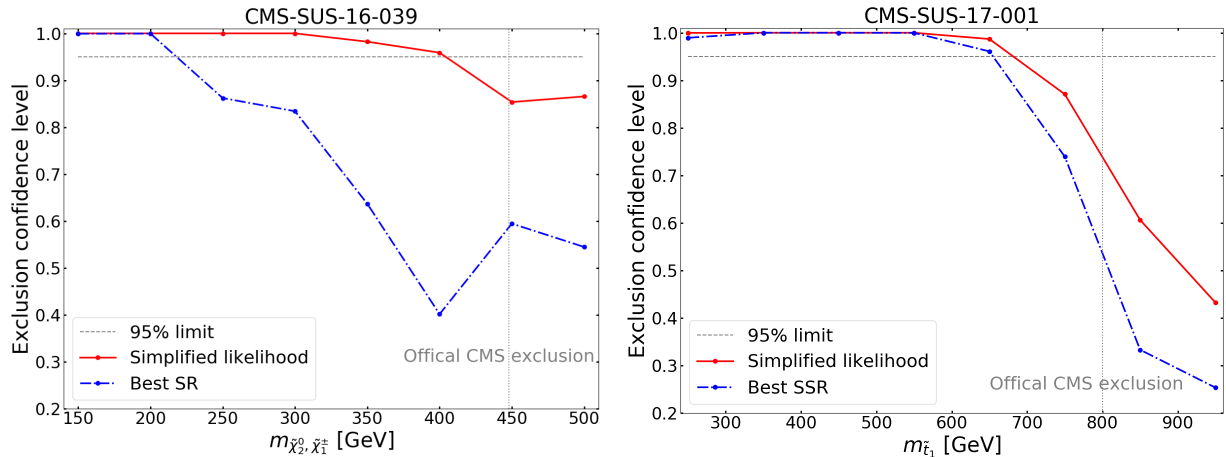
Figure 1: Exclusion CL from recasts of the CMS multilepton analysis [281] for the TChiWZ simplified model (left) and of the CMS dilepton stop search [286] for the T2tt simplified model (right). In both figures, $m_{\tilde{\chi}_1^0} = 50$ GeV. The official CMS bounds are indicated as vertical dotted lines.

MADGRAPH 5_AMC@NLO [19] and PYTHIA 8 [28], assuming wino-like $\tilde{\chi}_1^\pm$, $\tilde{\chi}_2^0$ with $m_{\tilde{\chi}_1^\pm} = m_{\tilde{\chi}_2^0}$ and 100% branching ratio into the $WZ + E_T^{\mathrm{miss}}$ final state (so-called TChiWZ simplified model). We normalise the event samples to cross sections evaluated at the next-to-leading order matched with next-to-leading-logarithmic threshold resummation (NLO+NLL) [283, 284], using the CTEQ6.6 PDF set [285].[1] We then reinterpret the results of the CMS-SUS-16-039 search in MADANALYSIS 5.

Figure 1 (left) displays the resulting exclusion CL as a function of the common chargino/neutralino mass $m_{\tilde{\chi}_1^\pm, \tilde{\chi}_2^0}$ for a fixed lightest neutralino mass $m_{\tilde{\chi}_1^0} = 50$ GeV. It turns out that in the conventional approach of using only the 'best' (*i.e.* the most sensitive) SR for limit setting (blue), only values up to $m_{\tilde{\chi}_1^\pm, \tilde{\chi}_2^0} \approx 220$ GeV can be excluded at the 95% CL. The combination of SRs in the simplified likelihood approach allows to extend this range to $m_{\tilde{\chi}_1^\pm, \tilde{\chi}_2^0} \approx 400$ GeV (red), which is only slightly below the official CMS bound (vertical dotted line).

Given the covariance matrix, one may also define new 'aggregated' search regions tailored to the new physics model of interest, provided they are defined as the union of existing analysis search regions. In this case the covariance matrix can be used to extract the total uncertainty on the background expectation in the aggregated regions [280]. The implementation of the simplified likelihood in SMODELS makes use of this option in order to reduce the computing time [68]. As some information (and thus precision) is lost in the aggregation process, care must be taken to aggregate SRs without too much loss in constraining power (see *e.g.* Fig. 1 in ref. [68] and the related discussion in there).

Because of the huge number of SRs in some analyses, CMS sometimes introduces 'super signal regions' (SSRs) in order to facilitate recasting. These SSRs are usually aggregated SRs, that should allow for the reproduction of official CMS bounds with good precision without the need of combination. One example available in the MADANALYSIS 5 PAD is the recast code [287] emulating the CMS search for stops in the dilepton final state CMS-SUS-17-001, which includes three SSRs [286]. Figure 1 (right) compares the constraints on stop pair production, $pp \to \tilde{t}_1 \tilde{t}_1^*$, followed by $\tilde{t}_1 \to \tilde{\chi}_1^0$ with 100% BR (T2tt simplified model) using only the best

---

[1]See https://twiki.cern.ch/twiki/bin/view/LHCPhysics/SUSYCrossSections.

SSR (blue), or combining the three SSRs in the simplified likelihood approach (red). As above, we simulated events with MADGRAPH 5_AMC@NLO and PYTHIA 8, and applied NLO-NLL cross sections [288] as quoted by the SUSY cross section working group. We observe that the combination gives only a slight, though still noticable, improvement.

Super signal regions are also defined in CMS-SUS-16-039. In this case they are, however, *not* appropriately aggregated regions from the full analysis, and neither of the mass points would be excluded in Figure 1 (left), as the exclusion CL would never reach the 95% level.

Last but not least, the covariances published by CMS encode only the linear correlation between the background contributions, *i.e.* they assume symmetric Gaussian uncertainties. To correctly account for asymmetries, ref. [289] proposes a convenient and easy-to-use simplified likelihood scheme that keeps the next-to-leading term in the large N expansion. We hope that this will be adopted in the future.

2 ATLAS full likelihoods

The ATLAS collaboration recently started to provide complete likelihoods associated with statistical fits used in searches for new physics on HEPDATA [290]. This is based on HISTFACTORY [291] and embedded in a JSON scheme, which enables the usage of the HISTFACTORY structure outside the ROOT framework. For a given likelihood, the PYHF package [292] allows for, *e.g.*, the calculation of the CL$_s$ value from the corresponding statistical model. So far, such JSON likelihood data is available for two analyses, the ATLAS 2019 sbottom multi-b search [293] and the search for direct stau production [53], both using the full Run 2 dataset $(139 \, \text{fb}^{-1})$.

For the usage of this full likelihood information in MADANALYSIS 5, the relevant JSON files must be located in the same analysis folder as the recast code (done automatically when downloading from the MADANALYSIS 5 online repository at the time of the PAD installation). Moreover, the .info file must include new <pyhf> elements specifying the names of the JSON files together with the corresponding channels (ensembles of SRs) and the regions they include, as defined in the JSON files. In the example of the sbottom search [293] (ATLAS-SUSY-2018-031), assuming that the signal does not leak into validation/control regions (VRs/CRs) as only SRs are currently being recasted, this gives for regions A

```
<pyhf id="RegionA">
  <name>atlas_susy_2018_031_SRA.json</name>
    <regions>
      <channel name="SR_meff">SRA_L SRA_M SRA_H</channel>
      <channel name="VRtt_meff"> </channel>
      <channel name="CRtt_meff"> </channel>
    </regions>
</pyhf>
```

and analogous for regions B and C. Whenever the exclusion is computed by means of the PYHF package, the results are reported in the CLs_output_summary.dat output file in the form

```
  <set> <tag> <SR> <best?> <exp> <obs> <CLs> ||
```

No statistical error information is printed (to the right of the double bars), as it is already accounted for in the likelihood calculation.

For these proceedings, we implemented the `ATLAS-SUSY-2018-031` analysis in the MAD-ANALYSIS 5 framework. Focusing on the benchmark point $m_{\tilde{b}_1} = 1100$ GeV, $m_{\tilde{\chi}_2^0} = 330$ GeV and $m_{\tilde{\chi}_1^0} = 200$ GeV from the ATLAS study, we simulated sbottom pair production followed by $\tilde{b}_1 \to b\tilde{\chi}_2^0$, $\tilde{\chi}_2^0 \to h\tilde{\chi}_1^0$ with MADGRAPH5_AMC@NLO and PYTHIA 8; we used the LO cross sections from MADGRAPH and merged matrix elements featuring up to two additional jets following the MLM prescription [151]. The result in the `CLs_output_summary.dat` file reads

```
defaultset atlas_susy_2018_031 [pyhf]-RegionA-profile 1 0.0020761 0.0013821 0.9959  ||
defaultset atlas_susy_2018_031 [pyhf]-RegionB-profile 0 -1        -1        0.0000  ||
defaultset atlas_susy_2018_031 [pyhf]-RegionC-profile 0 0.1139845 0.1846410 0.0293  ||
```

and includes expected (`<exp>`) and observed (`<obs>`) cross sections excluded at the 95% CL, as well as the exclusion level obtained for each likelihood (`<CLs>`). Further validation and tests are ongoing, both for the PYHF interface and the implementation of the ATLAS-SUSY-2018-031 analysis within MADANALYSIS 5. The integration of theoretical uncertainties into the likelihood is also planned.

Work on an interface of the PYHF package with SMODELS is also underway. This is much helped by the fact that both the sbottom and stau ATLAS analyses provide signal acceptance and efficiency maps for all SRs in addition to cross section upper limits, which is exactly what is needed by SMODELS. The implementation of these maps in the SMODELS database is currently being validated, with a release foreseen for the v1.2.3 database. Last but not least we note that the communication with the PYHF team on questions regarding the usage of the JSON scheme is handled via github's issue tracking system and is thus transparent and open to all, see *e.g.* https://github.com/scikit-hep/pyhf/issues/620.

3 Conclusions

After SMODELS v1.2, MADANALYSIS 5 v1.8 will also be able to exploit the covariance information provided by the CMS collaboration in the simplified likelihood scheme. We have demonstrated the gain in constraining power, and hope CMS will continue to make background correlation data available in digitised form for the final Run 2 results. We also advocate to use the scheme of ref. [289] whenever assymetric uncertainties are relevant for simplified likelihoods.

Moreover, the integration of the full likelihood information via the JSON format, as recently released by the ATLAS collaboration for two analyses, is on the way in both MAD-ANALYSIS 5 and SMODELS. We highly welcome this important move by ATLAS to publish full likelihoods.

Contribution 16

Determination of Independent Signal Regions in LHC Searches for New Physics

A. Buckley, B. Fuks, H. Reyes-González, W. Waltenberger, S. L. Williamson

Abstract

The first two runs of the LHC have aggregated an astonishing number of published searches for new physics – nearly 600 from ATLAS and CMS alone at the time of writing. Since no "smoking gun" signatures have been found, attention has turned to less canonical Beyond the Standard Model (BSM) models than the (typically simplified) ones originally used by the experiments to contextualise their results. Reinterpretation of BSM searches in the contexts of more complex or subtle models is hence now a very important topic, but full exploitation of the rich trove of experimental results requires care with analysis combination: with so many experimental results, manual cross-referencing of $\mathcal{O}(600)$ publications to avoid double-counting is not a realistic option. Indeed, even with the time to compare all pairs of released studies, it is non-trivial, to say the least, for a person outside the experimental collaborations to answer the question of which analyses can be considered to be approximately uncorrelated. This Les Houches contribution aims at filling this gap, using a probabilistic approach to identify pairs of analyses that can safely be considered uncorrelated in global BSM reinterpretation fits.

1 Introduction

At the time of this writing, the LHC search programmes for new physics has produced hundreds of publications with an even larger number of individual simplified model space (SMS) results. The results are typically presented as upper limits on production cross sections or signal efficiency "maps" for a small number of simplified models. It is therefore of utmost importance that the wider community is able to re-derive these results and to determine the viability of less explored models under the current collider constraints. To obtain an accurate prediction, a recasting of multiple analyses exploring different parts of the parameter space must often be carried out, but this raises the question: which analyses can be combined? In this manner, we want to determine subsets of analyses whose event selection criteria do not overlap.

Generally, analyses implemented by different collaborations (*e.g.* ATLAS *vs.* CMS) can safely be considered to be uncorrelated, as are those carried out at different centre of mass energies (*e.g.* 13 TeV *vs.* 7 TeV). In addition, within this work we look only at signal regions, and do not consider possible correlations between control regions, as we assume such correlations to be second order effects and negligible for reinterpretation purposes. Our considerations thus focus on the signal regions, and we attempt to answer the question of whether any given pair of

signal regions overlap in the space of all measured quantities or not. Using the analyses contained both in SModelS [68, 294–297] and MadAnalysis 5 [20, 71–73], we want to determine the parameter space covered by the topologies that populate these signal regions and generate events to cover all the signal regions, enabling us to infer correlations between the analyses.

To determine which pairs of analyses are uncorrelated, we pursue the following strategy. Restricting ourselves to analyses implemented both in the SModelS v1.2.2 and MadAnalysis 5 v1.8.20 frameworks, we use the SModelS database to extract the simplified models that a given analysis is sensitive to, alongside with the mass ranges for the BSM particles. We then sample this space of simplified model mass parameters and create random, realistic events from these simplified models using MadGraph5_aMC@NLO [19]. These events are then passed to a modified version of MadAnalysis 5, which as usual checks whether an event passes the cuts in each signal region (SR), but in addition records the corresponding set of SR cuts passed for every event. Using this information, a statistical bootstrap procedure is used to extract a correlation matrix relating every signal region through the events that co-populate them.

2 Implementation

To investigate the analysis correlations, we chose to use the overlap of analyses implemented both in SModelS and MadAnalysis 5: at the time of publication, these are ATLAS-SUSY-2015-06 [298], CMS-SUS-16-039 [281], CMS-SUS-16-033 [299] and CMS-SUS-17-001 [286], all being searches for supersymmetry (SUSY). A description of the signal regions under consideration is shown in tables 2 to 12 in the appendix.

2.1 Topology identification:

Using the SModelS database, we extract the topologies that a certain analysis is sensitive to, as denoted in table 1, and consequently the mass parameter space the analysis can access. A topology describes a specific cascade decay, which, in the case of simplified models, is reduced to a 2- or 3- body decay with symmetric branches. A full list of the topologies contained in SModelS is given in https://smodels.github.io/. In the case of 3- body decays, the topology is reduced further so that the mass of the intermediate particle is fixed as a function of that of the mother and granddaughter.

Two analyses may both be sensitive to a given topology, but in different yet overlapping regions of the simplified model space that depends on the masses of the mother and daughter particles, denoted by m_0 and m_1 respectively. We want to generate events that randomly populate the union of the two regions without doubly populating the regions that are in common. We deduce this convex mass hull using the efficiency maps in SModelS: the efficiency maps provide upper limits on the production cross sections as a function of the masses of the simplified model particles. If the efficiency map of the point chosen in the parameter space is 0, then we move on to probe a different part of the parameter space until eventually a contour can be interpolated around the range of mass points that can be touched by the different analyses. For topologies involving two-body decays, this curve is obtained by sampling values of m_0, and determining the minimum and maximum m_1 values for which the regions are populated by the corresponding signal. When three-body decays are involved, the scan is expanded tri-dimensionally to determine minimum and maximum values of m_2 (the mass of the granddaughter particle) for a given m_1 and m_0 for which the SRs are populated.

Tag	Analysis	Topologies
A0(A-K,SS)	CMS-SUS-16-039	TChiWZ,TChiWZ(off), TChiWH, TChipmSlepL, TChiChipmStauStau, TChiChipmSlepStau
A1	CMS-SUS-16-033	T1, T1bbbb, T1tttt(off), T2, T2bb, T2tt(off)
A2	CMS-SUS-17-001	T2tt(off), T6bbWW
A3	ATLAS-SUSY-2015-06	T1, T2

Table 1: Table showing the sample of analyses investigated, with the names of the topologies reached and the tag-name used to refer to the analysis in the figures that follow.

2.2 Event generation and analysis:

We produce 50000 events evenly distributed over the corresponding convex mass hulls for each topology. These events have been generated with `MadGraph5_aMC@NLO`, using the standard MSSM UFO implementation shipped with the package [300]. Hard-scattering events have been matched with parton showers, as described with `Pythia` 8.2 [28] that has also handled hadronisation. As parameter inputs, we used template SLHA files [42], specific for each topology.

Hadron-level events are passed to `MadAnalysis` 5, whose expert mode (from v1.8.20 onwards) has been augmented by two new functions (`DumpSR` and `HeadSR`) dedicated to the writing to a file of the information on how a given event populates the various signal regions of the recasted analyses under consideration. In practice, the main executable of the recasting module (located in `tools/PAD/Build/Main/main.cpp`) has to be modified so that `HeadSR` is called prior to the event loop (in the `Execute` function), and that `DumpSR` is called within the event loop (*i.e.* for each event). The former function writes, as the first line of the output file, the signal regions as they are ordered internally in the code. The latter function writes, for each event, a set of 0 and 1 indicated whether the event populates each signal region (following the internal ordering). Both functions take an `ostream` object as argument.

2.3 Statistical framework:

The augmented `MadAnalysis` 5 output consists in a grid of binary flags indicating the pass/-fail status of each of N_{evt} event for each of the N_{SR} signal-region selections. In general, each event can have more than one "true" SR flag. This defines the correlation or co-population which makes analysis combination problematic, as a single unusual event could produce multiple observed analysis excesses. It would not make sense to count all such measures of the same event as if they were independent. To reduce this large matrix of binary flags to a more useful figure, we first make it much *larger*: by use of bootstrap sampling from a unit Poisson distribution, every event is multiplied by a set of N_{boot} "bootstrap samples", with sampled weights $w \sim \text{Pois}(\mu = 1)$ which replace the 0/1 binary SR weights. The total data structure is now a $N_{\text{evt}} \times N_{\text{SR}} \times N_{\text{boot}}$ tri-dimensional array of SR event weights - the SRs in each bootstrap history correlated through their common weight fluctuation. The event axis is then summed over, reducing to a two-dimensional $N_{\text{SR}} \times N_{\text{boot}}$ array of SR weight sums $W = \sum_{\text{evt}} w$, over the N_{boot} "histories". This two-dimensional array allows us to compute the correlation between two SRs i and j as usual via the covariance:

$$\text{cov}_{ij} = \langle W_i W_j \rangle - \langle W_i \rangle \langle W_j \rangle, \tag{1}$$
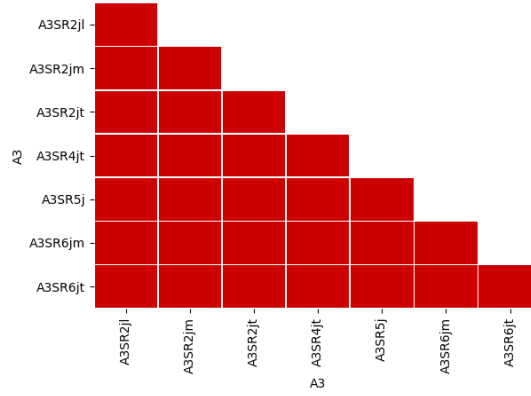
Figure 1: Matrix showing the correlation between the SRs of the A3 ATLAS analysis [298]. As expected for "inclusive" SRs, all the blocks in the matrix are red, denoting correlation between the SRs.

and

$$\rho_{ij} = \text{cov}_{ij}/\sqrt{\text{cov}_{ii}\text{cov}_{jj}} \,. \tag{2}$$

The averages here are computed over the bootstrap histories.

The correlations matrix ρ_{ij} acts as a sliding scale of event sharing between -1 and 1, and whether the combination of SRs i and j is acceptable can be decided by applying a cutoff $|\rho_{ij}| < \rho_{\max}$. With asymptotic statistics, ρ_{ij} should be positive, as there is no mechanism (such as normalisation by the sum of SR yields) to generate true negative correlations where an increase in yield for one SR due to weight fluctuations leads to the active depopulation of another. But with finite statistics random negative correlations can occur, and empirical study of their distribution can help in setting the $\rho_{\max}$ cutoff.

It is useful to note that this measure of correlation reflects where a pair of SRs are significantly correlated due to shared events, which is not the same as the logical existence of sharing. For example, naively one might imagine that an exclusive, low-statistics SR entirely contained within a much more inclusive, high-population one would be fully correlated with its parent. But this is not so: the fractional contribution of the events from the exclusive bin to the more inclusive one's weight-sum W may be negligibly small, such that a significant excess in the exclusive bin would not register as a significant change in the inclusive one. This normalised measure of sensitivity on the total yields of both SRs (which are the inputs to *e.g.* a Poisson profile likelihood calculation) automatically captures this nuance in a way that studies of cut overlaps cannot.

We have implemented this bootstrap procedure in a `Python` program called TACO (*Testing Analyses' COrrelations*), available at `https://github.com/hreyes91/TACO`. TACO takes as input a data frame in which each column corresponds to a SR, each row to an event, and which is filled with 1 and 0 depending on whether the event passes the cuts of the corresponding signal region. The program then generates a user-defined number of N_{boot} histories (here taken as 1200) and computes the correlations between the considered SRs from the produced $N_{\text{SR}} \times N_{\text{boot}}$ matrix. Afterwards, TACO determines if the SRs are approximately uncorrelated based on a user-defined $\rho_{\max}$ cut-off (here 0.05) and substitutes the ρ_{ij} coefficients with a 0 (if $|\rho_{ij}| < \rho_{\max}$) or a 1 (if $|\rho_{ij}| > \rho_{\max}$) to produce an "independence matrix", which is the final value of the calculation.
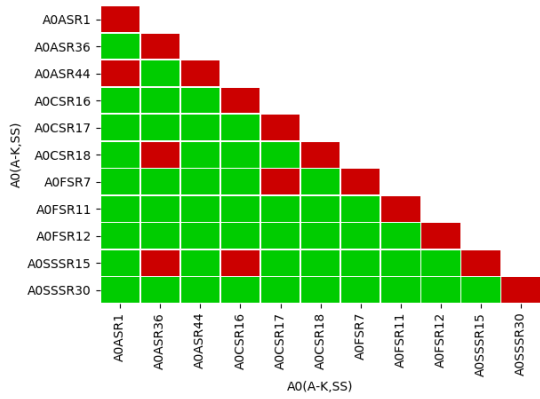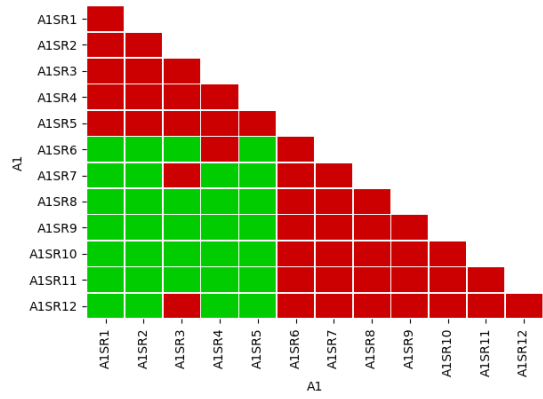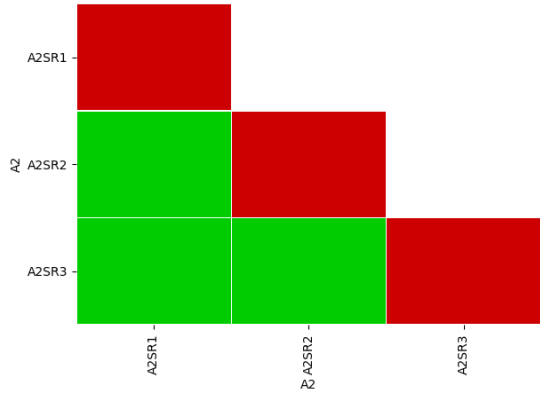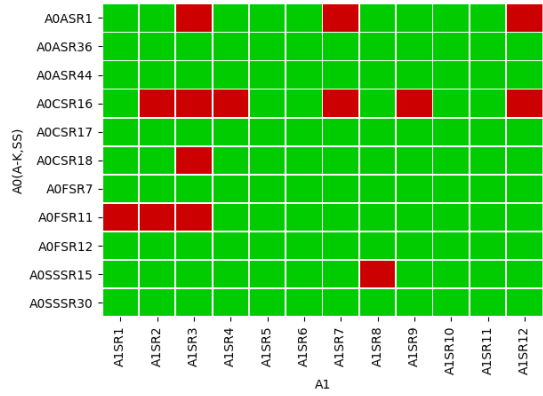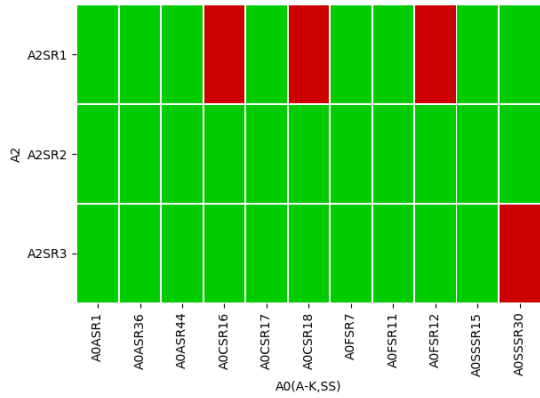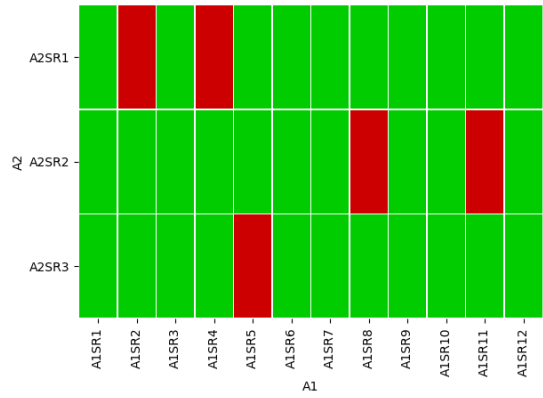
Figure 2: Matrices showing the correlations between the SRs of the CMS analyses under consideration that are populated with at least 300 events: A0(A-K,SS), A1 and A2. The green blocks denote that two SRs can be treated as approximately independent from each other, whereas the red blocks indicate that they are correlated.

The implementation of the bootstrap procedure was applied to the signal regions populated with at least 300 events; this includes those in the A1, A2, A3 analyses and 11 SRs from the A0(A-K,SS) analysis (see table 1 for the naming scheme). In our results given in Figs 1 and 2, green blocks denote SRs which are independent, whereas red blocks are not. In all figures exhibiting correlations between signal regions within a sole analysis (Figs. 1, 16.2(a), 16.2(b), 16.2(c)), the anti-diagonal elements are trivially correlated. Fig. 1 depicts the results originating from the A3 ATLAS analysis. As expected for "inclusive" SRs, these are tagged as correlated. For the considered CMS analyses, results are shown in Fig. 2 where we can see that "exclusive" SRs are normally estimated as uncorrelated. For instance, Fig. 16.2(b) shows that most of the A1SR(1-5) regions, where the number of b-jets is $N_b = 0$, are uncorrelated with the set of A1SR(6-12) regions in which $N_b \geq 1$. In addition, the the pairs of SRs that seem correlated feature a ρ parameter very close to the $\rho_{\max} = 0.05$ threshold, with $\rho = 0.06$. They could thus be expected to be found uncorrelated as soon as more events are included. In this way, the results we present are on the conservative side in the sense that correlated SRs will surely be flagged as correlated, but independent SRs can erroneously be flagged correlated if the number of bootstrap iterations is too low. Moreover, in Figs. 16.2(d), 16.2(e) and 16.2(f) the determination of the independency between SRs of *different* analyses is presented. As a quick sanity check, we see for example that the SRs A0CSR017 and ASCSR018 in fig 16.2(a) are independent; this is because despite looking in the same dilepton invariant and stansverse mass ranges, the missing transverse energy p_T^{miss} ranges do not overlap. For the most part, the SRs from the A0(A-K,SS), A1 and A2 analyses were determined as independent from each other, while the rest of these SRs are expected to be determined as such once the number of populating events is increased.

3   Conclusion

In this contribution, a probabilistic method for the determination of approximately uncorrelated pairs of analyses' SRs was developed. It is based on simplified models, and first results were presented using the intersection of analyses present in both `SModelS` and `MadAnalysis 5`. It is our pronounced hope that the effort will be repeated with a wider set of analyses with the aim to compile a complete detailed list of analyses that can be treated as independent from each other. Specifically, `CheckMATE` [69, 301] and its database is a potential future target for this effort. Given such a database, a potential future extension of this work is to identify the subset of independently populated SRs that maximises limit-setting power within a BSM parameter scan. The source code developed for this work can be accessed on Zenodo, see `http://doi.org/10.5281/zenodo.3634740`. In this document, only events originating from simplified model topologies were produced. In a future project, we wish to introduce also more complicated events to cover potential correlations that might be missed by too simplistic simplified models-based events.

Acknowledgements

in the context of the LABEX ILP (ANR-11-IDEX-0004- 02, ANR-10-LABX-63), which in particular funded the scholarship of SLW.

Appendix: Description of the considered signal regions

M_T [GeV]	p_T^{miss} [GeV]	$M_{ll} < 75$ GeV	$75 \geq M_{ll} < 105$ GeV	$M_{ll} \geq 105$ GeV
0–100	50–100	A0ASR1	A0ASR15	A0ASR32
	100–150	A0ARA2	A0ASR16	A0ASR33
	150–200	A0SRA3	A0ASR17	A0ASR34
	200-250	A0ASR4	A0ASR18	A0ASR35
	250–400	A0ASR5	A0ASR19	A0SR36
	400–500		A0ASR20	
	≥ 550		A0ASR21	
100–160	50–100	A0ASR6	A0ASR22	A0ASR37
	100-150	A0ASR7	A0ASR23	A0ASR38
	150–200	A0ASR8	A0ASR24	A0ASR39
	≥ 200	A0ASR9	A0ASR25	A0ASR40
≥ 160	50–100	A0ASR10	A0ASR26	A0ASR41
	100–150	A0ASR11	A0ASR27	A0ASR42
	150-200	A0ASR12	A0ASR28	A0ASR43
	200–250	A0ASR13	A0ASR29	A0ASR44
	250–400	A0ASR14	A0ASR30	
	≥ 400		A0SAR30	

Table 2: Summary of the A0A signal regions in the A0 analysis, cf. Ref. [281].

M_T(GeV)	p_T^{miss}(GeV)	$M_{ll} < 100$GeV	$M_{ll} \geq 100$GeV
0-120	50-100	A0BSR1	A0BSR4
	> 100	A0BSR2	A0BSR5
> 120	> 50	A0BSR3	A0BSR6

Table 3: Summary of the A0B signal regions in the A0 analysis, cf. Ref. [281].

p_T^{miss} [GeV]	$75 \geq M_{ll} < 105$ GeV	$M_{T2}(l_1 l_2)$[GeV]	$M_{ll} < 75$ GeV	$M_{ll} \geq 105$ GeV
50–100	A0CSR06		A0CSR01	A0CSR012
100–150	A0CSR07		A0CSR02	A0CSR013
150–200	A0CSR08		A0CSR03	A0CSR014
200–250	A0CSR09	0-100	A0CSR04	A0CSR015
250–300				
300–400	A0CSR10		A0CSR05	A0CSR016
≥ 400	A0CSR11			
50–200		≥ 100	A0CSR017	
≥ 200			A0CSR018	

Table 4: Summary of the A0C signal regions in the A0 analysis, cf. Ref. [281].

M_T [GeV]	p_T^{miss} [GeV]	$M_{ll} < 75$ GeV	$75 \geq M_{ll} < 105$ GeV	$M_{ll} \geq 105$ GeV
	50–100	A0DSR1	A0DSR6	A0DSR11
	100–150	A0DSR2	A0DSR7	A0DSR12
0–100	150–200	A0DSR3	A0DSR8	A0DSR13
	200–250	A0DSR4	A0DSR09	A0DSR14
	≥ 250	A0DSR5	A0DSR10	
≥ 100	50–200	A0DSR15		
	≥ 200	A0DS016		

Table 5: Summary of the A0D signal regions in the A0 analysis, cf. Ref. [281].

$M_{T2}(l_1, \tau)$ [GeV]	p_T^{miss} [GeV]	$M_{ll} < 60$ GeV	$60 \geq M_{ll} < 100$ GeV	$M_{ll} \geq 100$ GeV
	50–100	A0ESR1	A0ESR6	
	100–150	A0ESR2	A0ESR7	
0–100	150–200	A0ESR3	A0ESR8	A0ESR11
	200–250	A0ESR4	A0ESR9	
	≥ 250	A0ESR5	A0ESR10	
≥ 100	≥ 50	A0ESR15		

Table 6: Summary of the A0E signal regions in the A0 analysis, cf. Ref. [281].

$M_{T2}(l_1, \tau)$ [GeV]	p_T^{miss} [GeV]	$M_{ll} < 100$ GeV	$M_{ll} \geq 100$ GeV
	50–100	A0FSR1	A0FSR7
	100–150	A0FSR2	A0FSR8
0–100	150–200	A0FSR3	A0FSR9
	200–250	A0FSR4	
	250–300	A0FSR5	A0FSR10
	≥ 300	A0FSR6	
≥ 100	50–200	A0FSR11	
	≥ 200	A0FSR12	

Table 7: Summary of the A0F signal regions in the A0 analysis, cf. Ref. [281].

p_T^{miss} [GeV]	0 τ_h		1 τ_h	2 τ_h	
	nOSSF$\geq$2	nOSSF$<$ 2	nOSSF$\geq$ 0	nOSSF$\geq$ 2	nOSSF$<$ 2
0–50	A0GSR1	A0HSR1	A0ISR1	A0JSR1	A0KSR1
50–100	A0GSR2	A0HSR2	A0ISR2	A0JSR2	A0KSR2
100–150	A0GSR3	A0HSR3	A0ISR3	A0JSR3	
150–200	A0GSR4	A0HSR4	A0ISR4	A0JSR4	A0KSR3
$\geq$200	A0GSR5				

Table 8: Summary of the A0(G-K) signal regions in the A0 analysis, cf. Ref. [281].

N_{jets}		0			1		
M_T [GeV]		<100		>100	<100		>100
p_T^{ll} [GeV]		<50	>50		<50	>50	
$p_T^{\mathrm{miss}} < 100$ GeV		A0SSSR1	A0SSSR6	A0SSSR11	A0SSSR16	A0SSSR21	A0SSSR26
$100 \leq p_T^{\mathrm{miss}} < 150$ GeV	++	A0SSSR2	A0SSSR7	A0SSSR12	A0SSSR17	A0SSSR22	A0SSSR27
	- -	A0SSSR3	A0SSSR8	A0SSSR13	A0SSSR18	A0SSSR23	A0SSSR28
$150 \leq p_T^{\mathrm{miss}} < 200$ GeV		A0SSSR4	A0SSSR9	A0SSSR14	A0SSSR19	A0SSSR24	A0SSSR29
$p_T^{\mathrm{miss}} \geq 200$ GeV		A0SSSR5	A0SSSR10	A0SSSR15	A0SSSR20	A0SSSR25	A0SSSR30

Table 9: Summary of the A0SS signal regions in the A0 analysis, cf. Ref. [281].

	N_{jet}	$N_{b\text{-jet}}$	H_T [GeV]	H_T^{miss} [GeV]
A1SR1	≥ 2	0	≥ 500	≥ 500
A1SR2	≥ 3	0	≥ 1500	≥ 750
A1SR3	≥ 5	0	≥ 500	≥ 500
A1SR4	≥ 5	0	≥ 1500	≥ 750
A1SR5	≥ 9	0	≥ 1500	≥ 750
A1SR6	≥ 2	≥ 2	≥ 500	≥ 500
A1SR7	≥ 3	≥ 1	≥ 750	≥ 750
A1SR8	≥ 5	≥ 3	≥ 500	≥ 500
A1SR9	≥ 5	≥ 2	≥ 1500	≥ 750
A1SR10	≥ 5	≥ 3	≥ 750	≥ 750
A1SR11	≥ 7	≥ 1	≥ 300	≥ 300
A1SR12	≥ 5	≥ 1	≥ 750	≥ 750

Table 10: Summary of the signal regions in the A1 analysis, cf. Ref. [299].

$m_{T2}(l_1 l_2)$ [GeV]	$100 - 140$	$140 - 240$	> 240
$E_T^{\mathrm{miss}} > 200$ GeV	A2SR1	A2SR2	A2SR3

Table 11: Summary of the signal regions in the A2 analysis, cf. Ref. [286].

	A3SR2jl	A3SR2jm	A3SR2jt	A3SR4jt	A3SR5j	A3SR6jm	A3SR6jt
$E_T^{\text{miss}}[\text{GeV}] >$	200						
$p_T(j_1)[\text{GeV}] >$	200	300	200				
$p_T(j_2)[\text{GeV}] >$	200	50	200	100			
$p_T(j_3)[\text{GeV}] >$	-			100			
$p_T(j_4)[\text{GeV}] >$	-			100			
$p_T(j_5)[\text{GeV}] >$	-				50		
$p_T(j_6)[\text{GeV}] >$	-						50
$\Delta\phi(\text{jet}_{1,2,(3)}, E_T^{\text{miss}})_{\text{min}} >$	0.8	0.4	0.8	0.4			
$\Delta\phi(\text{jet}_{i>3}, E_T^{\text{miss}})_{\text{min}} >$	-			0.2			
$E_T^{\text{miss}}/\sqrt{H_T}\,[\text{GeV}^{1/2}] >$	15		20	-			
Aplanarity $>$	-			0.04			
$E_T^{\text{miss}}/m_{\text{eff}}(N_j) >$	-			0.2	0.25		0.2
$m_{\text{eff}}(\text{incl.})\,[\text{GeV}] >$	1200	1600	2000	2200	1600	1600	2000

Table 12: Summary of the signal regions in the A3 analysis, cf. Ref. [298].

Contribution 17

Using ADL for analysis comparison

H. B. Prosper, S. Sekmen, W. Waltenberger

Abstract

In this study, we explore the potential of analysis description languages to assist, and even automate, the comparison of multiple analyses, and report on recent progress towards these goals.

1 Introduction

The unprecedented amount of data collected by the LHC is inspiring physicists to continue designing an ever growing number and diversity of analyses. These analyses focus on different final states involving different types of objects with varying properties, different kinematic variables, upon which varying selections are applied. As a result, each analysis covers a subset of the multi-dimensional space of event properties. In some cases, it is readily apparent that these subsets are disjoint, as they are based on distinct object types. But, sometimes, the subsets overlap, especially when there are multiple analyses exploring similar final states.

This diversity is a tremendous physics resource because it has the potential to increase the amount of information that can be extracted from a given data-set. However, analysis diversity can also cause confusion when attempting to get a complete view of which signatures are covered, which ones are not, which analyses have disjoint subsets, and which ones have overlapping subsets. This information can be very helpful when designing a new analysis. For example, the information could suggest which sub-space of event properties could benefit from greater attention. This information is also crucial for interpretation studies whether conducted within or outside the experiments, where a typical task is choosing the set of analyses that are optimal for testing a given model of new physics. In this study, we explore the use of the analysis description language approach to develop methods and tools for comparing analyses in the space of event properties.

2 Analysis description languages

An analysis description language is a domain specific language (DSL) capable of describing the physics contents of an LHC analysis in a standard and unambiguous way. In this approach, the description of the analysis components is decoupled from the software frameworks that run the analysis. Analysis description languages, which can be used both by the experimental and phenomenological communities, would bring numerous benefits to the LHC community, ranging from analysis preservation that goes beyond the lifetimes of experiments or analysis software to facilitating the abstraction, design, visualization, validation, combination, reproduction, interpretation and overall communication of the contents of LHC analyses.

Several attempts have been made to build domain specific languages for analyses at particle colliders. These include the well-established ROOT TTreeFormula and TTree::Draw, YADL

145

(YAML ADL in the F.A.S.T. framework), LINQtoROOT, PartiQL and NAIL (NAtural Analysis Implementation Language). Here, we focus on ADL [302], whose development has continued well beyond its genesis at the Les Houches PhysTeV 2015 workshop.

ADL consists of a plain text file containing blocks with a keyword-value structure. The blocks make clear the separation of analysis components such as object definitions, variable definitions, and event selections. The keywords specify domain specific analysis concepts and operations, such as object, region, select, weight, etc. The syntax rules include standard mathematical and logical operations, comparison and optimization operators, reducers (e.g. size, max, min), 4-vector algebra and common HEP-specific functions (e.g. angular separations). The ADL file is complemented by self-contained functions encapsulating variables with complex algorithms (e.g. M_{T2}, aplanarity) or non-analytic variables (e.g. efficiency tables or variables resulting from a machine learning model. The ADL syntax is capable of referring to these functions.

Apart from documenting the flow of an analysis, ADL can also be used for running the analysis on events with the help of dedicated tools. For example, ADL2TNM [237] is a Python transpiler that converts an analysis written in ADL into C++ or Python event-by-event analysis code. CUTLANG [303, 304] is a runtime interpreter that directly runs an analysis written in ADL on events without the need for compilation.

3 ADL and analysis comparison

The domain specific and declarative nature of ADL makes it an ideal construct for comparing analyses. Having the analysis described in a single human-readable text file decoupled from framework code already makes comparison "by eye" considerably simpler than comparisons of descriptions in publications, analysis notes, and certainly simpler than comparing multiple C++-based analysis codes. Moreover, comparisons can be performed in more advanced, automated, ways by building tools of increasing sophistication as the need arises.

Such tools can be used standalone for comparative studies of the rich analysis spectrum available at the LHC. They can also be incorporated into interpretation tools such as SMOD-ELS [294, 295] to identify analyses that yield uncorrelated results, which we refer to as "uncorrelated analyses". Since SMODELS does not run analyses on events, but only directly uses interpretation results from the experiments, an additional tool is required to provide information on analysis comparisons. Within the context of SMODELS, comparison tools are also intended to be used, for example, to systematically scout for interesting combinations of analysis results or large-scale analysis combinations, as has been outlined in a recent talk [305].

The development of methods to compare analyses and their implementation in comparison tool prototypes are currently in progress. Indeed, both the prototype of ADL2TNM, examples of ADL files, as well as preliminary versions of the "by eye" and "by sampling" comparison methods, described in the subsections below, can be found at the repository

```
https://github.com/hbprosper/adl2tnm.
```

The Python programs in this repository have been tested with Python 3.6.7, but should work with newer versions. The programs may work with Python 2, but this is not supported.

In order to help test the development of these methods, 10 CMS SUSY searches at 13 TeV with 35.9 fb^{-1} of data–already included in the SModelS analysis database–have been implemented in ADL. These analyses are searches in the bb/cc final state [52] (for direct sbottom/stop production); jets+E_T^{miss} with H_T^{miss} [299]; same-sign dileptons [306]; one lepton final states

with M_J [307]; multileptons [308]; one lepton final states with $\delta\phi$ [309]; WH [310] (for EWK SUSY); $\gamma + E_T^{miss}$ [311]; $\gamma + H_T$ [312], and the fully hadronic final state [313] (for direct stop pair production). The ADL implementations of these analyses can also be found in the above repository.

In the following, we describe the methods being developed and how, concretely, ADL can be used for this purpose. We are developing analysis comparisons at four different, but complementary, levels of sophistication as explained in the following subsections.

3.1 Analysis comparison "by eye"

"'The simplest way of comparing analyses is obviously to view their ADL files. However, given the well-defined block structure and standard domain specific syntax in the ADL, this process can be made easier and more systematic. ADL file contents can be queried with the help of a script. For a given set of analyses, the user can list the complete set of objects attributes and event variables featured in any number of analyses, and search which selection was applied in quantities of interest. The user can query event level quantities like jet multiplicity, hardest jet p_T, E_T^{miss}, H_T, or any other variable listed in the analyses, and can receive information on which analysis and which selection region uses that quantity and what selection criteria are applied on it. Object level selection criteria, such as those on jet p_T, electron η, muon d_0, etc. can also be queried and listed for all analyses. As a result, the Python program (a simple prototype of which exists in the repository mentioned above) can give a collective view of the ranges covered by quantities of interest in multiple analyses. '

3.2 Analysis comparison through static analysis

The comparison by eye can be taken one step further by automating the comparison of selection criteria through a static analysis of ADL files. We are investigating three levels of comparison:

– The user can filter the list of analyses and/or selection regions whose selection criteria on a given variable is in a certain range. For example, one can ask for the list of analyses whose jet multiplicity is > 6 or which yields a discrete sub-space that overlaps the one defined by this criterion. An analysis or region requiring at least 4 jets would fall into this range while an analysis or region requiring 3 to 5 jets would not.

– The user can choose a set of selection variables and find out if their selection ranges overlap. For example, one can select lepton multiplicity and E_T^{miss} and find out if the selection criteria for these quantities overlap in a given set of analyses.

– A more extensive analysis comparison can be made using a default set of predefined quantities consisting of simple variables such as object multiplicities, E_T^{miss}, object momenta or pseudorapidities, etc.

In each case above, if an analysis does not impose a selection on a given quantity, the output explicitly states this.

The static analysis of ADL files is a very fast and practical approach, however, it is better suited for qualitative studies. One point to note is that this approach treats every quantity in an analysis as independent. For example, a high level variable like transverse mass M_T is considered independently of the lepton and E_T^{miss} from which it is calculated. However, the static analysis of ADL files can find and state all dependencies that are explicitly stated as

functions in the ADL files. For example, to guide the user, it can state that M_T is dependent on lepton and E_T^{miss}, or that both M_{T2} and the razor variables are dependent on jets and E_T^{miss}. In the latter example, the user can then perform a subsequent comparison on jets and E_T^{miss}.

3.3 Analysis comparison using physics events

Another way for analysis comparison is to run the set of analyses on real or simulated events and find out which subset of events, if any, simultaneously survive selection criteria from multiple analyses or selection regions. ADL2TNM and CUTLANG, the tools currently available to run, event by event, analyses written in ADL, can readily accomplish this task. In order to facilitate analysis comparison, for every event, ADL2TNM notes which regions accepted the event and writes the results to a flat ROOT tree with one branch per region. The ADL2TNM tree is provided to SMODELS for analysis of overlaps.

This approach is conceptually simple, leads to quantitative information about overlaps, and can be used to estimate the degree of correlation between regions or between analyses. However, one should note that having a broadly inclusive set of events with physics processes relevant for the analyses under study is a necessity for this approach to work.

3.4 Analysis comparison using random sampling

If the goal is simply overlap detection, there is an alternative option for quantitative comparison of analyses without the need for an inclusive set of physics events. This approach involves determining the union of multi-dimensional sets of event properties covered by a given set of analyses and populating the space with with a sufficiently dense set of randomly sampled points. The ADL construct is ideal for this approach, since its domain specific syntax and well-defined structure make it possible to systematically parse an ADL file and determine the space of event properties and setting boundaries on these.

The procedure begins by constructing the complete list of all event level variables (i.e., those with a single instance per event) upon which a selection is applied. Examples of such variables include jet multiplicity, the hardest lepton p_T, H_T, dilepton invariant mass, etc. Then, all the objects used to compute these variables are traced, and the set of properties with which these objects were selected are determined. These objects, their properties, and their multiplicities define the multi-dimensional space of event properties of an analysis. The union of the set of properties over multiple analyses defines the super-set of event properties that define the space to be populated with points.

In order to populate the space with points, the boundaries of the event properties need to be known. These boundaries can be defined once and for all using a suitable sample of physics events and be made available as a default. The selections on properties in the ADL files also impose boundaries, which will further limit the space to be populated. Once the space and boundaries are defined, random numbers are generated event by event to populate the space with a single point. However, we can reduce the amount of sampling to be done, event by event, by first sampling the object multiplicities, then sampling the objects' properties. The generated random numbers are then used for calculating higher order variables. The analysis proceeds exactly the same way as for real or simulated events.

Populating high-dimensional spaces can suffer from the curse of dimensionality. But, if we find ourselves similarly cursed, the curse can be lifted or at least mitigated with some degree of importance sampling. One advantage of internally generated pseudo-events is that

the generation is considerably faster than generating events with the correct physics-motivated multi-dimensional distributions. Therefore, it would be entirely feasible to generate billions of pseudo-events in order to populate the space with sufficient density.

4 Outlook

The analysis description language approach offers possibilities that were unanticipated at its inception. We describe one below. But, first, we make a few general remarks about the future of ADL.

In the near term, the grammar of ADL will be formally defined so that modern parsing tools can be deployed to render the current tools considerably more robust and to increase the level of automatic syntax validation with useful error reporting. Concurrently, the prototype tool to transpile from ADL to Python will be completed and brought to the same level of functionality as ADL2TNM. The major work to be done is moving all tools from the prototype stage to the production stage, which will require engaging the expertise of computer scientists to build the ADL abstract syntax trees (AST) that describe LHC analyses. Work in this direction is in progress.

One advantage of the analysis description language approach that was unanticipated, is that it lends itself to the creation of tools that could automate the determination of all the disjoint sub-spaces of the full bounded space of event properties such that the union of the former equals the latter. This offers the tantalizing possibility of running multiple, possibly correlated, analyses and automatically partitioning their results on real and simulated data into disjoint sets. If this could be done, it would go a long way towards automating the combination of analyses regardless of their degree of correlation. The point is that since each sub-space is disjoint by constructions, the count in each is statistically independent of the counts in the other sub-spaces. This would greatly simplify the construction of likelihood functions that describe the combination of the results from multiple analyses because the results that would be combined would be statistically independent yet contain the same information as the correlated results.

In the longer term, we envisage much more sophisticated static analysis of multiple ADL files using natural language processing combined with artificial intelligence. We believe this to be a realistic possibility. The first step would be to use the same technology that permits the automatic conversion of speech to text to make it possible to use natural speech to query a future ADL file database. The underlying analysis of the returned boolean statements would be done by an AI-enabled analyzer.

Contribution 18

CONTUR Update: Correlations and SM Theory

A. Buckley, J. M. Butterworth, L. Corpe, G. Watt, D. Yallup,

1 Introduction

CONTUR is a software package written in Python which allows new physics models to be compared to existing measurements, using analyses archived in RIVET [87, 314]. It was first presented in Ref. [88], where the concept was illustrated using a simplified Dark Matter model. Further physics results have been presented in the previous Les Houches proceedings [237](contributions 14 & 20) and subsequent publications [315–318], as well as in these proceedings[1]. During this time, the code has evolved and several new features have been implemented. In this contribution we give an overview of these functional and technical updates, and, for those not covered in other contributions, we also present some first results. Further details on some of the statistical treatment can be found in Ref. [319].

In addition to the functional developments described below, we note that the code now has a recommended stable release (1.0.0), is recommended for use with version 3 of RIVET [87], and is now distributed and developed via gitlab at `https://gitlab.com/hepcedar/contur`. The webpage with documentation is still accessible via hepforge `https://contur.hepforge.org/`. The command-line options to use the new features described below are all visible by typing `contur --help` as usual.

2 Use of correlation information on uncertainties

In looking for potential BSM contributions to the fiducial phase space of existing measurements, CONTUR scans multiple final states in the same run. Care must therefore be taken not to double-count the same BSM events multiple times, should the same events contribute to several different measurements, since to do some would overestimate the statistical power of the sensitivity. CONTUR avoids this by classifying the measurements into non-overlapping "analysis pools", either based on the experiment, the LHC run period, or the final state. For example, ATLAS 7 TeV and 8 TeV inclusive jet measurements are statistically independent and a combined sensitivity may be derived using both. They will be placed in separate pools. Likewise, the sensitivity from 8 TeV jet measurements in non-overlapping rapidity regions may be combined, as may measurements from ATLAS and CMS even if measured in an identical phase space. Sensitivity from a CMS dilepton measurement may also be combined with that from a CMS dijet measurement. However, an ATLAS 8 TeV multijet measurement *may not* be combined with an ATLAS 8 TeV inclusive jet measurement, since the same events may contribute to both. In this case, CONTUR will evaluate the sensitivity of both, but use only the most sensitive in deriving its final result[2].

---

[1]See sections 20, 21, 5 and 8.

[2]The classification of measurements into these non-overlapping analysis pools of statistically correlated measurements is done in an SQLite (`sqlite.org`) database bundled with CONTUR, called `analyses.sql`.

This deals well with statistical correlations. Correlated systematic uncertainties are trickier to handle. A particularly worrying possibility from the point of view of limit setting is that a more-or-less constant increase in a differential cross section due to some BSM contribution might be counted as an excess in each bin of the measurement, giving a strong exclusion, when in fact a single relatively insignificant excursion of a correlated systematic uncertainty (for example, in the integrated luminosity) could absorb the entire effect. In its initial, and still default, incarnation, CONTUR avoids this possibility by only allowing the most significantly discrepant bin in any given differential measurement to contribute to the final sensitivity. While being conservative, this approach has the obvious disadvantage of throwing away information and, for example, reducing sensitivity when a BSM resonant peak is split over more than one bin of a measurement. Increasingly, the experimental results uploaded to HEPData [320] include detailed information about the bin-to-bin correlations, and the latest version of CONTUR can now (optionally) make use of this.

2.1 Method

The measurements come with statistical uncertainties, and sometimes a systematic uncertainty, which are uncorrelated between bins, and potentially a series of systematic uncertainties which are correlated between bins. Within a single distribution, each of these correlated components is characterised (i.e. scaled) by a single nuisance parameter. A fit is then performed, varying these parameters to maximise the likelihood for measurement and theory to be consistent, assuming a Gaussian probability distribution for these scaling parameters centred on zero with a width of one. The covariance matrix is constructed and the likelihood of a given BSM signal injection being consistent with the measurement (and thus, by inference, an exclusion) is calculated with the data shifted according to the fitted nuisance parameters, and including the uncorrelated systematic uncertainties, the data statistical uncertainty and the Monte Carlo statistical uncertainty.

2.2 Implementation Details

The use of a bin-by-bin correlation information in CONTUR was made possible by updates to the YODA format and the back-end of the HEPData website. Previously, YODA histograms only had the capacity to store a total uncertainty for each bin. In response to the fact that LHC measurements are increasingly dominated by systematics uncertainties (which are often correlated between bins), the format was augmented to include correlation information. Starting from YODA 1.7, an `ErrorBreakdown` annotation in the header of YODA histograms was permitted, codifying the breakdown of uncertainty sources/nuisance parameters and their impacts on each bin. The annotation contents are in the YAML format to allow a quick and efficient read-in of the information. Internal YODA functions and methods were written so that if an uncertainty breakdown was present, it could be easily accessed and manipulated. In particular, it could be converted into a covariance matrix using standard linear algebra, assuming that statistical uncertainties (or uncertainties specifically marked as "uncorrelated") are treated as uncorrelated between bins (and affect only the diagonal of the covariance matrix). Other uncertainties are assumed to be 100% correlated between bins, and the outer product of the vector of impacts in each bin is taken to produce the covariance matrix for a given nuisance parameter or uncertainty source. An example of the format is shown below.

```
BEGIN YODA_SCATTER2D_V2 /REF/RIVET_ANALYSIS_NAME/d01-x01-y01
Variations: [""]
ErrorBreakdown: {
```

```
0: {'stat,Data_statistics': {dn: -2.5347e-06, up: 2.5347e-06},
'sys,DY_TH_Scale_uncertainty': {dn: -9.6354e-08, up: 9.6354e-08},
'sys,JET_GroupedNP_1': {dn: -9.6549e-07, up: 9.6549e-07}},
1: {'stat,Data_statistics': {dn: -8.6171e-06, up: 8.6171e-06},
'sys,DY_TH_Scale_uncertainty': {dn: -8.4579e-07, up: 8.4579e-07},
'sys,JET_GroupedNP_1': {dn: -8.6178e-06, up: 8.6178e-06}},
2: {'stat,Data_statistics': {dn: -2.6374e-06, up: 2.6374e-06},
'sys,DY_TH_Scale_uncertainty': {dn: -4.6791e-07, up: 4.6791e-07},
'sys,JET_GroupedNP_1': {dn: -6.7696e-06, up: 6.7696e-06}},
3: {'stat,Data_statistics': {dn: -2.0552e-06, up: 2.0552e-06},
'sys,DY_TH_Scale_uncertainty': {dn: -1.3018e-07, up: 1.3018e-07},
'sys,JET_GroupedNP_1': {dn: -4.9286e-07, up: 4.9286e-07}}}

IsRef: 1
Path: /REF/RIVET_ANALYSIS_NAME/d01-x01-y01
Title: Inclusive cross-section measurements
Type: Scatter2D
---
# xval        xerr-        xerr+        yval         yerr-        yerr+
1.500000e+02  1.500000e+02  1.500000e+02  3.953700e-05  2.714067e-06  2.714067e-06
4.000000e+02  1.000000e+02  1.000000e+02  3.694700e-04  1.221623e-05  1.221623e-05
6.500000e+02  1.500000e+02  1.500000e+02  1.746400e-04  7.280268e-06  7.280268e-06
9.500000e+02  1.500000e+02  1.500000e+02  2.680900e-05  2.117476e-06  2.117476e-06
END YODA_SCATTER2D_V2
```

There already exist dozens of HEPData entries where the uncertainty breakdown was provided when the results of the search or measurement were uploaded. The HEPData upload format allows for these as additional labels in each bin which specify the uncertainty name, as well as the signed or symmetrized, relative or absolute effect of that uncertainty on a given bin. Previously, there was no way to propagate this information when converting the HEPData entry into a YODA file, and the various sources were summed in quadrature to give a total uncertainty for the YODA histograms. The back-end of the HEPData website was therefore updated so that the additional uncertainty labels were converted into ErrorBreakdown annotations by default when propagating data into the YODA format. This ErrorBreakdown information was then propagated into the latest RIVET reference data during the usual synchronisation between RIVET and HEPData at the time of new RIVET releases. As a result of this change, the ErrorBreakdown information became available for the reference data of dozens of RIVET routines, and could then be used in CONTUR.

The CONTUR code needed to be updated in several ways to be able to take account of the uncertainty breakdowns available in many analyses. The current workflow is as follows. All reference data are first checked for error breakdowns. If the error breakdowns are available, covariance matrices are built as described above. To speed up the procedure, only nuisance parameters which have an effect of at least 1% anywhere on the range of a histogram are processed by default[3]. If theory predictions are being used (see Section 3), theory uncertainties on SM background predictions are treated as 100% correlated between bins by default, but may also be treated as 100% uncorrelated if desired. The matrices are checked to ensure they are in-

---

[3]This materiality cutoff is adjustable via a command-line option.

vertible. If no error breakdowns are available or the matrix is not invertible, the code falls back to the single-bin approximation described at the start of this section, and all bins are treated as a separate test. If the diagonalised covariance matrix has determinant zero, the entry is treated as pathological and discarded.

When evaluating the agreement between the reference data and the prediction(s) to determine the CL_s exclusion, a likelihood function $\mathcal{L}$ is constructed. This likelihood is the product of the Poisson probability to see an observed number of events in each bin, given the prediction (with or without signal). The nuisance parameters are included in the prediction, and each nuisance parameter is Gaussian-constrained. The nuisances are individually profiled by finding the best-fit value of the nuisance ν_i across all bins, using the error breakdown provided. The best-fit value of each nuisance parameter is either obtained analytically by solving $\partial \log \mathcal{L}/\partial \nu_i = 0$, or using a numerical maximization of the log-likelihood. The analytical solution is faster for histograms with less than 5 bins, but the numerical solution is faster for 5 bins or more. By default, the choice of method is made automatically.

The final agreement between data and prediction is obtained from the χ^2 by taking the dot product of the residuals in each bin (after profiling of each nuisance parameter) with the inverted total covariance matrix in the usual way. The p-values for the null and alternative hypotheses are calculated from the χ^2, and used to evaluate the CL_s exclusion. The CL_s is truncated at zero if a bin if found to agree better with BSM+SM than SM alone (something which can never happen unless theory predictions are being used, as described in Section 3.

2.3 Results

The correlation treatment was tested on a number of different models and final states. As an example, we focus here on a model which introduces a light scalar ϕ which decays to diphotons. Production and decay take place via effective couplings to gauge bosons which are set to one and suppressed by a scale Λ. Thus, as well as photons, the final states which are produce will include jets, leptons and missing energy, since the ϕ is generally produced in association with a W or Z. Correlation information for many relevant measurements is available, making this model a good exercise ground for their treatment. Figure 1 shows the sensitivity (scanned across Λ and M_ϕ, with and without the correlation information. It can be seen that the sensitivity without correlation information is very similar to that shown in [316], indicating both code stability over several CONTUR, RIVET, and HERWIG versions (the version used here is 7.2 [101, 189]) and a minor improvement due to a change in the treatment of the ATLAS $Z + \gamma$ measurement [208], where the electron and muon data are now treated separately rather then being assigned to the same analysis pool. When correlation information is used, the sensitivity is again very similar, with very modest improvement visible at the edges at high scales and low masses, where the limits also become somewhat smoother. The latter effect is expected since correlations should reduce the impact of the signal moving between bins of a measurement as the mass of the ϕ changes.

The overall exclusion comes from a mix of measurements, some of which do not have correlation information available. The impact of using correlations is seen more clearly on individual measurements where the information is provided. This is shown in Fig. 2, where the exclusion derived from the ATLAS 8 TeV inclusive photon and diphoton measurements is shown, with and without using correlation information. There is a marked increase in the sensitivity for $M_\phi > 60$ GeV or so. In the uncorrelated case, the sensitivity in this region is driven by the diphoton mass distribution of [321], where since the ϕ is a narrow resonance,
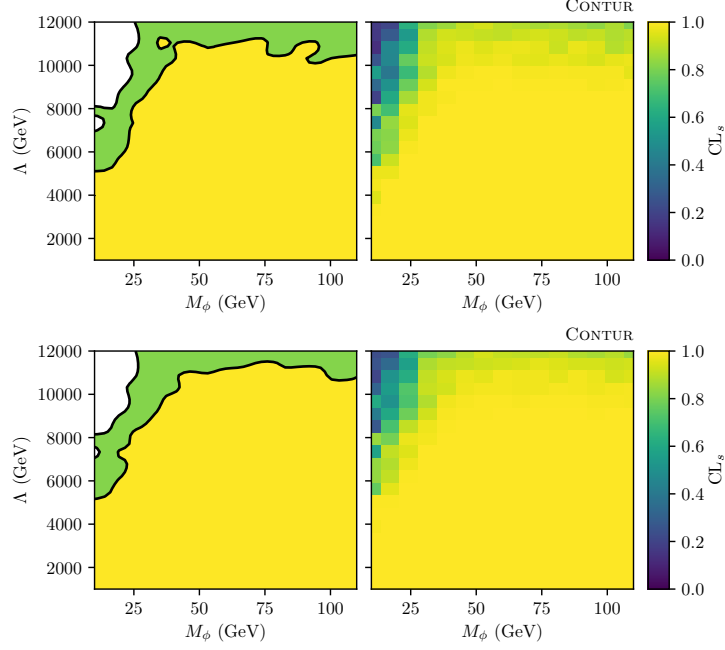
Figure 1: Exclusion with the default CONTUR approach (upper) and using correlation information (lower) for the light scalar model described in Ref. [237](20). The left hand plots show the 68% and 95% confidence levels, derived from the right hand plots which show the full heatmap on the right hand scale.

the signal appears generally in a single bin. In the correlated case, the strongest sensitivity comes from the transverse momentum of the diphoton system (from the same paper), where a systematic deviation builds up over several bins, increasing towards high $p_T^{\gamma\gamma} = p_T^{\phi}$.
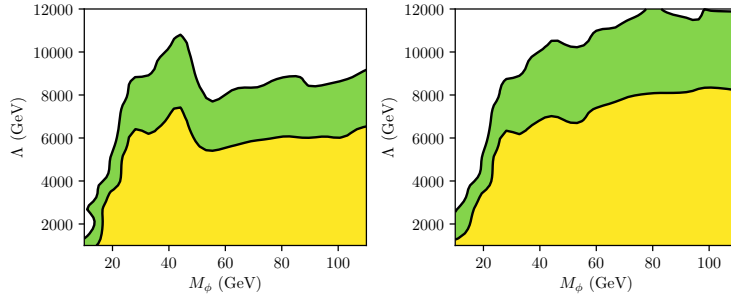
Figure 2: Exclusion from inclusive (di)photon measurements (see text) with the default CONTUR approach (left) and using correlation information (right) for the light scalar model described in Ref. [237](20). The 68% and 95% confidence levels are shown.

3 Use of SM theory predictions

By default CONTUR treats the data as being identically equal to the SM, an approximation justified to some extent by the fact that all the measurements used have been shown to agree with the SM, and at some level therefore equivalent to treating the whole data set as a data-driven

control region. However, if we wish to take SM predictions and their uncertainties at face value, this assumption is not good enough. In particular it may overestimate they exclusions in cases where the theory uncertainties on the SM are similar to or larger than those on the measurement, since the theory uncertainties are not used. Also, in cases where there is an excess of data over the SM (which my definition is not "significant", since all the measurement papers state consistency with the SM), stacking a BSM contribution on top of the SM may even improve the agreement with the measurement. CONTUR has the capacity to consider any theory calculation as the SM "background", if the prediction is provided as a YODA object and is visible via the usual RIVET search path[4]. A library of such predictions is being assembled gradually. We note that if experiments upload the theory predictions used in the paper to HEPData, they can be exported as YODA files, greatly facilitating this process.

Since the majority of measurements relevant to the light scalar model discussed in the previous section have theory predictions already available in CONTUR, (from [322–324]), we present some examples of their use here. To begin with, show the heatmap comparable to the upper half of Fig. 1, not using the theory predictions yet, but only using to measurements for which they are available. The only significant difference is a reduction in sensitivity at low M_ϕ, which is due to the removal of the ATLAS 7 TeV $Z/W + \gamma$ measurements [325], for which the SM prediction is not yet in CONTUR. This is shown in the upper half of Fig. 3.

The lower portion of Fig. 3 shows the exclusion coming from the same measurements, but now with SM theory predictions used as the null signal hypothesis, including the appropriate uncertainties[5]. There is a reduction in sensitivity. This is due to both factors discussed above. Since the theory uncertainties are generally not negligible compared to the experimental uncertainties for isolated photon measurements, all measurements show some reduction in sensitivity when the theory uncertainty is taken into account at face value, on the assumption it unconstrained by other data. For example, the SM prediction for the diphoton results [321] discussed previously, taken from Refs. [323, 324], have uncertainties similar to the measurement (in fact, larger at lower $p_T^{\gamma\gamma}$ and smaller at higher $p_T^{\gamma\gamma}$), reducing the sensitivity of this measurement to scales below about 3 TeV (compared to 6 TeV when the data are used as the null hypothesis).

This is not the dominant effect, however. The most sensitive measurement of high Λ for most M_ϕ is the ATLAS γ+missing E_T measurement from [208]. This measurement in fact shows a modest excess over the SM prediction, particularly for the $\gamma\gamma+$ missing E_T zero jet channel ($1.18^{+0.52}_{-0.44}$(stat.)$^{+0.48}_{-0.49}$(syst.) $\pm$ 0.02(lumi.) fb compared to $0.395^{+0.049}_{-0.037}$ fb from MCFM version 7.0 as used in [208] [6].) Thus, adding a small BSM contribution in fact improves the consistency with the data, and the exclusion limit is therefore reduced.

4 Use of search analyses

RIVET can now implement detector smearing and efficiencies, so that search analyses which have not been unfolded for detector effects may be implemented [327]. CONTUR is now able to make use of this feature. More details, and some studies, are presented in Section 20.

---

[4]Technically, instead of a path name beginning with /REF, the path name of the YODA histogram should begin with /THY.

[5]Theory uncertainties are treated as uncorrelated, since several have a significant statistical component, and treating them as 100% correlated gives a very poor agreement between measurements and the SM. The new correlation treatment for data uncertanties described in the previous section is not used.

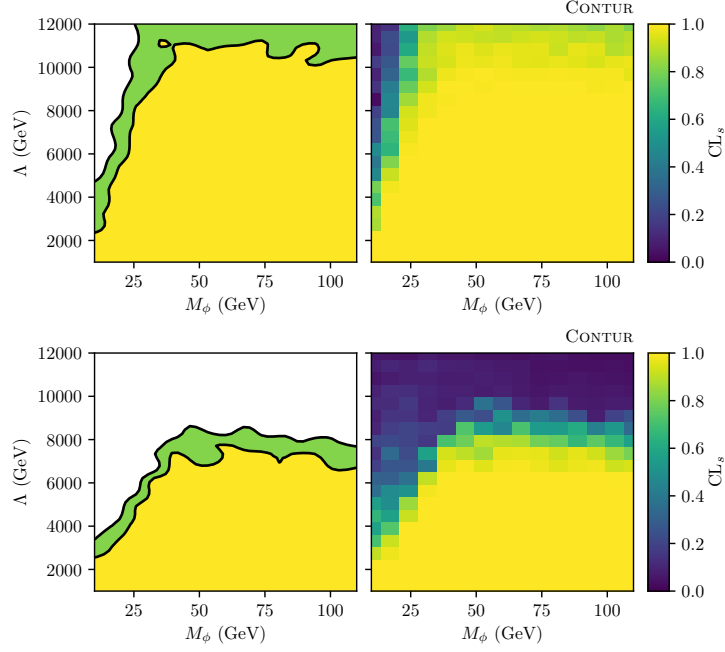[6]See [326] for the most recent version of MCFM.

Figure 3: Exclusion with the default CONTUR approach (upper) and using SM theory information (lower) for the light scalar model described in Ref. [237](20). The left hand plots show the 68% and 95% confidence levels, derived from the right hand plots which show the full heatmap on the right hand scale.

Acknowledgements

Contribution 19

Comparison of recasting tools

J. Y. Araz, A. Buckley, N. Desai, B. Fuks, T. Gonzalo, P. Gras, A. Kvellestad, A. Raklev, R. Ruiz de Austri, S. Sekmen

The plethora of LHC searches for new particles target an impressive range of scenarios of physics beyond the Standard Model (BSM). In addition to providing the raw search results, that consist in the expected Standard Model (SM) background rates and the observed number of events in each search region, the LHC experiments usually interpret their results in terms of a few specific BSM scenarios. In this context, often so-called *simplified models*, with only a few free parameters, are used due to the inherent difficulty of exploring many-dimensional parameter spaces. The phenomenology predicted by these models is generally much more restricted than that of the complete BSM models they originate from. Furthermore, many fundamentally different BSM models can give rise to similar signals in LHC searches.

In other words, the scientific potential of a given LHC search extends far beyond the BSM interpretations performed directly by the experiment. In order to realise this potential, the phenomenology community must be able to reinterpret the search results within BSM models that are different from, and often more general than, the particular BSM scenarios studied by the experiments. The success and reliability of such reinterpretation (or *recasting*) efforts depend on dedicated work from both experiment and theory: The experiments must provide sufficiently detailed information – preferably in standardised electronic formats – regarding how each search was performed. The phenomenology community must develop public tools that can utilise this information to reproduce and recast the LHC results with acceptable accuracy. In this section we focus on the contribution from the phenomenology side. We briefly describe some of the major public tools for LHC recasting, and check how closely they match each other in reproducing the experiment cutflow for a rather challenging BSM signal region.

1 Recasting tools

The computationally fastest way to reinterpret an LHC search in a new BSM model is to map the model to an appropriate set of simplified models for which the LHC experiments have already provided interpretations. This is the approach taken by the tool SMODELS [295]. The low computational cost makes this a well-suited approach for large BSM parameter scans. However, for complicated BSM models, the derived limits can often be overly conservative.

A more general, but computationally much more expensive, approach is to reproduce the experimental search directly on simulated events for the new BSM model. This is the method we focus on here. The software tools CHECKMATE [69, 301], RIVET [87, 314], MADANALYSIS [20, 71–73] and COLLIDERBIT [328], and the two interpreters ADL2TNM [237] and CUTLANG [303, 304], both working on an analysis description language [302], are all based on this full-simulation approach, but differ in terms of implementation and the targeted use-case.

CHECKMATE

CheckMATE2 (Check Models At Terascale Energies) is a programme package which accepts

simulated event files in many formats for any given model, and if necessary, generates events on-the-fly using the Monte Carlo generators MADGRAPH5_AMC@NLO [19] or PYTHIA 8 [28]. The programme then determines whether the model is excluded at the 95% confidence level (CL) by comparing predictions to published experimental results. The programme structure allows for easy addition of new analyses.

RIVET

The RIVET toolkit (Robust Independent Validation of Experiment and Theory) is a system developed for the validation and tuning of Monte Carlo event generators. A large (and ever growing) set of experimental analyses are supplied with RIVET (~ 950 analyses as of version 3.1.0, released in Dec 2019). RIVET has become the LHC standard for archiving measurement analysis logic in SM, top and Higgs physics, which can provide indirect constraints on BSM models. From RIVET 2.5 onward, a detector-emulation machinery is also available, based on analysis-specific efficiency and smearing functions. This feature permits the reproduction also of reconstruction-level direct BSM searches.

MADANALYSIS 5

The MADANALYSIS 5 package [20, 73] is a general framework for new physics phenomenology at particle colliders, which ease the design and the recasting of any collider analysis. Its recasting module relies on DELPHES [154] for simulating the response of the detector, allows for the automatical recast of the results of about 40 ATLAS and CMS analyses (in its to-be-released version 1.8.0), and estimate how they constrain any BSM signal by the evaluation of confidence level exclusions. Details on the re-implementations and their validation can be found on the MADANALYSIS Public Analysis Database (PAD) [71, 72][1]. In its upcoming v1.8 release, MADANALYSIS 5 will allow the user to use efficiency and smearing functions to parameterise the detector effects.

COLLIDERBIT

The Global and Modular BSM Inference Tool (GAMBIT) [329] is a multi-purpose inference tool capable of performing computationally intensive global fits of BSM models. Amongst the different physics modules that constitute GAMBIT, COLLIDERBIT [328] is responsible for the computation of collider observables and likelihoods. COLLIDERBIT has been designed with an emphasis on speed, due to its intended use in large parameter scans and global fits. In particular, COLLIDERBIT performs a fast simulation of LHC signal events using a parallelised version of PYTHIA 8. The events are passed through a homebrew detector simulation, BUCKFAST [328], which performs fast four-vector smearing, before they are subjected to efficiency functions published by the experiments. COLLIDERBIT is shipped with a large, and steadily growing, collection of implemented LHC searches, with a focus on searches for supersymmetry.[2]

ADL, ADL2TNM and CUTLANG

An Analysis Description Language (ADL) is a domain specific, declarative language describing the physics contents of a collider analysis (*e.g.* object and variable definitions, event selections) in a standard and unambiguous way, independent of analysis frameworks. ADL2TNM is

---

[1]https://madanalysis.irmp.ucl.ac.be/wiki/PublicAnalysisDatabase

[2]A light-weight, standalone version of COLLIDERBIT, COLLIDERBIT SOLO, will be released in the near future. This allows the user to apply COLLIDERBIT's fast detector simulation and collection of LHC analyses to HepMC events provided as input. For the recast comparisons discussed here, the COLLIDERBIT results were obtained using COLLIDERBIT SOLO with HepMC input.
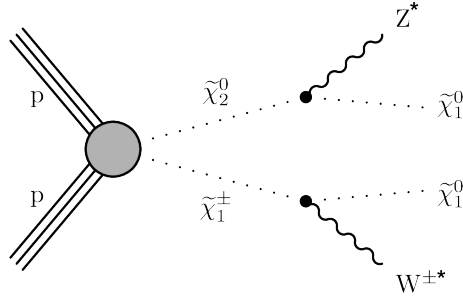
Figure 1: Representative Feynman diagram illustrating the signal process targeted by the considered CMS search. Figure taken from Ref. [330]

a PYTHON transpiler that converts an analysis written in ADL into its C++ or PYTHON version. CUTLANG is a runtime ADL interpreter that directly runs an analysis in ADL form on events without the need for compilation. ADL, ADL2TNM and CUTLANG are usable for both experimental and phenomenological analyses.

2 Comparison setup

Due to their differences in philosophy and implementation, it is worthwhile to investigate to what extent the results from the above tools differ when emulating the same LHC search. The spread in results may also speak in a quantitative manner to the general reliability of current recasting tools. For this purpose we compare how the different tools reproduce the cutflow for a particular signal region of a specific analysis, when provided with the same set of simulated signal events before detector simulation.

The starting point for our comparison is a CMS search at 13 TeV using final states with two low-p_T oppositely charged leptons and missing transverse momentum [330]. This search is designed to target production of a chargino and neutralino pair ($\tilde{\chi}_1^\pm \tilde{\chi}_2^0$), with subsequent decays down to the lightest stable neutralino ($\tilde{\chi}_1^0$), when the mass splittings between the supersymmetric particles are small. Such a specific search is by constrution sensitive to details in the implementation as focusing on non-usual soft objects. We illustrate the signal process considered in this CMS search by the Feynman diagram in Fig. 1. The low-p_T leptons in the signal arise from leptonic decays of the off-shell Z and W, while the two stable $\tilde{\chi}_1^0$ produce the missing transverse momentum.

The baseline for our recast comparison is the "electroweakino cutflow" provided by CMS in the auxiliary material for Ref. [330].[3] We summarise the cuts here for clarity:

1. two muons, each with a transverse momentum p_T lying in [5, 30] GeV;

2. opposite electric charges for the two muons;

3. transverse momentum of the dimuon pair $p_T(\mu\mu)$ larger than 3 GeV;

4. dimuon invariant mass $M(\mu\mu)$ between 4 and 50 GeV;

---

[3] http://cms-results.web.cern.ch/cms-results/public-results/publications/SUS-16-048/index.html

5. veto of events with a dimuon invariant mass $M(\mu\mu)$ between 9 and 10.5 GeV;

6. missing transverse momentum p_T^{miss} between 125 and 200 GeV;

7. μ and p_T^{miss} trigger requirement;

8. at least one ISR jet;

9. transverse hadronic energy H_T larger than 100 GeV;

10. p_T^{miss}/H_T between 0.6 and 1.4;

11. veto of events featuring b-tagged jets;

12. veto of events with a ditau invariant mass $M(\tau\tau)$ between 0 and 160 GeV;

13. transverse mass of each muon/missing energy system $M_T(\mu_i, p_T^{\text{miss}})$ less than 70 GeV.

We use the $(150, 142.5)$ GeV benchmark point from Ref. [330], meaning that we set $m_{\tilde{\chi}_1^{\pm}} = m_{\tilde{\chi}_2^0} = 150$ GeV and $m_{\tilde{\chi}_1^0} = 142.5$ GeV. For such a compressed electroweakino spectrum, the CMS search relies on a dedicated trigger for dimuon events with low missing p_T, which explains the focus on muon pairs in the CMS electroweakino cutflow. The above event selection cuts and the corresponding CMS cutflow numbers are reproduced in the two first columns of Table 1.

To clearly show the cutflow comparison across the different recast tools, we generate a common set of 250000 Monte Carlo $\tilde{\chi}_1^{\pm} \tilde{\chi}_2^0$ signal events using MADGRAPH5_AMC@NLO [19], with PYTHIA 8 [28] handling the electroweakino decays, the parton showering and hadronisation. The recast tools cutflows are all scaled according to the CMS numbers for cross-section times luminosity, *i.e.* to match the CMS starting point of 172004 signal events before any cuts. Following the CMS analysis, we require the produced $\tilde{\chi}_1^{\pm}$ and $\tilde{\chi}_2^0$ to decay exclusively into the lightest neutralino $\tilde{\chi}_1^0$ through an off-shell W and Z boson respectively. The CMS signal simulation assumes SM branching ratios for the virtual Z and W boson, but taking into account the Breit-Wigner shapes. We attempt to reproduce this using the PYTHIA 8 settings 23:mMin = 24:mMin = 1, which sets the lower limit of the allowed Z and $W^{\pm}$ Breit-Wigner mass ranges to 1 GeV.[4] The simulated events are stored in HepMC format, and later provided as input for the different recast tools.

3 Cutflow comparison

In order to obtain realistic signal rate estimates from a set of simulated events, detector effects must be taken into account. CMS uses a proprietary detector simulation based on the GEANT package [331], as well as faster version [332]. Recasting projects outside the experiments have to rely on available open-source detector simulators, or write their own. Of the recasting tools used in this comparison, CHECKMATE, MADANALYSIS and ADL use the fast detector simulation DELPHES [154]. MADANALYSIS can also use its own detector simulation, known as SUPERFASTSIM and relying on object reconstruction efficiency and smearing function [333], with two different reconstruction methods, one is clustered jet based (Jet) and one is

---

[4]Since performing this comparison we have been informed that CMS used 23:mMin = 24:mMin = 0.1 for their signal simulation. While this will have caused a systematic difference between the CMS signal events and our signal events, we expect the effect to be small compared to statistical uncertainties and the differences stemmig from the detector simulation.

	CMS	CHECKMATE	RIVET	MA DELPHES	MA Jet	MA Cons	ADL	COLLIDERBIT
All events	172004	172004	172004	172004	172004	172004	172004	172004
2 μ's, $p_T \in [5, 30]$	242.7	240.8	249.1	264.9	253.2	225.7	267.6	245.8
μ's oppositely charged	218.5	217.4	220.2	205.7	207.1	184.4	238.7	214.6
$p_T(\mu\mu) > 3$	213.8	212.6	217.4	201.6	203.0	181.6	233.9	209.9
$M(\mu\mu) \in [4, 50]$	103.3	117.0	128.7	124.5	118.3	106.6	127.3	122.8
$M(\mu\mu)$ veto [9, 10.5]	102.2	114.9	128.0	122.5	116.3	106.6	125.2	121.7
$p_T^{\text{miss}} \in [125, 200]$	9.8	8.9	8.3	7.6	8.3	6.2	6.2	9.6
$\mu + p_T^{\text{miss}}$ trigger	5.5	5.5	5.4	4.9	5.4	4.0	4.0	6.2
ISR jet	5.3	5.5	5.4	4.5	4.5	3.6	4.0	6.1
$H_T > 100$	4.1	4.8	5.4	4.0	4.5	3.6	4.0	5.4
$p_T^{\text{miss}}/H_T \in [0.6, 1.4]$	3.7	4.1	5.4	3.6	4.5	3.1	3.1	4.9
b-tag veto	3.0	4.1	2.7	2.2	4.5	2.2	3.1	4.0
$M(\tau\tau)$ veto	2.7	2.1	2.7	1.3	3.6	1.8	2.2	3.2
$M_T(\mu_i, p_T^{\text{miss}}) < 70$	2.2	2.1	2.2	1.3	3.1	1.8	1.8	2.6

Table 1: Comparison of cutflows for all recasting tools, including three cutflows using MADANALYSIS, one with DELPHES and two with SUPERFASTSIM with different reconstruction methods (Jet and Cons). All dimensionful kinematical variables in the first column are given in units of GeV.

substructure based (Cons). We include MADANALYSIS cutflows for all three detector simulation options in our comparison. Lastly, RIVET and COLLIDERBIT use their own home-brewed fast detector smearing. Although a detailed comparison of all detector simulations is beyond the scope of this work[5], we expect that most of the difference in the cutflows will arise from the different simulations. The last source of difference across all recasting tools lies in their specific implementation of the given CMS search, with efficiency functions and selection cuts.

The cutflows obtained with the different tools for the $(150, 142.5)$ GeV benchmark point can be seen in Table 1. A visual representation of the cutflow comparison is given in Fig. 2. This figure also includes grey bands indicating the statistical uncertainty on the CMS cutflow numbers, as provided in Ref. [330] (auxiliary material).

All of the recasting tools reproduce the CMS cutflow reasonably well, with the RIVET and CHECKMATE cutflows matching very well the CMS expectation after the last cut. MAD-ANALYSIS (with SUPERFASTSIM-Cons), ADL and COLLIDERBIT all give a final signal prediction within 20% of the CMS result, while MADANALYSIS with SUPERFASTSIM-Jets and with DELPHES end up $\sim 40\%$ above and below the CMS number, respectively. However, when interpreting these results it should be kept in mind that statistical uncertainties grow relatively large towards the end of the cutflow. We note that five out of seven tools lie in the CMS statistical 1σ band after the final cut.

In the early stages of the cutflow there are some notable discrepancies – in particular following the cut $M(\mu\mu) \in [4, 50]$ GeV, after which the recast cutflows significantly overshoots the CMS cutflow. The only exception is the MADANALYSIS Cons cutflow, but this cutflow undershoots the CMS one in the preceding steps. However, after the requirement that $p_T^{\text{miss}} \in$

---

[5]See Refs. [328] and [327] for a comparison between the fast detector simulators in COLLIDERBIT and RIVET, respectively, with DELPHES.

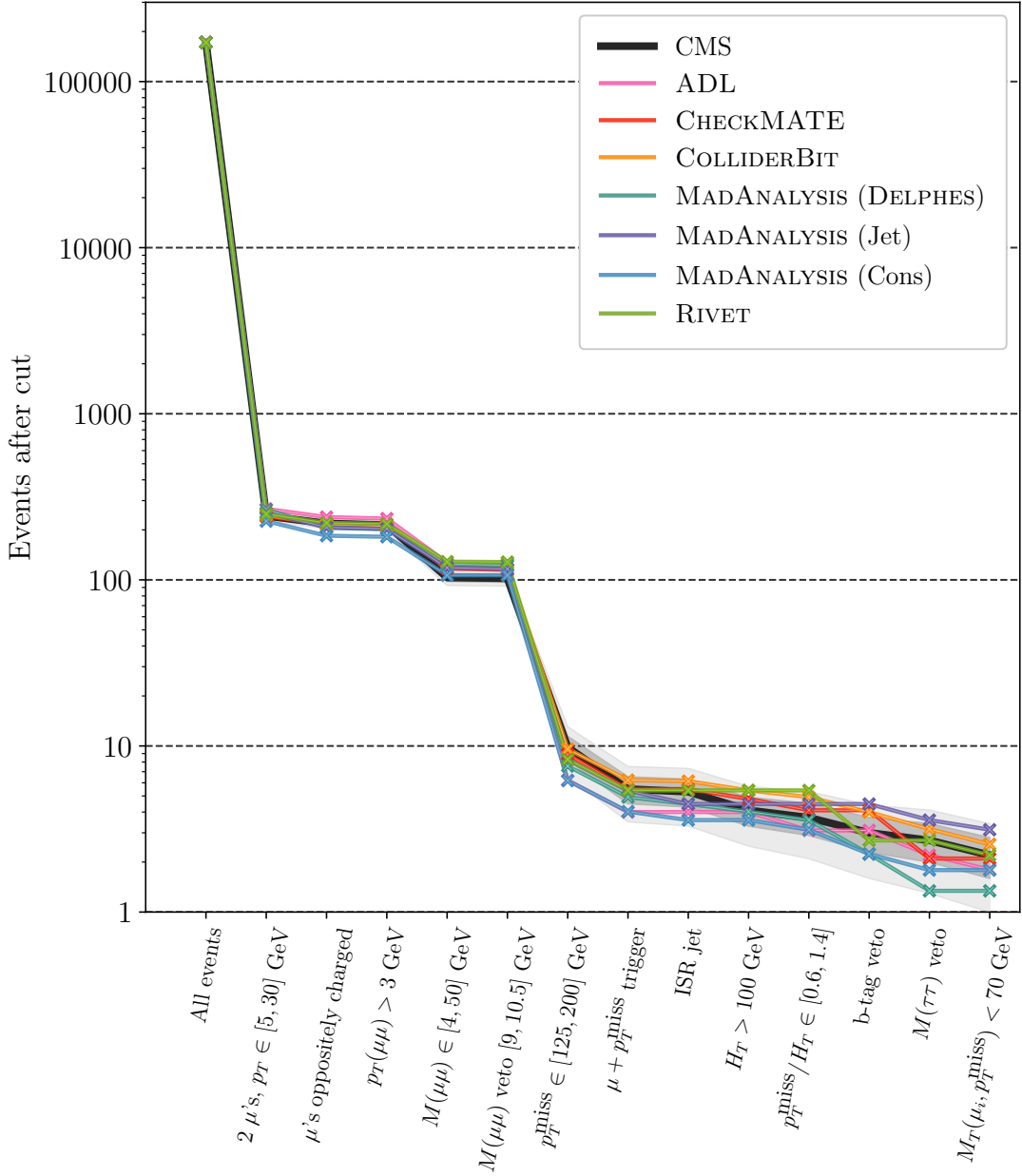[125, 200] GeV, all the recast cutflows stay within the 2σ uncertainty band of the CMS cutflow.

Figure 2: Visualisation of the cutflow comparison in Table 1. The inner and outer grey bands indicate the 1σ and 2σ statistical uncertainty for the CMS cutflow, respectively, as given in Ref. [330] (auxiliary material).

The three MADANALYSIS cutflows serve as a useful illustration of the impact different choices of fast detector simulation and reconstruction algorithms can have. Since all cutflows in our comparison start from the same set of truth-level signal events, and the three MADANAL-YSIS cutflows further share a common implementation of the cutflow logic, the discrepancies between these three cutflows are likely due to the differences in the detector simulation and reconstruction step.

4 Summary

The recasting of LHC searches in the context of complete BSM models gives a more powerful understanding of the results of the experiments. In this work we have performed a detailed comparison of the reinterpretation of a particular signal region of a CMS analysis with many of the publicly available recasting tools: CHECKMATE, RIVET, MADANALYSIS, ADL and COLLIDERBIT. We have shown that all of them reproduce fairly well the cutflow provided by CMS in a specific benchmark scenario, but there are minor discrepancies mainly due to using different detector simulation and reconstruction algorithms.

In the early stages of this comparison work we identified and corrected some clear discrepancies in the implementations of the CMS analysis across the different recast tools. The comparison presented here therefore illustrates the residual level of systematic discrepancy one can expect between the different recast tools and their detector simulation and reconstruction inputs after any obvious analysis logic differences have been dealt with. Such cross-checks highlight one of the benefits of having a handful of different recast tools with independent analysis implementations and detector simulation and reconstruction choices.

However, having multiple implementations of the same LHC search in different tools does represent a significant amount of duplicated effort. Developing a more unified software framework for implementation and preservation of BSM searches has the potential long-term benefit of freeing up significant resources in the recasting community. This could lead to a much larger combined set of implemented analyses available for reinterpretation studies, and also allow for even more in-depth validations of the analyses against the simulation results provided by the LHC experiments.

Contribution 20

Complementary of searches and measurements in re-interpretation

T. Berger-Hryn'ova, A. Buckley, J. M. Butterworth, L. Corpe, D. Yallup, M. van Beekveld, B. Fuks, T. Gonzalo, A. Kvellestad

Re-interpretation is an increasingly important topic in the high energy physics community. As no new particles have been discovered since the Higgs boson, the field is pivoting from a theory-driven approach to a data-driven approach. It is therefore crucial that Large Hadron Collider (LHC) measurements/searches are preserved, both in terms of analysis logic and results. Furthermore, it is necessary that infrastructure is developed to allow for the rapid and reliable re-interpretation of these LHC results. It could then easily be checked whether new proposed models are ruled out by existing results, avoiding the need to use resources on a dedicated search. Conversely, gaps in the existing analysis programme at the LHC could be identified, leading to the proposal of new analyses dedicated to these specific cases.

Searches are typically optimised towards one set of models, or a family of models, but could have sensitivity to new, as-yet-unproposed models. Measurements are typically preserved via the process of "unfolding" to particle-level (*i.e.* correcting for detector effects), and storing the analysis logic in a RIVET [87,314] routine. It is then straightforward to check how any potential new signal could have showed up in a measurement preserved in this way: one only needs to run simulated signal events through the routine. Indeed, a framework called CONTUR [88] has been built to automatically scan the bank of LHC measurements to verify whether a proposed new model is already excluded. Examples of how CONTUR can be used to set constraints on new models can be found in Refs. [315–317] and the procedure is also discussed in Section 18 of these proceedings.

Searches, however, are typically not unfolded. In such cases detailed re-interpretation requires some form of detector simulation, in addition to the signal event generation and implementation of the analysis logic. As different use cases require different levels of speed and accuracy in these simulations, several public tools have been developed in the phenomenology community for LHC search re-interpretation, such as CHECKMATE [69], MADANALYSIS 5 [71–73] and COLLIDERBIT (part of GAMBIT) [328, 329]. In addition, the package SMODELS [295] performs a fast re-interpretation without Monte Carlo (MC) simulations, by mapping predictions for total production cross sections for all signals of a given beyond-the-Standard-Model (BSM) model to the efficiencies associated with a set of searches targeting specific simplified model signatures. Conclusive statements about the viability of the initial model can then be drawn after a comparison with published excluded rates at the 95% confidence level. Currently each of these tools comes with its own database of implemented LHC searches.

In this contribution, we investigate two questions. Firstly, we examine whether, using the smearing functionality recently added to RIVET [327], it is possible to preserve searches in the same way as measurements are preserved, and thus automate the re-interpretation process for searches to be as fast and efficient as it is for measurements in tools such as CONTUR. Secondly

164

we examine a series of MSSM parameter points which have been identified as high-likelihood scenarios in a GAMBIT fit to results of searches for supersymmetry (SUSY), and see whether the measurements available to CONTUR have any complementary impact.

1 Preserving searches in RIVET

To test whether a RIVET routine for a search can be used in an automated framework like CONTUR, one should check whether detector-level distributions of the Standard Model (SM) background and signal in the analysis signal region can be reproduced within the uncertainties, using particle-level inputs only and a smearing approach to convert truth-level distributions into approximate detector-level ones. Two examples of how this can be achieved are shown below.

The first example consists of an ATLAS search [298] for supersymmetry in a final state featuring jets, missing energy and vetoing the presence of leptons, using $3.2 \, \text{fb}^{-1}$ of 13 TeV LHC data. The routine for this SUSY search uses RIVET's pre-loaded jet, b-tagging, missing energy and lepton efficiency and energy smearing functions to emulate the detector-level distributions of signal and background based on particle-level inputs. The second is a more involved example. We consider an ATLAS search for high-mass di-lepton resonances with $139 \, \text{fb}^{-1}$ of 13 TeV LHC data [13], where the resolution function provided in the experimental publication is integrated as a custom smearing function in the RIVET routine.

In both cases, it has been possible to produce a RIVET routine which is able to give a good representation of the background distribution(s) presented in the original ATLAS publication, so that both searches are therefore usable in the CONTUR framework for re-interpretations.

1.1 Example 1: a SUSY search preserved in RIVET

The $3.2 \, \text{fb}^{-1}$ zero-lepton SUSY search described in Ref. [298] has seven signal regions (SRs), which were designed to target three different possibilities for the all-hadronic decay of squarks and gluinos in simplified SUSY models that assume R-parity conservation. All the SRs require exactly zero reconstructed electrons or muons with momentum above 10 GeV, and at least 200 GeV of missing transverse energy. The selection defining the different SRs then imposes the presence of 2 to 6 jets with varying transverse momentum requirements and imposes a region-specific threshold on the inclusive effective mass, m_{eff}, defined as the scalar sum of the transverse momentum of all reconstructed jets and the missing transverse energy. The distributions of the SM background as a function of m_{eff} are included the corresponding HEPData entry[1] for the search. A few examples are shown in the top row of Figure 1. These background distributions are precisely what is needed as an output from a RIVET routine in order to use them in an automated framework like CONTUR.

Replicating the analysis selection at the detector-level requires that the truth-level energies of these objects is smeared in a way that mimics the ATLAS detector reconstruction and object identification performance. Thankfully, since the objects used in this search are "standard" ATLAS objects, the built-in jet, missing energy and lepton momentum smearing efficiencies, which have recently been introduced in RIVET [327], can be used for this purpose.

It was therefore possible to construct a RIVET routine dedicated for this search[2] using the smearing functions like:

---

[1]Tables 4–10 of https://www.hepdata.net/record/ins1458270
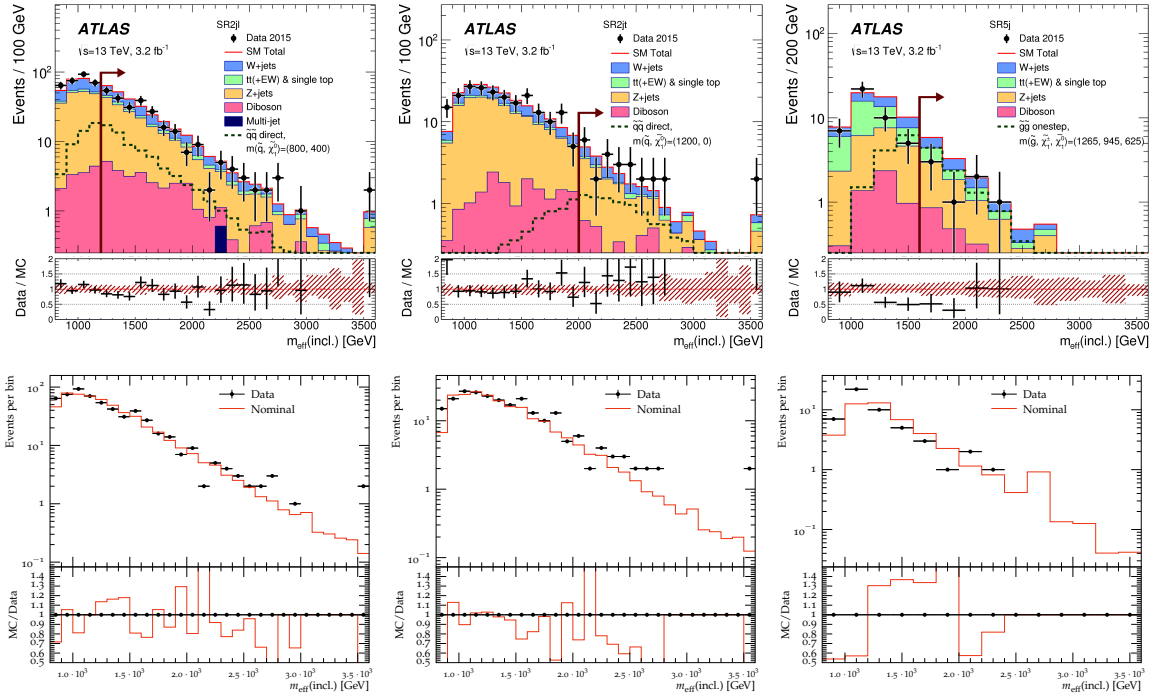[2]https://rivet.hepforge.org/analyses/ATLAS_2016_I1458270

Figure 1: Examples of some of the m_{eff} distributions presented in the ATLAS zero-lepton SUSY search [298] (top row), and comparisons of matching data and smeared MC simulation predictions obtained from the corresponding RIVET routine (bottom row). "Nominal" in the second row subfigures refers to the sum of the dominant SM processes which contribute, as described in the main body of the text.

```
// Initialise and register projections
FinalState calofs(Cuts::abseta < 4.8);
FastJets fj(calofs, FastJets::ANTIKT, 0.4);
declare(fj, "TruthJets");
declare(SmearedJets(fj, JET_SMEAR_ATLAS_RUN2,
        JET_BTAG_ATLAS_RUN2_MV2C20), "RecoJets");

MissingMomentum mm(calofs);
declare(mm, "TruthMET");
declare(SmearedMET(mm, MET_SMEAR_ATLAS_RUN2), "RecoMET");

PromptFinalState es(Cuts::abseta < 2.47 &&
                    Cuts::abspid == PID::ELECTRON, true, true);
declare(es, "TruthElectrons");
declare(SmearedParticles(es, ELECTRON_RECOEFF_ATLAS_RUN2,
        ELECTRON_SMEAR_ATLAS_RUN2), "RecoElectrons");

// + similar for muons
```

This RIVET routine has since been incorporated into the main RIVET distribution. Its performance was validated separately for the signal and SM background. For the SUSY signal, it

was possible to check that the analysis logic and smearing was working correctly using the sequential selections included in the auxiliary material attached to the original publication[3], in auxiliary Tables 1-7, or equivalently, in the HEPData entry. For the SM background, the performance of the routine was checked by investigating the properties of V plus jets events generated with SHERPA [334] and top-antitop events generated with POWHEG and PYTHIA [28, 335]. The comparison of the resulting distributions to those observed in data are shown in the bottom row of Figure 1.

This exercise demonstrates that approximate detector-level distributions from LHC searches can be reproduced using truth-level inputs and smearing functions in a RIVET routine.

1.2 Example 2: a dilepton "bump-hunt" search preserved in RIVET

In the high-mass di-lepton resonance search using 139 fb^{-1} of 13 TeV data collected with the ATLAS detector described in Ref. [13], events are required to contain two same-flavour leptons, with an invariant mass m_{ee} larger than 225 GeV. The background estimation is achieved using a fit to the observed data passing the analysis selection. Unlike the previous example, it is not possible to simply use default smearing functions to construct a RIVET routine, since the objects used in the search are "non-standard", and the final background estimation uses a data-driven technique. However, the analysis team used simulated events to extract a resolution function from the fit. This resolution function was provided in the auxiliary material for the publication[4] in Figures 10 and 11, and in the associated HEPData entry[5] in Tables 23 and 24.

The background distributions in the di-electron and di-muon channels from the original experimental article can be seen in Figure 2. The RIVET routine needs to be able to replicate these detector-level background shapes using truth-level inputs. In order to do this, the resolution functions from the original publication are integrated into the RIVET routine[6] in the following way,

```
// Smear the dilepton mass with a CB + Gauss function
double muCB, sigCB, alpCB, nCB, muG, sigG, kappa;

// for electrons (similar for muons)
const double lnm = log(mll);

static const vector<double> pmuCB = {0.13287, -0.410663, -0.0126743, 2.9547e-6};
muCB = pmuCB[0] + pmuCB[1]/lnm + pmuCB[2]*lnm + pmuCB[3]*pow(lnm, 4);

static const vector<double> psigCB = {0.0136624, 0.230678, 1.73254};
sigCB = sqrt(pow(psigCB[0],2) + pow(psigCB[1],2)/mll + pow(psigCB[2]/mll, 2));

alpCB = 1.59112;

static const vector<double> pnCB = {1.13055, 0.76705, 0.00298312};
nCB = pnCB[0] + pnCB[1]*exp(-pnCB[2]*mll);

static const vector<double> pmuG = {-0.00402708, 0.814172, -3.94281e-7, 7.97076e-6, -87.6397,
    -1.64806e-11};
muG = pmuG[0] + pmuG[1]/mll + pmuG[2]*mll + pmuG[3]*pow(lnm,3) + pmuG[4]/sqr(mll) +
    pmuG[5]*sqr(mll);

static const vector<double> psigG = {0.00553858, 0.140909, 0.644418};
sigG = sqrt(sqr(psigG[0]) + sqr(psigG[1])/mll + sqr(psigG[2]/mll));
```
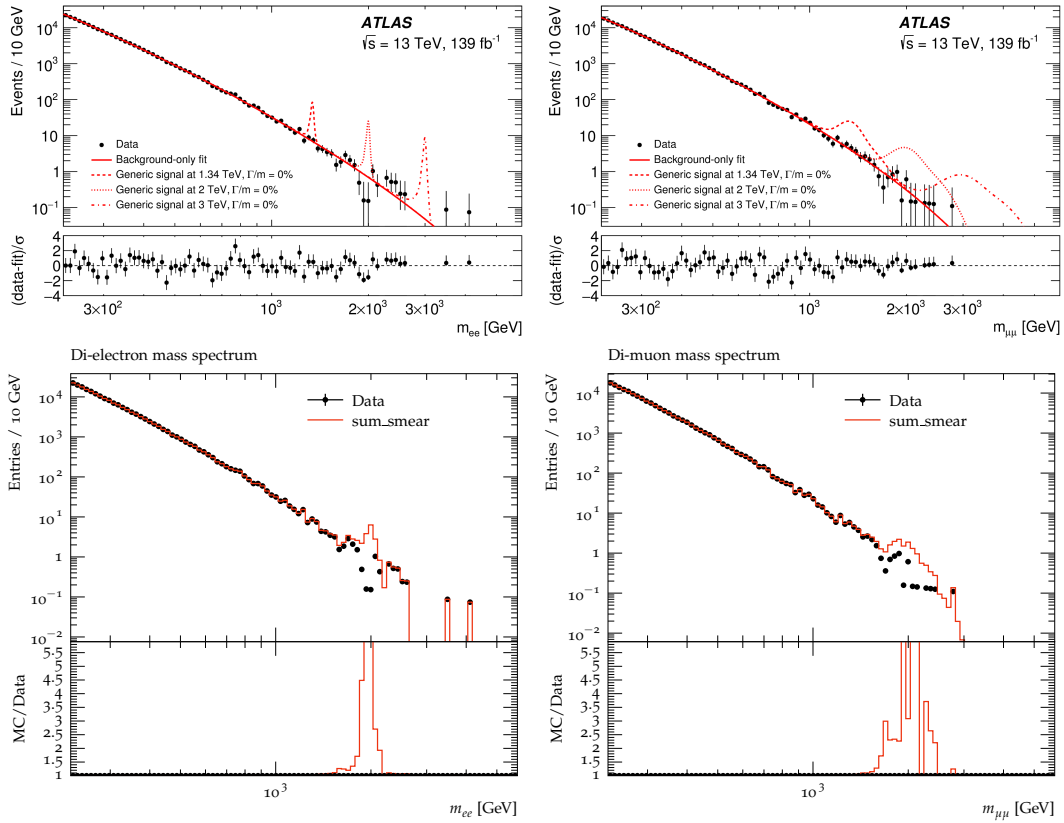
Figure 2: The dilepton invariant mass distributions in the SRs of the ATLAS dilepton resonance search of Ref. [13] (top row), and examples of a simple Z' signal generated with PYTHIA ($m_{Z'} = 2$ TeV) after smearing in the RIVET routine (bottom row). The "sum_smear" tag in the bottom row subfigures refers to the smeared Z' signal super-imposed on the observed background.

```
static const vector<double> pkappa = {0.347003, 0.135768, 0.00372497, −2.2822e−5,
    5.06351e−13};
kappa = pkappa[0] + pkappa[1]*exp(−pkappa[2]*mll) + pkappa[3]*mll + pkappa[4]*pow(mll,3);

static const vector<double> pkappa = {0.347003, 0.135768, 0.00372497, −2.2822e−5, 5.06351e−13};
kappa = pkappa[0] + pkappa[1]*exp(−pkappa[2]*mll) + pkappa[3]*mll + pkappa[4]*pow(mll,3);

// Smearing using calculated params(mll)
double mll_scale = −1;
do {
  mll_scale = (rand01() > kappa) ? randnorm(muG, sigG) : randcrystalball(alpCB, nCB, muCB,
    sigCB);
} while (fabs(mll_scale) > 0.5);
const double mll_reco = (1 + mll_scale) * mll;
```

The performance of the implemented smearing was checked by comparing the number of events passing the selection for a simple BSM model to those reported in the original article. An example of a 2 TeV Z' signal after smearing can be seen in Figure 2. This exercise shows that even for non-standard objects, it is possible to include detector-level results into RIVET and get good agreement with the fully-reconstructed results.

2 Comparison of performance of searches and measurements using CONTUR

The SUSY search mentioned in Section 1.1 probes final states featuring jets, missing energy and no lepton using 3.2 fb^{-1} of 13 TeV data. ATLAS has also published a measurement that is sensitive to BSM physics in the same final state. Specifically, this is a detector-corrected measurement of the ratio of fiducial cross sections for missing energy and jets, and dilepton pairs and jets [336]. This measurement was also made using the same dataset (3.2 fb^{-1} at 13 TeV) as the SUSY search. Since the measurement was unfolded to particle level, it already had a RIVET routine that was included within CONTUR. This measurement will be refered to as the "jetMET" measurement hereafter. Since the two analyses probe the same final state and use the same dataset, one would expect that they give similar sensitivity to new models when used for re-interpretation.

A benchmark dark matter model was chosen to compare the performance of the search and measurement of the jets+MET final state. The parameters were chosen as in Ref. [337], and a scan of the exclusion from each routine as a functions of the mass of the dark matter (DM) candidate (M_{DM}) and the mass of the Z' particle ($M_{Z'}$) predicted by the model was performed. The limits are calculated using the CL$_s$ method [338]. The results of both exclusion scans are shown in Figure 3. They show that the SUSY search, which was performed at detector-level, and whose RIVET routine was written using RIVET's built in smearing and efficiency tables, performs roughly as well as the jetMET measurement which was unfolded the particle-level. This demonstrates that searches and measurements of similar final states can both be used in machinery like CONTUR to provide fast and reliable re-interpretation of results when compared to new physics models.

3 Using search routines in CONTUR to probe new models

The high-mass di-lepton resonance routine was used to check the exclusion for a model which includes a vector leptoquark (LQ) singlet [22]. This type of model has been invoked to explain the observed anomalies in the B-sector [24]. The set of parameters where the leptoquark decays to second-generation fermions (with coupling $g_{b_L \mu_L}$) was tested. The CONTUR scan was performed as a function of the LQ mass (M_{VLQ}), and the results are shown in Figure 4 for for all 13 TeV measurements (top row) and just the high-mass di-lepton resonance search (bottom row). The sensitivity of the measurements to this model comes from ATLAS and CMS measurements of V+jets and $t\bar{t}$ processes, as well as differential measurements of the jet production cross-sections. The search is found to be slightly more constraining than the measurements at high LQ masses, and is therefore largely complementary with the measurements to help exclude new models in CONTUR.

4 Complementarity in SUSY parameter scans

As with many BSM searches at the LHC, searches for electroweakinos (neutralinos and charginos) are usually based on *simplified models*. These models use a reduced set of phenomenological parameters to simplify the complex task of optimizing the search and interpreting the results. However, this leaves open the question of what implications the search results have for the parameter spaces of more complete SUSY models. In [339], the GAMBIT global fitting framework, and in particular the COLLIDERBIT module, was used to re-interpret several ATLAS and CMS searches [330, 340–346] in the context of the full electroweakino sector of the Minimal Supersymmetric Standard Model (MSSM). This model, called the EWMSSM, is defined by four free
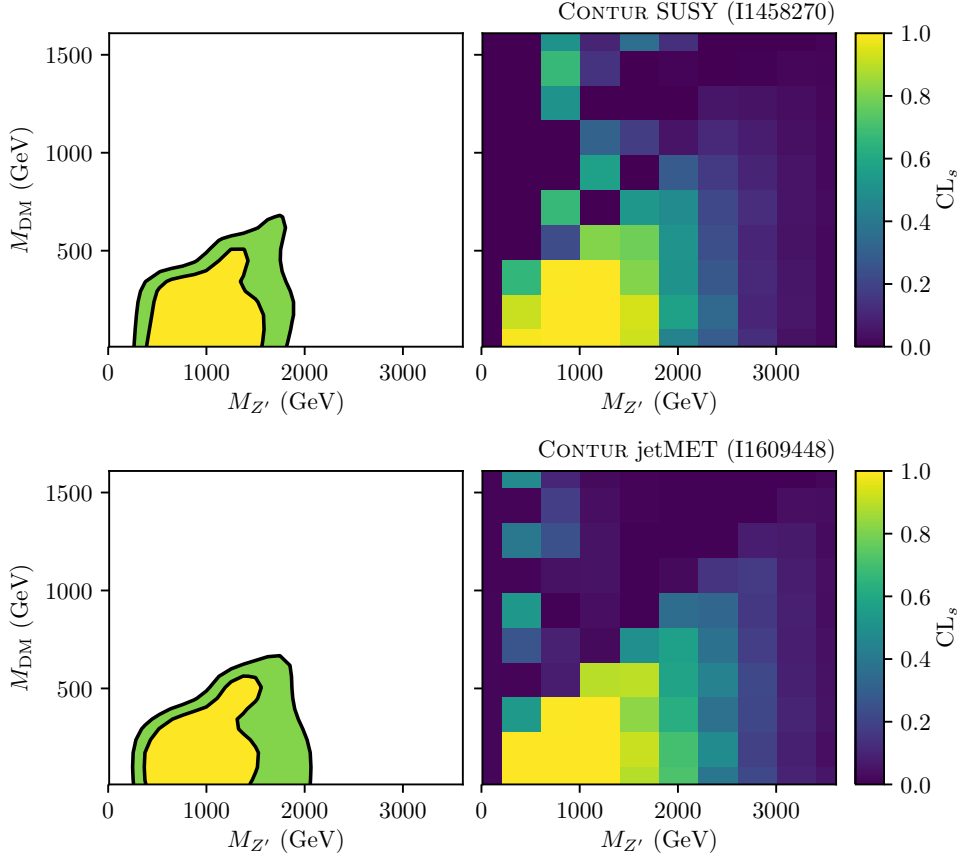
Figure 3: Comparison of the CONTUR exclusions for a benchmark dark matter model from an existing routine for a SM measurement of the jet+MET final state (lower panel), and for the SUSY routine described above (upper panel). The two analyses probe the same final state and use the same 3.2 fb^{-1} of 13 TeV data. They are found to provide similar sensitivity to the benchmark DM model.

parameters: M_1, M_2, μ and $\tan\beta$, which control the tree-level masses and mixings of the four neutralinos ($\tilde{\chi}_1^0$, $\tilde{\chi}_2^0$, $\tilde{\chi}_3^0$, $\tilde{\chi}_4^0$) and two charginos ($\tilde{\chi}_1^\pm$, $\tilde{\chi}_2^\pm$) of the MSSM. The gluino, sfermions and additional Higgs bosons are decoupled by setting the relevant MSSM mass parameters to several TeV.

The analysis in [339] shows that, in the MSSM, the masses of the charginos and neutralinos are only weakly constrained by the combination of electroweakino searches with 36 fb^{-1} of data at $\sqrt{s} = 13$ TeV. The loose constraints are in part a consequence of the parametric freedom of the EWMSSM compared to the simplified models, and partly due to a series of small data excesses that can offset tensions in other analyses. In fact, these small excesses conspire to produce a preferred subregion of the EWMSSM parameter space, at the 3σ level, compared to the SM-only expectation. The resulting best-fit EWMSSM subspace is shown in Figure 5, in terms of profile likelihood figures for different electroweakino mass planes. The 2σ region (relative to the best-fit point) predicts mass spectra with all the electroweakinos lighter than ~ 700 GeV. Further, the predicted spectra feature two mass gaps larger than m_Z, between the dominantly bino $\tilde{\chi}_1^0$ and the mostly wino (Higgsino) $\tilde{\chi}_2^0/\tilde{\chi}_1^\pm$, and between $\tilde{\chi}_2^0/\tilde{\chi}_1^\pm$ and the dominantly Higgsino (wino) $\tilde{\chi}_4^0/\tilde{\chi}_2^\pm$. The first of these mass gaps is evident in the first panel of Figure 5, where the 1σ region picks out the $m_{\tilde{\chi}_1^\pm} - m_{\tilde{\chi}_1^0} \sim m_Z$ region. The preference for these mass gaps comes
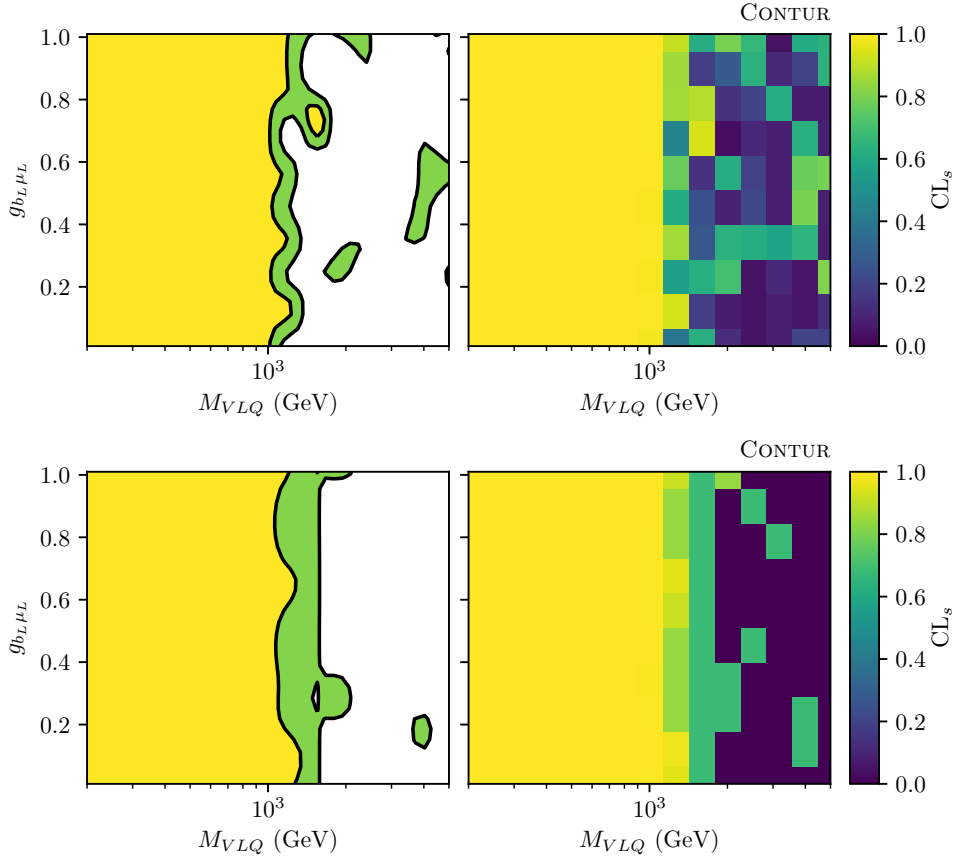
Figure 4: Comparison of the CONTUR exclusions for a LQ model from the 13 TeV measurements already in CONTUR (top row) and the 13 TeV high mass di-lepton resonance search (bottom row).

from the fact that the fitted excesses are seen in searches that target SUSY signals with on-shell Z and W bosons.

Here we investigate to what extent the collection of LHC measurements implemented in CONTUR can constrain these particular EWMSSM scenarios. To run CONTUR on the full set of EWMSSM parameter samples from the GAMBIT scan in [339] is beyond the scope of this work, due to the significant computational cost. Instead we extract three grids of EWMSSM points from the profile-likelihood surfaces shown in Figure 5 by binning the GAMBIT samples in each mass plane and extracting the best-fit point within each bin.[7] The resulting grids of EWMSSM points are illustrated in Figure 6. We include points that are within the 3σ region in the GAMBIT fit result, as indicated by the colouring in Figure 6. These parameter points are then passed to HERWIG [101] in the form of SLHA files [42]. CONTUR is used to scan over these points, as usual requesting HERWIG to generate all implied final states with one or more BSM particles outgoing from the matrix element, and looking for the impact on fiducial cross section measurements available in RIVET.

The resultant heatmaps of CL_s values from CONTUR are shown in Figure 7. It can be seen that many of the parameter points preferred in the GAMBIT combination of SUSY searches

---

[7]The extracted points are not necessarily unique to a single grid. For instance, the global best-fit point from the GAMBIT fit will appear in all three grids.
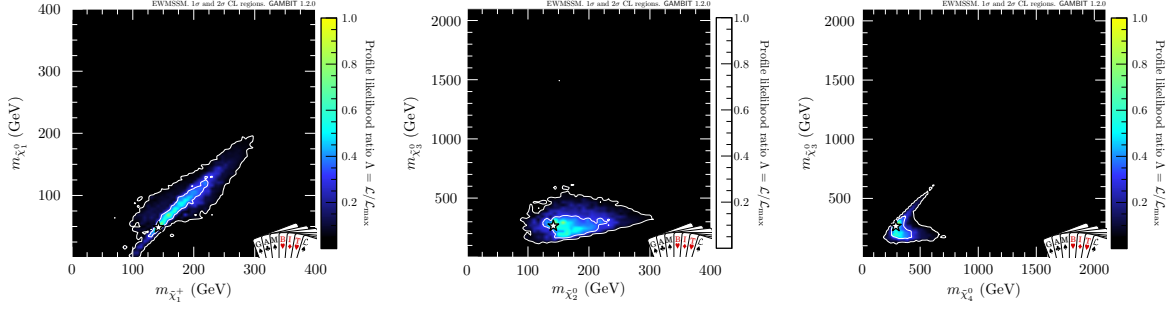
Figure 5: Results from the combination and re-interpretation of LHC 13 TeV searches in a global fit of the EWMSSM, from [339]. The figures show the profile likelihood ratio $\mathcal{L}/\mathcal{L}_{\max}$ in the $(m_{\tilde{\chi}_1^\pm}, m_{\tilde{\chi}_1^0})$ plane (left), the $(m_{\tilde{\chi}_2^0}, m_{\tilde{\chi}_3^0})$ plane (middle), and the $(m_{\tilde{\chi}_4^0}, m_{\tilde{\chi}_3^0})$ plane (right). The likelihood function used in the fit combines the likelihood contributions from all the re-interpreted ATLAS and CMS searches, as well as likelihood contributions from invisible Higgs and Z boson decays. $\mathcal{L}_{\max}$ is the likelihood of the global EWMSSM best-fit point, while $\mathcal{L}$ is the highest EWMSSM likelihood for the given point in mass space. The white star marks the location of the best-fit point and the white contours show the 1σ and 2σ preferred regions relative to this point.
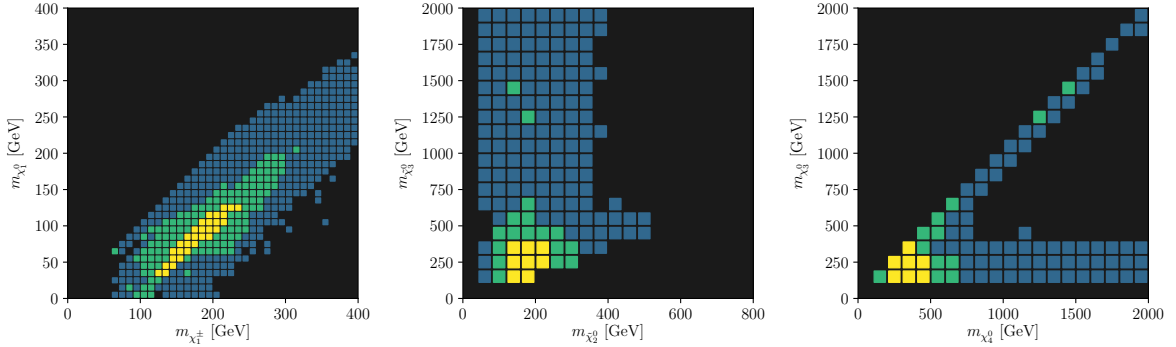
Figure 6: Grids of EWMSSM points extracted from the best-fit EWMSSM parameter space surface identified by the GAMBIT global fit in [339]. The yellow, green and blue points are within the 1σ, 2σ and 3σ preferred regions in the GAMBIT fit, respectively.

display tension with measurement results. For instance, in the $(m_{\tilde{\chi}_1^\pm}, m_{\tilde{\chi}_1^0})$ plane (left), the 30 points extracted from the 1σ region of the GAMBIT fit all end up with $\mathrm{CL}_s > 0.95$ in the CONTUR analysis. Similarly, in the $(m_{\tilde{\chi}_2^0}, m_{\tilde{\chi}_3^0})$ and $(m_{\tilde{\chi}_4^0}, m_{\tilde{\chi}_3^0})$ planes (middle and right), the measurements checked by CONTUR show exclusion sensitivity to many of the EWMSSM points with $m_{\tilde{\chi}_3^0} \lesssim 400$ GeV. This comes principally from the ATLAS WWW measurement [347] in the channel with two same-sign leptons and two jets. There is also sensitivity from the ATLAS four-lepton line shape measurement [348] for parameter points where the heavier electroweakinos ($\tilde{\chi}_3^0$, $\tilde{\chi}_4^0$ and $\tilde{\chi}_2^\pm$) are not completely decoupled. This is not surprising, as what mainly drives the preference for having these states relatively light in the GAMBIT fit is an excess seen in an ATLAS search for final states with four leptons plus missing energy [343]. This excess can
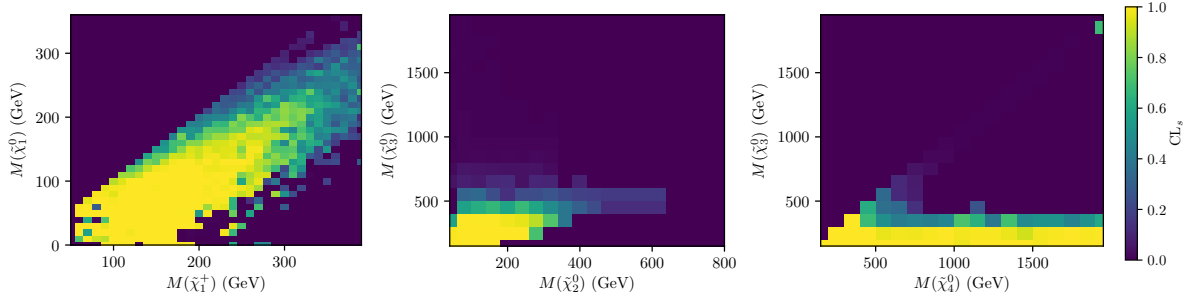
Figure 7: CONTUR exclusion sensitivity to the GAMBIT points shown in Fig. 6.

more easily be accommodated when at least $\tilde{\chi}_3^0$, and possibly also $\tilde{\chi}_4^0/\tilde{\chi}_2^{\pm}$[8], are not decoupled, since the decays $\tilde{\chi}_3^0(\tilde{\chi}_4^0) \to Z\tilde{\chi}_2^0$ and $\tilde{\chi}_2^{\pm} \to Z\tilde{\chi}_1^{\pm}$ increase the production rate for di-Z-boson events. Similarly, the production and decay of the heavier electroweakinos can increase the expected rates for multi-W-boson events, *e.g.* through decay processes such as $\tilde{\chi}_3^0(\tilde{\chi}_4^0) \to W^{\pm}\tilde{\chi}_1^{\pm}$, $\tilde{\chi}_2^{\pm} \to W^{\pm}\tilde{\chi}_2^0$ and $\tilde{\chi}_3^0 \to h\tilde{\chi}_1^0 \to W^{\pm}W^{(*)\pm}\tilde{\chi}_1^0$.

The best-fit EWMSSM points from the GAMBIT fit were preferred due their ability to fit excesses in some searches, while simultaneously avoiding strong tension with other searches. Since CONTUR in this mode is treating the signal as background, such excesses would not be taken into account. However, neither of these measurements shows an excess of data over the SM. Example figures, with the SM theory prediction indicated, are shown in Figure 8. Events from parameter points at higher masses also enter these and several other the fiducial cross sections – typically those involving (multiple) gauge boson production – indicating that with higher luminosity, with more precise and/or exclusive measurements, some of these scenarios may be accessible to this approach.

5 Summary

The analysis logic and reference data for two searches were preserved as RIVET routines using smearing techniques to obtain approximate detector-level distributions from particle-level inputs. These routines could then be used in an automated re-interpretation tool, in this case, CONTUR. The performance of these search routines was compared to that of measurements of similar final states for benchmark BSM models, and were found to be similar. This study shows that it is possible to use searches alongside measurements in automated re-interpretation workflows. This could speed up the re-interpretation of searches which are preserved in RIVET routines, since it bypasses the need for an ad-hoc re-interpretation on a case-by-case basis. For cases where lack of statistics precludes unfolding (for example in tails of distributions), these approaches are expected to be complementary in the context of CONTUR.

A selection of SUSY parameter points which are either favoured, or not excluded, by a combination of SUSY searches considered in GAMBIT, were run through CONTUR to check for sensitivity in the existing LHC measurements. Several of the parameter points at low $m_{\tilde{\chi}_3^0}$ are disfavoured by the measurements, particularly the four-lepton and same-sign-dilepton plus jet channels. There seems to be significant potential, and complementarity between measurements,

---

[8]Due to the dominantly wino or Higgsino nature of the $\tilde{\chi}_4^0$ state in these EWMSSM scenarios, the $\tilde{\chi}_2^{\pm}$ chargino is always close in mass to the $\tilde{\chi}_4^0$ neutralino.
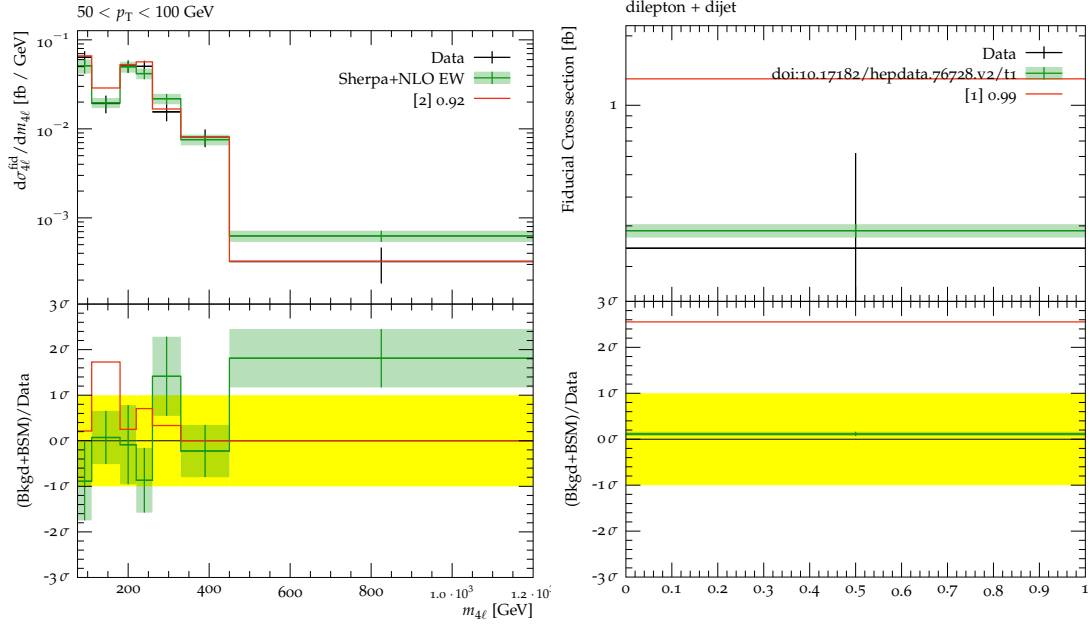
Figure 8: Example RIVET figures contributing to the CONTUR exclusion for the third GAMBIT hypersurface. On the left, the four-lepton lineshape at intermediate p_T^{4l} from [348], for an EWMSSM point with $(m_{\tilde{\chi}_1^0}, m_{\tilde{\chi}_2^0}, m_{\tilde{\chi}_3^0}, m_{\tilde{\chi}_4^0}, m_{\tilde{\chi}_1^\pm}, m_{\tilde{\chi}_2^\pm}) = (55, 94, 169, 199, 98, 205)$ GeV. On the right, the like-sign-dilepton plus dijet cross section from [347] for a point with $(m_{\tilde{\chi}_1^0}, m_{\tilde{\chi}_2^0}, m_{\tilde{\chi}_3^0}, m_{\tilde{\chi}_4^0}, m_{\tilde{\chi}_1^\pm}, m_{\tilde{\chi}_2^\pm}) = (74, 201, 202, 1686, 196, 1686)$ GeV. The upper figures show the cross section comparison between data (black), data and new physics (red) and the SM (green). The lower figures show the ratios expressed as a significance.

in regions where the SM contribution is large but well-known, and searches where the goal is usually to find regions where the SM contribution is small. This is an area of interesting further study in the HL-LHC period.

Contribution 21

Determining sensitivity of future measurements to new physics signals

D. Kar, L. Corpe

No definite signs of new physics have been observed in LHC data since the discover of the Higgs boson in 2012. This has brought into focus a few alternative strategies for the search for new physics. CONTUR [88] is one such approach, where existing unfolded measurements are used to set bounds on different BSM models (the procedure is also discussed in Section 18 of these proceedings). In this exercise, we ask the opposite question: if we expect a certain measurement to be performed at the LHC, what precision needs to be achieved in order to exclude a certain region of parameter space of a specific BSM model. This approach can be generalised: one could produce a list of topologies and phase spaces which, when measured with specified precision, can constrain unexplored region of parameter space of models. We leave that as a future exercise.

Since this is a proof-of-principle demonstration, the details and the viability of the model and parameter space is not of critical importance. A benchmark two-Higgs doublet model ("2HDM+a") is used, inspired by the combination of some of the ATLAS dark matter searches [187]. Figure 1 shows that for low values of the $\tan\beta$ parameter (which is related to the ratio of vacuum expectation values of the two Higgs doublets), this model can be sensitive to the four-top-quark production process. To test if a future four top cross-section measurement can constrain the model, we generate pseudodata with the PYTHIA [28] event generator. Since the cross-section is extremely small, we generate the largest background, semileptonic $t\bar{t}$ events, as proxy for the four top process. We only select events with at least 6 jets, 2 of which must be tagged as containing b quarks. We consider the H_T distribution, which is the scalar sum of p_T of all selected jets, constructed using the RIVET [87] analysis framework. All samples are normalised to 300 fb^{-1} of integrated luminosity.

We considered two scenarios for the uncertainties associated with the pseudo-measurement: 25% and 50% flat uncertainties, shown by solid and dashed error bars in Figure 2. Three different signal scenarios are overlaid, corresponding to $\tan\beta$ values between 0.1 to 0.5, keeping $m_a = 500$ GeV and $M_A = 600$ GeV, but the specific values are not the important aspect here. The signal samples where generated using HERWIG [101]. As can be seen from Figure 2, the "Signal1", corresponding to the lowest $\tan\beta$ value will be excluded by such a measurement alone. Intuitively, this is due to the fact that the additional signal, on top of the measured data, would be well beyond the uncertainties of the measurement. "Signal3", which corresponds to the highest $\tan\beta$ value, can't be excluded just by this measurement, since the signal would be within the uncertainties of the measurement if stacked on top of the data. It is hard to say anything about the intermediate "Signal2". This approach can be quantified more rigorously with CONTUR, which includes a set of available measurements at 7, 8 and 13 TeV center of mass energies from LHC (and we added this *fake* measurement). For "Signal2", the combined exclusion is about 98% and 84% for 25% and 50% flat uncertainties on all bins of our distribution. This indicates that if we can make the measurement with $\approx 25\%$ uncertainty, we can exclude

175

this signal at 95% confidence level, as opposed to making the measurement with $\approx 50\%$ uncertainty, which would not definitely exclude the model at this parameter point. For "Signal1", the exclusion is 100% for both the cases, while for "Signal3", the exclusion is about 60% and 45% respectively.
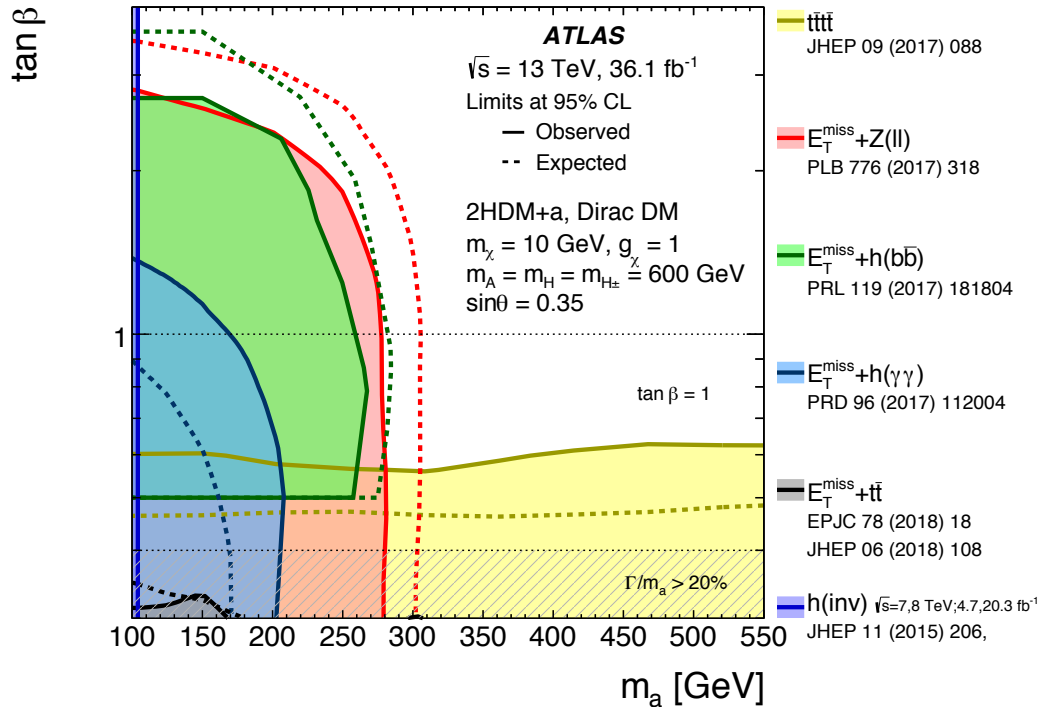

Figure 1: Regions in $(m_a, \tan\beta)$ planes from the model considered excluded by data from X+MET and $tttt$ measurements [187]. More more details, please refer to the cited article.

In this exercise, it is demonstrated that with the help of tools like RIVET and CONTUR, we can predict measurements at what precision can be sufficient exclude certain parameter space of certain models.
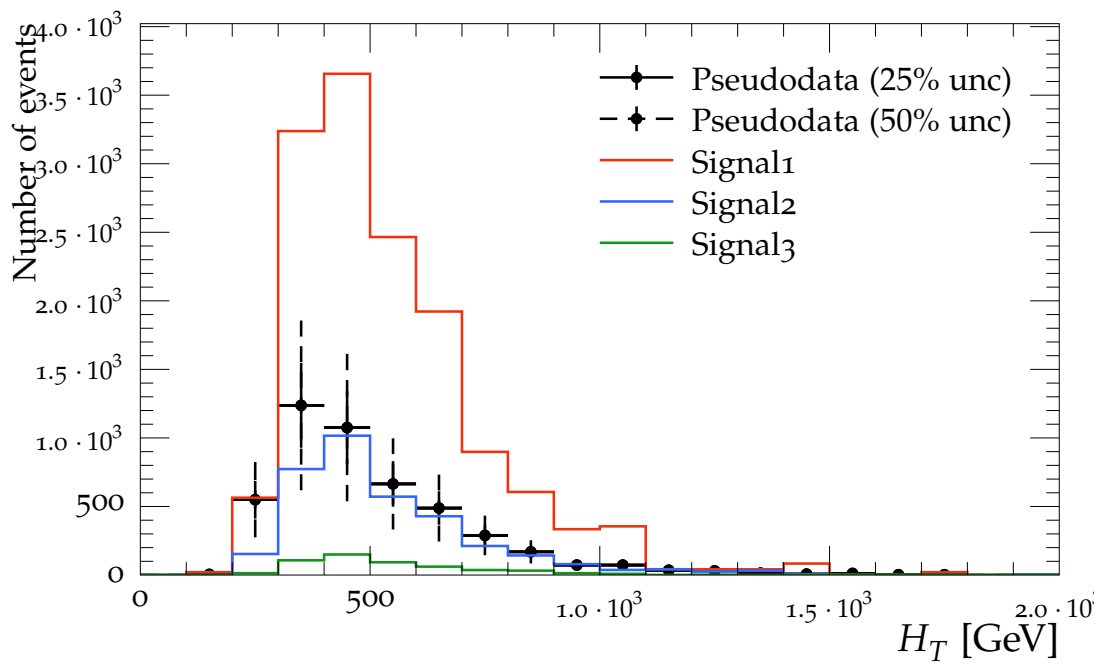
Figure 2: Distribution of H_T, normalised to 300 fb^{-1} of integrated luminosity, for pseudodata shown with 25% and 50% flat uncertainties, and three signal samples

Machine Learning

Contribution 22

Practical Machine Learning for regression and classification and applications in HEP phenomenology

S. Caron, A. Coccaro, S. Ganguly, S. Kraml, A. Lessa, S. Otten, R. Ruiz, H. Reyes-González, R. Ruiz de Austri, B. Stienen, R. Torre

Abstract

This contribution explains practical applications of Machine Learning (ML) in HEP phenomenology and here in particular the possibility to examine HEP models of new physics in their full dimensionality. ML models can be trained to provide likelihood evaluations, cross-sections and exclusion boundaries given the parameters of the HEP model. We discuss ways to accelerate the applicability of ML, to evaluate uncertainties in the ML model and to provide a sustainable reuse of training data and ML model. Various examples are discussed, such as the ML-based regression of cross sections in left-right symmetric models and in the inert doublet model (IDM) and the regression of likelihoods for the minimal supersymmetric standard model (MSSM7) as provided by the GAMBIT collaboration. Links to the training data can be found at https://www.phenoMLdata.org.

1 Introduction

In recent years machine learning (ML) has gained increasingly more traction in the particle physics community. Where machine learning was first used predominantly only in HEP experiments for the creation of metrics in a cut-and-count analysis, since a few years it also finds applications in various other branches of particle physics. This article is aimed at theorists and experimenters who want to understand how machine learning can be used for regression and classification in HEP phenomenology.

Many recent examples of the application of ML in phenomenology come from simulations and the exploration of theoretical models. Application range from simulations of particle physics events via so-called *generative* ML models [349–351] to proposals to search for new physics with the help of ML based *anomaly detection*, which is discussed elsewhere in these proceedings. Early ML applications in particle physics phenomenology and theory include the estimation of parton density functions [352] and various applications to jet physics as summarised in [353]. Furthermore it has been demonstrated that high-parameteric model exclusion boundaries [354] or likelihood (ratios) can be learned, explored and provided for further use via the use of ML models, see e.g. [355]. The ML model is made by learning numbers based on theoretical calculations or experimental measurements (e.g. cross-sections, likelihoods, posteriors, confidence level for exclusion) from training data given the parameters of the physical model and including even the experimental nuisance parameters [356]. Typically training data is provided by simulators (e.g. event generators) or by evaluating the likelihood of a given pa-

rameter set and theory with the help of experimental data. Examples could be a cross section of a new particle or an experimentally derived likelihood as a function of the parameters of a 20-dimensional Beyond the Standard Model (BSM) model. Here, an effective high-dimensional sampling of the full model parameter space is needed.

Even though ML allows to explore physical parameters in their full dimensionality, the application of such an approach has so far been limited. The keen interest of the experimental and theoretical community at Les Houches led to this note describing ways to accelerate progress in researching ML models for phenomenology.

First, we wish to encourage the experimental and theoretical communities to study and release model data in its full dimensionality. The publication of high-dimensional data should become a standard practice. Furthermore, we propose in this contribution a standardised way to publish high-dimensional training data, a way to publish the trained ML model, and a code database to provide examples to quickly (re-)train ML models on such data. We also present various examples, worked out within the Les Houches workshop, that follow this approach.

2 Project description

The idea of this project is to simplify the creation and reuse of ML models made for HEP phenomenology. For this we like to encourage to save the ML model, the HEP data set and the code to train the ML models. If the construction of ML models can be simplified, any publication on HEP phenomenology could use ML models to store probabilities, cross sections, and limits also for multidimensional HEP models.

2.1 Classification and Regression with uncertainties

The majority of machine learning in high energy physics uses supervised learning. Within supervised learning there are two main branches: classification and regression. In classification the ML algorithm learns to classify new data into a discrete number of classes (e.g. excluded or not excluded parameter configurations), whereas in regression the ML algorithms learns to predict a continuous quantity (e.g. a cross section). Both these branches can be seen as a prediction of an output variable y (or a set of output variables $\vec{y}$) given a set of input variables $\vec{x}$. The machine learning algorithm created with the data estimates the mapping function $\hat{f}(x) = y$ between the two. This estimator of the true mapping function $f(x)$ is learned from n examples where x_i and the true function values $f(x_i)$ are known.

Determining the best parameters of a particular ML model (e.g. a neural network) is called training. The core of machine learning is that this determination of parameters is automated based on data (hence called training data). As this data has a big influence on the performance of the algorithm, having a data set that is both large and information dense enough is often key to training a good machine learning algorithm. In low dimensional problems (i.e. problems with few input variables) with a computationally cheap data generation procedure data can easily be generated with random sampling or grid sampling. In HEP phenomenology, however, data generation typically requires the execution of a chain of numerical integration programs, e.g. event generators or simulations and often even a (time-consuming) comparison to experimental data. HEP more often than not deals with high dimensional functions for which the truth values are computationally costly to acquire. Techniques like active learning can predominantly sample parameter regions that are difficult to learn for the ML algorithm and can help to mitigate these problems e.g. to learn exclusion boundaries of HEP models [357].

Since there is freedom in the choice of ML models/algorithms, a limited amount of training data and uncertainties in the data, there are two uncertainties to consider. So called *aleatoric* uncertainties are uncertainties inherent to the data or data collection procedure, e.g. noise. These cannot be removed or reduced by adding more data points. Second, *epistemic* uncertainties are uncertainties that are introduced with our ML model for the estimator $\hat{f}(x) \approx f(x)$. An example of this type of uncertainty is the uncertainty related to the trained values of the parameters (e.g. the weights of a neural network) of the ML algorithm. One way to estimate such uncertainties in neural networks is by applying *dropout* of nodes that stays turned on during inference [358]. As dropout randomly disables a fraction of the network parameters, the output of the network will again change at each inference step. The spread of the output can then be interpreted as a measure of model uncertainty.

2.2 Collection of Machine Learning Models

The core of this initiative is formed by a collection of trained ML models. These models, whether they are neural networks or other types of models, should be stored together with meta data which allows them to be read by an end-user package. Such an end-user package would allow external users to quickly use ML models and access the predictions made by these models.

The format of the trained ML model can differ based on which library was used to create the trained model. For scikit-learn [359] for example the authors suggest [360] to serialise the entire model object with the `joblib` package in Python. For more neural network based packages a more natural choice would be to store the model in an .onnx-file. Especially .onnx-files guarantee a cross-library support of trained networks, giving a strong guarantee that information encoded in trained networks will still be usable in the coming future.

As to where to store these trained models, we think we can best look at the current best practice in the machine learning research community. There they use primarily GitHub for this. Trained models are often stored together with their training and production code and instructions in a README file on how to use the included codes. As most papers use data from publicly available sources (e.g. the MNIST data set [361] or credit card data set [362]), data is most of the time not included, but instead referred to.

We suggest to adopt this practice for high energy physics, with the only exception being for the data. Most of the already published papers in our field generate their own data. This makes it impossible to just cite the data location; the data needs to be stored somewhere as well. As the standard platform to publish data in particle physics phenomenology is Zenodo we suggest using that as a default location to store the data sets used for creating machine learning algorithms. This includes both training and testing data.

For this collection of models to work the inclusion of meta data is crucial. It should contain for example what the inputs for the model should be and what its output(s) represent(s). It will furthermore contain information that will make the use of the model more robust against mistakes. By including information on the boundaries of the training region, the package's code can warn the user if a model is used outside of its intended range. The specifics of the meta data and the exact storage format are currently in the process of being developed.

The advantage of this methodology is that the trained model can be bundled together with the meta data, so that the model can easily be communicated by the creating user, and easily be used by the external user. In this way efficient communication of for example high-dimensional results becomes possible. To encourage this, a searchable library of publicly available models

will be created, providing a single go-to location for neural networks in high energy physics.

2.3 Collection of Training Data

Alongside a trained model with meta data, each model instance should also come with a publicly accessible data set. For this we have set up webpage (https://www.phenoMLdata.org) and a Zenodo group[1], in which the high dimensional training data of each of the trained models will be published. We intend to also create a link with a tool like SPOT [363], which makes online and codeless visualisation of high dimensional data possible. A link to the data and the ML model could be added to the arXiv or INSPIRE entries of a HEP publication. This publishing of data is in our view essential to fully understand the trained models and to speed up the improvement of existing models.

2.4 Collection of Code to build Machine Learning models

To stimulate the adoption of machine learning in high energy physics even further each trained model will also have its training (and all other relevant) code published on platforms like GitHub. This code can then serve as example or as best-practice show case for both basic (e.g. how to train a network) to more complicated machine learning cases (e.g. how to extract epistemic and aleatoric uncertainties from a neural network).

3 Examples and best-practice

3.1 Examples of past phenomenological studies

Over the last years there are several examples where the use of ML techniques have shown to be very useful for phenomenology studies. Typically these methods have been applied to replace the event generation plus detector simulation chain using neural networks or Gaussian processes. This is usually the bottleneck of recasting and doing global fits of new physics models using LHC data.

The first use case was in the study of coverage properties on the constrained minimal supersymmetric standard model (cMSSM) parameter space inferred from a Bayesian posterior and the profile likelihood based on an ATLAS experiment sensitivity study [364]. The use of a shallow neural network allowed a fast prediction of the cMSSM mass spectrum gaining a factor of $\sim 10^4$ with respect to run a supersymmetry (SUSY) spectrum calculator as softsusy in sampling the cMSSM parameter space.

In a similar manner Buckley et al. [365] employed both a Bayesian deep neural network and a supported vectorial machine to interpolate between a grid of points in the cMSSM parameter space and therefore get fast predictions for the signal predicted by the model in the context of an ATLAS analysis.

Other phenomenological applications of ML in the SUSY context have been the development of SCYNeT [366] and SUSY-AI [354] packages. The first one uses neural network regression for a fast evaluation of the profile likelihood ratio using the 11-dimensional phenomenological minimal supersymmetric Standard Model (pMSSM) as an input. The authors have applied it to a global fit of the model including LHC data speeding up enormously the inference. Instead SUSY-AI does classification using a random forest algorithm which is trained with input data based in an analysis done by the ATLAS collaboration of the 19-dimensional

---

[1]https://zenodo.org/communities/phenoml_database/

pMSSM. Besides predicting whether a point of the model is excluded or not, it provides the epistemic uncertainty in the classification.

A recent application of deep neural networks have been developed to predict production cross sections of SUSY particles at the LHC. This is the case of DeepXS [367] which employs deep neural networks for a fast prediction of electro-weakino production cross-sections at the next-to-leading order in the pMSSM context. In this case the gain in speed is of order 10^7 compared with prospino [368] .

A further recent development has been the proposal of using deep neural networks for learning the full experimental information contained in the likelihood functions being used for the statistical inference in searches and measurements at the LHC [356]. The likelihoods learnt this way, so-called DNNLikelihoods, would allow a complete and framework-independent distribution of the physics analysis results, also enabling a precise combination with other experimental likelihoods, whenever the correlations among parameters are know.

Finally Kvellestad et al. [369] investigated the performance of deep neural networks to learn the signal mixture estimation of a ditau signal coming from a pair of degenerate Higgs bosons of opposite CP charge in the context of a Two-Higgs-Doublet model. They found a $\sim 20 \%$ improvement in the estimate of the uncertainty of signal mixture estimates, compared to estimates based on fitting, say, standard discriminating kinematic variables.

In addition to deep neural networks, Gaussian processes have been applied as fast predictors of LHC analyses efficiencies in the context of the reconstruction of a natural SUSY scenario [370] and dark matter simplify models [371] using LHC simulated data.

So far there is a very limited number of works which have followed somehow the prescription in line of what is suggested in Sec. 2 to publish results. This is the case of the DeepXS (https://github.com/SydneyOtten/DeepXS) and DNNLikelihood (https://github.com/riccardotorre/DNNLikelihood) projects where weights of the trained models and python scripts with neural networks implementations have been published on GitHub so the user can train the data himself. Furthermore training data are also available in Zenodo [2]. In the case of SUSY-AI pickle files containing the trained weights are available (for details see https://www.susy-ai.org), whereas data were made public by the ATLAS collaboration.

To the best of our knowledge the estimation of aleatoric and epistemic uncertainties of neural networks has not been applied in the HEP community.

3.2 Learning W_R Boson Production and Decay Rates

In light of its successful explanation of LHC data, the SM remains the best description of nature at high energies and short distances. Despite this success, there exists several experimental and theoretical motivations for the existence of new physics. One such example is the discovery [372, 373] of nonzero neutrino masses: in order to accommodate neutrino masses in a gauge-invariant and renormalizable manner, the SM must be extended by new particles and new couplings [374]. Such models that achieve this, known collectively as Seesaw models, can be tested at a variety of laboratory-based experiments, including the LHC and its potential successors [49, 375–377].

In practice, only benchmark and limiting cases of full, realistic, UV-complete Seesaw models are tested at the LHC due to the often cumbersome number of free parameters in the theory. For example: in the Left-Right Symmetric Model (LRSM) [378–382], which predicts

---

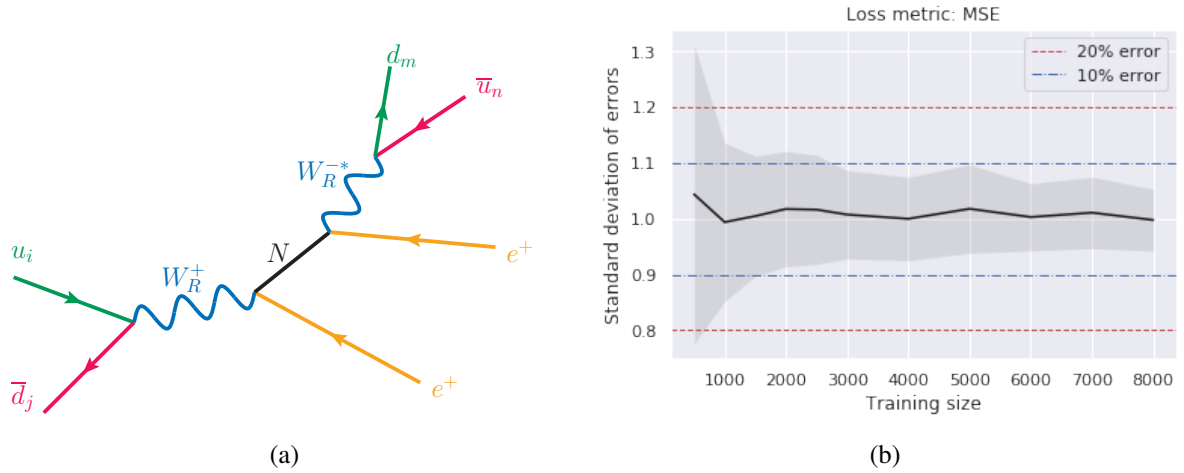[2]Links to the training data can be found at https://www.phenomldata.org

Figure 1: (a) Diagram within the Left-Right Symmetric Model (LRSM) containing a heavy neutrino and two new gauge bosons. (b) Spread of the prediction error made by the trained machine learning algorithm on the LRSM cross sections.

the existence of a new W_R gauge boson and heavy Majorana neutrinos as shown in Fig. 22.1(a), one typically assumes that W_R bosons can only decay to one charged lepton flavor and one heavy neutrino. Such a scenario is unlikely to be realized in nature as it is weakly motivated and not even observed in SM W boson decays. Were one able to efficiently interpolate and extrapolate from constraints on parameter space benchmarks, then LHC searches could be more fully utilized and subsequently make more general statements on new physics models. We explore this possibility here using ML techniques. As a first step, we attempt to quantify how efficiently a typical, off-the-shelf deep learning neural network can learn the production and decay cross sections for a W_R boson in the LRSM as a function of several (five) relevant mass and coupling parameters. Knowing then the acceptance and selection efficiencies as a function of inputs, which can be derived from Monte Carlo simulation, then one can in principle derive constraints on a fuller LRSM parameter space beyond that which was directly constrained.

3.2.1 Model and Model Inputs

For our purposes, it suffices to stipulate that the LRSM [378–382] is a gauge-extended scenario that postulates that the universe, in the UV limit, respects the gauge and parity symmetries $\mathcal{G}_{\mathrm{LRSM}} = \mathrm{SU}(3)_c \otimes \mathrm{SU}(2)_L \otimes \mathrm{SU}(2)_R \otimes \mathrm{U}(1)_{B-L} \otimes \mathcal{P}_X$. Here, $\mathrm{SU}(2)_R$ is a copy of the SM $\mathrm{SU}(2)_L$ gauge group and describes maximally parity violating, right-handed interactions. In addition, $\mathcal{P}_X$ is a discrete parity that ensures $L \leftrightarrow R$ field exchange symmetry. To protect LRSM, one RH neutrino (N_R) for each fermion generation is required. The residual $\mathrm{U}(1)$ that protects against anomalies conserves the difference between baryon and lepton numbers ($B - L$). After Left-Right symmetry breaking at a scale $v_R \gg v_{\mathrm{EW}} \approx 246$ GeV, the RH and $B-L$ gauge sector breaks down to the SM hypercharge gauge group, $\mathrm{SU}(2)_R \otimes \mathrm{U}(1)_{B-L} \otimes \mathcal{P} \to \mathrm{U}(1)_Y$. This in turn reduces to QED when EWSB occurs.

In the mass basis, the relevant interaction Lagrangian that describes massive $W_R^\pm$ bosons

from the $\mathrm{SU(2)}_R$ gauge group coupling to RH quarks and leptons is given by

$$\Delta\mathcal{L} = \frac{g_R}{\sqrt{2}} W^-_{R\mu} \sum_{i,j} \left[\overline{d}^i_L V^{\mathrm{R}}_{ij} \gamma^\mu P_R u^j_R \right] + \frac{g_R}{\sqrt{2}} W^-_{R\mu} \sum_{i,j} \left[\overline{e}^i_L Y^R_{ij} \gamma^\mu P_R N^j_R \right] + \mathrm{H.c.} \tag{1}$$

The mixing matrices V^R and Y^R describe the mixing between RH quarks and RH leptons with their respective mass eigenstates, in analogy to the CKM and PMNS matrices. We ignore quark mixing and approximate both the CKM matrix and V^R with 3×3 identity matrices. The gauge couplings g_L, g_R controls the strength of LH, RH currents and set $g_R = g_L \approx 0.65$ in accordance with LR symmetry.

We consider at $\sqrt{s} = 14$ TeV the canonical LRSM signature featuring the production of same-sign leptons and two light quarks via an s-channel W_R and N_1, shown in Fig. 22.1(a) and given by [383]:

$$u_i \overline{d_j} \to W^\pm_R \to \ell^\pm_1 N_1 \to \ell^\pm_1 \ell^\pm_2 d'_i \overline{u'_j}. \tag{2}$$

We decouple heavy neutrinos N_2 and N_3 and vary discretely the three mixing and two mass parameters

$$Y_{eN_1},\ Y_{\mu N_1},\ Y_{\tau N_1} \in \{10^{-4}, 10^{-3}, 10^{-2}, 10^{-1}, 1\}, \tag{3}$$
$$m_{N_1} \in \{15, 30, 45, 60, 75, 100, 150, 300,$$
$$450, 600, 750, 1000, 1500, 3000, 4500\}\ \mathrm{GeV}, \tag{4}$$
$$M_{W_R} \in \{1, 2, 3, 4, 5, 6, 8, 10, 12.5, 15, 17.5, 20\}\ \mathrm{TeV}. \tag{5}$$

Altogether, we compute a total of $N = 22.5$k cross sections, which constitutes our data set. We simulate the full $2 \to 4$ process at leading order and do not make the narrow width approximation. This means that a number of interesting kinematic limits are covered, including: non-resonant W_R production when $M_{W_R} \gtrsim \sqrt{s}$ [384, 385], the production of long-lived N_1 [385, 386], and boosted regimes such as when $m_{N_1} \ll M_{W_R} \ll \sqrt{s}$ [387, 388].

3.2.2 Computational Setup

To simulate the process in Eq. 2, we use `MadGraph5_aMC@NLO` [19] in conjunction with the `EffLRSM` UFO libraries [387, 388]. The NNPDF 3.1 NLO + LUXqed parton densities [389] are used and evolved using `LHAPDF6` [390]. Total widths for W_R and N_1 are computed on the fly for each parameter space point [254, 391]. The collinear factorization μ_f scale is dynamically to be half the sum of the transverse energy $E^k_T = \sqrt{p^{k2}_T + m^2_k}$ of all final-state particles k. No generator-level phase space cuts are applied.

3.2.3 Cross Section Learning

Using the generated data we trained a 3-layer neural network with elu [392] activation functions. As preprocessing we applied a base-10 logarithm to the input coupling strengths and to the cross sections that we aimed to predict. The data was z-score-normalized. The network was trained for 1000 epochs or until no mean squared error improvement was shown in 100 epochs (whichever occurred first).

Training was performed over random selections of the data in sizes of [500, 1000, 1500, 2000, 2500, 3000, 4000, 5000, 6000, 7000, 8000] events. 80% of the data was used for training, the remaining 20% for testing. For each of the training sizes the experiment was repeated 10
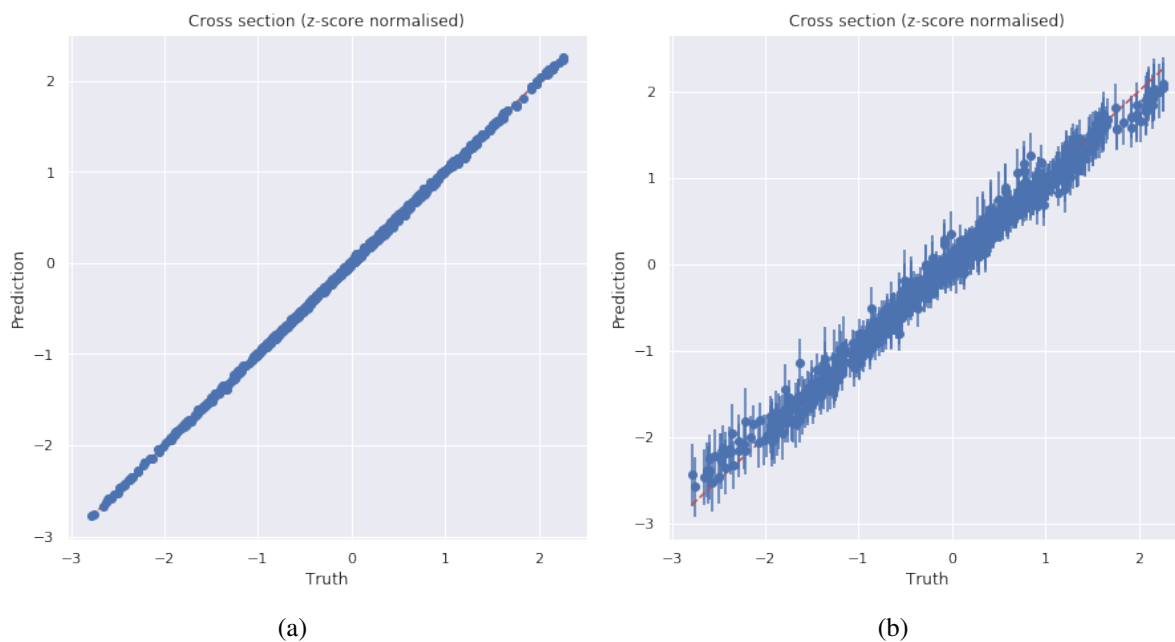
Figure 2: Truth-prediction plots for the trained algorithm without Monte Carlo Dropout (a) and with Monte Carlo Dropout (rate: 0.2) (b) (tentative). The cross sections are z-score normalised to help the training of the algorithm.

times (each with a new randomised selection of the total data). The test data was used to determine the relative error in the prediction of the cross section. This allowed us to determine the error made by the algorithm as function of the training size and, more importantly, when it becomes acceptable compared to the error made by the workflow through which the data was generated in the first place. The results of this procedure can be found in Figure 22.1(b).

A more direct indication of the performance of the algorithm can be made in the form of a truth-prediction plot, in which the prediction of the algorithm is plotted against the value that the algorithm ought to predict. For a perfect algorithm the predictions would form a perfect diagonal line in such a plot. As seen in Figure 22.2(a), after training we find good agreement between predicted and truth rates.

When applying an algorithm such as the one we trained, the user is not only interested in the prediction of the algorithm, but also in the prediction uncertainty due to the algorithm. To take all related sources of uncertainty into account, one also has to determine the uncertainty due to the model configuration and training (i.e. the epistemic uncertainty), as explained in Section 2.1. Using the Monte Carlo Dropout technique discussed in Section 2.1, it is possible to determine the event-by-event uncertainty on the predictions made by the algorithm. Although work on estimating the uncertainty (including the aleatoric uncertainty) is ongoing, a tentative result of this can be seen in Figure 22.2(b) where the dropout rate was set to 0.2. To compensate the network capacity for this dropout rate, the width of the network layers is increased from [50, 50] to [60, 60].

From comparing Figure 22.2(a) and Figure 22.2(b) we see that the trained algorithm has a reduced accuracy when the epistemic uncertainty is determined alongside a prediction. This is expected as the inclusion of dropout can degrade the performance of the algorithm. However,

by altering the configuration of the neural network it might be possible to counteract this loss in performance. To find this configuration, in future iterations of the network we plan on performing a hyperparameter scan for our model. Additionally, as our cross section data has some intrinsic uncertainty, as least from the Monte Carlo process through which it was calculated, we also plan on including aleatoric uncertainty determination.

3.3 Learning the production cross sections of the Inert Doublet Model.

One of the simplest extensions of the Standard Model (SM) is the addition of a second Higgs doublet in the so-called Two-Higgs-Double Models (2HDM). If a $\mathcal{Z}_2$ parity is further imposed, the model can easily avoid the bounds from flavor changing neutral currents and provide a dark matter candidate. This realisation of the 2HDM is known as the Inert Doublet Model (IDM) [393], where the SM doublet ($\mathbf{H_1}$) is $\mathcal{Z}_2$-even and the new doublet ($\mathbf{H_2}$) is odd. The scalar potential in this case is given by:

$$V = \mu_1^2|\mathbf{H_1}|^2 + \mu_2^2|\mathbf{H_2}|^2 + \lambda_1|\mathbf{H_1}|^4 + \lambda_2|\mathbf{H_2}|^4 + \lambda_3|\mathbf{H_1}|^2|\mathbf{H_2}|^2$$
$$+\lambda_4|\mathbf{H_1}^\dagger\mathbf{H_2}|^2 + \frac{\lambda_5}{2}[(\mathbf{H_1}^\dagger\mathbf{H_2})^2 + \text{h.c.}]. \tag{6}$$

The above parameters are chosen so only the SM Higgs, h, acquires a vacuum expectation value (vev), thus maintaining the $\mathcal{Z}_2$ symmetry unbroken. After imposing the correct values for the Higgs mass and vev, the model contain five free parameters which we choose to be the masses of the new scalars (H^0, A^0 and $H^\pm$):

$$M_{H^0}^2 = \mu_2^2 + \frac{1}{2}(\lambda_3 + \lambda_4 + \lambda_5)v^2, \tag{7}$$

$$M_{A^0}^2 = \mu_2^2 + \frac{1}{2}(\lambda_3 + \lambda_4 - \lambda_5)v^2, \tag{8}$$

$$M_{H^\pm}^2 = \mu_2^2 + \frac{1}{2}\lambda_3 v^2, \tag{9}$$

and the two couplings:

$$\lambda_2 \text{ and } \lambda_L \equiv \lambda_3 + \lambda_4 + \lambda_5. \tag{10}$$

In the above expressions, $v = 246$ GeV is the Higgs vev.

Searches for the inert scalars at the LHC are particularly challenging due to their small (electroweak) production cross sections. Since the new states are $\mathcal{Z}_2$-odd, they are pair produced at the LHC and the following 8 processes can be relevant for LHC searches:

$$pp \to H^0H^0, \ A^0A^0, \ H^0A^0, \ H^0H^+, \ A^0H^+, \ H^+H^-, \ H^0H^- \text{ and } A^0H^-. \tag{11}$$

See [394] and references therein for a discussion of LHC signatures and limits. The goal of this project is to train a Deep Neural Network to accurately predict the above (leading order) cross sections given as input the five free parameters of the model. In other words, to create a function that maps the free parameters of the IDM to their corresponding production cross sections:

$$g_\phi : x_{\text{IDM}} \equiv (M_{H^0}, M_{A^0}, M_{H^\pm}, \lambda_L, \lambda_2) \to \sigma_{\text{IDM}} \tag{12}$$

where σ_{IDM} represents a vector containing the 8 cross section values.

As a first step, 50000 samples were generated following the method of jittered sampling [395], from a parameter space chosen as:

$$50 < M_{H^0},\, M_{A^0},\, M_{H^\pm} < 3000\,\text{GeV}; \quad -2\pi < \lambda_2,\, \lambda_L < 2\pi. \tag{13}$$

All the cross sections were computed at leading order using MADGRAPH 2.6.4 [19] and the IDM UFO implementation from the FeynRules data base [394, 396]. Since the expected integrated luminosity at the High-Luminosity LHC is about $3\,\text{pb}^{-1}$, we imposed a lower limit on the cross sections of our data set of $\sigma_{\min} = 10^{-7}$ pb by discarding the cross sections below this limit. Afterwards, the remaining data was divided as training and test data in a 70:30 split.

An efficient training of the neural network requires some re-scaling of the input variables. For this, we followed the prescription and recommendations in [367] and pre-processed the model parameters via a z-score transformation:

$$x'_{\text{IDM}} = \frac{x_{\text{IDM}} - \mu(x_{\text{IDM}})}{\sigma(x_{\text{IDM}})}, \tag{14}$$

where $\mu(x_{\text{IDM}})$ and $\sigma(x_{\text{IDM}})$ are the mean and standard deviation of x_{IDM}, respectively. In addition the corresponding cross sections were logarithmically rescaled as:

$$\sigma'_{\text{IDM}} = \log\left[\frac{\sigma_{\text{IDM}}}{\min(\sigma_{\text{IDM}})}\right]. \tag{15}$$

The hyperparameters of the training algorithm were set as follows. As initializer of the neural network weights we chose He normal. In each hidden layer, we set LeakyReLU as an activation function. In order to obtain an approximation of the Bayesian uncertainties [358] as Monte Carlo dropout a "permanent" dropout layer was implemented after each hidden layer, where "permanent" means that the dropout is present not only during training, but also for inferences. To take into account the pre-processing of the target values we used a custom loss function that minimises the mean absolute percentage error (MAPE) of the original cross sections:

$$L(\sigma'_{\text{true}}, \sigma'_{\text{pred}}) = \frac{1}{N} \sum_{i=1}^{N} \left|1 - \exp(\sigma'_{\text{pred}} - \sigma'_{\text{true}})\right|, \tag{16}$$

where N is the batch-size which we choose to be 32. Furthermore, we applied the Adam optimizer with an initial learning rate of $\alpha_{\text{init}} = 10^{-3}$ and the EarlyStopping callback with a patience of 50. After 500 epochs have ended or EarlyStopping has terminated the iteration, the learning rate was divided by 2 and the training continues until 10 of those iterations were completed. To choose the best configuration, we ran a scan over the rest of the hyperparameters: the number of hidden layers, the number of artificial neurons, λ of the L2 regularization term and the dropout fraction, and trained a neural network with each combination for the $pp \to H^0 H^0$ process. Finally, we trained one neural network for each of the remaining production processes using the configuration that better minimised the MAPE for the first process. This configuration is formed by 6 hidden layers with 192 artificial neurons, $\lambda = 10^{-5}$ and a dropout fraction of 1%. The training data set, the code and the trained neural networks are presented in the GitHub repository https://github.com/SydneyOtten/IDM_XS fulfilling the criteria from sections 2.2, 2.3 and 2.4.

In order to test the performance of the neural network, 100 sample predictions were drawn for each point in the test data and their mean $\mu(\sigma_{pred})$ and standard deviation $\text{std}(\sigma_{pred})$ was

	H^0H^0	A^0A^0	H^+H^-	H^0A^0	H^0H^+	A^0H^+	H^0H^-	A^0H^-
$\mu(\text{RE})$	0.0303	0.1049	0.2259	0.0058	0.0076	0.0048	0.0057	0.0072
$\mu(\text{CV})$	0.0850	0.1880	0.1508	0.0272	0.0402	0.0276	0.0276	0.0287
within 1 std	0.9833	0.9509	0.9812	0.9981	0.9995	0.9997	0.9886	0.9817

Table 1: Summary of the accuracy of the predictions of the trained neural network from the test data: mean relative error, $\mu(\text{RE})$, mean coefficient of variance, $\mu(\text{CV})$, and fraction of test points whose true values lie within 1 std from the mean correspondent prediction, denoted as "within 1 std", for the eight production processes.

computed. From this, we computed the relative error (RE),

$$\text{RE} = \left| \frac{(\sigma_{pred} - \sigma_{true})}{\sigma_{true}} \right|, \tag{17}$$

which quantifies the distance between $\mu(\sigma_{pred})$ and the true cross section σ_{true}, and the coefficient of variance (CV),

$$\text{CV} = \frac{\text{std}(\sigma_{pred})}{\mu(\sigma_{pred})}, \tag{18}$$

which describes the estimation of the Bayesian uncertainty.

The results are summarised in Table 1. For the processes of associated production of two different inert scalars, we obtained quite good results. The best one overall is for A^0H^+ production, with $\mu(\text{RE}) \approx 0.005$, $\mu(\text{CV}) \approx 0.03$, and the 1 std interval around the mean predicted cross section containing the true value for 99.97% of the test points. For the pair-production processes, however, the outcomes are not ideal: we observe large REs and CVs, specially the regions with large cross sections. The worst case is A^0A^0 production with $\mu(\text{RE}) \approx 0.1$ and $\mu(\text{CV}) \approx 0.19$, and 1 std around the mean prediction containing the true value for only 95.09% of the test points. The mean predicted vs. the true cross section for these two cases is shown in Fig. 3. We see here that 1. $\sigma(pp \to A^0A^0)$ reaches much higher values than $\sigma(pp \to A^0H^+)$ and 2. the largest uncertainties arise for the highest cross sections. To understand this further, we plot in Fig. 4 the true cross section vs. the mass of the final state, with CV shown as color code. We observe that as the cross sections get larger so does the CV, a fact that is more notorious for the pair-production processes, which reach much higher values, specially when $2M_{A^0} \approx M_h$ where h-mediated production becomes kinematically allowed. Moreover, as expected, the cross sections peak towards low masses; in this region the density of points is rather low, which is also a cause of larger uncertainties. This suggests that the target values (i.e. the values of the cross sections) of the training sample should be more evenly distributed. Nevertheless, there is the positive conclusion that, in general, we observe a direct proportionality between the relative error and the standard deviation of the predictions. This is very important in order to ensure a correct interpretation of the uncertainty on the prediction.

In summary, we obtained first results from trained neural networks that predict the LHC production cross sections for inert scalars in the IDM, with an estimation of the Bayesian uncertainty. The next step of this project will focus on reducing this uncertainty and, by making sure that the true value is inside the 1 std uncertainty interval of the prediction, reducing the relative error of the predictions over the full parameter space for all the processes under consideration. One way to achieve this regards implementing Dropout-based Active Learning [397].
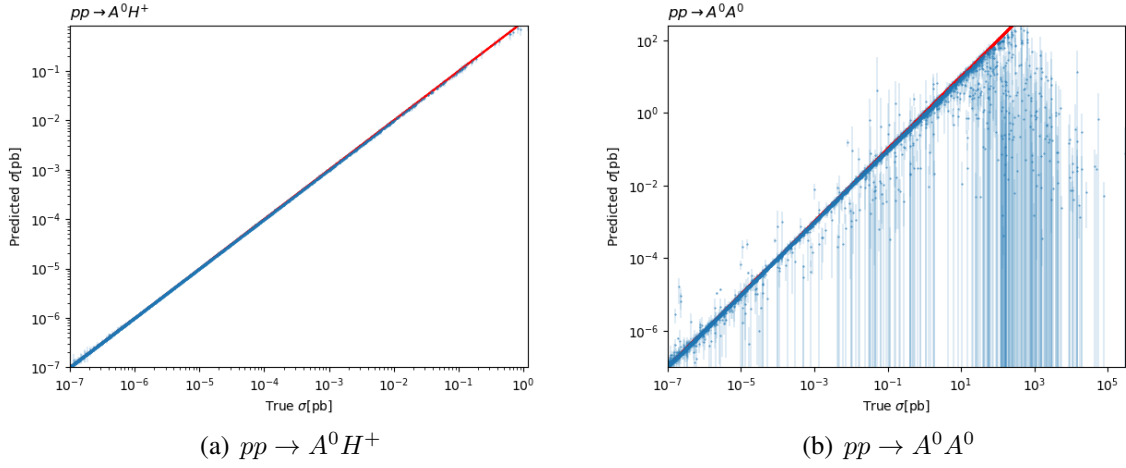
(a) $pp \to A^0 H^+$ (b) $pp \to A^0 A^0$

Figure 3: Mean predicted vs. true cross section for the processes with (a) the best and (b) the worst performance. The error bars correspond to 1 std from the mean prediction in each point.
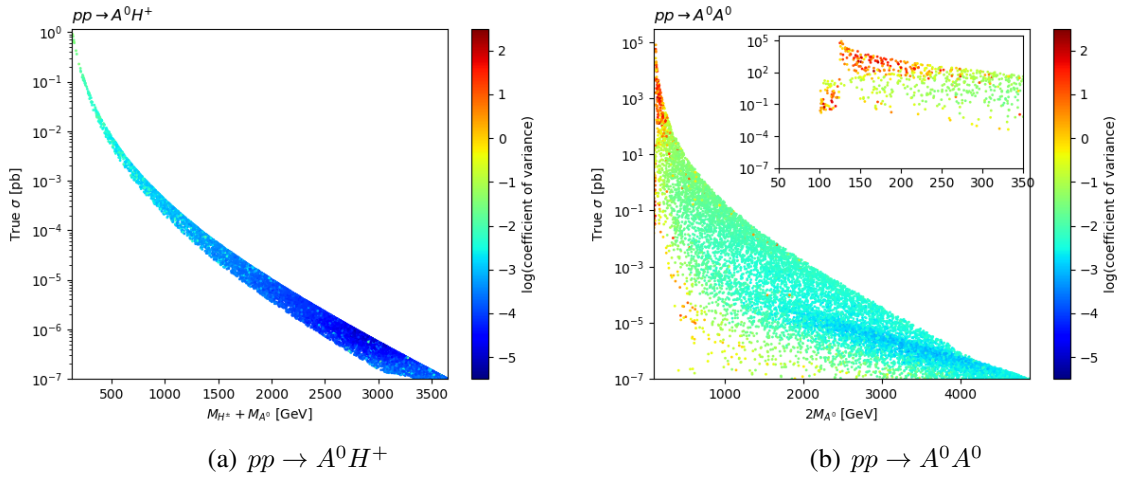

(a) $pp \to A^0 H^+$ (b) $pp \to A^0 A^0$

Figure 4: True cross section vs. effective mass for the processes with (a) the best and (b) the worst performance. In color, the logarithm of the coefficient of variance is shown.

3.4   Global fits of Gambit Zenodo data

The GAMBIT collaboration has released the data resulting from their global fits of a variety of beyond Standard Model models [339, 398–404] in Zenodo. These data can be trained using deep learning methods to predict, for instance, dark matter and LHC observables or likelihoods related with those observables for a posteriori interpolation.

One example is the seven-dimensional Minimal Supersymmetric Standard Model (MSSM7) [400] for which we have created a machine learning model in the form of two stacked deep neural networks to perform a regression on the MSSM7 combined likelihood. A total of 22.6 million samples were used for the training and evaluation of the models. Data exploration reveals that ≈ 595000 of those samples have a likelihood of 0 whereas all the other samples range from ≈ -450 to -255. The great void between -255 and 0 enhances the difficulty for a single neural network to perform well in every likelihood region. This particular inhomogeneity of the

data raises the standard deviation from ≈ 7 when excluding the zero likelihoods to ≈ 42 when including them. Thus, it was no surprise to find an extraordinarily well performing deep network when excluding the zeros from the training procedure. However, when training a neural network on the full data set, we achieved an accuracy of $100\,\%$ for identifying zero likelihoods. We have implemented a stacking mechanism that combines the knowledge of two deep neural networks by merging them into a deep hybrid network.

Deep Hybrid Network Architecture and Training

The two neural networks comprising the hybrid architecture were constructed and trained with `Tensorflow` and `Keras`. Their most important difference is due to the data they were being trained on:

Net A is trained on the full data set including the samples with a likelihood of 0.

Net B is trained on the full data set excluding the samples with a likelihood of 0.

The stacking mechanism is therefore simple: firstly, the input is processed by net A. If it predicts a 0, the final prediction is 0. If it does not predict 0, query net B and give its prediction as the final result. Nets A and B share most of their hyperparameters. Thus, if not explicitly mentioned otherwise, the subsequent network features are true for the procedures of both nets:

Data Preprocessing: The input, as well as the output, are z-score normalised, i.e. for sample x_i, it is transformed into x_i' and

$$x_i' = \frac{x_i - \bar{\mu}(x)}{\sigma(x)}, \tag{19}$$

where $\bar{\mu}$ and σ are the mean and standard deviation. However, for the parameters Q and $\mathrm{sgn}(\mu)$, $\bar{\mu} = 0$ and $\sigma = 1$. After normalising the data, it is split into three parts: first of all, 5% of the $2.26 \cdot 10^7$ samples are stored as test samples the neural networks will not see at all during their training. The other 95% are then again split into training and validation samples with a ratio of 9:1 respectively. The training samples are the ones that the loss function gets to compare to the model predictions while the validation samples are only used as a monitor for the performance. However, as will be explained in the training paragraph, the Network will be slightly biased towards the validation set.

Network Topology: The input is processed by 8 layers of fully connected neurons with 64 (net A) or 100 (net B) neurons with the `selu` activation function. The initial weights are drawn from a normal distribution with $\mu = 0$, $\sigma_{\mathrm{netA}} = 0.125$ and $\sigma_{\mathrm{netB}} = 0.1$.

Training: The loss function measuring the deviation of the model predictions and true values is minimised by the `ADAM` [405] optimiser with default values beside the learning rate and a batch-size of 180000 and has been customised with respect to the data preprocessing. Our loss function is a modification of the mean absolute error (MAE):

$$\mathrm{Loss}\left(\hat{y}_i(x_i), y_i(x_i)\right) = \frac{1}{N} \sum_{i=1}^{N} \sigma(y) \cdot |\hat{y}_i - y_i|, \tag{20}$$

where $\hat{y}_i$ is the predicted and y_i is the true label for input x_i. Additionally, a learning rate scheduling with $\alpha_i = 0.01$, $\alpha_f = 10^{-5}$ and a factor of 1.7 dividing the learning
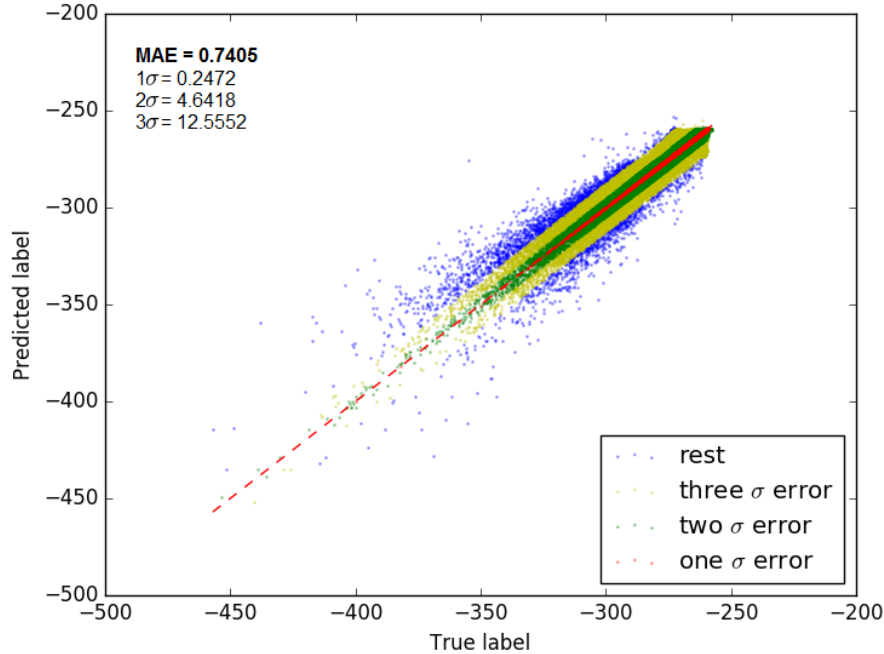
Figure 5: A validation plot of net B, showing the true label y_i on the x-axis and the predicted label $\hat{y}_i$ on the y-axis with a mean absolute error (MAE) of 0.7405. The test points are additionally showing the error bounds: 1σ in red, 2σ in green, 3σ in yellow and the rest in blue.

rate for each iteration. One iteration is equivalent to 2500 epochs of training or until the `EarlyStopping` routine has ended the iteration with a patience of 200 epochs. For each iteration, the model parameters giving the best validation loss are loaded into the architecture and the optimisation continues which causes the bias mentioned earlier.

Performance measurement

To measure the performance of the model, we evaluate both neural networks by comparing their predictions to 5% of the corresponding data sets (the test sets). The test set of net A consists of 1.13 million points, including 50650 samples whose likelihood is 0. Although the training procedure for net A is a typical regression, its function in the stack is to classify whether the parameter space point corresponds to a likelihood of 0 or not. Therefore, the only interesting measure for net A is the binary classification accuracy which was 100 %. For net B, an evaluation plot is shown in Figure 5.

4 Conclusions

Machine Learning (ML) can find various applications in HEP phenomenology. In this contribution, the use of ML based regression and classification of information for high-dimensional HEP models was discussed with emphasis on best practices for a sustainable reuse of phenomenological information. To give an example, phenomenological studies of the likelihood of a particular HEP model should publish the multidimensional records of all likelihood evaluations. Such data can be used to train ML models which allow to evaluate the likelihood of this HEP model in its full dimensionality. The ML code and the trained ML model should then

be published with appropriate meta data specifying input and output variables, boundaries of the training regions, etc., to allow an easy reuse. We propose to build a HEP-wide framework storing such information.

As proof of concept and feasibility, we showed various examples of applications such as ML-based regression of cross sections in left-right symmetric models (LRSM) and in the two-higgs doublet model (2HDM) and the regression of likelihoods for the minimal supersymmetric standard model (MSSM7) as provided by the GAMBIT collaboration.

Contribution 23

Model-Independent Signal Detection: A Challenge using Benchmark Monte Carlo Data and Machine Learning

M. van Beekveld, S. Caron, A. De Simone, A. Farbin, L. Hendriks, A. Jueid, A. Leinweber, J. Mamuzic, E. Merényi, A. Morandini, C. Nellist, S. Otten, M. Pierini, R. Ruiz de Austri, S. Sekmen, J. Schouwenberg, R. Vilalta, M. White

Abstract

We discuss model-independent signal detection algorithms, with a particular focus on approaches that are based on unsupervised machine learning. We also offer a set of simulated LHC events, corresponding to $10\,\mathrm{fb}^{-1}$ of data. These events can be used as a benchmark dataset, for example for the comparison of signal detection algorithms. We explain the main features, the data format and describe the use of this data for an upcoming data challenge. The data is available at the webpage https://www.phenoMLdata.org.

1   Introduction and Goals

Problem

The Standard Model (SM) has been tremendously successful in describing particle physics phenomena. Nevertheless, many questions still remain unanswered, e.g. the origin of neutrino masses, the nature of dark matter, or the dynamics of electroweak symmetry breaking. Therefore, it is commonly accepted that physics beyond the SM (BSM) is needed in order to provide answers to the questions not addressed in the SM. A key ingredient for the journey towards a new physics discovery is handling the huge amount of complex experimental data collected at LHC. LHC data was initially analyzed for various signals that were predicted by high energy models that extend the SM. Typical examples are supersymmetry (SUSY) or models with extra dimensions. Since these searches did not show any significant deviations from the SM, the LHC search strategy was expanded by using so-called "simplified models" and "effective models". For simplified models, a certain production and a decay of a new hypothetical particle is assumed, and the model is tested using LHC data by optimizing data selection criteria on the energy, momenta and types of particle predicted by the model. For effective models, a new effective interaction is added to the SM Lagrangian and the new interaction is typically constrained with the measurement of SM processes. A sign of new particles typically shows up as an overproduction of events (compared to the SM) in a specific data-selection where the number of events expected from SM processes is compared to the number of measured events in statistical tests. A hint of new physics requires that the "SM-only" hypothesis is highly disfavoured. Often the test is quantified with the help of a p-value defined as the probability that a given result (or a more significant result) occurs under the SM hypothesis. A typical requirement for the discovery of an *expected* signal (such as the Higgs particle) is $p < 3 \times 10^{-7}$ corresponding to 5 standard deviations (5σ).

To date, no signal of BSM physics has been found at the LHC. However, the new physics could look different than generally assumed. This project deals with the question of how to search for a signal in collider data without adopting a specific signal hypothesis.

Attempts

A few attempts have been made to systematically search for new physics without signal assumption by scanning specific observables, such as the sum of the transverse momenta, or the invariant mass. Scans have been done with the help of model-independent (i.e. unsupervised) algorithms to locate anomalies. Such general searches without an explicit BSM signal assumption have been been performed by the DØ Collaboration [406–409] at the Tevatron using an unsupervised multivariate signal detection algorithm termed SLEUTH, by the H1 Collaboration [410, 411] at HERA using a 1-dimensional signal detection algorithm, and by the CDF Collaboration [412, 413] at the Tevatron (using again 1-dimensional algorithms). A version of these 1-dimensional signal detection algorithms used in general searches is known as BUM-PHUNTER in the HEP community [414]. At the LHC, versions of such searches have been performed by the ATLAS Collaboration at $\sqrt{s} = 13$ TeV [415], and preliminary versions have been performed by the ATLAS and CMS Collaboration at $\sqrt{s} = 7$ and 8 TeV. Here, the ATLAS experiment proposed that the observation of one or more significant deviations in some phase-space region(s) can serve as a trigger to perform dedicated and model-dependent analyses where these 'data-derived' phase-space region(s) can be used as signal region(s). Such an analysis can then determine the level of significance by testing the SM hypothesis in these signal regions in a second dataset. Since the signal region is known also control selection can be defined to determine the background expectations in the signal region(s).

The field of machine learning (ML), sitting at the intersection of computational statistics, optimization, and artificial intelligence, has witnessed unprecedented progress over the past decade. Research in ML has recently led to the development of new and enhanced anomaly detection methods that could be used and extended for applications employing LHC or astroparticle data. Examples of such outlier detection algorithms recently proposed for HEP include density-based methods [416], model-independent searches with multi-layer perceptrons [417] , autoencoders [418–420], variational autoencoders [349, 421] or ML extended bump-hunting algorithms [422, 423].

Methodology

This contribution aims to initiate a comparison of signal detection algorithms. To this end, we supply a benchmark dataset containing simulated high-energy collision data. Furthermore, we provide a (non-exhaustive) list of methods that may be employed to extract a possible signal from this dataset in a model-independent and/or unsupervised way.

2 Data Description

2.1 Data generation procedures

We generate LHC events corresponding to a center-of-mass energy of 13 TeV. Events for the background and signal processes are generated at leading order (LO) with up to two additional partons in the matrix element using the event generator MG5_aMC@NLO v6.3.2 (Madgraph) and versions above [19] with the NNPDF PDF set [424] using 5 flavors in the definition of the proton. Madgraph is interfaced to Pythia 8.2 [28], that handles the showering of the ma-

trix element level generated events. The matching with the parton shower, needed in the case when one or more additional jets are generated in Madgraph, is done using the MLM merging prescription [425]. Then, a quick detector simulation is performed with Delphes 3 [153, 154], using a modified version of the ATLAS detector card. Pileup is not included in this dataset. A repository of the data scripts that are used to generate the events is on GitHub [1].

The final state objects, as described in Table 1, are stored in a one-line-per-event text file (see below Section 2.2 for details). An event consists of a variable number of objects. An event is stored when at least one of the following requirements are fulfilled:

- At least one (b)-jet with transverse momentum $p_T > 60$ GeV and pseudorapidity $|\eta| < 2.8$, or

- at least one electron with $p_T > 25$ GeV and $|\eta| < 2.47$, except for $1.37 < |\eta| < 1.52$, or

- at least one muon with $p_T > 25$ GeV and $|\eta| < 2.7$, or

- at least one photon with $p_T > 25$ GeV and $|\eta| < 2.37$.

Of course, these are unrealistic trigger requirements, but we aim to create a flexible data set that allows for different types of studies that might need different selection criteria. The η-restriction on the electrons models a veto in the crack regions as often applied in ATLAS analyses. Such a veto can also be applied to photons by the user. Note that for the processes with the largest cross sections ($W^\pm/\gamma/Z+$jets and QCD jet production) we have applied cuts on $H_T > 100$ GeV and 600 GeV respectively to make the data generation manageable. The observable H_T is defined as the scalar sum of the transverse momenta of all jets (with $p_{T,j_i} > 20$ GeV and $|\eta_{j_i}| < 2.8$):

$$H_T = \sum_i |p_{T,j_i}|. \tag{1}$$

Therefore, if one includes any of these processes in their analysis, one must make sure that the same cuts are also applied to the the other processes, which impacts the cross sections that are indicated in Table 2 (and therefore the event weights).

The requirements on the final states objects that are stored are

- (b-)jet: $p_T > 20$ GeV and $|\eta| < 2.8$,

- electron/muon: $p_T > 15$ GeV and $|\eta| < 2.7$,

- photon: $p_T > 20$ GeV and $|\eta| < 2.37$.

This means that, for example, a jet with $p_T = 10$ GeV is not included in the dataset. The detector simulation as performed by Delphes removes any electrons with $|\eta| > 2.5$, as the reconstruction efficiency is set to 0 beyond that point.

The scale choice is set dynamically by Madgraph during the event generation. The resulting cross sections are not reweighted with any of the available higher-order and/or resummed cross sections. All relevant SM (background) processes that have been generated are summarized in Table 2. For each process, the total number of generated events (N_{tot}) is at least the number that is needed for 10 fb^{-1} of data ($N_{10\,\text{fb}^{-1}}$).

---

[1] https://github.com/melli1992/unsupervised_darkmachines

Symbol ID	Object
j	jet
b	b-jet
e-	electron (e^-)
e+	positron (e^+)
m-	muon (μ^-)
m+	antimuon (μ^+)
g	photon (γ)

Table 1: Definition of symbols used for final-state objects. Only b-quark jets are tagged, no τ- or c-jets have been defined.

For the BSM scenarios (signal events) we have chosen two SUSY channels: gluino ($\tilde{g}$) pair and lightest stop ($\tilde{t}_1$) pair production. The production channels and decays are

$$pp \to \tilde{g}\tilde{g}, \quad \tilde{g} \to t\bar{t}\tilde{\chi}_1^0,$$
$$pp \to \tilde{t}_1\tilde{t}_1, \quad \tilde{t}_1 \to t\tilde{\chi}_1^0.$$

For the gluino events, we used a simplified model in which the lightest SUSY particle is a 1 GeV neutralino. The considered masses of the gluino are indicated in Table 3. All other SUSY particle are set to 4.5 TeV. For the stop production scenarios, we assume a more realistic SUSY scenario with a varying lightest neutralino ($\tilde{\chi}_1^0$) mass. The masses of $\tilde{t}_1$ and $\tilde{\chi}_1^0$ are provided in Table 3. Again for this scenario, all other SUSY masses are set to 4.5 TeV.

We include a second BSM model corresponding to a leptophobic topcolor Z' model [426], where an on-shell Z' boson is produced that subsequently decays into a pair of top quarks:

$$pp \to Z' \to t\bar{t}. \tag{2}$$

The masses of the Z' are provided in Table 3. In Table 3, one may find the process ID, cross sections σ, and total number of generated events N_{tot} of the BSM processes mentioned above. Generally, the processes with lower cross sections are harder to extract out of the background events, as such processes result in a lower number of signal events. A notable exception that is present in the BSM dataset is the scenario where the lightest stop mass is 220 GeV (process ID stop_01). Although the cross section of this production scenario is relatively high, the signal events are nearly indistinguishable from the background events due to their topology, making it extremely difficult to separate the signal events from the background events.

2.2 Description of the data format

The data are provided in a one-line-per-event text format (CSV file), where each line has variable length and contains 3 event-specifiers, followed by the kinematic features for each object in the event. The format of CSV files are:

```
event ID; process ID; event weight; MET; METphi; obj1, E1, pt1, eta1,
            phi1; obj2, E2, pt2, eta2, phi2; ...
```

SM processes			
Physics process	Process ID	σ (pb)	N_{tot} ($N_{10\,\text{fb}^{-1}}$)
$pp \to jj$	njets	$19718_{H_T > 600\,\text{GeV}}$	415331302 (197179140)
$pp \to W^{\pm}(+2j)$	w_jets	$10537_{H_T > 100\,\text{GeV}}$	135692164 (105366237)
$pp \to \gamma(+2j)$	gam_jets	$7927_{H_T > 100\,\text{GeV}}$	123709226 (79268824)
$pp \to Z(+2j)$	z_jets	$3753_{H_T > 100\,\text{GeV}}$	60076409 (37529592)
$pp \to t\bar{t}(+2j)$	ttbar	541	13590811 (5412187)
$pp \to W^{\pm}t(+2j)$	wtop	318	5252172 (3176886)
$pp \to W^{\pm}\bar{t}(+2j)$	wtopbar	318	4723206 (3173834)
$pp \to W^{+}W^{-}(+2j)$	ww	244	17740278 (2441354)
$pp \to t+\text{jets}(+2j)$	single_top	130	7223883 (1297142)
$pp \to \bar{t}+\text{jets}(+2j)$	single_topbar	112	7179922 (1116396)
$pp \to \gamma\gamma(+2j)$	2gam	47.1	17464818 (470656)
$pp \to W^{\pm}\gamma(+2j)$	Wgam	45.1	18633683 (450672)
$pp \to ZW^{\pm}(+2j)$	zw	31.6	13847321 (315781)
$pp \to Z\gamma(+2j)$	Zgam	29.9	15909980 (299439)
$pp \to ZZ(+2j)$	zz	9.91	7118820 (99092)
$pp \to h(+2j)$	single_higgs	1.94	2596158 (19383)
$pp \to t\bar{t}\gamma(+1j)$	ttbarGam	1.55	95217 (15471)
$pp \to t\bar{t}Z$	ttbarZ	0.59	300000 (5874)
$pp \to t\bar{t}h(+1j)$	ttbarHiggs	0.46	200476 (4568)
$pp \to \gamma t(+2j)$	atop	0.39	2776166 (3947)
$pp \to t\bar{t}W^{\pm}$	ttbarW	0.35	279365 (3495)
$pp \to \gamma\bar{t}(+2j)$	atopbar	0.27	4770857 (2707)
$pp \to Zt(+2j)$	ztop	0.26	3213475 (2554)
$pp \to Z\bar{t}(+2j)$	ztopbar	0.15	2741276 (1524)
$pp \to t\bar{t}t\bar{t}$	4top	0.0097	399999 (96)
$pp \to t\bar{t}W^{+}W^{-}$	ttbarWW	0.0085	150000 (85)

Table 2: Generated background processes (first column) with the corresponding identification (second column), the LO cross section σ in pb (third column) and the total number of generated events N_{tot} (fourth column). In the last column, we also indicate the number of events corresponding to 10 fb^{-1} of data ($N_{10\,\text{fb}^{-1}}$).

BSM processes			
Physics process	Process ID	σ (pb)	N_{tot} ($N_{10\,\text{fb}^{-1}}$)
$pp \rightarrow \tilde{g}\tilde{g}$ (1 TeV)	gluino_01	0.20	50000 (2013)
$pp \rightarrow \tilde{g}\tilde{g}$ (1.2 TeV)	gluino_02	0.05	50000 (508)
$pp \rightarrow \tilde{g}\tilde{g}$ (1.4 TeV)	gluino_03	0.014	50000 (144)
$pp \rightarrow \tilde{g}\tilde{g}$ (1.6 TeV)	gluino_04	0.004	50000 (44)
$pp \rightarrow \tilde{g}\tilde{g}$ (1.8 TeV)	gluino_05	0.001	50000 (14)
$pp \rightarrow \tilde{g}\tilde{g}$ (2 TeV)	gluino_06	$4.8 \cdot 10^{-4}$	50000 (5)
$pp \rightarrow \tilde{g}\tilde{g}$ (2.2 TeV)	gluino_07	$1.7 \cdot 10^{-4}$	50000 (2)
$pp \rightarrow \tilde{t}_1\tilde{t}_1$ (220 GeV), $m_{\tilde{\chi}_1^0} = 20$ GeV	stop_01	26.7	500000 (267494)
$pp \rightarrow \tilde{t}_1\tilde{t}_1$ (300 GeV), $m_{\tilde{\chi}_1^0} = 100$ GeV	stop_02	5.7	500000 (56977)
$pp \rightarrow \tilde{t}_1\tilde{t}_1$ (400 GeV), $m_{\tilde{\chi}_1^0} = 100$ GeV	stop_03	1.25	250000 (12483)
$pp \rightarrow \tilde{t}_1\tilde{t}_1$ (800 GeV), $m_{\tilde{\chi}_1^0} = 100$ GeV	stop_04	0.02	250000 (201)
$pp \rightarrow Z'$ (2 TeV)	Zp_01	0.38	50000 (3865)
$pp \rightarrow Z'$ (2.5 TeV)	Zp_02	0.12	50000 (1221)
$pp \rightarrow Z'$ (3 TeV)	Zp_03	0.044	50000 (443)
$pp \rightarrow Z'$ (3.5 TeV)	Zp_04	0.018	50000 (179)
$pp \rightarrow Z'$ (4 TeV)	Zp_05	0.008	50000 (81)

Table 3: Generated signal processes (first column) with the corresponding identification (second column), the LO cross section σ in pb (third column) and the total number of generated events N_{tot} (fourth column). In the last column, we also indicate the number of events corresponding to 10 fb^{-1} of data ($N_{10\,\text{fb}^{-1}}$).

The `event ID` is an event specifier. It is an integer to identify the generation of that particular event, included for debugging purposes only. The `process ID` is a string referring to the process that generated the event, as mentioned in Tables 2 and 3. The event weight w is defined as

$$w = \frac{\sigma}{N_{\text{lines}}} \times \left(10\,\text{fb}^{-1}\right), \tag{3}$$

with σ the cross section for a particular process, and N_{lines} the number of events in a single CSV file. With the release of this contribution we provide files for $N_{\text{lines}} = N_{10\,\text{fb}^{-1}}$ (with $N_{10\,\text{fb}^{-1}}$ in Table 2), such that all weights are 1. Additionally, when $N_{10\,\text{fb}^{-1}} < 20000$, we provide a second CSV file with $N_{\text{lines}} = 20000$. These conclude the event specifiers of each line in the CSV file. Concerning the kinematic features, the `MET` and `METphi` entries are the magnitude E_T^{miss} and the azimuthal angle $\phi_{E_T^{\text{miss}}}$ of the missing transverse energy vector of the event. The E_T^{miss} is based on the truth E_T^{miss}, meaning the transverse energy of those objects that genuinely escape detection. The object identifiers (`obj1`, `obj2`,...) are strings identifying each object in the event, using the identifiers of Table 1. Each object identifier is followed by 4 comma-separated values fully specifying the 4-vector of the object: `E1`, `pt1`, `eta1`, `phi1`. The quantities `E1` and `pt1` respectively refer to the full energy E and transverse momentum p_T of `obj1` in units of MeV. The quantities `eta1` and `phi1` refer to the pseudo-rapidity η and azimuthal angle ϕ of
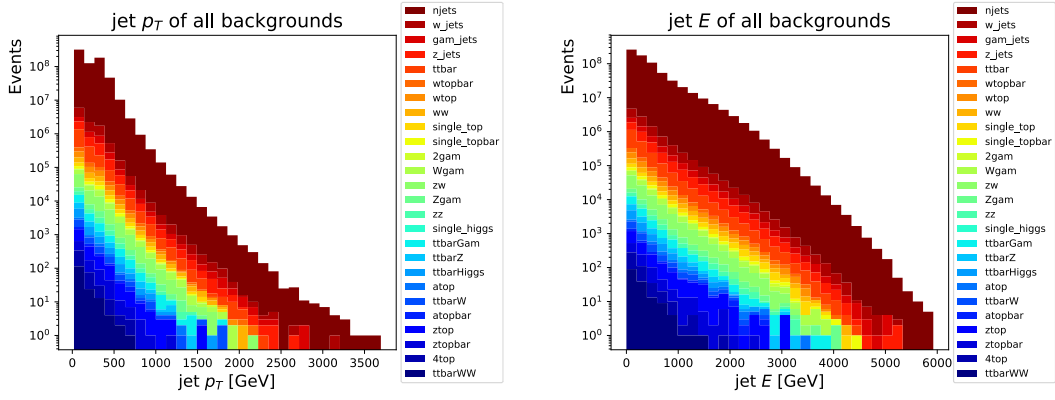
Figure 1: Transverse momentum p_T (left) and energy E (right) in GeV of the jets for all backgrounds.
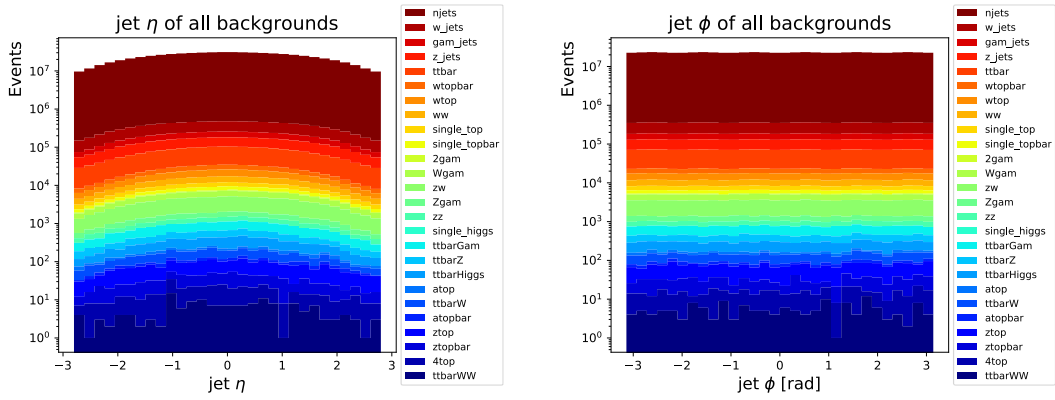

Figure 2: Pseudorapidity η (left) and azimuthal angle ϕ (right) of the jets for all backgrounds.

`obj1.`
As an example, an event corresponding to the final state of the $t\bar{t} + 2j$ process with two b-jets (with $E = 33.2$ GeV and $E = 55.8$ GeV) and one jet (with $E = 100.4$ GeV) reads:

94;ttbar;1;112288;1.74766;b,331927,147558,-1.44969,-1.76399;j,100406,85589,-0.568259,-1.17144;b,55808.8,54391.4,-0.198215,1.726

In Figures 1-4 we show the (stacked) distributions of the kinematic variables E, p_T, η, and ϕ of the jets and leptons in all of the generated background processes. In Figure 6 we show the number of jets N_{jet} and leptons (N_{lepton}) for the generated backgrounds. The E_T^{miss} and $\phi_{E_T^{\mathrm{miss}}}$ distributions are shown in Figure 5, and the H_T distribution is shown in Figure 7. Note that only for Figure 7, we have filtered out the events with $H_T < 600$ GeV. For the other Figures, we show the events for all values of H_T for most backgrounds, except for the ones with tags njets ($H_T > 600$ GeV), w_jets, gam_jets and z_jets ($H_T > 100$ GeV). We stress again that for any analysis, the same kinematic cuts on *all* the background and signal events should be made.

2.3 Data storage

The generated MC data is stored in the form of ROOT files (including all stable hadrons) and in CSV files including only the information as described above. The CSV files corresponding to 10 fb^{-1} of data per process are available in https://www.PhenoMLdata.org for further
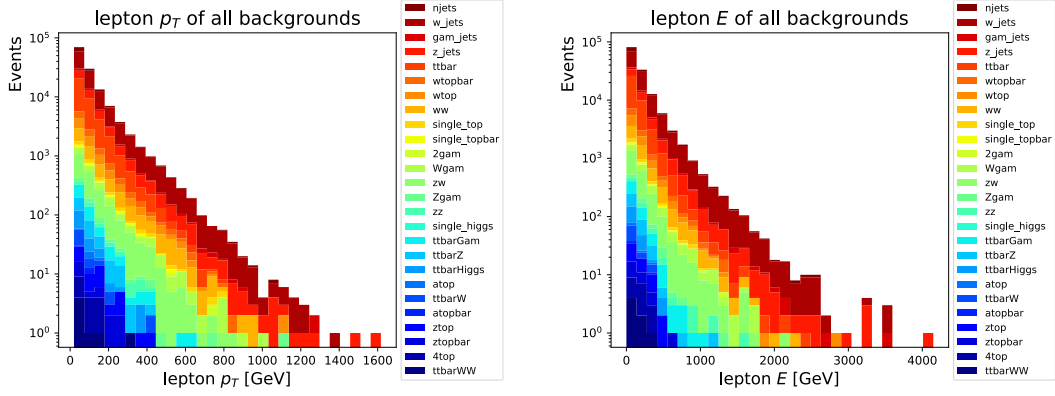
Figure 3: Transverse momentum p_T (left) and energy E (right) in GeV of the leptons (e^+, e^-, μ^+, μ^-) for all backgrounds.
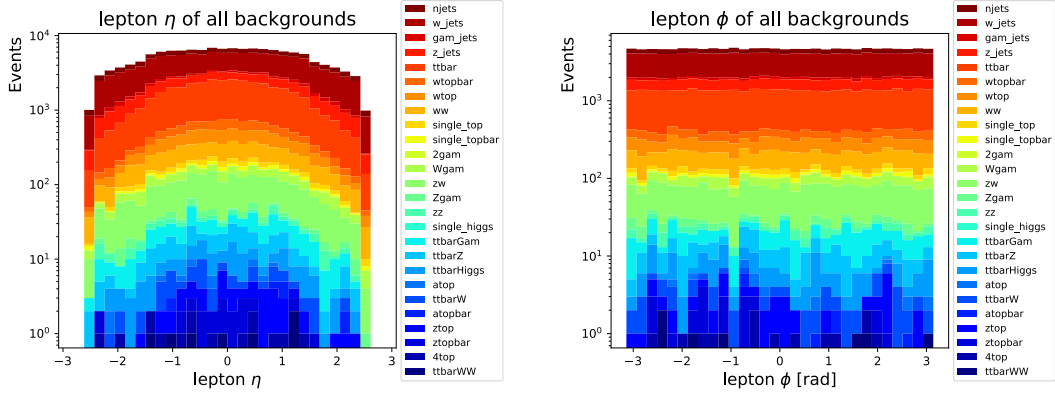
Figure 4: Pseudorapidity η (left) and azimuthal angle ϕ (right) of the leptons (e^+, e^-, μ^+, μ^-) for all backgrounds.
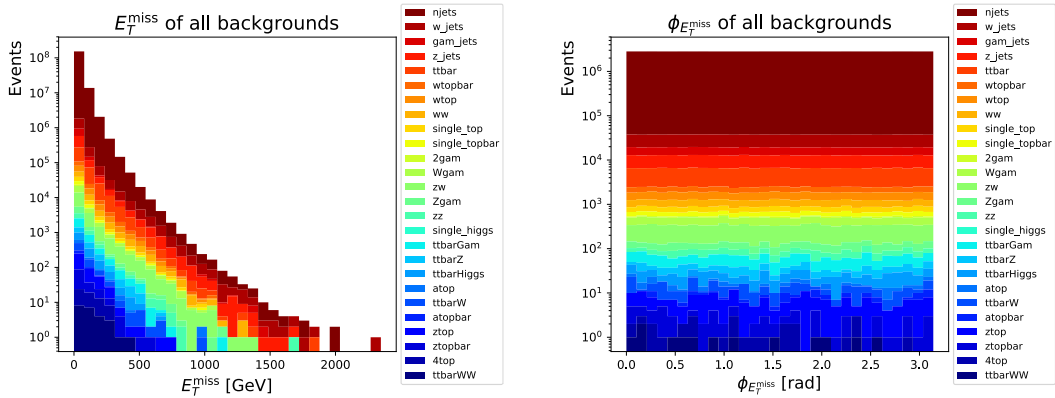
Figure 5: Missing transverse energy E_T^{miss} in GeV and azimuthal angle $\phi_{E_T^{\mathrm{miss}}}$ for all backgrounds.
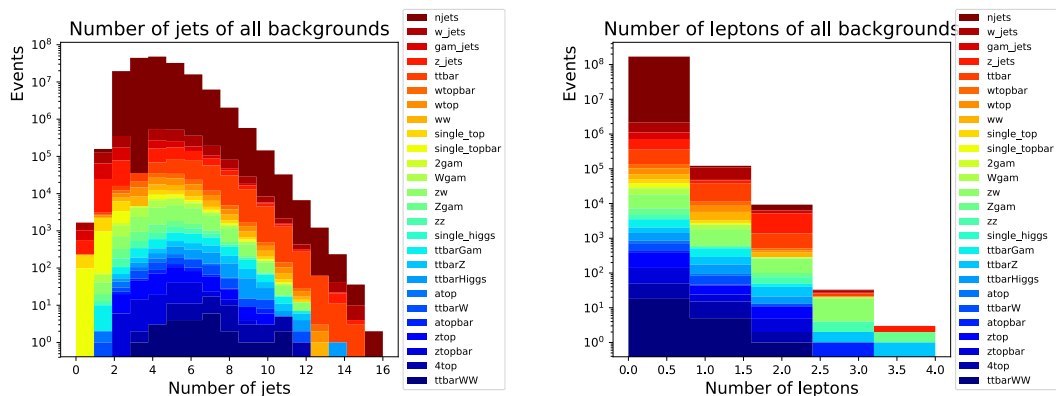
Figure 6: Number of jets (left) and leptons (right).
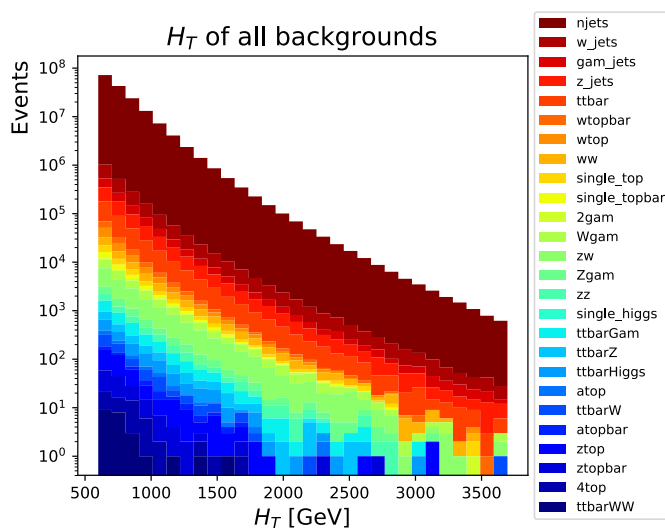
Figure 7: The scalar sum of the jet transverse momenta H_T in GeV (see Eq. (1)) for the all backgrounds with $H_T > 600$ GeV imposed.

validation. We encourage the community to explore the data, and report any issue to the authors of the proceedings. In the near future we plan to extend the dataset and to make the full set of ROOT files available, which currently take about 150 TB of disk space.

2.4 Benchmarking

The dataset presented in this paper is the result of an effort started back in 2018 in one of the working groups of the DarkMachines initiative [2]. We plan to use this dataset as a benchmark dataset to open a challenge, addressed to both particle physics and computer science communities. The challenge will aim at stimulating these communities to design and employ new methods/algorithms for detecting and characterizing signals in datasets featuring degenaracy, high dimensionality, and low signal-to-noise ratios, such as those faced when searching for new physics at the LHC.

Anomaly detection datasets used in ML are e.g. credit card fraud detection data [427]. Other

challenges similar in spirit have been previously ran, e.g. in 2006 teams of theorists compared LHC data analysis approaches with mock datasets [3] and a QCD-oriented LHC Olympics 2020 [428] [4] On the other hand, we provide data set with very high statistics and including event-level features as well as full 4-vectors features, with several potential use cases.

The dataset in this paper (corresponding to an integrated luminosity of 10 fb^{-1} of data) can be used by the interested readers for training and validation, using the BSM signal samples provided. For the challenge, we will provide a statistically independent dataset, where signal events are included. These signal events are generated e.g. by one or more (undisclosed) types of BSM processes. The goal of the challenge will be to identify and characterize such signals. The submitted solutions will be judged and ranked according to specified metrics, based on the classification performance of the proposed algorithm with respect to the dataset with true labels assigned. More details will be provided when officially opening the challenge, and in a follow-up paper.

3 Approaches to the problem

The task at hand is to distinguish background from signal events. Since signal events are very similar to background events in terms of their topology, it is usually impossible to identify them by looking at individual events. Therefore, one needs to take into account effects that only appear when examining distributions in a collection of events. Since the signal and background events can be viewed as samples drawn from an (unknown in the case of signal) multidimensional probability distribution, and we only have a finite amount of data, we are restricted to statistical investigations, e.g. in the form of a hypothesis test against the null hypothesis that the given dataset does not contain any signal. In this section, we aim to give some examples for a signal detection algorithm.

In order to maximize the power of the test, it may be very helpful to transform the low-level (raw) features of the events into high-level ones. This crucial step of feature selection/engineering can be performed by using unsupervised learning techniques [429], e.g. by creating low-dimensional (latent) model of the data.

There are at least four different approaches to design the signal detection algorithm and train it on data.

(a) Training the algorithm on real data, possibly being a mixture of signal and background. This is necessary when a reliable or accurate model for the background is not available. It will then be tested on another independent sample of real data.

(b) Training the algorithm on computer-generated backgrounds. It will then be tested on real data.

(c) Training the algorithm by two-sample comparison of background data and real data (e.g. [416, 417])

(d) Training the algorithm on a specific signal and background. This is what is typically done at LHC. Another possibility would be to train the algorithm on a large number of possible signals with a large variety.

---

[3] see e.g. http://public-archive.web.cern.ch/en/Spotlight/SpotlightOlympics-en.html

[4] The LHC Olympics 2020 is a low statistics dataset and a challenge to study anomalies in jets, i.e. to build an "anomaly jet detection algorithm" with inputs being the kinematical features of stable hadrons.

In all cases, the outcome can be reduced to constructing one or more variables which maximize the power to discriminate signal from background (e.g. the probability of being an outlier, see Fig 8).

In the cases where the training involves a real dataset, it is possible to replace it by a mock dataset where signals of various kinds are injected. This is done to validate the algorithm and assess its performance to spot outliers.

In the approaches involving the background-only data, one should keep in mind that the simulated data are not a perfect description of the LHC data, and mismodeling may show up as fake new physics signals.

Several traditional ML techniques and various deep learning techniques enable the design of an algorithm that promise to serve our purpose of identifying new physics from LHC data: Kernel Density Estimation [430], Gaussian Mixture Models [431], Flow models [432], Variational Autoencoders [433] and GANs [434]. In the subsequent subsections we have listed four overlapping approaches to the problem of finding new physics: anomaly detection, clustering, dimensional reduction and density estimation, all of whom could potentially be supported by the above-mentioned ML techniques.

3.1 Anomaly detection

Anomaly detection generally describes the process of identifying unexpected events in a dataset. With the aid of ML tools, this can be achieved in a supervised, semi-supervised or unsupervised manner. Since, in a model-independent scenario, we do not have labels for new physics signals, we are in principle only interested in the unsupervised approach. Nevertheless, one could label the SM expectation of some observable. A special feature of this label is that it does not correspond to an individual event, but to a collection of events. This allows us to employ all the possible approaches mentioned above, while still being unsupervised with respect to the signal. A successful anomaly detection algorithm would then be able to tag the signal events as outliers. A potential problem of the approaches is that very rare SM events may also be part of the collection of outliers.

We present an instructive toy example in Figure 8. We simulated data from a background expectation distributed exponentially and we combined it with a narrow Gaussian signal anomaly. In order to give an anomaly score to the points we trained the Local Outlier Factor (LOF) [435] on a background-only simulation, and subsequently used it on the dataset containing both inliers and outliers (this would correspond to approach (b) mentioned above). Despite its simplicity, this example shows two interesting characteristics. First, it is clear that feature selection is important, since the variable on the x-axis is discriminating, while the variable on the y-axis is less discriminating. This is because the exponential distribution of the background has a different variance in the two directions. Second, the example has the characteristics that it is difficult to separate an anomaly from the background with a simple selection on one of the two plotted variables. The purpose of anomaly detection in this context is not to find *all* anomalous points, but to be able to reliably state when a point (or a set of points) is anomalous and worth studying. The LOF gives a score to all points in order to assess how much they differ from the background. On the right-hand side of Figure 8, we see that most outliers have a high probability of being part of the signal, and not belong to the background.

Once all points are assigned an anomaly score, one may compare the distribution of such scores to a validation set containing only SM events. Therefore, we use the framework of a two-sample
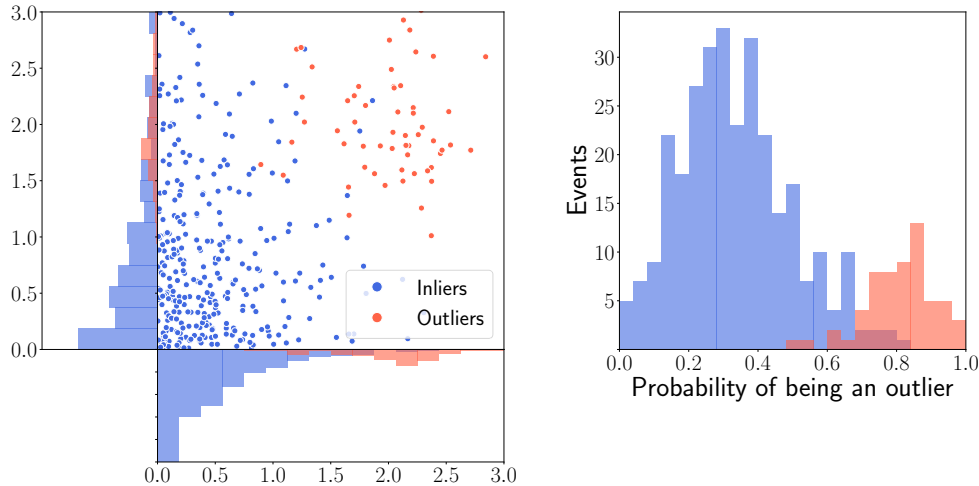
Figure 8: *Left:* A narrow Gaussian anomaly centered around $(2, 2)$ (in red) is added to an exponentially-distributed background (in blue). *Right:* The probability of belonging to the signal events (outliers) is assigned to each point of the dataset and we can perform a counting. In this case, higher probabilities are correctly assigned to the outliers.

test, aimed at detecting statistically significant differences in the score distributions of inliers and outliers.

3.2 Clustering

We expect data amenable for analysis to lack in class labels (e.g. it is not known if the data is a signal event); it will then be necessary to extract information in an unsupervised fashion. A solution is to invoke clustering techniques [436, 437], where the goal is to group the data into clusters, each cluster bearing certain unique properties. Specifically, the goal is to partition the data such that the average distance between objects in the same cluster (the average intra-distance) is significantly less than the distance between objects in different clusters (the average inter-distance). Several approaches have been developed to cluster data based on diverse criteria, such as the cluster representation (e.g. flat, hierarchical), the criterion function to identify sensible clusters (e.g. sum-of-squared errors, minimum variance), and the proximity measure that quantifies the degree of similarity between data objects (e.g. Euclidean distance, Manhattan norm, inner product). Our goal is to experiment with a variety of clustering approaches to gain a better understanding of the type of patterns emerging from clustering structures.

In order to analyze clusters to identify novel groupings that may point to new physics, one approach is to use what is known as *cluster validation* [438], where the idea is to assess the value of the output of a clustering algorithm by computing statistics over the clustering structure. Clusters with high degree of *cohesiveness*, where events within the group are sampled from regions of high probability density, are particularly relevant for analysis. In addition, one could carry out a form of *external cluster validation* [439], where the idea is to compare the output clusters to existing, known classes of particles. While finding clusters resembling existing classes may serve to confirm existing theories, clusters bearing no resemblance to known classes can potentially drive the search for new physics models.

205

3.3 Dimensionality Reduction

Data stemming from LHC arrive in copious amounts, are highly dimensional, and lack class labels; clustering can be useful to find patterns hidden in the data, a task whose importance has been highlighted in the previous section. Unfortunately, highly dimensional data create a plethora of complications during the data analysis process. Two possible solutions exist: we can either pre-process the data through dimensionality reduction techniques [440], or we can make use of specialized approaches [441].

Dimensionality reduction can be done through feature selection, by determining which features are most relevant, i.e. those that possess a high power to discriminate signal from background. This may come with some information loss, but it is commonly the case at the LHC that only a subset of information is needed to distinguish among different types of data. Another approach is to invoke principal component analysis: the data is transformed while eliminating cross correlations among the new features; the resulting subset can be further analyzed to filter out irrelevant features.

Another promising direction is to use ML to attain a reduced representation of the data by performing non-linear transformations [442, 443]. This approach can have a strong impact in the search for new physics since it implements data transformations that can unveil hidden patterns corresponding to new particle signals.

3.4 Density estimation

Events produced at the LHC (either real or simulated) can be thought as samples drawn from an unknown probability density function (PDF) that characterizes the complex physical processes leading to the generation of the events themselves. The PDF of a new physics signal might be different from the PDF of the SM. However, also the estimated PDFs of the SM, and the one from real experimental data may be different. Spotting and analyzing the differences in these two densities can provide a great deal of information about the underlying process (i.e. the true physical model) that generates the signal events.

However, estimating the PDF reliably starting from the raw data is far from trivial, especially if the number of features is high. This constitutes an active field of research in data science and, depending on the specific task, different approaches may be suitable [430, 444]. One such approach is kernel density estimation, which estimates the PDF by a sum of kernel functions (e.g. multivariate Gaussians) centered around each data point [445].

Assuming density estimation can be performed accurately, there are several ways to use it for model independent unsupervised analysis. For instance, one can compare the PDFs of real and simulated data from the LHC to detect differences. They point towards interesting signal regions, which can be used in order to guide further scrutiny. Furthermore, one could also perform clustering and anomaly detection in a way independent from the approaches mentioned before, see e.g. [446, 447].

One difficulty in applying density estimation on the dataset described in this work is the fact that the events change in dimensionality because the number of objects is not the same in every event. Additionally, there are both continuous data (for example energy and angles) and categorical data (object symbol). To circumvent these issues, one might try to map events to a different parameter space, a potential methodology is described in Ref. [349].

4 Conclusions

In this paper we have described a dataset aimed at constituting a benchmark for future model-independent studies of new physics detection at the LHC. We described the details of the data generation and the data format, which allow the user to easily handle the data with any programming language. We encourage the community to acquire familiarity with this dataset, which will also form the basis for a signal detection challenge to be announced soon. The challenge will be addressed to both computer scientists and particle physicists, fostering fruitful collaborations between them. Furthermore, we outlined some approaches, inspired by machine learning, to the problem of signal identification in background-dominated situations, like the ones commonly faced in high-energy physics.

With a benchmark dataset such as the one described in this paper it is possible to test and compare different techniques and algorithms for signal detection. We believe the effort of designing and comparing new algorithms tailored to the needs of high-energy physics will prove very useful for the future of the field.

Bibliography

[1] The BABAR Collaboration, *Phys. Rev. D* **88** (Oct, 2013) 072012. 7

[2] Belle Collaboration, *Phys. Rev. Lett.* **118** (May, 2017) 211801. 7

[3] R. Aaij *et. al.*,, **LHCb** Collaboration, *Phys. Rev. Lett.* **113** (2014) 151601, [1406.6482]. 7

[4] LHCb Collaboration, *Journal of High Energy Physics* **2017** (Aug, 2017) 55. 7

[5] A. Greljo, J. Martin Camalich, and J. D. Ruiz-Álvarez, *Phys. Rev. Lett.* **122** (2019), no. 13 131803, [1811.07920]. 7, 21

[6] G. Aad *et. al.*,, **ATLAS** Collaboration, *JHEP* **08** (2016) 009, [1606.01736]. 7, 8, 10, 11, 12, 19

[7] M. Aaboud *et. al.*,, **ATLAS** Collaboration, *JHEP* **10** (2017) 182, [1707.02424]. 8, 10

[8] A. Greljo and D. Marzocca, *Eur. Phys. J.* **C77** (2017), no. 8 548, [1704.09015]. 8, 9, 10

[9] V. Cirigliano, M. Gonzalez-Alonso, and M. L. Graesser, *JHEP* **02** (2013) 046, [1210.4553]. 9

[10] J. de Blas, M. Chala, and J. Santiago, *Phys. Rev.* **D88** (2013) 095011, [1307.5068]. 9

[11] M. Farina, G. Panico, D. Pappadopulo, J. T. Ruderman, R. Torre, and A. Wulzer, *Phys. Lett.* **B772** (2017) 210–215, [1609.08157]. 9

[12] S. Alioli, M. Farina, D. Pappadopulo, and J. T. Ruderman, *Phys. Rev. Lett.* **120** (2018), no. 10 101801, [1712.02347]. 9

[13] G. Aad *et. al.*,, **ATLAS** Collaboration, *Phys. Lett.* **B796** (2019) 68–87, [1903.06248]. 10, 165, 167, 168

[14] **CMS Collaboration** Collaboration, Tech. Rep. CMS-PAS-SMP-16-009, CERN, Geneva, 2016. 10

[15] A. M. Sirunyan *et. al.*,, **CMS** Collaboration, *JHEP* **04** (2019) 114, [1812.10443]. 10

[16] B. Grzadkowski, M. Iskrzynski, M. Misiak, and J. Rosiek, *JHEP* **10** (2010) 085, [1008.4884]. 10

[17] S. Schael *et. al.*,, **ALEPH, DELPHI, L3, OPAL, SLD, LEP Electroweak Working Group, SLD Electroweak Group, SLD Heavy Flavour Group** Collaboration, *Phys. Rept.* **427** (2006) 257–454, [hep-ex/0509008]. 10

[18] A. Alloul, N. D. Christensen, C. Degrande, C. Duhr, and B. Fuks, *Comput. Phys. Commun.* **185** (2014) 2250–2300, [1310.1921]. 11, 31, 52, 59, 118, 124

[19] J. Alwall, R. Frederix, S. Frixione, V. Hirschi, F. Maltoni, O. Mattelaer, H. S. Shao, T. Stelzer, P. Torrielli, and M. Zaro, *JHEP* **07** (2014) 079, [1405.0301]. 11, 23, 59, 71, 87, 91, 109, 113, 117, 123, 132, 136, 158, 160, 185, 188, 195

[20] E. Conte, B. Fuks, and G. Serret, *Comput. Phys. Commun.* **184** (2013) 222–256, [1206.1599]. 12, 44, 63, 71, 136, 157, 158

[21] Y. Amhis *et. al.*,, **HFLAV** Collaboration, *Eur. Phys. J.* **C77** (2017), no. 12 895, [1612.07233]. 21

[22] I. Doršner and A. Greljo, *JHEP* **05** (2018) 126, [1801.07641]. 21, 22, 23, 169

[23] A. M. Sirunyan *et. al.*,, **CMS** Collaboration, *JHEP* **07** (2018) 115, [1806.03472]. 21, 36, 40

[24] D. Buttazzo, A. Greljo, G. Isidori, and D. Marzocca, *JHEP* **11** (2017) 044, [1706.07808]. 22, 33, 169

[25] D. Marzocca, *JHEP* **07** (2018) 121, [1803.10972]. 22, 33

[26] P. Pani and G. Polesello, *Phys. Dark Univ.* **21** (2018) 8–15, [1712.03874]. 22

[27] S. Alioli, P. Nason, C. Oleari, and E. Re, *JHEP* **06** (2010) 043, [1002.2581]. 23

[28] T. Sjöstrand, S. Ask, J. R. Christiansen, R. Corke, N. Desai, P. Ilten, S. Mrenna, S. Prestel, C. O. Rasmussen, and P. Z. Skands, *Comput. Phys. Commun.* **191** (2015) 159–177, [1410.3012]. 23, 42, 66, 71, 91, 123, 132, 137, 158, 160, 167, 175, 195

[29] C. Degrande, C. Duhr, B. Fuks, D. Grellscheid, O. Mattelaer, and T. Reiter, *Comput. Phys. Commun.* **183** (2012) 1201–1214, [1108.2040]. 23, 59, 103, 118

[30] ATLAS Collaboration,, "Calibration of the performance of b-tagging for c and light-flavour jets in the 2012 ATLAS data." ATLAS-CONF-2014-046, Geneva, Jul, 2014. 23

[31] ATLAS Collaboration,, "Expected performance of the ATLAS detector at the High-Luminosity LHC." ATL-PHYS-PUB-2019-005, Geneva, Jan, 2019. 23

[32] M. Aaboud *et. al.*,, **ATLAS** Collaboration, *JHEP* **06** (2019) 144, [1902.08103]. 27, 36, 37, 38, 39, 49

[33] R. Aaij *et. al.*,, **LHCb** Collaboration, *JHEP* **08** (2017) 055, [1705.05802]. 31

[34] R. Aaij *et. al.*,, **LHCb** Collaboration, *Phys. Rev. Lett.* **122** (2019), no. 19 191801, [1903.09252]. 31

[35] R. Aaij *et. al.*,, **LHCb** Collaboration, *Phys. Rev. Lett.* **115** (2015), no. 11 111803, [1506.08614]. [Erratum: Phys. Rev. Lett.115,no.15,159901(2015)]. 31

[36] R. Aaij *et. al.*,, **LHCb** Collaboration, *Phys. Rev. Lett.* **120** (2018), no. 17 171802, [1708.08856]. 31

[37] R. Aaij *et. al.*,, **LHCb** Collaboration, *Phys. Rev.* **D97** (2018), no. 7 072013, [1711.02505]. 31

[38] M. Blanke, in *29th International Conference on Lepton and Photon Interactions (LP2019) Toronto, Ontario, Canada, August 5-10, 2019*, 2019. 1908.09713. 31

[39] F. S. Queiroz, K. Sinha, and A. Strumia, *Phys. Rev.* **D91** (2015), no. 3 035006, [1409.6301]. 31

[40] M. J. Baker *et. al.*, *JHEP* **12** (2015) 120, [1510.03434]. 31, 36, 45

[41] A. M. Sirunyan *et. al.*,, **CMS** Collaboration, *Phys. Lett.* **B795** (2019) 76–99, [1811.10151]. 31, 36, 43

[42] P. Z. Skands *et. al.*, *JHEP* **07** (2004) 036, [hep-ph/0311123]. 32, 137, 171

[43] J. Alwall, M. Herquet, F. Maltoni, O. Mattelaer, and T. Stelzer, *JHEP* **06** (2011) 128, [1106.0522]. 32, 103

[44] G. Bélanger, F. Boudjema, A. Pukhov, and A. Semenov, *Comput. Phys. Commun.* **192** (2015) 322–329, [1407.6129]. 32, 46

[45] M. Tanabashi *et. al.*,, **Particle Data Group** Collaboration, *Phys. Rev.* **D98** (2018), no. 3 030001. 32, 61

[46] A. Azatov, D. Barducci, D. Ghosh, D. Marzocca, and L. Ubaldi, *JHEP* **10** (2018) 092, [1807.10745]. 33

[47] A. Crivellin, D. Müller, and T. Ota, *JHEP* **09** (2017) 040, [1703.09226]. 33

[48] A. Crivellin, D. Müller, and F. Saturnino, 1912.04224. 33

[49] A. Abada *et. al.*,, **FCC** Collaboration, *Eur. Phys. J. ST* **228** (2019), no. 4 755–1107. 35,

183

[50] M. Aaboud *et. al.*,, **ATLAS** Collaboration, *Phys. Rev.* **D98** (2018), no. 3 032008, [1803.10178]. 36, 37

[51] A. M. Sirunyan *et. al.*,, **CMS** Collaboration, *Eur. Phys. J.* **C77** (2017), no. 10 710, [1705.04650]. 36, 41, 42

[52] A. M. Sirunyan *et. al.*,, **CMS** Collaboration, *Phys. Lett.* **B778** (2018) 263–291, [1707.07274]. 36, 41, 42, 146

[53] G. Aad *et. al.*,, **ATLAS** Collaboration, 1911.06660. 36, 41, 42, 133

[54] **ATLAS Collaboration** Collaboration, Tech. Rep. ATLAS-CONF-2019-040, CERN, Geneva, Aug, 2019. 36, 43, 44

[55] M. Aaboud *et. al.*,, **ATLAS** Collaboration, *JHEP* **01** (2018) 126, [1711.03301]. 36, 43, 44

[56] G. Aad *et. al.*,, **ATLAS** Collaboration, *Eur. Phys. J.* **C76** (2016), no. 1 5, [1508.04735]. 37, 53

[57] M. Aaboud *et. al.*,, **ATLAS** Collaboration, *Eur. Phys. J.* **C79** (2019), no. 9 733, [1902.00377]. 37

[58] A. M. Sirunyan *et. al.*,, **CMS** Collaboration, *Eur. Phys. J.* **C78** (2018) 707, [1803.02864]. 37

[59] A. M. Sirunyan *et. al.*,, **CMS** Collaboration, *Phys. Rev.* **D98** (2018), no. 3 032005, [1805.10228]. 37, 49

[60] A. M. Sirunyan *et. al.*,, **CMS** Collaboration, *JHEP* **03** (2019) 170, [1811.00806]. 37

[61] M. Aaboud *et. al.*,, **ATLAS** Collaboration, *Phys. Rev. Lett.* **121** (2018), no. 19 191801, [1808.00336]. [Erratum: Phys. Rev. Lett.122,no.8,089901(2019)]. 37

[62] M. Aaboud *et. al.*,, **ATLAS** Collaboration, *JHEP* **12** (2017) 085, [1709.04183]. 37

[63] M. Aaboud *et. al.*,, **ATLAS** Collaboration, *JHEP* **06** (2018) 108, [1711.11520]. 37

[64] M. Aaboud *et. al.*,, **ATLAS** Collaboration, *JHEP* **11** (2017) 195, [1708.09266]. 37

[65] ATLAS Collaboration,, "Optimisation of the ATLAS b-tagging performance for the 2016 LHC Run." ATL-PHYS-PUB-2016-012, 2016. 38

[66] ATLAS Collaboration,, "Performance and Calibration of the JetFitterCharm Algorithm for c-Jet Identification." ATL-PHYS-PUB-2015-001, 2015. 38

[67] A. M. Sirunyan *et. al.*,, **CMS** Collaboration, *JINST* **13** (2018), no. 05 P05011, [1712.07158]. 40, 113

[68] F. Ambrogi *et. al.*, 1811.10624. 41, 130, 132, 136

[69] D. Dercks, N. Desai, J. S. Kim, K. Rolbiecki, J. Tattersall, and T. Weber, *Comput. Phys. Commun.* **221** (2017) 383–418, [1611.09856]. 42, 140, 157, 164

[70] P. Schwaller and J. Zurita, *JHEP* **03** (2014) 060, [1312.7350]. 43

[71] B. Dumont, B. Fuks, S. Kraml, S. Bein, G. Chalons, E. Conte, S. Kulkarni, D. Sengupta, and C. Wymant, *Eur. Phys. J.* **C75** (2015), no. 2 56, [1407.3278]. 43, 71, 136, 157, 158, 164

[72] E. Conte and B. Fuks, *Int. J. Mod. Phys.* **A33** (2018), no. 28 1830027, [1808.00480]. 43, 44, 63, 71, 130, 136, 157, 158, 164

[73] E. Conte, B. Dumont, B. Fuks, and C. Wymant, *Eur. Phys. J.* **C74** (2014), no. 10 3103, [1405.3982]. 44, 63, 71, 136, 157, 158, 164

210

[74] M. Garny, J. Heisig, B. Lülf, and S. Vogl, *Phys. Rev.* **D96** (2017), no. 10 103521, [1705.09292]. 45, 46, 57, 68, 69, 70, 71

[75] R. T. D'Agnolo, D. Pappadopulo, and J. T. Ruderman, *Phys. Rev. Lett.* **119** (2017), no. 6 061102, [1705.08450]. 45, 57, 68

[76] K. A. Mohan, D. Sengupta, T. M. P. Tait, B. Yan, and C. P. Yuan, *JHEP* **05** (2019) 115, [1903.05650]. 45

[77] N. Aghanim *et. al.*,, **Planck** Collaboration, 1807.06209. 46, 60, 69

[78] M. Garny, J. Heisig, M. Hufnagel, and B. LÃŒlf, *Phys. Rev.* **D97** (2018), no. 7 075002, [1802.00814]. 46, 69

[79] A. Albert *et. al.*,, **Fermi-LAT, DES** Collaboration, *Astrophys. J.* **834** (2017), no. 2 110, [1611.03184]. 47

[80] A. Cuoco, J. Heisig, M. Korsmeier, and M. Krämer, *JCAP* **1804** (2018) 004, [1711.05274]. 47

[81] F. Ambrogi, C. Arina, M. Backovic, J. Heisig, F. Maltoni, L. Mantani, O. Mattelaer, and G. Mohlabeng, *Phys. Dark Univ.* **24** (2019) 100249, [1804.00044]. 47

[82] M. Ackermann *et. al.*,, **Fermi-LAT** Collaboration, *Phys. Rev.* **D91** (2015), no. 12 122002, [1506.00013]. 47

[83] H. Abdallah *et. al.*,, **HESS** Collaboration, *Phys. Rev. Lett.* **120** (2018), no. 20 201101, [1805.05741]. 47

[84] M. Aaboud *et. al.*,, **ATLAS** Collaboration, *Phys. Rev. Lett.* **121** (2018), no. 21 211801, [1808.02343]. 49

[85] A. M. Sirunyan *et. al.*,, **CMS** Collaboration, *Phys. Rev.* **D100** (2019), no. 7 072001, [1906.11903]. 49

[86] A. M. Sirunyan *et. al.*,, **CMS** Collaboration, *Phys. Rev.* **D100** (2019), no. 5 052003, [1905.10853]. 49, 51, 53

[87] C. Bierlich *et. al.*, 1912.05451. 50, 83, 85, 124, 150, 157, 164, 175

[88] J. M. Butterworth, D. Grellscheid, M. Krämer, B. Sarrazin, and D. Yallup, *JHEP* **03** (2017) 078, [1606.05296]. 50, 82, 85, 150, 164, 175

[89] N. Bizot, G. Cacciapaglia, and T. Flacke, *JHEP* **06** (2018) 065, [1803.00021]. 50

[90] J. Serra, *JHEP* **09** (2015) 176, [1506.05110]. 50

[91] M. Chala, *Phys. Rev.* **D96** (2017), no. 1 015028, [1705.03013]. 50

[92] J. A. Aguilar-Saavedra, D. E. López-Fogliani, and C. Muñoz, *JHEP* **06** (2017) 095, [1705.02526]. 50

[93] G. Cacciapaglia, T. Flacke, M. Park, and M. Zhang, *Phys. Lett.* **B798** (2019) 135015, [1908.07524]. 50, 53

[94] A. Anandakrishnan, J. H. Collins, M. Farina, E. Kuflik, and M. Perelstein, *Phys. Rev.* **D93** (2016), no. 7 075009, [1506.05130]. 50

[95] R. Benbrik *et. al.*, 1907.05929. 50

[96] H. Han, L. Huang, T. Ma, J. Shu, T. M. P. Tait, and Y. Wu, *JHEP* **10** (2019) 008, [1812.11286]. 50

[97] B. Gripaios, *JHEP* **02** (2010) 045, [0910.1789]. 50

[98] T. Faber, Y. Liu, W. Porod, M. Hudec, M. Malinský, F. Staub, and H. Kolešová, 1812.07592. 50

[99] B. Fuks and H.-S. Shao, *Eur. Phys. J.* **C77** (2017), no. 2 135, [1610.04622]. 51

[100] G. Cacciapaglia, A. Carvalho, A. Deandrea, T. Flacke, B. Fuks, D. Majumder, L. Panizzi, and H.-S. Shao, *Phys. Lett.* **B793** (2019) 206–211, [1811.05055]. 51

[101] J. Bellm *et. al.*, 1912.06509. 52, 83, 86, 153, 171, 175

[102] M. Aaboud *et. al.*,, **ATLAS** Collaboration, *JHEP* **10** (2018) 159, [1802.06572]. 52

[103] M. Aaboud *et. al.*,, **ATLAS** Collaboration, *JHEP* **11** (2017) 191, [1708.00727]. 52

[104] M. Aaboud *et. al.*,, **ATLAS** Collaboration, *JHEP* **04** (2019) 046, [1811.12113]. 52, 87

[105] A. M. Sirunyan *et. al.*,, **CMS** Collaboration, *Phys. Rev.* **D97** (2018), no. 11 112003, [1803.08856]. 52, 54, 87

[106] V. Khachatryan *et. al.*,, **CMS** Collaboration, *Phys. Rev.* **D95** (2017), no. 9 092001, [1610.04191]. 52, 54

[107] A. M. Sirunyan *et. al.*,, **CMS** Collaboration, *JHEP* **06** (2018) 002, [1803.03991]. 52, 54

[108] M. Aaboud *et. al.*,, **ATLAS** Collaboration, *Phys. Rev.* **D98** (2018), no. 1 012003, [1801.02052]. 52

[109] M. Aaboud *et. al.*,, **ATLAS** Collaboration, *New J. Phys.* **18** (2016), no. 9 093016, [1605.06035]. 53

[110] M. Aaboud *et. al.*,, **ATLAS** Collaboration, *JHEP* **05** (2018) 195, [1711.02692]. 54

[111] M. Aaboud *et. al.*,, **ATLAS** Collaboration, *JHEP* **08** (2019) 033, [1903.02942]. 54

[112] J. R. Ellis, J. E. Kim, and D. V. Nanopoulos, *Phys. Lett.* **145B** (1984) 181–186. 56

[113] M. Kawasaki and T. Moroi, *Prog. Theor. Phys.* **93** (1995) 879–900, [hep-ph/9403364]. 56

[114] M. Bolz, A. Brandenburg, and W. Buchmüller, *Nucl. Phys.* **B606** (2001) 518–544, [hep-ph/0012052]. [Erratum: Nucl. Phys.B790,336(2008)]. 56

[115] L. Covi, L. Roszkowski, and M. Small, *JHEP* **07** (2002) 023, [hep-ph/0206119]. 56

[116] J. Pradler and F. D. Steffen, *Phys. Lett.* **B648** (2007) 224–235, [hep-ph/0612291]. 56

[117] V. S. Rychkov and A. Strumia, *Phys. Rev.* **D75** (2007) 075011, [hep-ph/0701104]. 56

[118] J. McDonald, *Phys. Rev. Lett.* **88** (2002) 091304, [hep-ph/0106249]. 56, 59

[119] T. Asaka, K. Ishiwata, and T. Moroi, *Phys. Rev.* **D73** (2006) 051301, [hep-ph/0512118]. 56

[120] L. J. Hall, K. Jedamzik, J. March-Russell, and S. M. West, *JHEP* **03** (2010) 080, [0911.1120]. 56

[121] T. Hambye, M. H. G. Tytgat, J. Vandecasteele, and L. Vanderheyden, *Phys. Rev.* **D98** (2018), no. 7 075017, [1807.05022]. 56

[122] F. Kahlhoefer, *Phys. Lett.* **B779** (2018) 388–392, [1801.07621]. 56

[123] R. T. Co, F. DÉramo, L. J. Hall, and D. Pappadopulo, *JCAP* **1512** (2015), no. 12 024, [1506.07532]. 57

[124] G. Bélanger *et. al.*, *JHEP* **02** (2019) 186, [1811.05478]. 57, 58, 59, 60

[125] P. Gondolo and G. Gelmini, *Nucl. Phys.* **B360** (1991) 145–179. 58

[126] K. Griest and D. Seckel, *Phys. Rev.* **D43** (1991) 3191–3203. 58

[127] M. Garny and J. Heisig, *Phys. Rev.* **D98** (2018), no. 9 095031, [1809.10135]. 58

[128] C. E. Yaguna, *JHEP* **08** (2011) 060, [1105.1654]. 59

[129] N. Bernal, X. Chu, C. Garcia-Cely, T. Hambye, and B. Zaldivar, *JCAP* **1603** (2016),

no. 03 018, [1510.08063]. 59

[130] A. Belyaev, N. D. Christensen, and A. Pukhov, *Comput. Phys. Commun.* **184** (2013) 1729–1769, [1207.6082]. 59

[131] G. Bélanger, F. Boudjema, A. Goudelis, A. Pukhov, and B. Zaldivar, *Comput. Phys. Commun.* **231** (2018) 173–186, [1801.03509]. 59

[132] R. Essig, J. Mardon, and T. Volansky, *Phys. Rev.* **D85** (2012) 076007, [1108.5383]. 61

[133] L. Lavoura, *Eur. Phys. J.* **C29** (2003) 191–195, [hep-ph/0302221]. 62

[134] A. M. Baldini *et. al.*,, **MEG** Collaboration, *Eur. Phys. J.* **C76** (2016), no. 8 434, [1605.05081]. 62

[135] G. Aad *et. al.*,, **ATLAS** Collaboration, 1908.08215. 63, 65

[136] **CMS** Collaboration, *CMS-PAS-EXO-16-022* (2016). 63, 64, 65

[137] A. M. Sirunyan *et. al.*,, **CMS** Collaboration, *JHEP* **08** (2018) 016, [1804.07321]. 63, 64, 65, 72

[138] M. Aaboud *et. al.*,, **ATLAS** Collaboration, *Phys. Rev.* **D99** (2019), no. 9 092007, [1902.01636]. 63, 65, 66, 68, 71, 73

[139] M. Garny, J. Heisig, M. Hufnagel, B. Lülf, and S. Vogl, *PoS* **CORFU2018** (2019) 092, [1904.00238]. 68

[140] M. Aaboud *et. al.*,, **ATLAS** Collaboration, *Phys. Rev.* **D94** (2016), no. 3 032005, [1604.07773]. 68, 69, 70

[141] **ATLAS** Collaboration, ATLAS-CONF-2019-040. 68, 70

[142] S. Chatrchyan *et. al.*,, **CMS** Collaboration, *JHEP* **07** (2013) 122, [1305.0491]. 68, 70, 71

[143] V. Khachatryan *et. al.*,, **CMS** Collaboration, *, CMS-PAS-EXO-16-036* (2016). 68, 70, 71

[144] G. Aad *et. al.*,, **ATLAS** Collaboration, *JHEP* **01** (2015) 068, [1411.6795]. 68, 71

[145] M. Aaboud *et. al.*,, **ATLAS** Collaboration, *JHEP* **06** (2018) 022, [1712.02118]. 69, 70, 72, 73

[146] M. Aaboud *et. al.*,, **ATLAS** Collaboration, *Phys. Rev.* **D97** (2018), no. 5 052012, [1710.04901]. 69, 70, 73

[147] A. M. Sirunyan *et. al.*,, **CMS** Collaboration, *Phys. Lett.* **B797** (2019) 134876, [1906.06441]. 69, 74

[148] S. Junius, L. Lopez-Honorez, and A. Mariotti, *JHEP* **07** (2019) 136, [1904.07513]. 69

[149] 71

[150] F. Ambrogi,. 71

[151] M. L. Mangano, M. Moretti, F. Piccinini, and M. Treccani, *JHEP* **01** (2007) 013, [hep-ph/0611129]. 71, 134

[152] M. Cacciari, G. P. Salam, and G. Soyez, *JHEP* **04** (2008) 063, [0802.1189]. 71

[153] M. Cacciari, G. P. Salam, and G. Soyez, *Eur. Phys. J.* **C72** (2012) 1896, [1111.6097]. 71, 103, 196

[154] J. de Favereau, C. Delaere, P. Demin, A. Giammanco, V. Lemaître, A. Mertens, and M. Selvaggi,, **DELPHES 3** Collaboration, *JHEP* **02** (2014) 057, [1307.6346]. 71, 91, 103, 158, 160, 196

[155] A. M. Sirunyan *et. al.*,, **CMS** Collaboration, 1909.03460. 71

[156] C. G. Lester and D. J. Summers, *Phys. Lett.* **B463** (1999) 99–103, [hep-ph/9906349].

71

[157] **ATLAS** Collaboration,. ATLAS-CONF-2014-047, 2014. 72

[158] **ATLAS** Collaboration,. ATL-PHYS-PUB-2019-011, 2019. 73

[159] M. Aaboud *et. al.*,, **ATLAS** Collaboration, *Eur. Phys. J.* **C79** (2019), no. 6 481, [1902.03094]. 73

[160] A. M. Sirunyan *et. al.*,, **CMS** Collaboration, *Phys. Rev.* **D99** (2019), no. 3 032011, [1811.07991]. 73

[161] W. Beenakker, C. Borschensky, M. Krämer, A. Kulesza, and E. Laenen, *JHEP* **12** (2016) 133, [1607.07741]. 74

[162] W. Beenakker, S. Brensing, M. Kramer, A. Kulesza, E. Laenen, and I. Niessen, *JHEP* **08** (2010) 098, [1006.4771]. 74

[163] A. M. Sirunyan *et. al.*,, **CMS** Collaboration, *Submitted to: Eur. Phys. J.* (2018) [1809.10733]. 78

[164] G. Aad *et. al.*,, **ATLAS** Collaboration, *Phys. Rev.* **D101** (2020), no. 1 012002, [1909.02845]. 78, 89

[165] E. Gildener and S. Weinberg, *Phys. Rev.* **D13** (1976) 3333. 78, 80

[166] J. F. Gunion and H. E. Haber, *Phys. Rev.* **D67** (2003) 075019, [hep-ph/0207010]. 78

[167] S. Weinberg, *Phys.Rev.Lett.* **19** (1967) 1264–1266. 78

[168] K. Lane and W. Shepherd, *Phys. Rev.* **D99** (2019), no. 5 055015, [1808.07927]. 78, 79, 80, 83

[169] S. R. Coleman and E. J. Weinberg, *Phys. Rev.* **D7** (1973) 1888–1910. 78

[170] J. S. Lee and A. Pilaftsis, *Phys. Rev.* **D86** (2012) 035004, [1201.4891]. 78, 80

[171] S. L. Glashow and S. Weinberg, *Phys. Rev.* **D15** (1977) 1958. 79

[172] G. C. Branco, P. M. Ferreira, L. Lavoura, M. N. Rebelo, M. Sher, and J. P. Silva, *Phys. Rept.* **516** (2012) 1–102, [1106.0034]. 79

[173] V. Khachatryan *et. al.*,, **CMS** Collaboration, *JHEP* **11** (2015) 018, [1508.07774]. 79, 81, 83

[174] M. Aaboud *et. al.*,, **ATLAS** Collaboration, *JHEP* **11** (2018) 085, [1808.03599]. 79, 81, 83

[175] A. M. Sirunyan *et. al.*,, **CMS** Collaboration, 1908.09206. 79, 81

[176] K. Hashino, S. Kanemura, and Y. Orikasa, *Phys. Lett.* **B752** (2016) 217–220, [1508.03245]. 80

[177] R. A. Battye, G. D. Brawn, and A. Pilaftsis, *JHEP* **08** (2011) 020, [1106.3482]. 80

[178] A. Pilaftsis, *Phys. Lett.* **B706** (2012) 465–469, [1109.3787]. 80

[179] K. Lane and E. Pilon, 1909.02111. 81

[180] A. M. Sirunyan *et. al.*,, **CMS** Collaboration, 1908.01115. 81

[181] M. Aaboud *et. al.*,, **ATLAS** Collaboration, *Phys. Lett.* **B783** (2018) 392–414, [1804.01126]. 81

[182] A. M. Sirunyan *et. al.*,, **CMS** Collaboration, 1911.03781. 81

[183] A. M. Sirunyan *et. al.*,, **CMS** Collaboration, *Phys. Rev.* **D99** (2019), no. 1 012005, [1810.11822]. 82

[184] A. M. Sirunyan *et. al.*,, **CMS** Collaboration, *Phys. Lett.* **B780** (2018) 501–532, [1709.07497]. 83

[185] M. Bauer, U. Haisch, and F. Kahlhoefer, *JHEP* **05** (2017) 138, [1701.07427]. 85

[186] A. M. Sirunyan *et. al.*,, **CMS** Collaboration, *Eur. Phys. J.* **C79** (2019), no. 3 280, [1811.06562]. 85

[187] M. Aaboud *et. al.*,, **ATLAS** Collaboration, *JHEP* **05** (2019) 142, [1903.01400]. 85, 175, 176

[188] T. Abe *et. al.*,, **LHC Dark Matter Working Group** Collaboration, *Phys. Dark Univ.* (2019) 100351, [1810.09420]. 85

[189] M. Bahr *et. al.*, *Eur. Phys. J.* **C58** (2008) 639–707, [0803.0883]. 87, 153

[190] J. Bellm *et. al.*, *Eur. Phys. J.* **C76** (2016), no. 4 196, [1512.01178]. 87

[191] G. Aad *et. al.*,, **ATLAS** Collaboration, *JHEP* **03** (2013) 128, [1211.6096]. 87

[192] S. Chatrchyan *et. al.*,, **CMS** Collaboration, *JHEP* **05** (2013) 090, [1303.4811]. 87

[193] M. Aaboud *et. al.*,, **ATLAS** Collaboration, *Eur. Phys. J.* **C77** (2017), no. 7 474, [1703.04362]. 87

[194] V. Khachatryan *et. al.*,, **CMS** Collaboration, *JHEP* **03** (2017) 032, [1606.01522]. 87

[195] G. Aad *et. al.*,, **ATLAS** Collaboration, *JHEP* **08** (2016) 104, [1604.02997]. 87

[196] D. Curtin *et. al.*, *Phys. Rev.* **D90** (2014), no. 7 075004, [1312.4992]. 89

[197] H. Georgi, D. B. Kaplan, and L. Randall, *Phys. Lett.* **169B** (1986) 73–78. 89, 95, 96

[198] I. Brivio, M. B. Gavela, L. Merlo, K. Mimasu, J. M. No, R. del Rey, and V. Sanz, *Eur. Phys. J.* **C77** (2017), no. 8 572, [1701.05379]. 89, 90, 95, 96, 97

[199] M. Bauer, M. Neubert, and A. Thamm, *JHEP* **12** (2017) 044, [1708.00443]. 89, 90, 91, 95, 96

[200] M. Bauer, M. Neubert, and A. Thamm, *Phys. Rev. Lett.* **119** (2017), no. 3 031802, [1704.08207]. 89, 97, 98

[201] J. Quevillon and C. Smith, *Eur. Phys. J.* **C79** (2019), no. 10 822, [1903.12559]. 89, 95

[202] A. S. Chisholm, S. Kuttimalai, K. Nikolopoulos, and M. Spannowsky, *Eur. Phys. J.* **C76** (2016), no. 9 501, [1606.09177]. 89

[203] S. Baum and N. R. Shah, 1808.02667. [JHEP12,044(2018)]. 89

[204] J. M. No, *Phys. Rev.* **D93** (2016), no. 3 031701, [1509.01110]. 89

[205] S. Gopalakrishna, S. Jung, and J. D. Wells, *Phys. Rev.* **D78** (2008) 055002, [0801.3456]. 89

[206] H. Davoudiasl, H.-S. Lee, and W. J. Marciano, *Phys. Rev.* **D85** (2012) 115019, [1203.2947]. 89

[207] H. Davoudiasl, H.-S. Lee, I. Lewis, and W. J. Marciano, *Phys. Rev.* **D88** (2013), no. 1 015022, [1304.4935]. 89

[208] G. Aad *et. al.*,, **ATLAS** Collaboration, *Phys. Rev.* **D93** (2016), no. 11 112002, [1604.05232]. 89, 153, 155

[209] **CMS Collaboration** Collaboration,, *The CMS electromagnetic calorimeter project: Technical Design Report*. Technical Design Report CMS. CERN, Geneva, 1997. 90

[210] **CMS Collaboration** Collaboration,C. Collaboration, ,, *CMS Physics: Technical Design Report Volume 1: Detector Performance and Software*. Technical Design Report CMS. CERN, Geneva, 2006. 90

[211] **ATLAS Collaboration** Collaboration, Tech. Rep. ATLAS-CONF-2012-079, CERN, Geneva, Jul, 2012. 90

[212] M. Aaboud *et. al.*,, **ATLAS** Collaboration, *JHEP* **10** (2017) 112, [1708.00212]. 90, 92

[213] A. M. Sirunyan *et. al.*,, **CMS** Collaboration, *JHEP* **11** (2018) 152, [1806.05996]. 90

[214] M. Aaboud *et. al.*,, **ATLAS** Collaboration, *Eur. Phys. J.* **C76** (2016), no. 12 666, [1606.01813]. 91

[215] C. Anastasiou, C. Duhr, F. Dulat, E. Furlan, T. Gehrmann, F. Herzog, A. Lazopoulos, and B. Mistlberger, *JHEP* **05** (2016) 058, [1602.00695]. 91, 93

[216] C. Uzziel Perez,, **CMS** Collaboration,. 91

[217] S. Chatrchyan *et. al.*,, **CMS** Collaboration, *Phys. Lett.* **B720** (2013) 309–329, [1210.2422]. 91

[218] A. L. Read, *Journal of Physics G: Nuclear and Particle Physics* **28** (2002), no. 10 2693–2704. 91, 118

[219] M. Aaboud *et. al.*,, **ATLAS** Collaboration, *JHEP* **06** (2018) 166, [1802.03388]. 93, 94, 100

[220] A. M. Sirunyan *et. al.*,, **CMS** Collaboration, *Phys. Lett.* **B796** (2019) 131–154, [1812.00380]. 93

[221] **ATLAS Collaboration** Collaboration, Tech. Rep. ATLAS-CONF-2018-018, CERN, Geneva, Jun, 2018. 93

[222] CMS-PAS-HIG-15-011,, **CMS** Collaboration,. 94, 95, 96, 100

[223] A. M. Sirunyan *et. al.*,, **CMS** Collaboration, *JHEP* **11** (2018) 018, [1805.04865]. 94

[224] G. Aad *et. al.*,, **ATLAS** Collaboration, *Phys. Rev.* **D92** (2015), no. 5 052002, [1505.01609]. 94

[225] A. Elagin, P. Murat, A. Pranko, and A. Safonov, *Nucl. Instrum. Meth.* **A654** (2011) 481–489, [1012.4686]. 95

[226] L. Bianchini, J. Conway, E. K. Friis, and C. Veelken, *J. Phys. Conf. Ser.* **513** (2014) 022035. 95

[227] G. Alonso-Álvarez, M. B. Gavela, and P. Quilez, *Eur. Phys. J.* **C79** (2019), no. 3 223, [1811.05466]. 96

[228] A. Ahmed, B. M. Dillon, B. Grzadkowski, J. F. Gunion, and Y. Jiang, *Phys. Rev.* **D95** (2017), no. 9 095019, [1512.05771]. 102

[229] A. Angelescu, G. Moreau, and F. Richard, *Phys. Rev.* **D96** (2017), no. 1 015019, [1702.03984]. 102

[230] T. Sjostrand, S. Mrenna, and P. Z. Skands, *Comput. Phys. Commun.* **178** (2008) 852–867, [0710.3820]. 103

[231] M. Cacciari, in *Deep inelastic scattering. Proceedings, 14th International Workshop, DIS 2006, Tsukuba, Japan, April 20-24, 2006*, pp. 487–490, 2006. hep-ph/0607071. [,125(2006)]. 103

[232] S. Fichet and G. von Gersdorff, *JHEP* **03** (2014) 102, [1311.6815]. 104

[233] S. Fichet, G. von Gersdorff, O. Kepka, B. Lenzi, C. Royon, and M. Saimpert, *Phys. Rev.* **D89** (2014) 114004, [1312.5153]. 104

[234] C. Baldenegro, S. Fichet, G. von Gersdorff, and C. Royon, *JHEP* **06** (2017) 142, [1703.10600]. 104

[235] A. Belyaev, G. Cacciapaglia, H. Cai, G. Ferretti, T. Flacke, A. Parolini, and H. Serodio, *JHEP* **01** (2017) 094, [1610.06591]. 104

[236] S. Fichet, G. von Gersdorff, E. Ponton, and R. Rosenfeld, *JHEP* **09** (2016) 158, [1607.03125]. 104

[237] G. Brooijmans *et. al.*, in *Les Houches 2017: Physics at TeV Colliders Standard Model Working Group Report*, 2018. 1803.10379. 105, 146, 150, 154, 156, 157

[238] M. Cepeda *et. al.*, *CERN Yellow Rep. Monogr.* **7** (2019) 221–584, [1902.00134]. 108, 109

[239] B. Henning, D. Lombardo, M. Riembau, and F. Riva, *Phys. Rev. Lett.* **123** (2019), no. 18 181801, [1812.09299]. 108, 109, 110, 115

[240] J. Ellis, C. W. Murphy, V. Sanz, and T. You, *JHEP* **06** (2018) 146, [1803.03252]. 109

[241] S. van Beek, E. R. Nocera, J. Rojo, and E. Slade, *SciPost Phys.* **7** (2019), no. 5 070, [1906.05296]. 109

[242] A. Biekötter, T. Corbett, and T. Plehn, *SciPost Phys.* **6** (2019), no. 6 064, [1812.07587]. 109

[243] E. da Silva Almeida, A. Alves, N. Rosa Agostinho, O. J. P. Éboli, and M. C. Gonzalez-Garcia, *Phys. Rev.* **D99** (2019), no. 3 033001, [1812.01009]. 109

[244] I. Brivio, S. Bruggisser, F. Maltoni, R. Moutafis, T. Plehn, E. Vryonidou, S. Westhoff, and C. Zhang, 1910.03606. 109

[245] J. De Blas, G. Durieux, C. Grojean, J. Gu, and A. Paul, *JHEP* **12** (2019) 117, [1907.04311]. 109

[246] A. Falkowski and D. Straub, 1911.07866. 109

[247] C. Degrande, F. Maltoni, K. Mimasu, E. Vryonidou, and C. Zhang, *JHEP* **10** (2018) 005, [1804.07773]. 109

[248] V. Barger, K. Hagiwara, and Y.-J. Zheng, 1912.11795. 109

[249] T. Plehn and M. Spannowsky, *J. Phys.* **G39** (2012) 083001, [1112.4441]. 112

[250] C. Anders, C. Bernaciak, G. Kasieczka, T. Plehn, and T. Schell, *Phys. Rev.* **D89** (2014), no. 7 074047, [1312.1504]. 112

[251] M. Aaboud *et. al.*,, **ATLAS** Collaboration, *Eur. Phys. J.* **C79** (2019), no. 5 375, [1808.07858]. 112

[252] **CMS Collaboration** Collaboration, Tech. Rep. CMS-PAS-JME-16-003, CERN, Geneva, 2017. 112

[253] **CMS Collaboration** Collaboration, Tech. Rep. CMS-PAS-JME-18-002, CERN, Geneva, 2019. 112

[254] P. Artoisenet, R. Frederix, O. Mattelaer, and R. Rietkerk, *JHEP* **03** (2013) 015, [1212.3460]. 113, 185

[255] R. D. Ball, S. Carrazza, L. Del Debbio, S. Forte, Z. Kassabov, J. Rojo, E. Slade, and M. Ubiali,, **NNPDF** Collaboration, *Eur. Phys. J.* **C78** (2018), no. 5 408, [1802.03398]. 113

[256] **ATLAS Collaboration** Collaboration, Tech. Rep. CERN-LHCC-2017-005. ATLAS-TDR-025, CERN, Geneva, Apr, 2017. 113

[257] D. Contardo, M. Klute, J. Mans, L. Silvestris, and J. Butler,. 113

[258] G. Perez, Y. Soreq, E. Stamou, and K. Tobioka, *Phys. Rev.* **D92** (2015), no. 3 033016, [1503.00290]. 114

[259] T. Han, B. Nachman, and X. Wang, *Phys. Lett.* **B793** (2019) 90–96, [1812.06992]. 114, 115

[260] **ATLAS Collaboration** Collaboration, Tech. Rep. ATL-PHYS-PUB-2018-016, CERN, Geneva, Aug, 2018. 114, 115

[261] K. Agashe, R. Contino, and A. Pomarol, *Nucl. Phys.* **B719** (2005) 165–187, [hep-ph/0412089]. 116

[262] A. Pomarol and J. Serra, *Phys. Rev.* **D78** (2008) 074026, [0806.3247]. 116, 117

[263] R. Röntsch and M. Schulze, *JHEP* **07** (2014) 091, [1404.1005]. [Erratum: JHEP09,132(2015)]. 117

[264] J. A. Dror, M. Farina, E. Salvioni, and J. Serra, *JHEP* **01** (2016) 071, [1511.03674]. 117, 119

[265] S. Banerjee, C. Englert, R. S. Gupta, and M. Spannowsky, *Phys. Rev.* **D98** (2018), no. 9 095012, [1807.01796]. 117

[266] S. Banerjee, R. S. Gupta, J. Y. Reiness, and M. Spannowsky, *Phys. Rev.* **D100** (2019), no. 11 115004, [1905.02728]. 117

[267] S. Banerjee, R. S. Gupta, J. Y. Reiness, S. Seth, and M. Spannowsky, 1912.07628. 117

[268] S. Banerjee, F. Krauss, and M. Spannowsky, *Phys. Rev.* **D100** (2019) 073012, [1904.07886]. 118

[269] C. Patrignani *et. al.*,, **Particle Data Group** Collaboration, *Chin. Phys.* **C40** (2016), no. 10 100001. 123

[270] I. Brivio and M. Trott, *Phys. Rept.* **793** (2019) 1–98, [1706.08945]. 123

[271] **ATLAS** Collaboration, Tech. Rep. ATL-PHYS-PUB-2017-018, CERN, Geneva, Nov, 2017. 123

[272] **CMS** Collaboration, Tech. Rep. CMS-PAS-HIG-19-005, CERN, Geneva, 2020. 123

[273] D. de Florian *et. al.*,, **LHC Higgs Cross Section Working Group** Collaboration, 1610.07922. 123

[274] A. M. Sirunyan *et. al.*,, **CMS** Collaboration, *Phys. Rev.* **D99** (2019), no. 11 112003, [1901.00174]. 123

[275] C. Hays, V. Sanz Gonzalez, and G. Zemaityte, Tech. Rep. LHCHXSWG-2019-004, CERN, Geneva, May, 2019. 123

[276] **ATLAS Collaboration** Collaboration, Tech. Rep. ATL-PHYS-PUB-2019-042, CERN, Geneva, Oct, 2019. 123

[277] O. Mattelaer, *Eur. Phys. J.* **C76** (2016), no. 12 674, [1607.00763]. 124

[278] R. Contino, M. Ghezzi, C. Grojean, M. Muhlleitner, and M. Spira, *JHEP* **07** (2013) 035, [1303.3876]. 125

[279] A. Alloul, B. Fuks, and V. Sanz, *JHEP* **04** (2014) 110, [1310.5150]. 125

[280] **CMS** Collaboration, Tech. Rep. CMS-NOTE-2017-001, CERN, Geneva, Jan, 2017. 130, 132

[281] A. M. Sirunyan *et. al.*,, **CMS** Collaboration, *JHEP* **03** (2018) 166, [1709.05406]. 131, 132, 136, 141, 142, 143

[282] B. Fuks and S. Mondal,. DOI: 10.7484/INSPIREHEP.DATA.HE48.D9HD.1. 131

[283] B. Fuks, M. Klasen, D. R. Lamprea, and M. Rothering, *JHEP* **10** (2012) 081, [1207.2159]. 132

[284] B. Fuks, M. Klasen, D. R. Lamprea, and M. Rothering, *Eur. Phys. J.* **C73** (2013) 2480, [1304.0790]. 132

[285] P. M. Nadolsky, H.-L. Lai, Q.-H. Cao, J. Huston, J. Pumplin, D. Stump, W.-K. Tung, and C. P. Yuan, *Phys. Rev.* **D78** (2008) 013004, [0802.0007]. 132

[286] A. M. Sirunyan *et. al.*,, **CMS** Collaboration, *Phys. Rev.* **D97** (2018), no. 3 032009, [1711.00752]. 132, 136, 143

[287] S. Bein, S.-M. Choi, B. Fuks, S. Jeong, D. W. Kang, J. Li, and J. Sonneveld,. DOI: 10.7484/INSPIREHEP.DATA.MMM1.876Z. 132

[288] C. Borschensky, M. Krämer, A. Kulesza, M. Mangano, S. Padhi, T. Plehn, and X. Portell, *Eur. Phys. J.* **C74** (2014), no. 12 3174, [1407.5066]. 133

[289] A. Buckley, M. Citron, S. Fichet, S. Kraml, W. Waltenberger, and N. Wardle, *JHEP* **04** (2019) 064, [1809.05548]. 133, 134

[290] **ATLAS** Collaboration, Tech. Rep. ATL-PHYS-PUB-2019-029, CERN, Geneva, Aug, 2019. 133

[291] **ROOT** Collaboration,K. Cranmer, G. Lewis, L. Moneta, A. Shibata, and W. Verkerke, , Tech. Rep. CERN-OPEN-2012-016, New York U., New York, Jan, 2012. 133

[292] L. Heinrich, M. Feickert, G. Stark, R. Turra, and J. Forde,. DOI: 10.5281/zenodo.3334365. 133

[293] G. Aad *et. al.*,, **ATLAS** Collaboration, *JHEP* **12** (2019) 060, [1908.03122]. HEPData entry: 10.17182/hepdata.89408. 133

[294] S. Kraml, S. Kulkarni, U. Laa, A. Lessa, W. Magerl, D. Proschofsky-Spindler, and W. Waltenberger, *Eur. Phys. J.* **C74** (2014) 2868, [1312.4175]. 136, 146

[295] F. Ambrogi, S. Kraml, S. Kulkarni, U. Laa, A. Lessa, V. Magerl, J. Sonneveld, M. Traub, and W. Waltenberger, *Comput. Phys. Commun.* **227** (2018) 72–98, [1701.06586]. 136, 146, 157, 164

[296] J. Dutta, S. Kraml, A. Lessa, and W. Waltenberger, *LHEP* **1** (2018), no. 1 5–12, [1803.02204]. 136

[297] J. Heisig, S. Kraml, and A. Lessa, *Phys. Lett.* **B788** (2019) 87–95, [1808.05229]. 136

[298] M. Aaboud *et. al.*,, **ATLAS** Collaboration, *Eur. Phys. J.* **C76** (2016), no. 7 392, [1605.03814]. 136, 138, 144, 165, 166

[299] A. M. Sirunyan *et. al.*,, **CMS** Collaboration, *Phys. Rev.* **D96** (2017), no. 3 032003, [1704.07781]. 136, 143, 146

[300] N. D. Christensen, P. de Aquino, C. Degrande, C. Duhr, B. Fuks, M. Herquet, F. Maltoni, and S. Schumann, *Eur. Phys. J.* **C71** (2011) 1541, [0906.2474]. 137

[301] M. Drees, H. Dreiner, D. Schmeier, J. Tattersall, and J. S. Kim, *Comput. Phys. Commun.* **187** (2015) 227–265, [1312.2591]. 140, 157

[302] G. Brooijmans *et. al.*, in *9th Les Houches Workshop on Physics at TeV Colliders (PhysTeV 2015) Les Houches, France, June 1-19, 2015*, 2016. 1605.02684. 146, 157

[303] S. Sekmen and G. Unel, *Comput. Phys. Commun.* **233** (2018) 215–236, [1801.05727]. 146, 157

[304] G. Unel, S. Sekmen, and A. M. Toon, in *19th International Workshop on Advanced Computing and Analysis Techniques in Physics Research: Empowering the revolution: Bringing Machine Learning to High Performance Computing (ACAT 2019) Saas-Fee, Switzerland, March 11-15, 2019*, 2019. 1909.10621. 146, 157

[305] https://indico.cern.ch/event/795041/contributions/3345061/. 146

[306] A. M. Sirunyan *et. al.*,, **CMS** Collaboration, *Eur. Phys. J.* **C77** (2017), no. 9 578,

[1704.07323]. 146

[307] A. M. Sirunyan *et. al.,*, **CMS** Collaboration, *Phys. Rev. Lett.* **119** (2017), no. 15 151802, [1705.04673]. 147

[308] A. M. Sirunyan *et. al.,*, **CMS** Collaboration, *JHEP* **02** (2018) 067, [1710.09154]. 147

[309] A. M. Sirunyan *et. al.,*, **CMS** Collaboration, *Phys. Lett.* **B780** (2018) 384–409, [1709.09814]. 147

[310] A. M. Sirunyan *et. al.,*, **CMS** Collaboration, *JHEP* **11** (2017) 029, [1706.09933]. 147

[311] A. M. Sirunyan *et. al.,*, **CMS** Collaboration, *Phys. Lett.* **B780** (2018) 118–143, [1711.08008]. 147

[312] A. M. Sirunyan *et. al.,*, **CMS** Collaboration, *JHEP* **12** (2017) 142, [1707.06193]. 147

[313] A. M. Sirunyan *et. al.,*, **CMS** Collaboration, *JHEP* **10** (2017) 005, [1707.03316]. 147

[314] A. Buckley, J. Butterworth, L. Lonnblad, D. Grellscheid, H. Hoeth, J. Monk, H. Schulz, and F. Siegert, *Comput. Phys. Commun.* **184** (2013) 2803–2819, [1003.0694]. 150, 157, 164

[315] S. Amrith, J. M. Butterworth, F. F. Deppisch, W. Liu, A. Varma, and D. Yallup, *JHEP* **05** (2019) 154, [1811.11452]. 150, 164

[316] J. M. Butterworth, *J. Phys. Conf. Ser.* **1271** (2019), no. 1 012013, [1902.03067]. 150, 153, 164

[317] B. C. Allanach, J. M. Butterworth, and T. Corbett, *JHEP* **08** (2019) 106, [1904.10954]. 150, 164

[318] J. M. Butterworth, M. Chala, C. Englert, M. Spannowsky, and A. Titov, *Phys. Rev.* **D100** (2019), no. 11 115019, [1909.04665]. 150

[319] D. Yallup,, *Constraining new physics with fiducial measurements at the LHC*. PhD thesis, University College London, London, UK, 12, 2019. To appear; submitted Sept 2019. 150

[320] E. Maguire, L. Heinrich, and G. Watt, *J. Phys. Conf. Ser.* **898** (2017), no. 10 102006, [1704.05473]. 151

[321] M. Aaboud *et. al.,*, **ATLAS** Collaboration, *Phys. Rev.* **D95** (2017), no. 11 112005, [1704.03839]. 153, 155

[322] X. Chen, T. Gehrmann, N. Glover, M. Höfer, and A. Huss, *Submitted to: J. High Energy Phys.* (2019) [1904.01044]. 155

[323] B. Boussaha, F. Iddir, and L. Semlala, *Adv. High Energy Phys.* **2018** (2018) 4174602, [1803.09176]. 155

[324] S. Catani, L. Cieri, D. de Florian, G. Ferrera, and M. Grazzini, *Phys. Rev. Lett.* **108** (2012) 072001, [1110.2375]. [Erratum: Phys. Rev. Lett.117,no.8,089901(2016)]. 155

[325] G. Aad *et. al.,*, **ATLAS** Collaboration, *Phys. Rev.* **D87** (2013), no. 11 112003, [1302.1283]. [Erratum: Phys. Rev.D91,no.11,119901(2015)]. 155

[326] J. Campbell and T. Neumann, *JHEP* **12** (2019) 034, [1909.09117]. 155

[327] A. Buckley, D. Kar, and K. Nordström, 1910.01637. 155, 161, 164, 165

[328] C. Balázs *et. al.,*, **GAMBIT** Collaboration, *Eur. Phys. J.* **C77** (2017), no. 11 795, [1705.07919]. 157, 158, 161, 164

[329] P. Athron *et. al.,*, **GAMBIT** Collaboration, *Eur. Phys. J.* **C77** (2017), no. 11 784, [1705.07908]. [Addendum: Eur. Phys. J.C78,no.2,98(2018)]. 158, 164

[330] A. M. Sirunyan *et. al.*,, **CMS** Collaboration, *Phys. Lett.* **B782** (2018) 440–467, [1801.01846]. 159, 160, 161, 162, 169

[331] S. Agostinelli *et. al.*,, **GEANT4** Collaboration, *Nucl. Instrum. Meth.* **A506** (2003) 250–303. 160

[332] S. Abdullin, P. Azzi, F. Beaudette, P. Janot, and A. Perrotta,, **CMS** Collaboration, *J. Phys. Conf. Ser.* **331** (2011) 032049. 160

[333] J. Y. Araz, B. Fuks, and G. Polykratis, in preparation. 160

[334] E. Bothmann *et. al.*,, **Sherpa** Collaboration, *SciPost Phys.* **7** (2019), no. 3 034, [1905.09127]. 167

[335] S. Frixione, P. Nason, and C. Oleari, *JHEP* **11** (2007) 070, [0709.2092]. 167

[336] M. Aaboud *et. al.*,, **ATLAS** Collaboration, *Eur. Phys. J.* **C77** (2017), no. 11 765, [1707.03263]. 169

[337] F. Kahlhoefer, K. Schmidt-Hoberg, T. Schwetz, and S. Vogl, *JHEP* **02** (2016) 016, [1510.02110]. 169

[338] A. L. Read, *J. Phys.* **G28** (2002) 2693–2704. [,11(2002)]. 169

[339] P. Athron *et. al.*,, **GAMBIT** Collaboration, 1809.02097. 169, 170, 171, 172, 190

[340] M. Aaboud *et. al.*,, **ATLAS** Collaboration, *Eur. Phys. J.* **78** (2018), no. 12 995, [1803.02762]. 169

[341] M. Aaboud *et. al.*,, **ATLAS** Collaboration, *Phys. Rev.* **D98** (2018), no. 9 092012, [1806.02293]. 169

[342] M. Aaboud *et. al.*,, **ATLAS** Collaboration, *Phys. Rev.* **D98** (2018), no. 9 092002, [1806.04030]. 169

[343] M. Aaboud *et. al.*,, **ATLAS** Collaboration, *Phys. Rev.* **D98** (2018), no. 3 032009, [1804.03602]. 169, 172

[344] **CMS** Collaboration,. 169

[345] A. M. Sirunyan *et. al.*,, **CMS** Collaboration, *JHEP* **03** (2018) 076, [1709.08908]. 169

[346] **CMS** Collaboration, Tech. Rep. CMS-PAS-SUS-16-039, CERN, Geneva, 2017. 169

[347] M. Aaboud *et. al.*,, **ATLAS** Collaboration, *Eur. Phys. J.* **C77** (2017), no. 3 141, [1610.05088]. 172, 174

[348] M. Aaboud *et. al.*,, **ATLAS** Collaboration, *JHEP* **04** (2019) 048, [1902.05892]. 172, 174

[349] S. Otten, S. Caron, W. de Swart, M. van Beekveld, L. Hendriks, C. van Leeuwen, D. Podareanu, R. Ruiz de Austri, and R. Verheyen, 1901.00875. 179, 195, 206

[350] B. Hashemi, N. Amin, K. Datta, D. Olivito, and M. Pierini, 1901.05282. 179

[351] R. Di Sipio, M. Faucci Giannelli, S. Ketabchi Haghighat, and S. Palazzo, *JHEP* **08** (2020) 110, [1903.02433]. 179

[352] R. D. Ball *et. al.*,, **NNPDF** Collaboration, *JHEP* **04** (2015) 040, [1410.8849]. 179

[353] A. J. Larkoski, I. Moult, and B. Nachman, 1709.04464. 179

[354] S. Caron, J. S. Kim, K. Rolbiecki, R. Ruiz de Austri, and B. Stienen, *Eur. Phys. J.* **C77** (2017), no. 4 257, [1605.02797]. 179, 182

[355] J. Brehmer, K. Cranmer, G. Louppe, and J. Pavez, *Phys. Rev. Lett.* **121** (2018), no. 11 111801, [1805.00013]. 179

[356] A. Coccaro, M. Pierini, L. Silvestrini, and R. Torre, 1911.03305. 179, 183

[357] S. Caron, T. Heskes, S. Otten, and B. Stienen, *Eur. Phys. J.* **C79** (2019), no. 11 944, [1905.08628]. 180

[358] Y. Gal and Z. Ghahramani, *arXiv e-prints* (June, 2015) arXiv:1506.02142, [1506.02142]. 181, 188

[359] F. Pedregosa, G. Varoquaux, A. Gramfort, V. Michel, B. Thirion, O. Grisel, M. Blondel, P. Prettenhofer, R. Weiss, V. Dubourg, J. Vanderplas, A. Passos, D. Cournapeau, M. Brucher, M. Perrot, and E. Duchesnay, *Journal of Machine Learning Research* **12** (2011) 2825–2830. 181

[360] https://scikit-learn.org/stable/modules/model_persistence.html. 181

[361] Y. LeCun and C. Cortes,. https://www.bibsonomy.org/bibtex/2935bad99fa1f65e03c25b315aa3c1032/mhwombat. 181

[362] A. Dal Pozzolo, O. Caelen, A. J. Reid, and G. Bontempi, *Symposium on Computational Intelligence and Data Mining (CIDM), IEEE* (2015). 181

[363] F. Diblen, J. Attema, R. Bakhshi, S. Caron, L. Hendriks, and B. Stienen, 1809.08893. 182

[364] M. Bridges, K. Cranmer, F. Feroz, M. Hobson, R. Ruiz de Austri, and R. Trotta, *JHEP* **03** (2011) 012, [1011.4306]. 182

[365] A. Buckley, A. Shilton, and M. J. White, *Comput. Phys. Commun.* **183** (2012) 960–970, [1106.4613]. 182

[366] P. Bechtle, S. Belkner, D. Dercks, M. Hamer, T. Keller, M. Krämer, B. Sarrazin, J. Schütte-Engel, and J. Tattersall, *Eur. Phys. J.* **C77** (2017), no. 10 707, [1703.01309]. 182

[367] S. Otten, K. Rolbiecki, S. Caron, J.-S. Kim, R. Ruiz De Austri, and J. Tattersall, *Eur. Phys. J.* **C80** (2020), no. 1 12, [1810.08312]. 183, 188

[368] W. Beenakker, R. Hopker, and M. Spira, hep-ph/9611232. 183

[369] A. Kvellestad, S. Maeland, and I. Strümke, *Eur. Phys. J.* **C78** (2018), no. 12 1010, [1804.07737]. 183

[370] G. Bertone, M. P. Deisenroth, J. S. Kim, S. Liem, R. Ruiz de Austri, and M. Welling, *Phys. Dark Univ.* **24** (2019) 100293, [1611.02704]. 183

[371] G. Bertone, N. Bozorgnia, J. S. Kim, S. Liem, C. McCabe, S. Otten, and R. Ruiz de Austri, *JCAP* **1803** (2018) 026, [1712.04793]. 183

[372] Q. R. Ahmad *et. al.*,, **SNO** Collaboration, *Phys. Rev. Lett.* **89** (2002) 011301, [nucl-ex/0204008]. 183

[373] Y. Ashie *et. al.*,, **Super-Kamiokande** Collaboration, *Phys. Rev.* **D71** (2005) 112005, [hep-ex/0501064]. 183

[374] E. Ma, *Phys. Rev. Lett.* **81** (1998) 1171–1174, [hep-ph/9805219]. 183

[375] Y. Cai, J. Herrero-Garcia, M. A. Schmidt, A. Vicente, and R. R. Volkas, *Front.in Phys.* **5** (2017) 63, [1706.08524]. 183

[376] Y. Cai, T. Han, T. Li, and R. Ruiz, *Front.in Phys.* **6** (2018) 40, [1711.02180]. 183

[377] A. Abada *et. al.*,, **FCC** Collaboration, *Eur. Phys. J. ST* **228** (2019), no. 5 1109–1382. 183

[378] J. C. Pati and A. Salam, *Phys. Rev.* **D10** (1974) 275–289. [Erratum: Phys. Rev.D11,703(1975)]. 183, 184

[379] R. N. Mohapatra and J. C. Pati, *Phys. Rev.* **D11** (1975) 566–571. 183, 184

[380] R. N. Mohapatra and J. C. Pati, *Phys. Rev.* **D11** (1975) 2558. 183, 184

[381] G. Senjanovic and R. N. Mohapatra, *Phys. Rev.* **D12** (1975) 1502. 183, 184

[382] G. Senjanovic, *Nucl. Phys.* **B153** (1979) 334–364. 183, 184

[383] W.-Y. Keung and G. Senjanovic, *Phys. Rev. Lett.* **50** (1983) 1427. 185

[384] R. Ruiz, *Eur. Phys. J.* **C77** (2017), no. 6 375, [1703.04669]. 185

[385] M. Nemevsek, F. Nesti, and G. Popara, *Phys. Rev.* **D97** (2018), no. 11 115018, [1801.05813]. 185

[386] G. Cottin, J. C. Helo, and M. Hirsch, *Phys. Rev.* **D97** (2018), no. 5 055025, [1801.02734]. 185

[387] M. Mitra, R. Ruiz, D. J. Scott, and M. Spannowsky, *Phys. Rev.* **D94** (2016), no. 9 095016, [1607.03504]. 185

[388] O. Mattelaer, M. Mitra, and R. Ruiz, 1610.08985. 185

[389] V. Bertone, S. Carrazza, N. P. Hartland, and J. Rojo,, **NNPDF** Collaboration, *SciPost Phys.* **5** (2018), no. 1 008, [1712.07053]. 185

[390] A. Buckley, J. Ferrando, S. Lloyd, K. Nordström, B. Page, M. Rüfenacht, M. Schönherr, and G. Watt, *Eur. Phys. J.* **C75** (2015) 132, [1412.7420]. 185

[391] J. Alwall, C. Duhr, B. Fuks, O. Mattelaer, D. G. Öztürk, and C.-H. Shen, *Comput. Phys. Commun.* **197** (2015) 312–323, [1402.1178]. 185

[392] Y. Bengio and Y. LeCun, eds., *4th International Conference on Learning Representations, ICLR 2016, San Juan, Puerto Rico, May 2-4, 2016, Conference Track Proceedings*, 2016. 185

[393] N. G. Deshpande and E. Ma, *Phys. Rev.* **D18** (1978) 2574. 187

[394] G. Belanger, B. Dumont, A. Goudelis, B. Herrmann, S. Kraml, and D. Sengupta, *Phys. Rev.* **D91** (2015), no. 11 115011, [1503.07367]. 187, 188

[395] D. Bellhouse,, 1981. 188

[396] A. Goudelis, B. Herrmann, and O. Stål, *JHEP* **09** (2013) 106, [1303.3010]. 188

[397] E. Tsymbalov, M. Panov, and A. Shapeev, *Analysis of Images, Social Networks and Texts* (2018) 247–258. 189

[398] P. Athron *et. al.*,, **GAMBIT** Collaboration, *Eur. Phys. J.* **C77** (2017), no. 8 568, [1705.07931]. 190

[399] P. Athron *et. al.*,, **GAMBIT** Collaboration, *Eur. Phys. J.* **C77** (2017), no. 12 824, [1705.07935]. 190

[400] P. Athron *et. al.*,, **GAMBIT** Collaboration, *Eur. Phys. J.* **C77** (2017), no. 12 879, [1705.07917]. 190

[401] P. Athron, J. M. Cornell, F. Kahlhoefer, J. Mckay, P. Scott, and S. Wild, *Eur. Phys. J.* **C78** (2018), no. 10 830, [1806.11281]. 190

[402] P. Athron *et. al.*,, **GAMBIT** Collaboration, *Eur. Phys. J.* **C79** (2019), no. 1 38, [1808.10465]. 190

[403] S. Hoof, F. Kahlhoefer, P. Scott, C. Weniger, and M. White, *JHEP* **03** (2019) 191, [1810.07192]. [Erratum: JHEP11,099(2019)]. 190

[404] M. Chrzaszcz, M. Drewes, T. E. Gonzalo, J. Harz, S. Krishnamurthy, and C. Weniger, 1908.02302. 190

[405] D. P. Kingma and J. Ba, 1412.6980. 191

[406] B. Abbott *et. al.*,, **D0** Collaboration, *Phys. Rev.* **D62** (2000) 092004, [`hep-ex/0006011`]. 195

[407] D0 Collaboration,, **D0** Collaboration, *Phys. Rev. D* **64** (2001) 012004, [`hep-ex/0011067`]. 195

[408] D0 Collaboration,, **D0** Collaboration, *Phys. Rev. Lett.* **86** (2001) 3712–3717, [`hep-ex/0011071`]. 195

[409] D0 Collaboration,, **D0** Collaboration, *Phys. Rev. D* **85** (2012) 092015, [`1108.5362`]. 195

[410] A. Aktas *et. al.*,, **H1** Collaboration, *Phys. Lett.* **B602** (2004) 14–30, [`hep-ex/0408044`]. 195

[411] F. D. Aaron *et. al.*,, **H1** Collaboration, *Phys. Lett.* **B674** (2009) 257–268, [`0901.0507`]. 195

[412] T. Aaltonen *et. al.*,, **CDF** Collaboration, *Phys. Rev.* **D78** (2008) 012002, [`0712.1311`]. 195

[413] T. Aaltonen *et. al.*,, **CDF** Collaboration, *Phys. Rev.* **D79** (2009) 011101, [`0809.3781`]. 195

[414] G. Choudalakis, in *Proceedings, PHYSTAT 2011 Workshop on Statistical Issues Related to Discovery Claims in Search Experiments and Unfolding, CERN,Geneva, Switzerland 17-20 January 2011*, 2011. `1101.0390`. 195

[415] M. Aaboud *et. al.*,, **ATLAS** Collaboration, *Eur. Phys. J.* **C79** (2019), no. 2 120, [`1807.07447`]. 195

[416] A. De Simone and T. Jacques, *Eur. Phys. J.* **C79** (2019), no. 4 289, [`1807.06038`]. 195, 203

[417] R. T. D'Agnolo and A. Wulzer, *Phys. Rev.* **D99** (2019), no. 1 015014, [`1806.02350`]. 195, 203

[418] M. Farina, Y. Nakai, and D. Shih, `1808.08992`. 195

[419] A. Blance, M. Spannowsky, and P. Waite, *JHEP* **10** (2019) 047, [`1905.10384`]. 195

[420] J. Hajer, Y.-Y. Li, T. Liu, and H. Wang, `1807.10261`. 195

[421] O. Cerri, T. Q. Nguyen, M. Pierini, M. Spiropulu, and J.-R. Vlimant, *JHEP* **05** (2019) 036, [`1811.10276`]. 195

[422] E. M. Metodiev, B. Nachman, and J. Thaler, *JHEP* **10** (2017) 174, [`1708.02949`]. 195

[423] J. H. Collins, K. Howe, and B. Nachman, *Phys. Rev. Lett.* **121** (2018), no. 24 241803, [`1805.02664`]. 195

[424] R. D. Ball *et. al.*,, **NNPDF** Collaboration, *Eur. Phys. J.* **C77** (2017), no. 10 663, [`1706.00428`]. 195

[425] M. L. Mangano, M. Moretti, F. Piccinini, R. Pittau, and A. D. Polosa, *JHEP* **07** (2003) 001, [`hep-ph/0206293`]. 196

[426] R. M. Harris and S. Jain, *Eur. Phys. J.* **C72** (2012) 2072, [`1112.4928`]. 197

[427] A. Dal Pozzolo, O. Caelen, Y.-A. Le Borgne, S. Waterschoot, and G. Bontempi, *Expert Systems with Applications* **41** (08, 2014) 4915–4928. 202

[428] G. Kasieczka, B. Nachman, and D. Shih,, Apr, 2019. 203

[429] K. Albertsson *et. al.*, *J. Phys. Conf. Ser.* **1085** (2018), no. 2 022008, [`1807.02876`]. 203

[430] D. Scott,, *Multivariate Density Estimation: Theory, Practice, and Visualization*. Wiley

Series in Probability and Statistics. Wiley, 2015. 204, 206

[431] G. J. McLachlan and K. E. Basford,, *Mixture models: Inference and applications to clustering*, vol. 38. M. Dekker New York, 1988. 204

[432] D. P. Kingma, T. Salimans, R. Jozefowicz, X. Chen, I. Sutskever, and M. Welling, in *Advances in neural information processing systems*, pp. 4743–4751, 2016. 204

[433] D. P. Kingma and M. Welling, 1312.6114. 204

[434] I. Goodfellow, J. Pouget-Abadie, M. Mirza, B. Xu, D. Warde-Farley, S. Ozair, A. Courville, and Y. Bengio, in *Advances in Neural Information Processing Systems 27* (Z. Ghahramani, M. Welling, C. Cortes, N. D. Lawrence, and K. Q. Weinberger, eds.), pp. 2672–2680. Curran Associates, Inc., 2014. 204

[435] M. M. Breunig, H.-P. Kriegel, R. T. Ng, and J. Sander, in *Proceedings of the 2000 ACM SIGMOD international conference on Management of data*, pp. 93–104, 2000. 204

[436] J. Han, J. Pei, and M. Kamber,, *Data Mining: Concepts and Techniques*. The Morgan Kaufmann Series in Data Management Systems. Elsevier Science, 2011. 205

[437] T. Hastie, R. Tibshirani, and J. Friedman,, *The elements of statistical learning: data mining, inference and prediction*. Springer, 2 ed., 2009. 205

[438] S. Theodoridis and K. Koutroumbas,, *Pattern Recognition, Fourth Edition*. Academic Press, Inc., USA, 4th ed., 2008. 205

[439] B. E. Dom, in *Proceedings of the Eighteenth Conference on Uncertainty in Artificial Intelligence*, (San Francisco, CA, USA), pp. 137–145, Morgan Kaufmann Publishers Inc., 2002. 205

[440] T. Kohonen, *Biological Cybernetics* **43** (Jan, 1982) 59–69. 206

[441] I. Assent, *WIREs Data Mining and Knowledge Discovery* **2** (2012), no. 4 340–350, [https://onlinelibrary.wiley.com/doi/pdf/10.1002/widm.1062]. 206

[442] G. E. Hinton and R. R. Salakhutdinov, *Science* **313** (July, 2006) 504–507. 206

[443] Y. Bengio, A. Courville, and P. Vincent, *IEEE Trans. Pattern Anal. Mach. Intell.* **35** (2013), no. 8 1798–1828. 206

[444] Z. Wang and D. W. Scott, *WIREs Computational Statistics* **11** (2019), no. 4 e1461, [https://onlinelibrary.wiley.com/doi/pdf/10.1002/wics.1461]. 206

[445] B. W. Silverman,, *Density Estimation for Statistics and Data Analysis*. Chapman & Hall, London, 1986. 206

[446] H.-P. Kriegel, P. Kröger, J. Sander, and A. Zimek, *WIREs Data Mining and Knowledge Discovery* **1** (2011), no. 3 231–240, [https://onlinelibrary.wiley.com/doi/pdf/10.1002/widm.30]. 206

[447] B. Nachman and D. Shih, 2001.04990. 206